Report Title:

Micro-Structured Sapphire Fiber Sensors for Simultaneous Measurements of High-T and Dynamic Gas Pressure in Harsh Environments

Type of Report:

Final Project Technical Report

Reporting Period Start/Stop Date:

October 1, 2009 – Sepetember 30, 2014

Principal Authors' Names:

Dr. Hai Xiao
Dr. Hai-Lung Tsai
Dr. Junhang Dong

Date Report Issued:

December 31, 2014

DOE Award Number:

DE-FE0001127

Name and Address of Submitting Organization:

Missouri University of Science and Technology
202 Centennial Hall
300 W. 12th St.
Rolla, MO 65409-1330

Disclaimer

"This report was prepared as an account of work sponsored by an agency of the United States Government. Neither the United States Government nor any agency thereof, nor any of their employers, makes any warranty, express or implied, or assumes any legal liability or responsibility for the accuracy, completeness, or usefulness of any information, apparatus, product, or process disclosed, or represents that its use would not infringe privately owned rights. Reference herein to any specific commercial product, process, or service by trade name, trademark manufacturer, or favoring by the United States Government or any agency thereof. The views and opinions of authors expressed herein do not necessarily state or reflect those of the United States Government or any agency thereof."

Abstract

This is the final report for the program "Micro-Structured Sapphire Fiber Sensors for Simultaneous Measurements of High Temperature and Dynamic Gas Pressure in Harsh Environments", funded by NETL, and performed by Missouri University of Science and Technology, Clemson University and University of Cincinnati from October 1, 2009 to September 30, 2014. Securing a sustainable energy economy by developing affordable and clean energy from coal and other fossil fuels is a central element to the mission of The U.S. Department of Energy's (DOE) National Energy Technology Laboratory (NETL). To further this mission, NETL funds research and development of novel sensor technologies that can function under the extreme operating conditions often found in advanced power systems.

The main objective of this research program is to conduct fundamental and applied research that will lead to successful development and demonstration of robust, multiplexed, micro-structured silica and single-crystal sapphire fiber sensors to be deployed into the hot zones of advanced power and fuel systems for simultaneous measurements of high temperature and gas pressure. The specific objectives of this research program include: 1) Design, fabrication and demonstration of multiplexed, robust silica and sapphire fiber temperature and dynamic gas pressure sensors that can survive and maintain fully operational in high-temperature harsh environments. 2) Development and demonstration of a novel method to demodulate the multiplexed interferograms for simultaneous measurements of temperature and gas pressure in harsh environments. 3) Development and demonstration of novel sapphire fiber cladding and low numerical aperture (NA) excitation techniques to assure high signal integrity and sensor robustness.

To achieve the above challenging goals, we have formed a multidisciplinary research team consisting of three professors from two universities. The team worked collaboratively on fundamental and applied research on the following three major technical areas:

1) Novel assembly-free microstructured fiber optic sensors by femtosecond laser micromachining. During the project period, the team has successfully established a fully automated fs laser micromachining system for intelligent fabrication of various fiber optic sensor devices. Specifically, we have successfully designed, fabricated and demonstrated the concepts of many new fiber senor devices including:

a) Open cavity optical fiber inline extrinsic Fary-Perot interferometer

b) Sealed cavity optical fiber extrinsic Fabry-Perot interferometer

c) Intrinsic optical fiber inline Fabry-Perot interferometer

d) Optical fiber hybrid extrinsic/intrinsic Fabry-Perot interferometer (HEIFPI)

e) Optical fiber inline Michelson interferometer

f) Optical fiber inline Mach-Zehnder interferometer

g) Fiber Bragg grating

f) Long period fiber grating

h) Reflective mode surface enhanced Raman scattering probe

i) Optical fiber inline waveplate

j) Optical fiber inline polarizer

k) Optical fiber inline micro fluidic channel

Many of these new devices have been successfully demonstrated for sensing applications, showing better performance than their counterparts fabricated using the traditional micro-assembly based methods. These novel silica and sapphire fiber sensors have great potentials that are yet to be fully discovered for measurements of various important parameters in high temperatures and high pressure harsh environments.

2) Novel signal processing methods. We have successfully designed and demonstrated the proposed novel wavelength division multiplexing based signal processing method to simultaneous interrogation of a number of cascaded microstructured optical fiber sensors. In addition to completion of the proposed method, we have also invented a brand new sensing concept – the optical carrier based microwave interferometry (OCMI) sensing technology. For the first time, High performance interferograms can now be obtained routinely using OCMI on highly multimode optical fibers (including the uncladded sapphire fibers). In addition, the new OCMI technology, together with the modern communication technology and fs laser micromachining technique, allow us to achieve spatially continuous, fully distributed sensing using practically any optical waveguides.

3) Novel sapphire cladding. We have successfully cladded the sapphire fibers and validated their performance up to 1200℃. This is the first demonstration of such optically-functional high-temperature cladding for sapphire fibers. We successfully synthesized spinel thin film as cladding coating of the sapphire fiber using polymeric precursor method. The coating process has been fully optimized to obtain defect-free and optically functional cladding layers. The

coated sapphire fibers were fully characterized experimentally to show their superior optical properties and high temperature stabilities.

In addition, we have established a high temperature sensor testing facility with the full capability of testing the developed sensors under high temperature and high pressure conditions. We have also conquered many engineering challenges towards the practical deployment and application of the developed sensors and instrumentation. For example, we have successfully designed and implemented a new method to package the developed sapphire fiber sensor for high temperature measurement and successfully validated the packaged sensor at high temperatures up to 1600°C.

In summary, under the close collaborations among the three research groups, we have completed all the tasks and fulfilled the proposed research objectives. All the technical milestones have been achieved and the project has been completed successfully. The technical breakthroughs obtained under this project provide novel harsh environment sensing technologies that can be directly used in existing and next generation power and fuel systems for *in situ* monitoring and advanced control of key operational parameters to achieve the challenging goals of enhanced efficiency, reduced emission, and improved reliability/availability/maintainability. The research may also have profound impacts on the general field of harsh environment sensing as it fosters a number of new inventions that may benefit the sensors and instrumentation community as well as the entire energy sector.

Table of Contents

List of Figures

1. Background and Technology Reviews

1.1 Introduction

This research was initially motivated by developing novel sensing or monitoring in extreme environments of fossil energy systems. The societal impact of improvements in efficiency of existing fossil-fuel infrastructure can be very substantial. According to the International Energy Agency's 2002 World Energy Outlook, renewable energy sources (including hydro) provided about 5% of the world's energy use in 2000, and they project the growth in renewables to barely keep-up with the growth in demand providing 6.5% in 2030 [42]. Energy forecast predict that fossil fuels will be the dominant energy source in the foreseeable future and that by 2030 we will rely on fossil fuel for about 80% of our energy needs. Coal continues to be the dominant fossil fuel around the world for electric power generation [43]. Production of affordable and clean-coal energy is thus the key to secure a sustainable economic development. Towards this goal, the research community and industry have been working diligently to develop and implement various advanced technologies for improved operation efficiency/safety/reliability/availability/ maintainability, enhanced fuel-flexibility and reduced (or even near-zero) emissions [44]. It has long been realized that operations of coal-based power plants must be optimized at all levels by utilizing advanced process controls. Low-cost, reliable, in situ sensors are highly demanded for advanced process control and lifecycle management in existing and future advanced power and fuel systems. The Electric Power Research Institute (EPRI) estimated that approximately $409 million can be saved annually in the existing fossil-fuel-based power generation plants in the United States by implementing advanced monitoring and control technology to achieve a 1% increase in efficiency [43].

Next generation coal power plants (e.g., the new IGCC plant) use synthesis gas (syngas) produced by coal gasification that may operate at temperatures as high as 1450ºC. Recent studies have shown that gas turbines operating at elevated temperatures will not only increase efficiency (about 60% efficiency improvement on average), but also reduce emissions through improvement in waste product removal and storage [4]. In addition, future coal power plants need to be fuel-flexible. Coal syngas and high-hydrogen content (HHC) fuels could vary considerably in fuel composition and heating value. The variations could lead to instabilities and excessive pressure pulsations, resulting in component fatigue, mechanical failures and costly outages and repair.

It has been estimated that more than 1000 sensors are needed in a typical power plant to ensure its correct operation [43]. These sensors share the common requirement of being able to survive and operate in the high temperature, high pressure and corrosive/erosive harsh environments for a long period of time. Among the parameters of interests, temperature and dynamic gas pressure are the two important parameters that need to be constantly monitored to ensure proper operation of the system [7]. Temperature sensors are needed throughout the entire system for in situ measurements of the flame, gas and surface temperatures at various sections. The information of dynamic pressures within a combustion turbine may be used to detect and correct instabilities before they cause serious damage [8-11].

Although power plant control systems have been constantly upgraded, improvements in sensors and instrumentation have lagged behind. The bulk of the efforts have focused on signal processing and signal conditioning, rather than the basic sensing elements and devices. Consequently, the various sensors used in today's typical power plant have remained virtually unchanged since 1970. Unfortunately, these sensors are incapable of operating directly in the

locations of high temperature and high pressure harsh environments. Current sensor technologies capable of operating in harsh conditions are extremely limited. Given that clean-coal power production will be the necessity and reality for many years to come, fundamental and applied research is required to address the significant technological challenges and capability gaps in harsh environment sensors needed for monitoring existing and future power and fuel systems.

1.2 Overview of current technologies

Sensors and sensor systems that are capable of surviving and operating in harsh environments have found many applications in modern industry. Examples include oil and gas extraction, power generation, coal gasification, gas turbine operation, aircraft engineer design and monitoring, and petrochemical refining and separation. The term “hash environment” can be the summary of a lot of extreme conditions including high temperature, high pressure, chemically corrosive/erosive, toxic, explosive, radioactive, and strong electromagnetic disturbance. These extreme conditions normally prevent the usage of commercially available, general purpose electrical sensors. Optical fiber sensors, with its glass nature and optical interrogation principle, may provide a viable solution for sensing and monitoring in these harsh conditions. However, for the time being, the real sensing techniques/configurations that can withstand the extremely harsh environment posed by the high temperature, high pressure and corrosive agent in power system, e.g., coal gasifiers and gas turbines, etc, are still limited.

Although power plant control systems have been constantly upgraded, improvements in sensors and instrumentation have lagged behind. The bulk of the efforts have focused on signal processing and signal conditioning - the smart electronics, rather than the basic sensing elements

and devices. Consequently, the various sensors used in today's typical power plant have remained virtually unchanged since 1970. Unfortunately, these sensors are incapable of operating directly in the locations of high temperature and high pressure harsh environments. In this program, we focus our research on developing novel sensors for *in situ*, simultaneous measurements of temperature and dynamic pressure. The measurements of these parameters are required throughout the entire process of a power/fuel system but the current available technologies fall in short. The requested research investment is thus well justified for its broad impacts. The multidisciplinary research efforts in this program will not only advance the fundamental science involved in harsh environment sensing, but also lead to the development of the state-of-the-art sensors and new measurement techniques that are directly applicable to process monitoring and control.

1.2.1 Sensors currently used in power plant monitoring

Temperature sensors: Currently, resistance temperature detectors (RTDs) and thermocouples are among the most commonly used temperature sensors for measurements of flame temperatures, liquid entering and exiting heaters, fuel temperatures, and turbine heat. Thermocouples have been used for measurement of temperatures above 2000°C with cooling. [13] Specially designed RTDs with an on-line calibration mechanism can maintain 1 percent accuracy at 1100°C. [12] However, packaging of the sensor components such as the resistance wire, insulators, sheath, and end seals is always a challenge for achieving and maintaining desired electrical properties. At high temperatures, the large thermal and mechanical stresses often cause mechanical failures to these temperature sensors due to mismatch in coefficient of thermal expansion (CTE) of dissimilar materials. In addition, the metal/alloy wires in a thermocouple and the metal lead/joint in a RTD cannot withstand a corrosive environment. [13,

14] As a result, RTDs and thermocouples have limited lifetime, poor reliability, and high maintenance cost.

Pressure sensors: Power plant operators currently rely on pressure switches and nonfluid-filled or fluid-filled pressure transmitters to measure pressure drop, for example, of feed-water sent to boilers or steam sent to turbines. These instruments lose their accuracy over time and must be recalibrated frequently due to the adverse operating environment. **[5]** The drift of these pressure transmitters can increase heat rates, decrease turbine efficiency, and lower plant safety. In addition, such drift is difficult to detect during steady-state operation when the transmitter appears to function normally. Dynamic pressures can be measured by pressure transducers, which typically utilize strain-gauge technology in their construction, and cannot endure the extreme temperatures at the combustor. Piezoelectric crystal (e.g., quartz) devices have also been used for measurement of dynamic gas pressure in gas turbines at high temperatures (~700°C). [8-11] However, the maximum operating temperature of piezoelectric pressure sensors are limited. In addition, they suffer from electromagnetic interference (EMI) and large temperature cross-sensitivity.

1.2.2 Current state-of-the-art harsh environment sensing technologies

High temperature electronic sensors: Specially designed electronic sensors and circuits have been investigated for high temperature applications. Many of the research efforts have focused on the silicon-on-insulator (SOI) technology. Representative examples include thin or thick film SOI devices for temperature measurement, [15] piezoresistive SOI sensors for stress/strain measurement, [16] and surface acoustic wave (SAW) SOI sensors for pressure measurement.[17] These sensors had shown high resolution for applications in high temperatures

up to 700°C. Sensors have also been developed using silicon carbide (SiC) and silicon nitride (SiN) substrates which can operate at temperatures as high as 800°C. **[18]** However, these electronic devices are inherently sensitive to EMI, which renders relatively low accuracy in measurement. In addition, the strong temperature dependence (thus large temperature cross-sensitivity) has also made it difficult to develop sensors for measurement of parameters other than temperature.

MEMS sensors: Microelectromechanical systems (MEMS) technology has been investigated for fabrication of miniaturized sensors to measure temperature, pressure, strain and accelerations. These MEMS devices are commonly manufactured using standard IC processing along with anisotropic etching and wafer bonding. [19-22] MEMS-based sensors have the advantages of small size, high sensitivity, low cost, potential of large production, and batch fabrication process for a large production yield. Optically interrogated MEMS devices are expected to be more suitable than electrically interrogated MEMS devices for harsh environment applications. [19, 20] However, a major problem associated with most MEMS sensors is their inherent cross sensitivity to temperature. For example, the influence of temperature on a piezoresistive MEMS pressure sensor can cause a drift of about 100Pa per day, which makes them deficient for long-term measurement. [21] The packing is always a challenge for MEMS sensors. As a result, applications of MEMS sensors have been limited in temperatures below 600°C. [22]

Fiber optic sensors: Optical fiber sensors are very attractive for applications in harsh environment due to their proven advantages of small size, lightweight, immunity to EMI, resistance to chemical corrosion, high sensitivity, large bandwidth, and remote operation capability. [23, 24] Among the many types of fiber sensors, fiber Bragg gratings (FBG), long

period fiber gratings (LPFG), and Fabry-Perot interferometers (FPI) are among the mostly-investigated for high temperature applications. Fiber grating sensors have the advantages of immunity to the optical power loss variation of the optical network and the capability of multiplexing many sensors to share the same signal processing unit. [25-28] LPFGs made by CO2 laser irradiation, chemical etching, mechanical dicing and electric arc modification have successfully survived temperatures up to 1200°C. [29] However, their long-term reliability at very high temperatures (>1000°C) has been a concern due to the degradation of optical properties and mechanical strength. Moreover, fiber grating sensors exhibit relatively large cross-dependence of temperature which limits their scale of applications in harsh environments.

Hermetically packaged extrinsic fiber Fabry-Perot interferometers (EFPI) have also been successfully applied to harsh environment sensing. [30-33] Laser fusion or electric arc sealed EFPI sensors were successfully tested for measurement of temperature (up to 800°C) and pressure (up to 10,000 psi). Micromachined single-crystal silicon carbide EFPI temperature and pressure sensors have also been demonstrated for high temperature applications. [34, 35] However, fabrications of these EFPI sensors involve complicated procedures of assembling multiple components, which compromises the robustness of the device due to the limited thermal and mechanical strength of the joints. The mismatch of the coefficient of thermal expansion (CTE) of the various parts can also seriously lower the thermal stability of the device.

Sapphire fiber based sensors: The long-term operating temperature of standard telecommunication fiber-based sensors is limited by the annealing point (1120°C) of fused silica glass. To further increase the operating temperatures, researchers turned to single-crystal sapphire fibers which have a high melting point of about 2053°C, low optical loss in a large spectrum window, superior mechanical strength, and excellent resistance to chemical corrosion.

Up to date, a number of sapphire fiber sensors have been demonstrated by various research groups. Examples include: 1) sapphire rod blackbody radiation-based temperature sensors, [36] 2) sapphire fiber temperature sensors based on birefringence-balanced polarimetry, [37] 3) EFPI sensors made by bonding sapphire fibers on a ceramic substrate for measurement of temperature, strain, and pressure, [38, 39] and 4) intrinsic Fabry-Perot interferometric (IFPI) sensors by attaching a sapphire fiber to a sapphire plate for temperature measurement. [40] Although these sensors have been demonstrated for high temperature (>1000°C) applications in laboratory and field tests, their long term stability is a concern due to the use of ceramic epoxies in device fabrication. For example, CTE mismatch of the assembled pieces may cause structural failure of the sensor device at high temperatures. More recently, sapphire fiber grating based temperature sensors were also demonstrated. [41, 42] However, the gratings have very weak signal strengths due to the highly multimode nature of non-cladded sapphire fibers, resulting in poor measurement accuracy.

A major issue related to existing sapphire sensor stems from the uncladded nature of sapphire fibers. Single-crystal sapphire fibers cannot be grown as a core-clad structure from the established rod-in-a-tube method because convective currents in the molten zone quickly destroy the geometrical structure of the source rod. [43, 44] Uncladded sapphire fibers suffer from a number of undesirable characteristics such as unpredictable optical loss and highly multimode operation. The unpredictable optical loss during applications may impose a large error to the measurement results. The highly multimode nature makes it difficult to obtain high quality signal in conventional assembly-based sensor structures especially when optical interference is used as the sensing principle. A number of high temperature materials have been explored for cladding sapphire fibers, including for example, polycrystalline alumina (Al2O3), metal niobium, silicon

carbide (SiC), yttrium stabilized zirconia (YSZ), and other alloys (e.g., SiOxNy, MgxSiOy and TixSiyO with a variable x/y ratio). [45-47] However, none represents a universally acceptable solution. Cladding materials that are both optically and thermally suitable are yet to be found.

1.3 Requirements, Opportunities and Challenges

1.3.1 General requirements on harsh environment sensors

There exist a number of important considerations and critical requirements for sensors targeting harsh environment applications.

First, the sensor needs to survive the harsh environment. This requires that the sensor material, structure, package, and connection must be robust to experience drastic changes in environmental conditions such as a large temperature swing.

Second, the sensor structure needs to be stable to operate in these extreme conditions. The common concerns for sensors targeting harsh environment applications include the long-term stability and cross-sensitivity. Long-term stability requires that the sensor does not drift as a result of structural degradation when placed in an extreme environment. Cross-sensitivity, especially the temperature cross-sensitivity, could result in large amount of measurement error induced by changes in environmental parameters other than the one to be measured/monitored. In most cases, more than one adverse parameter can be found in a typical harsh environment. For example, in a combustion engine, high temperature and high pressure coexist at the same time. In this case, a pressure sensor for engine monitoring should have zero response to temperature change.

Third, the accessibility of the sensor needs to be considered. Sometimes, engineers found that even if the sensor itself survived harsh environments, it is hard to route the cable to attach the sensor or the cable may not survive the environment as the sensor does. Or it is simply not possible to place the sensor in the shielded environment, for example, to monitor the inner environment of an ignition chamber of a combustion engine, once needs to intrusively deploy the sensors, making the ignition less efficient or even bringing in safety issues.

1.3.3 Challenges and opportunities

Based on the above reviews, it is clear that, in spite of the large amount of progress made in the past toward high temperature harsh environment sensing, there still exist technical challenges and issues that are missing appropriate solutions and the current state-of-art technologies do not provide satisfactory solutions. Among most of the high temperature sensors, survivability is still an issue, since they are manufactured through assembling a number of components. And in most cases, these components are made by different materials, which making it less mechanically stable at higher temperatures. The CTE mismatch of different components would induce dominant stress in between the different components and eventually damage the device from inside at elevated temperatures. This problem challenges the packaging of the sensors associated with assembly process. Another common issue among these sensors is the temperature cross-sensitivity. Although it may be more evident for electric based sensors, temperature cross-sensitivity is critical in optical based sensor as well at higher temperatures. To deal with this, the conventional way is to place a high accuracy temperature sensor next to the original sensor designed for a specific parameter monitoring. Apparently, this would increase the sensor operating expense. In addition, the strong electromagnetic field may couple into the sensor system, either from sensor probe or from the trace routing to the sensor head.

Based on above reviews, we conclude that electronic sensors cannot survive the extremely high temperature (~1600°C) harsh conditions involved in next generation power plant monitoring and control. The sapphire fiber based sensor is one of the most promising candidates for operations in high temperature harsh environments. However, the following technical issues must be sufficiently addressed through fundamental research before the sensors can be applied to real-world applications.

Issue #1: The existing sapphire sensors lack the required robustness and long-term stability.

Issue #2: The existing sapphire sensors have shown large temperature cross-sensitivity which imposes a difficulty for measurement of parameters other than temperature.

Issue #3: Uncladded sapphire fibers impose a number of undesirable characteristics for sensing applications, e.g., unpredictable loss and highly multimode operation.

Supported by NETL (National Energy Technology Laboratory), U.S. Department of Energy, the proposed research aims to address these technical challenges and bridge the technological gaps in harsh environment sensing. This work is performed collaboratively among three universities including Missouri University of Science and Technology, the University of Cincinnati and Clemson University.

1.4 References

1. S. Maley, R. R. Romanosky, and Z.Y. Chen, “Sensors and Controls Workshop: Summary Report”, DOE/NETL Workshop Proceedings, 2002/1162, November 2001.

2. R. R. Romanosky, “The 2002 NETL Sensors and Control Program Portfolio Review and Roadmapping Workshop: Gas, Emissions, and Process Monitoring”, DOE/NETL Workshop Proceedings, Pittsburgh, PA, USA, October 2002.

3. D.G. Hawkins, D.A. Lashof and R.H. Williams, “What to Do about Coal,” Scientific American Magazine, p.68-75, 2006.

4. J. H. Ausubel, “Big Green Energy Machines,” The Industrial Physicist, American Inst. of Physics Journal, p.20-24, 2004.

5. M. Valenti, “A new generation of power plant sensors,” Business Exchanges-Mechanical Engineering, http://www.allbusiness.com/professional-scientific/scientific-research-development/468579-1.html, September 1, 1994.

6. S. Maley and R. R. Romanosky, “Plant Process Control Workshop-Summary Report,” U.S. Department of Energy, National Energy Technology Laboratory, Morgantown, June, 2006.

7. D. K. Manley, A. Mcllroy, and C. A. Taatjes, “Research needs for future internal combustion engines,” AIP Physics Today, p.47-52, Nov. 2008.

8. A.J.L. Verhage, H.J. Jansen, and P.M.P. Stevens, “Predictive Diagnostics for Combustion Chamber Damage and Flame Instabilities in Gas Turbines,” ECOS Conference, Twente, Netherlands, 2000.

9. R. Swanekamp, “Raising the Reliability of Advanced Gas Turbines,” Power Engineering Magazine, v.146, p. 24-34, 2002.

10. C.G. James, A.J.L. Verhage, “Dynamic Pressure Monitoring in Gas Turbines,” - Technical Note, SKF Reliability Systems, 2002. Available at http://www.skf.com/files/058467.pdf.

11. L. S. Langston, “Fahrenheit 3,600: Everywhere you look, the gas turbine industry is running hot,” ASME Mechanical Engineering Magazine, v.129, p.34-37, 2007.

12. J. Bareiss, P. Buck, B. Matschecko, “RIMAP demonstration project. Risk-based life management of piping system in power plant Heilbronn,” International Journal of Pressure Vessels and Piping, v. 81, p.807-813, 2004.

13. K. Metzner, U. Wilke, “European THERFAT project - thermal fatigue evaluation of piping system Tee-connections,” Nuclear Engineering and Design, v. 235, p. 473-484, 2005.

14. R. E. Bentley, “Thermocouple materials and their properties,” Chap. 2 in Theory and Practice of Thermoelectric Thermometry: Handbook of Temperature Measurement, v.3, p. 25-81, Springer-Verlag Singapore, 1998.

15. Z.H. Wu, P.T. Lai, J.K.O. Sin, “A new high-temperature thermal sensor based on large-grain polysilicon on insulator,” Sensors and Actuators A-Physical, v.130, p.129-134, 2006.

16. Z.Y. Wang, K. Tian, Y.Z. Zhou, L.Y. Pan, C.H. Hu, L.T. Liu, “A high-temperature silicon-on-insulator stress sensor,” Journal of Micromechanics and Microengineering, v.18, p.045018, 2008.

17. Y.L. Zhao, L.B. Zhao, Z.D. Jiang, “High temperature and frequency pressure sensor based on silicon-on-insulator layers,” Measurement Science and Technology, v.17, p.519-523, 2006.

18. N.G. Wright, A.B. Horsfall, “SiC sensors: a review,” Journal of Physics D-Applied Physics, v.40 p.6345-6354, 2007.

19. D. R. Sparks, S.C. Chang, and D.S. Eddy, “Application of MEMS Technology in automotive sensors and actuators”, Proceedings of the 1998 International Symposium on Micromechatronics and Human Science, MHS '98, p. 9-15, 1998.

20. J. Zhou, S. Dasgupta, H. Kobayashi, J.M. Wolff, H.E. Jackson, J.T. Boyd, “Optically interrogated MEMS pressure sensors for propulsion applications,” Optical Engineering; v.40, p.598-604, 2001.

21. B.S. Douma, P. Eigenraam, and P. Hatlem, “Modeling the pressure and temperature sensitivity of an optically-excited micromachined silicon sensor for permanently installed downhole monitoring systems,” Sensors and Actuators, A-Physical, v.31, p.215-219, 1992.

22. M. Tanaka, “An industrial and applied review of new MEMS devices features,” Microelectronic Engineering, v.84, p.1341-1344, 2007.

23. E. Udd, “Fiber Optic Sensors: An Introduction for Engineers and Scientists”, John Wiley & Sons, Inc., 1991.

24. A. Morris, M. Kourmpetis, I.D. Dear, M. Sjodahl, J.P. Dear, “Optical strain monitoring techniques for life assessment of components in power generation plants,” Proceedings of the Institution of Mechanical Engineers, Part A-Journal of Power and Energy, v.221, p.1141-1152, 2007.

25. P. Ferraro and G. De Natale, “On the possible use of optical fiber Bragg gratings as strain sensors for geodynamical monitoring,” Optics and Lasers in Engineering, v.37, p.115-30, 2002.

26. A.D. Kersey, “Optical fiber sensors for permanent downwell monitoring applications in the oil and gas industry”, IEICE Transaction on Electronics, v.E83C, p.400-404, 2002.

27. P.M. Nellen, P. Mauron, A. Frank, U. Sennhauser, K. Bohnert, P. Pequignot, P. Bodor, and H. Brandle, “Reliability of fiber Bragg grating based sensors for downhole applications,” Sensors and Actuators, A-Physical, v.103, p.364-376, 2003.

28. C. Zhan, Y. Zhu, S. Yin, P. Ruffin, “Multi-parameter harsh environment sensing using asymmetric Bragg gratings inscribed by IR femtosecond irradiation,” Optical Fiber Technology, v.13, p.98-107, 2007.

29. D.D. Davis, T.K. Gaylord, E.N. Glytsis and S.C. Mettler, “Very-high-temperature stable CO2-laser-induced long-period fiber gratings,” Electronics Letters, v.35, p.740-742, 1999.

30. H. Xiao, J. Deng, Z. Wang, W. Huo, P. Zhang, M. Luo, G. R. Pickrell, R. G. May, and A. Wang, “Fiber optic pressure sensor with self-compensation capability for harsh environment applications,” Optical Engineering, v.44, p. 054403, 2005.

31. A. Wang, H. Xiao, J. Wang, Z. Wang, W. Zhao, and R.G. May, “Self-calibrated interferometric-intensity-based optical fiber sensors", Journal of Lightwave Technology, v.19, p.1495-1501, 2001.

32. M. Luo, J. Hui, J. Dong, R.A. Normann, and H. Xiao, “Fiber Optic Fabry-Perot Interferometric Sensor Interrogated by the Amplified Spontaneous Emission of an Erbium-Doped Fiber Amplifier for Geothermal Applications,” SPIE: Optics East, Boston, MA, in Proc. of SPIE, vol.6008, p.60081H-1. Oct. 2005.

33. A. Wang, G. Pickrell, H. Xiao, B. Qi, R.G. May, "Miniature Laser Bonded Self-Calibrating Interferometric Fiber Optic Sensor," R&D 100 award 2004.

34. N. A. Riza, M. A. Arain, and F. A. Perez., "Harsh Environments Minimally Invasive Optical Sensor using Free-space Targeted Single Crystal Silicon Carbide," IEEE Sensors Journal, v.6, p.672-685, 2006.

35. N. A. Riza, F. N. Ghauri, and F. Perez, "Silicon Carbide-based remote wireless optical pressure sensor," IEEE Photon. Tech. Lett Journal, v.19, p.504-506, 2007.

36. G.A. Bufetova, V.V. Kashin, D.A. Nikolaev, "Zonal doped crystal fibers for temperature measurements," Laser Physics Letters, v.4, p.440-443, 2007.

37. Y.B. Zhang, G.R. Pickrell, B. Qi, A.B. Wang, "Single-crystal sapphire-based optical high-temperature sensor for harsh environments," Optical Engineering, v.43, p.157-164, 2004.

38. H. Xiao, J. Deng, G.R. Pickrell, R.G. May, and A. Wang, "Single crystal sapphire fiber-based strain sensor for high temperature applications," *Journal of Lightwave Technologies*, v. 21, p.2276-2283, 2003.

39. Y.Z. Zhu, Z.Y. Huang, F.B. Shen, A.B. Wang, "Sapphire-fiber-based white-light interferometric sensor for high-temperature measurements," Optics Letters, v.30, p.711-713, 2005.

40. Y.Z. Zhu, A.B. Wang, "Surface-mount sapphire interferometric temperature sensor," Applied Optics, v. 45, p. 6071-6076, 2006.

41. D. Grobnic, S.J. Mihailov, C.W. Smelser, H.M. Ding, "Sapphire fiber Bragg grating sensor made using femtosecond laser radiation for ultrahigh temperature applications," IEEE Photonics Technology Letters, v.16, p.2505-2507, 2004.

42. C. Zhan, J. H. Kim, S. Yin, P. Ruffin, and C. Luo, "High temperature sensing using higher-order-mode rejected sapphire fiber gratings," Optical Memory and Neural Networks, v.16, p.204–210, 2007.

43. G.N. Merberg and J. Harrington, "Optical and mechanical properties of single-crystal sapphire optical fibers," Applied Optic, v.32, p.3201-3209, 1993.

44. R. K. Nubling and J. A. Harrington, “Optical properties of single-crystal sapphire fibers,” Applied Optic, v.36, p.5934-5940, 1997.

45. S. B. Desu, R. O. Claus, R. Raheem, and K. A. Murphy, “High temperature sapphire optical sensor fiber coatings,” SPIE proceedings, v.1307, p.2-9, 1990.

46. A. R. Raheem-Kizchery, S. B. Desu, and R. O. Claus, “High temperature refractory coating materials for sapphire waveguides,” SPIE proceedings, v.1170, p.513-517, 1989.

47. J. B. Davis, J. P. A. Lfvander, and A. G. Evans, “Fiber coating concepts for brittle-Matrix composites,” Journal of American Ceramic Society, v.76, p.1249-1257, 1993.

2. Objectives and Approaches

2.1 Objectives

The main objective of this research program is to conduct fundamental and applied research that will lead to successful development and demonstration of robust, multiplexed, micro-structured silica and single-crystal sapphire fiber sensors to be deployed into the hot zones of advanced power and fuel systems for simultaneous measurements of high temperature (upto 1600°C) and dynamic gas pressure.

The specific objectives of this research program include:

1) Design, fabrication and demonstration of multiplexed, robust silica and sapphire fiber temperature and dynamic gas pressure sensors that can survive and maintain fully operational in high-temperature harsh environments. This objective has been achieved by a novel, assembly-free hybrid extrinsic/intrinsic Fabry-Perot interferometer (HEIFPI) that is optimally designed for multiplexing and one-step fabricated by femtosecond (fs) laser micromachining for robustness.

2) Development and demonstration of a novel method to demodulate the multiplexed interferograms for simultaneous measurements of temperature and dynamic gas pressure in harsh environments. This objective has been achieved by a novel signal processing approach based on advanced digital filtering in combination with microwave-photonic instrumentation.

3) Development and demonstration of novel sapphire fiber cladding and low numerical aperture (NA) excitation techniques to assure high signal integrity and sensor robustness. This objective will be achieved by the novel double-cladding concept realized by polymeric precursor

nanofilm deposition/solidification and the singlemode-multimode-sapphire (SMS) fiber splicing technique.

To achieve the above challenging goals, we have formed a multidisciplinary research team consisting of three professors from two universities. The team has demonstrated combined expertise and history of successful collaborations in closely related areas to assure the successful execution of the planed tasks and delivery of the proposed objectives. Although this project mainly focused on solving the fundamental and engineering challenges involved in design, fabrication, integration, and application of the proposed novel sensors and measurement system, we collaborated with researchers and engineers at Ameren Corp. (a power utility company headquartered in St. Louis, MO). The Ameren engineers provided expert consultations throughout the project. Upon successful demonstration of the sensors in laboratory tests, we have also explored the opportunity of installing and testing our sensors using Ameren's test facilities.

2.2 Approaches

In this project, we performed fundamental and applied research that led to the successful development and demonstration of robust, multiplexed, micro-structured sensors that use silca and single-crystal sapphire fibers. The project has three main objectives: (1) to incorporate silica and sapphire fibers into sensors that are fully operational at high temperatures in a simulated harsh environment; (2) to develop and demonstrate novel sensors to simultaneously measure temperature and gas pressure in harsh environments; and (3) to develop and demonstrate novel sapphire fiber cladding and low numerical excitation techniques to ensure high signal integrity and sensor robustness.

2.2.1 Assembly-free sensors by femtosecond laser micromachining

The initial sensor design is the hybrid extrinsic/intrinsic Fabry-Perot interferometer (HEIFPI) sensors directly micro-machined on a silica or sapphire fiber using an ultrafast laser. This hair-thin, cylindrical filament made of fused silica or single-crystal sapphire would able to transmit light by confining it within regions of different optical indices of refraction. To achieve this object, we used fs laser to fabricate micromathined structures on different substrates to figure out the optimal fabrication parameters and tried to realize this sensing idea on silica and sapphire optical fibers.

We have successfully fabricated the hybrid extrinsic/intrinsic Fabry-Perot interferometer (HEIFPI) sensors directly micro-machined on silica optical fibers. The sensing performance of simultaneous measurement of temperature and pressure are presented. Taking advantages of this modern fabrication technique, we have also successfully developed a series of fiber optic sensors based on different sensing mechanisms using micro-machined substrates and fiber devices. These novel silica fiber sensors have been successfully demonstrated for measurements of high temperatures and gas pressures in harsh environments, which proved the feasibility of the sensor concepts.

2.2.2 Novel signal processing methods

During the procedure to fabricate sapphire HEIFPI sensor, we discovered that it is relatively difficult to achieve a high quality sapphire fiber interferometer with high signal quality, which is mostly due to the single crystal properties and highly multimode nature of sapphire fiber. To solving this inherent challenge, we steered our research by combining microwave with optics

together and successfully invented a brand new, novel sensing concept, optical carrier based microwave interferometry (OCMI) sensing technology. For the first time, High performance interferograms can now be obtained routinely using OCMI on highly multimode optical fibers (including the uncladded sapphire fibers). In addition, the new OCMI technology, together with the modern communication technology and fs laser micromachining technique, allow us to achieve spatially continuous, fully distributed sensing using practically any optical waveguides. The new concept of OCMI is described in detail, including the theory, simulation, instrumentation, experimental results on silica glass fibers and single crystal sapphire fibers.

2.2.3 Novel sapphire cladding

In addition, we have successfully cladded the sapphire fibers and validated their performance up to 1200℃. This is the first demonstration of such optically-functional high-temperature cladding for sapphire fibers. The synthesis and characterization of spinel thin film as cladding coating of sapphire fiber are presented and the NA of the cladded sapphire fibers and other properties are also discussed.

3. Femtosecond Laser Micromachining System

The latest advancement in femtosecond (fs) based micromachining technology has opened a new window of opportunity for fabrication of micro-devices and sensors. Direct exposure of most solid materials (including fused silica glass) to high power fs laser pulses may lead to the ablation of a thin layer of materials at the laser focal point. Due to the muliphoton nature of the laser-material interaction, the ablation process can be conducted on the material surface as well as within its bulk. As a result, true three-dimensional (3D) micro photonic devices can be fabricated with sub-micron accuracy. Examples of assembly-free microdevices and sensors include microlenses, microfluidic channels, fiber inline FPI, fiber Bragg grating, long period fiber grating, etc.

3.1 Fs Laser Micromachining System

A home integrated femtosecond (fs) laser fabrication system has been successfully developed with the capability for automated fabrication of various microdevices and sensors. This integrated system has been used for fabrication of various sensors and devices on different materials and substrates to support the proposed research and demonstrate the concepts. As shown in Figure 3-1, the system includes the following groups: fs laser source, regenerative amplifier, laser beam delivering optics, computer controlled fabrication stages, microscopic vision system, and control software.

The first part is the fs laser source (Type I in Figure 3-1), where a high power pump laser coherent Verdi V18 (522 nm) continuously delivering stabilized light into the mode-locking oscillator (Mira 900) to form ultrafast laser pulses. Mode-locking is accomplished based on the widely used and reliable Kerr Lens Mode-locking (KLM) technique. This simple, all-solid-state

approach is analogous to mode-locking by a fast saturable absorber. Group velocity dispersion (GVD) in the Mira 900 is compensated by a simple 2-prism sequence in the cavity. Easy adjustment of these prisms balances self-phase modulation in the Ti:Sapphire rod with the GVD compensation, resulting in shortened and stabilized 'soliton-like' pulses.

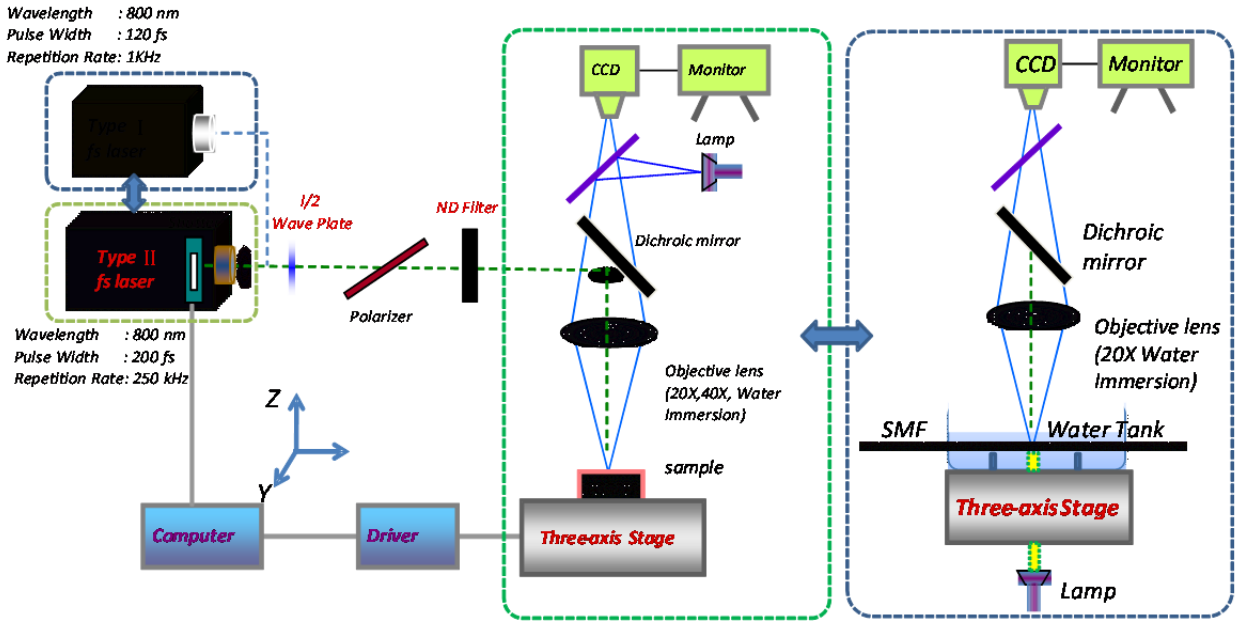

Figure 3-1. Schematic of Fs laser fabrication system for fabrication of various devices and sensors on planar and fiber substrates.

The ultrashort laser pulses are fed into a regenerative amplifier (Type 2 in Figure 3-1) to carry more energy for each pulse, which makes it possible to achieve very high gain and thus pulse energies in the milijoule range after amplifier. Typical pulse repetition rates are of the order of 100 kHz (tunable from 1 kHz to 250 kHz), whereas the highest pulse energies are achieved at lower repetition rates.

The fabrication stage is constructed by four computer-controlled automated precision stages including two linear stages (x and y axis), one elevation stage (z axis) and one linear actuator that

is used to drive a rotary stage. A computer program is developed to control the stages to make them move as desire path. As a result, working together with the on/off switch of the laser, the fabrication system can sculpture a broad variety of three-dimensional geometries. Figure 3-2 shows the photograph of the whole system, including source, amplifier, laser beam delivering stages and computer control system/software.

The entire system was built on an air-isolated optical table to avoid vibration caused instabilities. In addition, the entire room was under constant temperature and humidity monitoring. One of the unique capabilities developed is the automated fabrication software which allows us to fabricate any complicated 3D structures by controlling the movement of the stages and the laser power using computer software.

Practically, any desired patterns can be input to the computer in an image file and the control software can automatically figure out the tool path as well as control the output powers of the laser to ablate the desired pattern. The patterns can be on the surface of the substrate or inside the substrate without damage the outer surface.

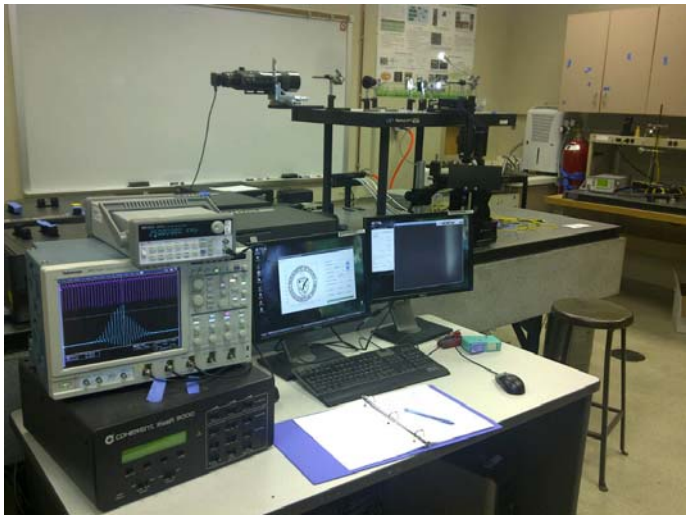

(a)

(b)

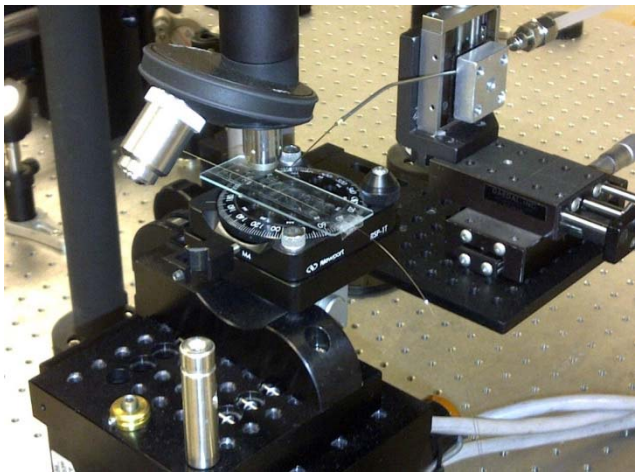

(c)

Figure 3-2. Photographs of the developed femtosecond laser micromachining system (a) the whole system, (b) the laser source and amplifier, (c) the computer controlled stages.

3.2 Patterns Fabricated Using the Developed System

Figure 3-3 shows some examples of the patterns fabricated using the developed fs laser micromachining system. These patterns are fabricated on the surface of single crystal sapphire substrates. The direct ablation is facilitated by air-blowing to remove debris. The smallest features that can be achieved is about 1μm in width.

Figure 3-3. Microscopic images of example patterns fabricated on sapphire substrates using the developed femtosecond laser micromachining system. The direct ablation is facilitated by air-blowing to remove debris. The smallest features that can be achieved is about 1μm in width.

We have also developed a number of techniques to improve the fabrication precision. Specifically, we have developed an automated air-blowing technique to remove the ablated debris during the fabrication process, which have proven to be critical to improve the quality of the fabrication by reducing the deposition of particles resulted from the fs laser ablation. We have also developed the liquid immersing technique that has proven to be effective to reduce the optical distortion of a non-flat surface such as an optical fiber. By choosing a liquid whose refractive index matches that of the substrate to be fabricated, the interface is eliminated and the laser pulses can be delivered to the places meant to be. As a result, the fabrication precision has been dramatically improved.

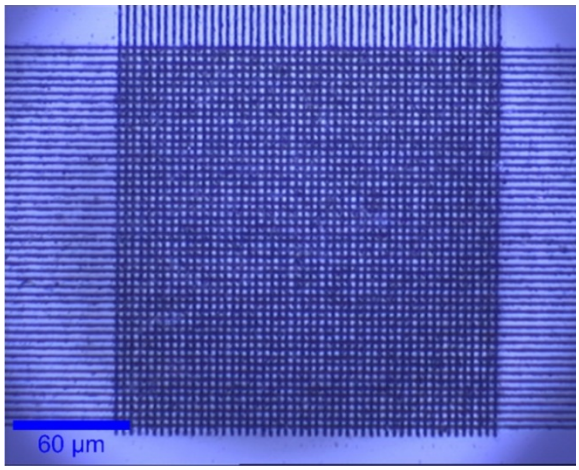

Figure 3-4. Confocal microscopic image of a crossed line patterns fabricated inside a sapphire substrate with the line width and period of 2 µm, respectively. The patterns are 100 µm below the surface of the substrate.

Figure 3-4 shows the line patterns fabricated inside a sapphire substrate with the line width and period of 2 µm, respectively. The patterns are 100 µm below the surface of the substrate and the image is acquired using a confocal microscope. The clearly identified line shapes and crossing points indicated the high quality of fs laser micromachining

Figure 3-5 shows the microscopic images of a PTL logo fabricated on the surface of a fused silica substrate (a) and inside an optical fiber (b). Both of the patterns are fabricated using the water immersed fabrication, in which the substrate and optical fiber is completely immersed in water. As a result, the refractive index difference between the optical substrates and the surrounding environment is reduced significantly. The optical beam distortion is also minimized to obtain high quality structures in fs laser micromachining.

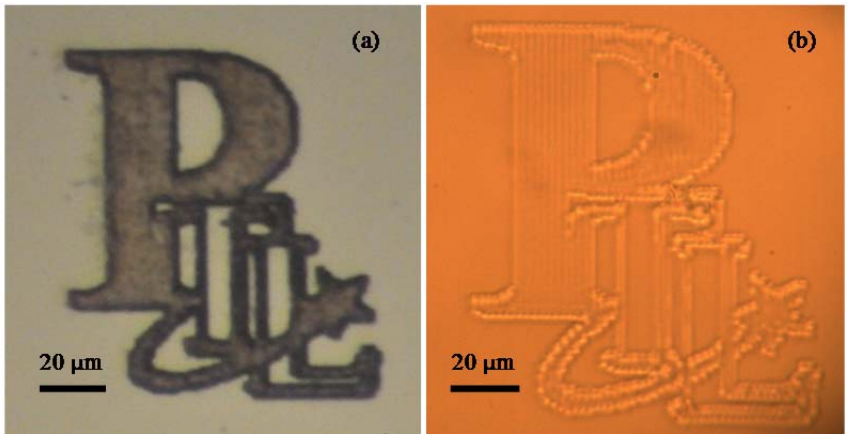

Figure 3-5. Confocal microscopic images of PTL logo fabricated on the surface of a fused silica substrate (a) and inside a silica optical fiber (b). The fabrication is performed by immersing the substrates inside water to reduce the distortion of the optical beams.

3.3 Example Fiber Sensors Fabricated Using the Developed fs Laser System

Using the developed fs laser micromachining system, we have also successfully fabricated many novel fiber optic sensors in flat substrates as well as in silica and sapphire fibers. The detailed sensors and testing of their performance are provided in other sections of this report. Here we quickly list some well-known fiber sensors fabricated using the developed system to show the capabilities of the developed system.

Figure 3-6 (a) shows the microscopic image of a fiber Bragg Grating Fabricated by the fs laser point-by-point irradiation method. The period of the grating is 1.58μm and the total length is about 20mm. As shown in the figure, the laser ablated patterns inside the core of a single mode fiber is quite uniform and defect-free. Figure 3-6 (b) shows the reflection spectrum of the fiber grating, in which the resonance can be clearly identified. This proves that the fs laser micromachining has the necessary 3D precision to fabricate high performance fiber sensors.

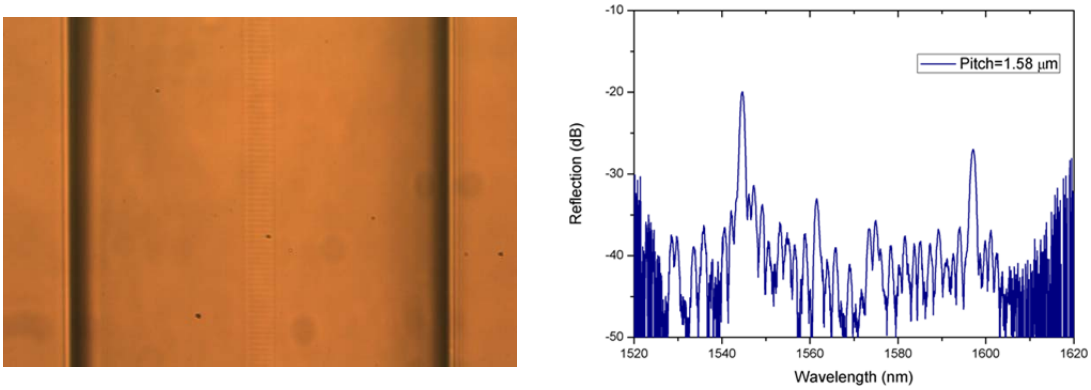

Figure 3-6. (a) Microscopic image of a fiber Bragg grating fabricated using fs laser point-by-point irradiation of periodic patterns inside the core of a singlemode optical fiber. (b) Reflection spectrum of the FBG showing resonant wavelengths in the desired Bragg wavelengths.

Figure 3-7 shows the electron scanning microscope (SEM) images of an extrinsic Fabry-Perot interferometer (EFPI) fabricated in an single crystal sapphire fiber with a diameter of 75μm. The interferometer is formed by drilling a square hall into the tip of the sapphire fiber. As a result, the two reflections from the two sidewalls of the square hole form the interference pattern. The fs laser ablated surface has a good quality and showing a shape that matches the pre-determined sizes and dimensions.

To prove the high temperature capability of the fabricated device, the sapphire fiber EFPI sensor was placed in a high temperature environment of 1600°C for three days. As shown in Figure 3-7 (b) and (d), the device successfully survived the high temperature tests without any high temperature stress induced cracks or structural breakdowns. In addition, the high temperature stress tests also helped smoothing of the surface which helps improving the signal quality of the fabricated sensor device.

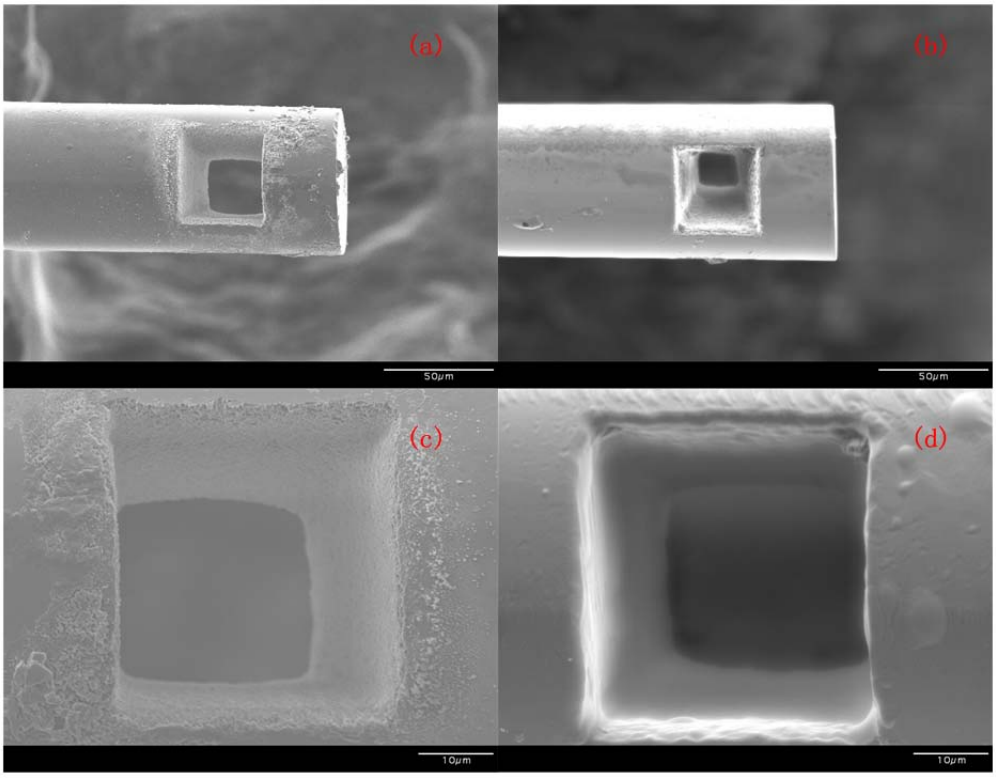

Before high temperature heating After heated at 1600ºC for 3 days

Figure 3-7. EFPI cavity fabricated on a single crystal sapphire fiber with a diameter of 75μm and high temperature survivability test. (a) and (c) SEM images of the cavity before high temperautre tests. (b) and (d) SEM images of the cavity after placed in an 1600°C environment for 3 days.

4. Assembly-Free Fiber Inline Extrinsic Fabry-Perot Interferometers

4.1 Introduction

Optical fiber Fabry-Perot (FP) interferometric sensors have been well-demonstrated for various sensing applications in the past. The FP cavity can be either intrinsic (e.g., a section of fiber between two dielectric mirrors [1]) or extrinsic (e.g., an air gap between two cleaved fiber endfaces [2]). The two reflections at the two end-surfaces of the FP cavity form an interference signal that is a function of the length and refractive index of the cavity. The deflection of the cavity due to changes in environment causes a phase shift in the interference pattern. As a result, a fiber FP sensor is capable of measuring various parameters including temperature, pressure, strain, acoustics and flow. With advantages such as small size, immunity to electromagnetic interference (EMI) and corrosion resistance, these fiber FP sensors are particularly attractive for applications involving harsh environments [3, 4].

Various methods have been reported to fabricate fiber extrinsic FP sensors in the past, evolving from epoxy-based assembly in the early days [5] to the more recent fusion-based assembly using a CO_2 laser [3] or an electric arc fusion splicer [6]. These methods involve complicated procedures of assembling multiple components together. The length of the cavity varies in each device and the performance is neither predictable nor controllable. The multiple parts assembly also compromises the robustness of the device due to the limited strength of the joints. The mismatch of the coefficient of thermal expansion (CTE) of the various parts can also seriously lower the thermal stability of the device. As a result, the demonstrated devices have shown limited capability to survive high temperatures.

The latest advancement in femtosecond (fs) laser technology has opened a new window of opportunity for one-step fabrication of micro-devices with true three-dimensional (3D) configurations. Direct exposure of most solid materials (including fused silica glass) to ultraintense fs laser pulses results in the quick establishment of free electron plasma at the focal point, leading to the ablation of a thin layer of materials [7]. Fs laser pulses with extremely high peak power produce nearly no thermal damage as the pulse duration is shorter than the thermalization time [8]. Due to the muliphoton nature of the interaction, the ablation process can be conducted on the material surface as well as within its bulk. Fs lasers have been successfully used for directly writing optical waveguides [9, 10] and micromachining microchannels and microchambers in glasses [11].

We successfully developed a novel fiber inline FPI structure with an open cavity formed by one-step micromachining a micro-notch in a single mode optical fiber using a fs laser. The device has an all-glass structure and does not involve assembly of multiple components. As a result, we expect that the device will survive very high temperatures. In addition, the accessible FP cavity makes it possible to be used as an ultra-compact chemical sensor based on refractive index measurement.

4.2 Device Fabrication

The device fabrication was carried out using a home-integrated fs laser 3D micromachining system as schematically shown in Figure 4-1. The repetition rate, center wavelength and pulse width of the fs laser (Legend-F, Coherent, Inc.) were 1kHz, 800nm and 120fs, respectively. The maximum output power of the fs laser was approximately 1W. We used the combination of waveplates and polarizers to reduce the laser power to about 20mW, and then used several

neutral density (ND) filters to further reduce the laser power to desirable values. The attenuated laser beam was directed into an objective lens (Olympus UMPLFL 20X) with a numerical aperture (NA) of 0.45 and focused onto the single mode optical fiber (Corning SMF 28) mounted on a computer-controlled five-axis translation stage (Aerotech, Inc.) with a resolution of 1μm.

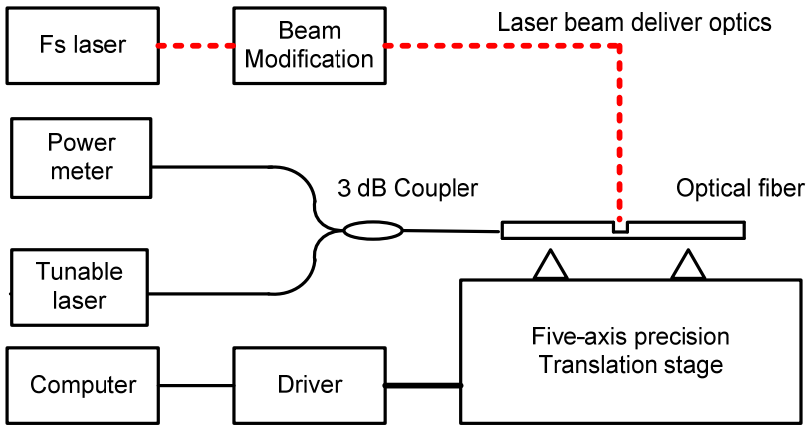

Figure 4-1. Block diagram of the fiber inline EFPI device fabrication system using a fs laser

During fabrication, the interference signal of the fiber FP device was continuously monitored. A tunable laser source (HP 8168E) was connected to one of the input ports of the 3dB fiber coupler. The output port of the coupler was connected to the device under fabrication. Controlled by the computer, the tunable laser continuously scanned through its wavelength range (1475-1575nm) at the rate of 1nm per step. The signal reflected from the device at each wavelength step was recorded by an optical power meter (Agilent 8163A). The fabrication was stopped after a well-formed interference pattern was recorded.

Figure 4-2 shows the schematic structure and scanning electron microscope (SEM) images of the fabricated fiber FP device, where Figure 4-2 (b) shows that a micro-notch was formed on the optical fiber. Figure 4-2 (c) shows the fs laser ablated surface. The cavity length was about 30μm as estimated from the SEM image. The depth of ablation was around 72 μm, just passing the fiber core.

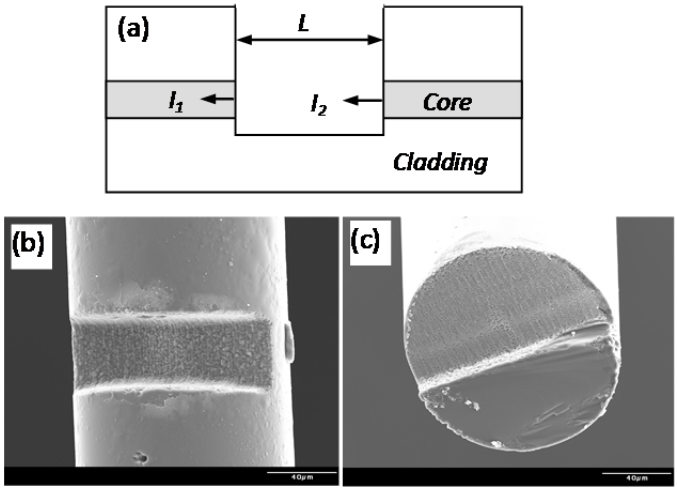

Figure 4-2. Schematic structure and SEM images of fiber inline FPI device fabricated by fs laser ablation. (a) Structural illustration, (b) top view, and (c) cross section.

4.3 Sensor Tests and Results

Figure 4-3 shows the interference spectrum of an inline fiber FPI device fabricated by the fs laser. The background loss of this particular device was about 16dB. This relatively high loss was mainly caused by two reasons: 1) the light scattering loss at the laser-ablated surface, and 2) the non-perpendicular surface orientation with respect to the fiber axis, which was partially evidenced by the non-flat interference peak intensities shown in Figure 3-7. We believe that the surface roughness can be reduced by reducing the laser scanning steps, of course, at the expense of a long device fabrication time. The non-perpendicular surface orientation can also be

minimized by careful adjustment of the stages. Nevertheless, the interference spectrum indicated a high fringe visibility, exceeding 14dB, which is sufficient for most sensing applications.

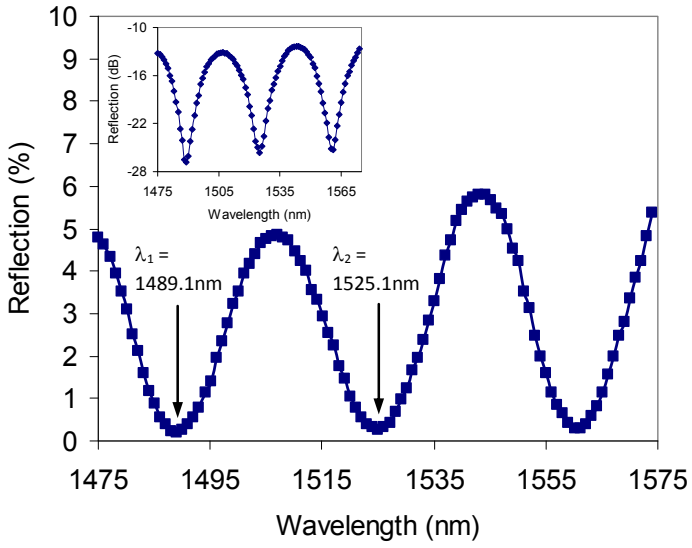

Figure 4-3. Interference spectrum of the fabricated fiber inline FPI device. Insert: interference fringe plotted in dB scale.

Due to the low reflectivity of the laser-ablated surface, multiple reflections have negligible contributions to the optical interference. The low finesse FP device can thus be modeled using the two-beam optical interference equation:

$$I = I_1 + I_2 + 2\sqrt{I_1 I_2}\cos\left(\frac{4\pi L}{\lambda} + \varphi_0\right), \tag{4-1}$$

where, I is the intensity of the interference signal; I_1 and I_2 are the reflections at the cavity surfaces, respectively; φ_0 is the initial phase of the interference; L is the optical length of the cavity; λ is the optical wavelength.

According to Equation (4-1), the two adjacent interference minimums have a phase difference of 2π. That is

$$\left(\frac{4\pi L}{\lambda_1}+\varphi_0\right)-\left(\frac{4\pi L}{\lambda_2}+\varphi_0\right)=2\pi \tag{4-2}$$

where λ_1 and λ_2 are the wavelengths of two adjacent valleys (Figure 4-3) in the interference spectrum. The optical length of the FP cavity can thus be found as $L=0.5\lambda_1\lambda_2/(\lambda_2-\lambda_1)$. Based on the interference spectrum shown in Figure 3-8, we calculated that the FP cavity length was 30.797μm, which was very close to the length estimated by SEM imaging.

The fabricated device was tested for its ability to survive high temperatures. The sensor was placed in a programmable electric tubular furnace. The temperature of the furnace was increased from room 50°C to 1100°C (limited by the highest temperature of the furnace used) at a step of 50°C and the interference spectra at these temperatures were recorded using a similar interrogation system as shown in Fig. 1. However, to improve the accuracy, we replaced the tunable laser with a broadband source made by multiplexing a C-band and an L-band Erbium doped fiber ASE (amplified spontaneous emission) sources. The interference fringe reflected from the device was recorded by an optical spectrum analyzer (OSA, HP 70952B).

The cavity length as a function of the temperature is plotted in Figure 4-4, where it increased nearly linearly following the increase of temperature. The fiber FP device successfully survived high temperatures up to 1100°C. However, as temperature increased to 1100°C, the interference fringe visibility was dropped by about 2dB compared to that at room temperature. The temperature sensitivity of this particular FP device was estimated to be 0.074pm/°C based on the linear fit of the measurement data. The equivalent CTE of the fiber FP device was 2.4×10^{-6}/°C,

which was about four times larger than the known CTE of the fiber cladding (fused silica, 5.5×10^{-7}/°C). Therefore, we concluded that the large device CTE was mainly caused by the bending of the cavity, partially evidenced by the decreasing interference visibility at high temperatures.

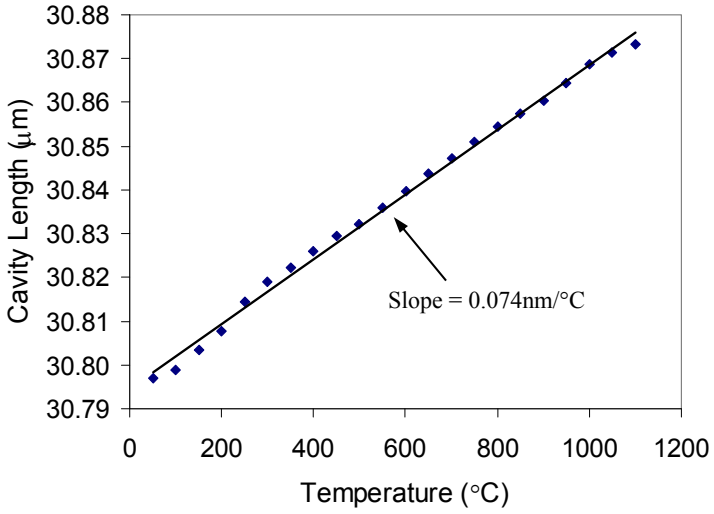

Figure 4-4. Fiber inline FP device in response to temperature change.

4.4 Summary

A novel fiber inline FP device with an accessible cavity was fabricated by one-step fs laser micromaching. Although the roughness of the laser ablated surfaces introduced a considerable background loss, the fringe visibility of the device was high enough for most sensing applications. The device successfully survived high temperatures up to 1100°C. The device can be directly utilized for temperature sensing or strain monitoring in harsh environments. More importantly, the unique accessible FP cavity makes it attractive to develop ultra-compact chemical sensors based on refractive index measurement.

4.5 References

1. C.E. Lee and H.F. Taylor, “Interferometric optical fiber sensors using internal mirrors,” Electron. Lett., 24, 193-194 (1988).
2. R.O. Claus, M.F. Gunther, A. Wang, and K.A. Murphy, “Extrinsic Fabry-Perot sensor for strain and crack opening displacement measurements for –200 to 900C,” J. Smart Mater. Struct., 1, 237-242 (1992).
3. A. Wang, H. Xiao, J. Wang, Z. Wang, W. Zhao, and R.G. May, “Self-calibrated interferometric-intensity-based optical fiber sensors,” J. Lightwave Technol., 19, 1495-1501 (2001).
4. H. Xiao, J. Deng, G. Pickrell, R. G. May, and A. Wang, “Single-Crystal Sapphire Fiber-Based Strain Sensor for High-Temperature Applications,” J. Lightwave Technol., 21, 2276-(2003).
5. V. Bhatia, K.A. Murphy, R.O. Claus, M.E. Jones, J.L. Grace, T. A. Tran, and J.A. Greene, “Optical fiber based absolute extrinsic Fabry-Perot interferometric sensing system,” Meas. Sci. Technol., 7, 58-61 (1996).
6. Y. Zhang, X. Chen, Y. Wang, K. L. Cooper, and A. Wang, “Microgap Multicavity Fabry–Pérot Biosensor,” J. Lightwave Technol., 25, 1797-1804 (2007).
7. M. Li, S. Menon, J.P. Nibarger, and G.N. Gibson, “Ultrafast Electron Dynamics in Femtosecond Optical Breakdown of Dielectrics,” Phys. Rev. Lett., 82, 2394-2397 (1999).
8. L. Jiang and H. L. Tsai, “Plasma modeling for ultrashort pulse laser ablation of dielectrics,” J. Appl. Phys. vol. 100, p.023116, 200649-52
9. K. M. Davis, K. Miura, Naoki Sugimoto, and Kazuyuki Hirao, “Writing waveguides in glass with a femtosecond laser,” Optics Letters, Vol. 21, Issue 21, pp. 1729-1731, 1996.
10. A. Szameit, D. Bloemer, J. Burghoff, T. Pertsch, S. Nolte, F. Lederer, and A. Tuennermann, “Hexagonal waveguide arrays written with fs-laser pulses,” Appl. Phys. B. 82, 507-512 (2006).

11. H. Sun, F. He, Z. Zhou, Y. Cheng, Z. Xu, K. Sugioka, and K. Midorikawa, "Fabrication of microfluidic optical waveguides on glass chips with femtosecond laser pulses," Opt. Lett. 32, 1536-1538 (2007).

5. Assembly-Free Fiber EFPI Sensor for Refractive Index Sensing

5.1 Introduction

Miniaturized and robust optical sensors capable of accurate and reliable measurement of refractive index of liquids have attracted tremendous interest in recent years due to their broad applications in chemical and biological sensing. Preferably, these devices shall have a small size, high sensitivity, fast response time and large dynamic range. Many existing devices operate based on evanescent field interactions. Examples include long period fiber gratings (LPFG) [1], chemically etch-eroded fiber Bragg gratings (FBG) [2], optical microresonators/ microcavities [3], fiber surface plasmon resonance (SPR) devices [4], photonic crystals [5], etc. In general, these devices have shown high sensitivity for refractive index measurement. Characterized as the resonance wavelength shift in response to refractive index changes, it has been reported that LPFGs can provide a sensitivity as high as 6000 nm/RIU (refractive index unit) while microresonators can reach 800 nm/RIU [6]. However, the evanescent field-based devices have a nonlinear response to refractive index, meaning that the sensitivity varies at different refractive index ranges. The dynamic range of refractive index measurement is also limited. In addition, many existing devices have shown large temperature cross-sensitivity. As a result, temperature variation induced errors need to be corrected in real time.

Low finesse fiber Fabry-Perot interferometers (FPI) have been widely used as optical sensors for measurement of a variety of parameters such as pressure, strain, temperature, etc. [7]. However, they have been commonly made with a sealed cavity. [8-10] As a result, their applications have been mainly limited to the measurement of physical parameters. In a fiber FPI, the phase of the interference signal is linearly proportional to the optical length of the cavity,

defined as the product of the cavity length and the refractive index of the medium filling the cavity. When exposed to the external environment, a FPI cavity can be used to measure the refractive index change with a linear response by tracking the phase shift of the interference signal. Compared with other types of sensors, a FPI refractive index sensor has the unique advantage of constant sensitivity over a large dynamic range. Xiao et al. reported a FPI refractive index sensor formed by two polished fiber endfaces hosted in a holey sleeve [11]. The holey sleeve allows gas to freely enter and leave the cavity. A resolution of 10^{-5} was estimated in monitoring the changes in the refractive index of gases. However, the sensor assembly was complicated and required the use of epoxy and various components made of different materials. As a result, the device had a strong dependence on temperature. Recently, Ran et al. described a refractive index sensor by adding a sealed Fabry-Perot cavity near the tip of a single-mode fiber [12]. In this case, the sealed FPI itself was not a sensing device and only served as a signal modulator. The external refractive index variation changed the reflectivity of the exposed fiber tip. The variation of the maximum contrast of the interference fringes was used to determine the amount of refractive index change. The device had a refractive index resolution of $\sim 4\times10^{-5}$.

Recently, Rao et al. reported a miniaturized fiber inline FPI device fabricated by micromachining a rectangular non-through hole into a single-mode or photonic crystal fiber using a femtosecond (fs) laser [13]. The single-mode fiber FPI device had a fringe visibility of about 2 dB. Later, a 157 nm laser was used to improve the quality of fabrication and a 26 dB fringe visibility was obtained using a photonic crystal fiber which had a strong absorption at the wavelength of 157 nm [14]. Our group also demonstrated an inline FPI device with a fringe visibility of 16 dB by fs laser one-step micromachining a micro-notch on a single-mode fiber [15]. The all-glass structured inline FPI has very small temperature dependence and more

attractively, an open micro-notch cavity that allows prompt access to liquid samples for direct refractive index measurement. In this project, we experimentally investigated using an open-cavity assembly-free FPI sensor for temperature-insensitive refractive index sensing.

5.2 Sensor Principle

Figure 5-1 shows the structural schematic, the scanning electron microscope (SEM) image, and the simulated interference spectrum of the fiber inline FPI device. The device was made by machining a micro-notch on a single-mode fiber using a fs laser (Legend-F, Coherent, Inc.) with a repetition rate, center wavelength, and pulse width of 1 kHz, 800 nm and 120 fs, respectively [15]. The cavity length was about 60 μm as estimated from the SEM image. The defects shown in the picture were caused by too large a laser power and were eliminated by reducing the laser power. The depth of the micro-notch was around 72 μm, just passing the fiber core. The FPI cavity was made very close (~2 mm) to the end of the fiber. With such a short bending arm, the chance of bending induced device breakage is small.

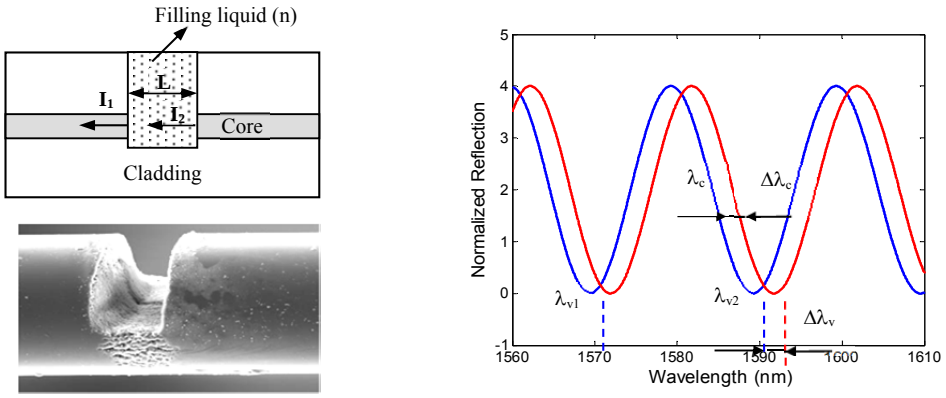

Figure 5-1. Fiber inline FPI fabricated by fs laser micromachining, (a) structural schematic, (b) SEM image, and (c) simulated interference spectrum.

Due to the low reflectivity of the laser-ablated surface, multiple reflections have negligible contributions to the optical interference. The low finesse FP device can thus be modeled using the two-beam optical interference equation [16]:

$$I = I_1 + I_2 + 2\sqrt{I_1 I_2}\cos\left(\frac{4\pi n \cdot L}{\lambda} + \phi_0\right) \tag{5-1}$$

where, I is the intensity of the interference signal; I_1 and I_2 are the reflections at the cavity endfaces, respectively; φ_0 is the initial phase of the interference; L is the cavity length; n is the refractive index of the medium filling the cavity; λ is the optical wavelength in vacuum.

According to Equation (5-1), the interference signal reaches its minimum (I_{min}) when the phase of the cosine term becomes an odd number of π. That is

$$I = I_{\min}, \quad \text{when} \quad \frac{4\pi n \cdot L}{\lambda_v} + \phi_0 = (2m+1)\pi \tag{5-2}$$

where *m* is an integer and λ_v is the center wavelength of the specific interference valley.

The two adjacent interference minimums have a phase difference of 2π. Therefore the optical length of the cavity can be calculated by:

$$L \cdot n = \frac{1}{2}\left(\frac{\lambda_{v1}\lambda_{v2}}{\lambda_{v2} - \lambda_{v1}}\right) \tag{5-3}$$

where λ_{v1} and λ_{v2} are the center wavelengths of two adjacent valleys (Fig. 1c) in the interference spectrum. In theory, Equation (5-3) can be used to calculate either the absolute refractive index (n) or the absolute length (L) of the cavity if one of them is known. However, the measurement based on Equation (5-3) has a poor resolution because the period is not a sensitive function of the optical path change [11,16].

In many cases, only the relative refractive index change is of interest and the range of refractive index variation is small so the phase shift is less than 2π. In this case, the phase ambiguity issue can be avoided. The relative refractive index change can be calculated based on the spectral shift of the interferogram.

In Equation (5-2), taking the derivative of n with respect to λ_v, one finds:

$$\frac{dn}{d\lambda_v} = \frac{1}{4\pi L} \quad . \tag{5-4}$$

Assuming the cavity length is maintained constant during measurement, the amount of refractive index change (Δn) can be computed based on the wavelength shift ($\Delta\lambda_v$ as shown in Figure 5-1(c) of a particular interference valley using the following equation derived based on Equation (5-4):

$$\Delta n = \frac{\Delta\lambda_v}{\lambda_v} n \, , \tag{5-5}$$

where the relative refractive index change is directly proportional to the spectral shift of the interferogram. It is worth noting that Equation (5-5) is also applicable to other characteristic spectral positions such as the interference peak and the center point of the interferogam (λ_c and $\Delta\lambda_c$ in Fig. 1c where the curve is relatively linear). The advantage of using the center point in calculation is that its spectral position can be resolved with a higher resolution compared to the valley or the peak that typically has a flat bottom or top. In addition, curve fitting of the interference fringe can also improve the measurement accuracy.

Comparing Equations (5-3) and (5-5), one finds that Equation (5-3) can be used to calculate the absolute refractive index while Equation (5-5) only provides the relative change of the

refractive index. However, the calculation based on Equation (5-5) has a much higher resolution than that obtained using Equation (5-3). When used to monitor the relative refractive index change of water with a nominal refractive index of 1.333, the sensitivity of measurement is 1163 nm/RIU at the wavelength of 1550 nm according to Equation (5-5). The actual detection limit depends directly on the resolution with which the spectral shift of the interferogram can be determined. If a resolution of 10 pm is achieved in the determination of interferogram shift, a detection limit of 8.6×10^{-6} RIU is attainable. With a rough resolution of 1 nm, the detection limit of 8.6×10^{-4} RIU can still be achieved.

5.3 Experiments and Results

The interference spectrum of the fabricated device in air at room temperature is shown in Figure 3-10. The loss of this particular device was about 20 dB higher than that of a FPI formed by cleaved fiber endfaces. The interference spectrum indicated a fringe visibility of about 5 dB, which was sufficient for most sensing applications. The length of the FPI cavity was found to be 63.144 μm with the refractive index of air set to be 1.0003 for air at the wavelength of 1550 nm. The calculated value was very close to the cavity length estimated by the SEM image.

To evaluate its capability for refractive index measurement, the fiber FPI device was tested using various liquids including methanol, acetone and isopropanol at room temperature. The interrogation of the FPI sensor is schematically shown in Figure 5-2. A broadband source made by multiplexing a C-band (AFC, BBS-1550A-TS) and an L-band (Highwave, HWT-BS-L-P) erbium-doped fiber amplified-spontaneous-emission (ASE) source was used to excite the device through a 3 dB fiber coupler. The reflected interference signal from the sensor was detected by

an optical spectrum analyzer (OSA, HP70952B). The spectral resolution of OSA was set to 0.5 nm and 1600 data points were obtained per OSA scan.

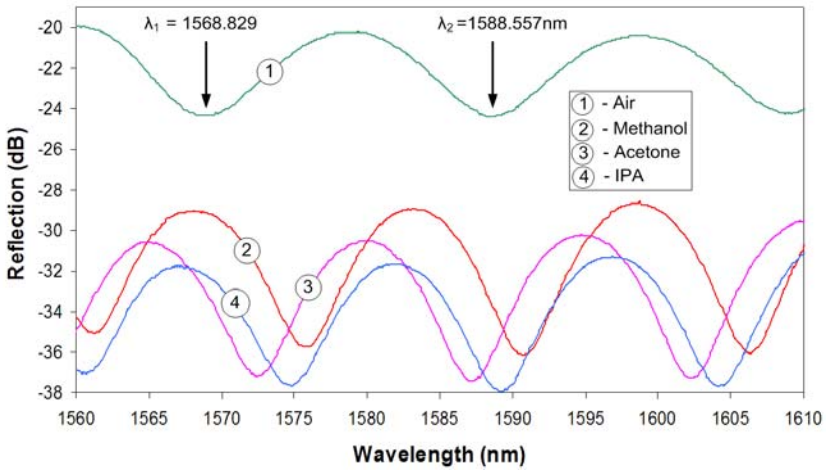

Figure 5-2. Interference spectra of the FPI device in air, methanol, acetone and isopropanol.

The interference spectra of the device immersed in various liquids are also shown in Figure 5-2 for comparison. The signal intensity dropped when the device was immersed in liquids as a result of the reduced refractive index contrast and thus lower Fresnel reflections from the cavity endfaces. However, the interference fringes maintained a similar visibility. The spectral distance between the two adjacent valleys also decreased, indicating the increase of refractive index of the medium inside the cavity. Using the interference equation, the refractive indices of the liquids were calculated to be: $n_{methanol}$ = 1.3283, $n_{acetone}$ = 1.3577, and $n_{isopropanol}$ = 1.3739, which were close to the commonly accepted values.

We also studied the device's capability for temperature-insensitive refractive index sensing by measuring the temperature-dependent refractive index of deionized water. As shown in Figure 5-2, the fiber FPI device was attached to the tip of a thermometer and immersed into deionized

water in a beaker. The beaker is placed in a large container for water/ice bath and the container was placed on a stirring/hot plate (Corning PC-420D). A magnetic stirrer was used to equilibrate the temperature during experiment. The system was first heated till the water inside the beaker reached 90^{o}C read from the thermometer. Then the heater was turned off to allow the system to cool down smoothly while the interference spectrum was recorded at every degree centigrade of temperature dropping. Ice was added into the water-bath container to help cool the system at low temperatures. The measurement ended till the temperature inside the beaker dropped to 3^{o}C.

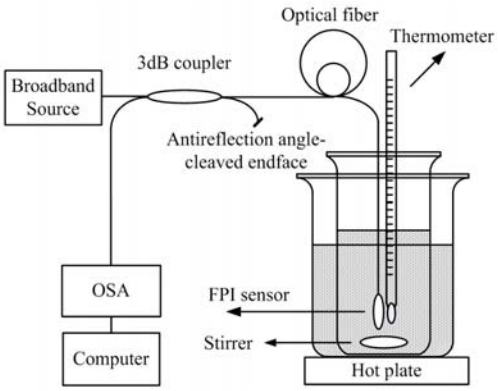

Figure 5-3. Experimental setup for refractive index measurement.

Figure 5-3 shows the measured refractive index of deionized water as a function of temperature. As the temperature increases, the interference fringe shifts to a shorter wavelength indicating the decrease in its refractive index. Assuming a constant cavity length over the entire temperature range, we calculated the refractive index change by tracing the spectral shift of the interferogram. To improve the accuracy of spectral shift measurement, the interference fringes were first normalized to have the same average intensities, then curve-fitted using a fourth-order polynomial. The spectral shift was computed as the difference in wavelength between the two fitted curves at the center point.

To achieve an improved resolution, a relative measurement method was used. We first computed the change in refractive index from 20°C to a specific temperature using Equation (5-5) based on the spectral shift in their interferograms. The change was then added to the refractive index value at 20°C to calculate the refractive index of water at that temperature. Point-by-point, the refractive indices of deionized water at various temperatures were obtained. The measurement results, as shown in Figure 5-4, indicate that the refractive index of water decreases nonlinearly as its temperature increases. The amount and shape of the measured refractive index of water change as a function of temperature agreed well with the previously reported measurement data.

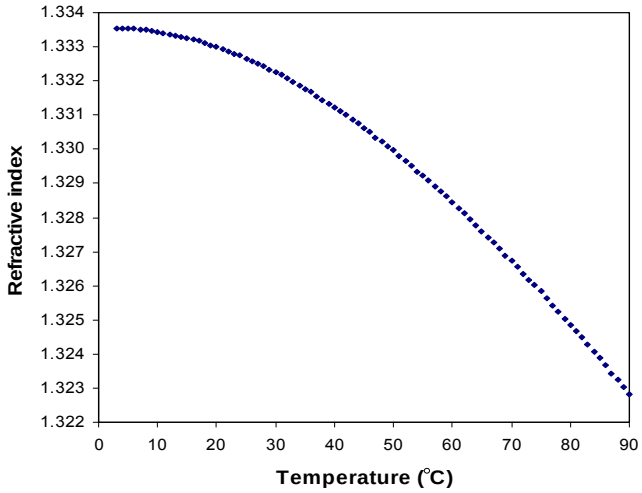

Figure 5-4. Measured refractive index of water as a function of temperature.

The above measurement results also included the error contribution of the temperature cross-sensitivity of the device. To evaluate the temperature cross-sensitivity of the sensor, we conducted an experiment in which the sensor was placed in an electrical oven and the temperature of the oven was increased from 20 to 100°C. The 80°C temperature variation in air caused a total interferogram shift in the amount less than 0.1 nm, or at a rate less than 0.00125

nm/°C. Based on Equation (5-5), the temperature cross-sensitivity of the device was less than 1.1×10^{-6} RIU/°C. Therefore, the total temperature cross-sensitivity induced measurement error was less than 9.4×10^{-5} RIU in Figure 3-12 over the temperature variation of 87°C. The temperature dependence of the device was small and contributed only about 0.9% to the total refractive index variation over the entire temperature range.

5.3 Summary

In conclusion, we demonstrated a miniaturized fiber inline FPI device with an open cavity fabricated by one-step fs laser micromachining for highly sensitive refractive index measurement. The device was evaluated for refractive index measurement of various liquids and the results matched well with the reported data. The inline fiber FPI was also tested to measure the temperature-dependent refractive index of deionized water from 3 to 90°C with a sensitivity of 1163 nm/RIU. The temperature cross-sensitivity of the device was less than 1.1×10^{-6} RIU/°C. The small size, all-fiber inline structure, small temperature dependence, linear response, high sensitivity, and most attractively, an open cavity that is accessible to the external environment, make the new fiber inline FPI an attractive refractive index sensor that has many applications in chemical and biological sensing.

5.4 References

1. I. Del Villar, I. R. Matias, and F. J. Arregui, "Enhancement of sensitivity in long-period fiber gratings with deposition of low-refractive-index materials," Opt. Lett. **30**, 2363-2365 (2005).

2. W. Liang, Y. Huang, Y. Xu, R. K. Lee, and A. Yariv, "Highly sensitive fiber Bragg grating refractive index sensors," Appl. Phys. Lett. **86**, 151122:1-3 (2005).

3. I. M. White, H. Oveys, and X. Fan, "Liquid-core optical ring-resonator sensors," Opt. Lett. **31**, 1319-1321 (2006).

4. B. Gauvreau, A. Hassani, M. Fassi Fehri, A. Kabashin, and M. A. Skorobogatiy, "Photonic bandgap fiber-based Surface Plasmon Resonance sensors," Opt. Express **15**, 11413-11426 (2007).

5. N. Skivesen, A. Tetu, M. Kristensen, J. Kjems, L. H. Frandsen, and P. I. Borel, "Photonic-crystal waveguide biosensor," Opt. Express **15**, 3169-3176 (2007).

6. I. M. White and X. Fan, "On the performance quantification of resonant refractive index sensors," Opt. Express **16**, 1020-1028 (2008).

7. Y. J. Rao, "Recent progress in fiber-optic extrinsic Fabry-Perot interferometric sensors," Opt. Fiber Technol. **12**, 227-237 (2006).

8. V. Bhatia, K.A. Murphy, R.O. Claus, M.E. Jones, J.L. Grace, T. A. Tran, and J.A. Greene, "Optical fiber based absolute extrinsic Fabry - Perot interferometric sensing system," Meas. Sci. Technol. **7**, 58-61 (1996).

9. H. Xiao, J. Deng, G. Pickrell, R. G. May, and A. Wang, "Single-Crystal Sapphire Fiber-Based Strain Sensor for High-Temperature Applications," J. Lightwave Technol. **21**, 2276-2283 (2003).

10. Y. Zhang, X. Chen, Y. Wang, K. L. Cooper, and A. Wang, "Microgap Multicavity Fabry–Pérot Biosensor," J. Lightwave Technol. **25**, 1797-1804 (2007).

11. G.Z. Xiao, A. Adnet, Z.Y. Zhang, F.G. Sun, and C.P. Grover, "Monitoring changes in the refractive index of gases by means of a fiber optic Fabry-Perot interferometer sensor," Sensor Actuat. A-Phys. **118**, 177-182 (2005).

12. Z. L. Ran, Y. J. Rao, W. J. Liu, X. Liao, and K. S. Chiang, "Laser-micromachined Fabry-Perot optical fiber tip sensor for high-resolution temperature-independent measurement of refractive index," Opt. Express **16**, 2252-2263 (2008).

13. Y. J. Rao, M. Deng, D. W. Duan, X. C. Yang, T. Zhu, and G. H. Cheng, "Micro Fabry-Perot interferometers in silica fibers machined by femtosecond laser," Opt. Express **15**, 14123-14128 (2007).

14. Z. L. Ran, Y. J. Rao, H. Y. Deng, and X. Liao, "Miniature in-line photonic crystal fiber etalon fabricated by 157 nm laser micromachining," Opt. Lett. **32**, 3071-3073 (2007).

15. T. Wei, Y. Han, H-L. Tsai, and H. Xiao, "Miniaturized fiber inline Fabry-Perot interferometer fabricated with a femtosecond laser," Opt. Lett. **33**, 536-538 (2008).

16. B. Qi, G. R. Pickrell, J. Xu, P. Zhang, Y. Duan, W. Peng, Z. Huang, W. Huo, H. Xiao, R. G. May, and A. Wang, "Novel data processing techniques for dispersive white light interferometer," Opt. Eng. **42**, 3165-3171 (2003).

17. J. B. Hawkes, and R. W. Astherimer, "Temperature coefficient of the refractive index of water," J. Opt. Soc. Am. **38**, 804-806 (1948).

6. Fiber Inline Michelson Interferometer Fabricated by fs Laser

6.1 Introduction

In recent years, assembly-free all-glass optical fiber micro sensors have attracted many research interests. These assembly-free devices are commonly made by fabricating an optical structure directly on an optical fiber without assembling discrete components together. In addition to the well-known advantages such as compact size, light weight, immunity to electromagnetic interferences (EMI), resistance to corrosion, and remote operation, assembly-free, all-glass fiber sensors have the robustness to survive and operate in high-temperature harsh environments [1].

The mostly-known assembly-free fiber devices are fiber gratings [2, 3], including both the fiber Bragg grating (FBG) and the long period fiber grating (LPFG). Various methods have been explored for fabrication of these gratings, including direct laser writing, ion-implantation and arc fusion [4-9]. Some of them have shown high temperature capabilities up to 1200°C [9]. However, the thermal stability of the laser induced refractive index modulation is a concern and the long term stability of these gratings in high temperatures is yet to be proven.

In addition to fiber gratings, various assembly-free micro fiber interferometers have been reported by directly fabricating solid microstructures directly on the optical fiber [10-14]. For example, fiber inline Fabry-Perot (FP) and Mach-Zehnder (MZ) interferometers have been fabricated using femtosecond (fs) laser pulses and demonstrated for high-temperature harsh environment sensing applications. These micro inline devices do not need to assemble pieces together. As a result, the robustness of the device is significantly improved due to the

elimination of bonding various components made of different materials with different coefficients of thermal expansion (CTE).

However, the reported fiber inline FP and MZ interferometers are made by cutting a groove into the fiber or drilling a hole through the fiber. As such, the mechanical strength of the device has been significantly weakened. Another issue associated with the FP and MZ interferometers is that the devices are very sensitive to bending. Bending could induce a large and sometimes unpredictable change in optical path difference that could make it difficult to interpret the sensor signal. In addition, the MZ interferometer works in the transmission mode, which makes it difficult to install the sensor in a harsh environment because the sensor has to be sealed at both ends.

In this project, we developed a new fiber inline micro device, the Michelson interferometer, fabricated by femtosecond laser micromachining. The new device can work as a temperature sensor with the unique advantages of robustness, operating in the reflection mode and insensitivity to bending. As a result, the Michelson inline interferometer is expected to provide a good solution for measurement of high temperatures.

6.2 Sensor Principle and Fabrication

Figure 6-1 illustrates the schematic of the optical fiber Michelson inline interferometer. The device is made by cutting a step structure into the optical fiber at its tip, where the step stops at the center of the fiber core. The light propagating inside the fiber core thus splits into two paths which are reflected at two different places. One is at the end face of the cut-in step and the other is at the end face of the optical fiber. The two reflections, which are denoted as I_1 and I_2,

respectively, superimpose in the fiber core to generate an interference pattern just like a typical Michelson interferometer.

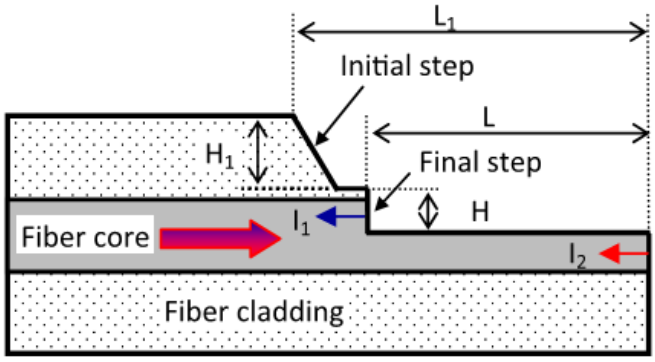

Figure 6-1. Schematic of the step-structured fiber inline Michelson interferometer.

The Michelson interferometer can be modeled using the following two-beam optical interference equation:

$$I = I_1 + I_2 + 2\sqrt{I_1 I_2}\cos(\frac{2\pi \bullet OPD}{\lambda} + \phi_0) \tag{6-1}$$

where I is the intensity of the interference signal, ϕ_0 is the initial phase of the interference (normally equal to zero), and λ is the optical wavelength in vacuum. The round-trip OPD of the Michelson interferometer is given by

$$OPD = 2n_{core}L \tag{6-2}$$

where n_{core} is the refractive index of the fiber core and L is the length of the step structure.

Figure 6-2 shows the block diagram of the fs laser micromachining system used for fabrication of the fiber Michelson interferometer. The laser used for fabrication was a regeneratively amplified Ti: Sapphire fs laser (Coherent, Inc.). The central wavelength, pulse

width, and repetition rate of the laser were 800 nm, 200 fs, and 250 kHz, respectively. The maximum output power of the laser was 1 W. The actual power used for fabrication was controlled by adjusting the laser beam optics, including a halfwave plate, a polarizer, and several neutral density filters. The laser was switched on or off by electrically gating the internal clock. The actual laser energy used for fabrication was approximately 0.4 μJ per pulse.

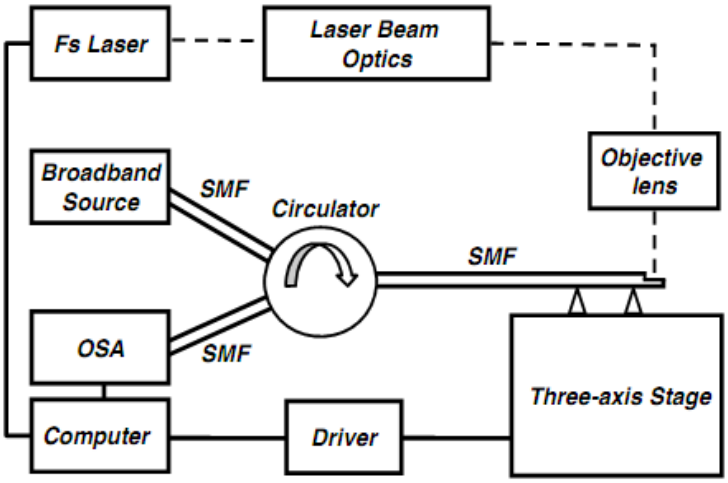

Figure 6-2. Block diagram of the fs laser micromachining system used for fabrication of the fiber Michelson interferometer.

A standard telecommunication single-mode optical fiber (Corning SMF-28) was used in all experiments. The fiber was cleaned and mounted on a high-precision, computer-controlled three-axial translation stage (Newport, Inc.) with a resolution of 0.1 μm. The fs laser beam was focused onto the optical fiber through an objective lens (Zeiss EC Epiplan, 20×) with a numerical aperture (NA) of 0.4. The spot size of the focused beam was about 1 μm. An online monitoring system was used to monitor the performance of the device during the micromachining process. The monitoring system consists of an Erbium-doped fiber amplified spontaneous emission

broadband light source, a fiber circulator, and an optical spectrum analyzer (OSA, AQ6319), as shown in Figure 6-2.

To obtain a high-quality interference signal, the step structure needs to have its wall perpendicular to the fiber axis. In addition, the depth cutting into the core needs to be controlled precisely. However, the focused fs laser beam has a cone shape due to the large NA of the objective lens. As a result, it is difficult to fabricate a deep structure with its wall perpendicular to the fiber axis. We adopted a two-step structure as shown in Figure 6-3. An initial step is fabricated with a length of L_1 that is longer than the final interferometer length of L. The initial step has a depth of H_1 which is barely touching the fiber core so that the light propagating inside the fiber core is not disturbed, as determined by observing the reflection spectrum.

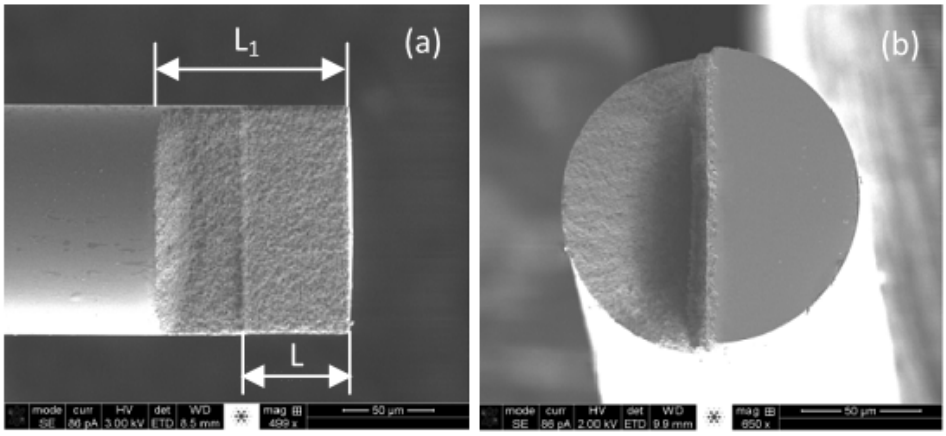

Figure 6-3. SEM images of the fabricated fiber inline Michelson interferometer: (a) top view and (b) endface view.

Upon completion of the initial step, a second step structure is fabricated by cutting a shallow step with a length of L and a depth of H. The fabrication was stopped after an interference pattern with a large fringe visibility was observed. Figures 6-3 (a) and (b) show the scanning electron microscope (SEM) images of the fiber inline Michelson interferometer. The initial step

has a length L_1 = 100 μm, and the interferometer has a length L = 55 μm. The initial step has a depth of H_1 = 57.5 μm. The final depth H is about 5 μm.

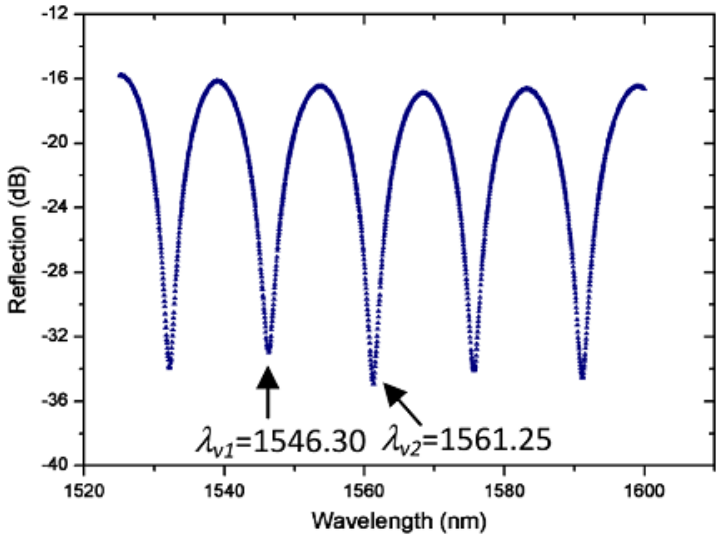

Figure 6-4. Reflection spectrum of the fiber inline Michelson interferometer.

As shown in Figure 6-4, the reflection spectrum of the fabricated structure shows a clean interference pattern with a large fringe visibility of about 18 dB, which is adequate for most sensing applications. The excess loss of the device was about 20 dB, which was mainly caused by the roughness of the fs laser ablated surfaces (both the I_1 endface and the flat surface between I_1 and I_2). To a certain extent, the surface quality can be improved by reducing the laser scanning step size and immersing the device into a liquid during fabrication. The length of the interferometer can be calculated based on the spectral positions (λ_{v1} and λ_{v2} in Figure 6-4) of two adjacent minima of the interferogram using the following equation:

$$L = \frac{1}{2n_{core}}\left(\frac{\lambda_{v1}\lambda_{v2}}{\lambda_{v2}-\lambda_{v1}}\right) \tag{6-3}$$

Using Equation (6-3) and the interference spectrum shown in Figure 6-4, we calculated that the step structure length L was 54.993 μm, which was very close to the length estimated by SEM imaging.

6.3 Tests and Results

To demonstrate the feasibility as a high-temperature sensor, the fabricated device was placed in an electric furnace and the inference spectrum was monitored as the temperature varied programmatically from 50 to 1000°C at a step of 50°C. At each step, 10 min waiting time was programmed to stabilize the temperature. The device was illuminated using a broadband light source and the interference spectra were recorded by an OSA. As the temperature increased, the interferogram was found shifting toward the long wavelength region. The wavelength shift as a function of temperature change is plotted in Figure 6-5. Linear regression was used to fit the response curve and the slope of the fitted line was computed to find the temperature sensitivity. The temperature sensitivity of this particular Michelson interferometer device was estimated to be 14.72 pm/°C in terms of wavelength shift versus temperature. The response curve shown in Figure 6-5 is nonlinear in the large temperature range. As a result, it is necessary to use high-order fitting to achieve high measurement accuracy.

When the Michelson interferometer is subjected to temperature variation, both the refractive index of the core (n_{core}) and the length (L) will change due to the thermo-optic effect and the thermal expansion of the fiber, respectively. The change in OPD of the interferometer can be expressed as a function of temperature change (ΔT) as follows:

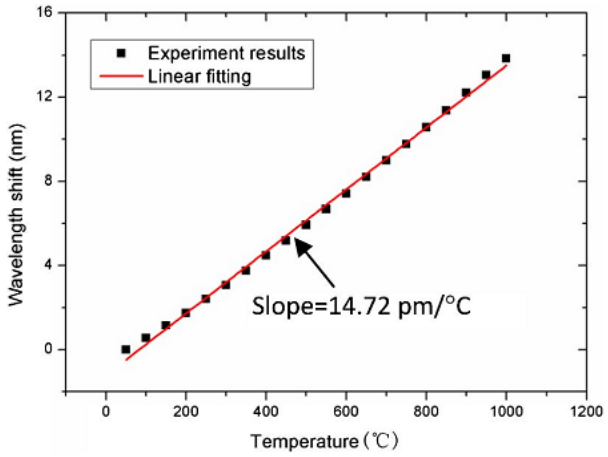

Figure 6-5. Temperature-induced wavelength shifts of the fiber inline Michelson interferometer.

$$\Delta OPD = OPD(\alpha_{TO} + \alpha_{CTE})\Delta T \tag{6-4}$$

where α_{TO} and α_{CTE} are the thermo-optics coefficient and thermal expansion coefficient of silica fiber with typical values of $\alpha_{TO} = 8.3 \times 10^{-6}°C^{-1}$ and $\alpha_{CTE} = 0.55 \times 10^{-6}°C^{-1}$, respectively. Based on Equations (6-2) and (6-3), the spectral shift of the interferogram as a function of temperature can be expressed as:

$$\Delta\lambda_0 = \lambda_0(\alpha_{TO} + \alpha_{CTE})\Delta T \tag{6-5}$$

where λ_0 is the characteristic spectral position (e.g., the minimum or maximum) in the interferogram and $\Delta\lambda_0$ is the wavelength shift at λ_0. The temperature sensitivity of the device mainly results from the thermo-optic effect of the device. For example, at the interference valley of 1561.25 nm shown in Figure 6-4, the temperature sensitivity of the Michelson interferometer is calculated to be 13.82 pm/°C based on Equation (6-5), which is very close to the temperature sensitivity of 14.72 pm/°C estimated from the fitted line in Figure 6-5. The smooth temperature

response curve and the close-to-calculation temperature sensitivity indicate that there was no obvious bending contribution to temperature measurement using the device.

6.4 Summary

In summary, a reflection-type fiber inline Michelson interferometer was fabricated by fs laser micromachining. The assembly-free device had a high fringe visibility and responded to high temperatures close to theoretical predictions. The proposed microdevice is simple to fabricate, potentially low-cost, mechanically robust, and miniaturized in size, which makes it very attractive for high-temperature sensing probes in harsh environments.

6.5 References

1. A. Wang, H. Xiao, J. Wang, Z. Wang, W. Zhao, and R. G. May, "Self-calibrated interferometric-intensity-based optical fiber sensors," Journal of Lightwave Technology 19, 1495-1501 (2001).
2. A. D. Kersey, M. A. Davis, H. J. Patrick, M. LeBlanc, K. P. Koo, C. G. Askins, M. A. Putnam, and E. J. Friebele, "Fiber grating sensors," Journal of Lightwave Technology 15, 1442-1462 (1997).
3. S. A. Vasil'ev, O. I. Medvedkov, I. G. Korolev, A. S. Bozhkov, A. S. Kurkov, and E. M. Dianov, "Fibre gratings and their applications," Kvantovaya Elektronika 35, 1085-1103 (2005).
4. Y. Kondo, K. Nouchi, T. Mitsuyu, M. Watanabe, P. G. Kazansky, and K. Hirao, "Fabrication of long-period fiber gratings by focused irradiation of infrared femtosecond laser pulses," Optics Letters 24, 646-648 (1999).

5. D. N. Nikogosyan, "Long-period gratings in a standard telecom fibre fabricated by high-intensity femtosecond UV and near-UV laser pulses," Measurement Science and Technology 17, 960-967 (2006).

6. G. Rego, O. Okhotnikov, E. Dianov, and V. Sulimov, "High-temperature stability of long-period fiber gratings produced using an electric arc," Journal of Lightwave Technology 19, 1574-1579 (2001).

7. H. Alemohammad, E. Toyserkani, and A. J. Pinkerton, "Femtosecond laser micromachining of fibre Bragg gratings for simultaneous measurement of temperature and concentration of liquids," Journal of Physics D: Applied Physics 41(2008).

8. C. Lião, Y. Wang, D. N. Wang, and L. Jin, "Femtosecond laser inscribed long-period gratings in all-solid photonic bandgap fibers," IEEE Photonics Technology Letters 22, 425-427 (2010).

9. J. Canning, M. Stevenson, S. Bandyopadhyay, and K. Cook, "Extreme silica optical fibre gratings," Sensors 8, 6448-6452 (2008).

10. Y. J. Rao, M. Deng, D. W. Duan, X. C. Yang, T. Zhu, and G. H. Cheng, "Micro Fabry-Perot interferometers in silica fibers machined by femtosecond laser," Optics Express 15, 14123-14128 (2007).

11. T. Wei, Y. Han, H. L. Tsai, and H. Xiao, "Miniaturized fiber inline Fabry-Perot interferometer fabricated with a femtosecond laser," Optics Letters 33, 536-538 (2008).

12. L. Zhao, L. Jiang, S. Wang, H. Xiao, Y. Lu, and H. L. Tsai, "A high-quality Mach-Zehnder interferometer fiber sensor by femtosecond laser one-step processing," Sensors 11, 54-61 (2011).

13. Y. Wang, Y. Li, C. Liao, D. N. Wang, M. Yang, and P. Lu, "High-temperature sensing using miniaturized fiber in-line Mach-Zehnder interferometer," IEEE Photonics Technology Letters 22, 39-41 (2010).

14. M. Park, S. Lee, W. Ha, D. K. Kim, W. Shin, I. B. Sohn, and K. Oh, "Ultracompact intrinsic micro air-cavity fiber mach-zehnder interferometer," IEEE Photonics Technology Letters 21, 1027-1029 (2009).

15. B. Qi, G. R. Plckrell, J. C. Xu, P. Zhang, Y. Duan, W. Peng, Z. Huang, W. Huo, H. Xiao, R. G. May, and A. Wang, "Novel data processing techniques for dispersive white light interferometer," Optical Engineering 42, 3165-3171 (2003).

16. S. Takahashi and S. Shibata, "Thermal variation of attenuation for optical fibers," Journal of Non-Crystalline Solids 30, 359-370 (1979).

7. Sealed Cavity EFPI High Temperature Tolerant Pressure Sensor

7.1 Introduction

In-line fiber optic sensors, such as Fabry-Perot, Mach Zehnder, Michelson and Sagnac interferometeric sensors, have been widely used to sense temperature, strain, pressure, refractive index, etc [1, 2]. Miniaturized fiber optic pressure sensors have many important applications such as down-hole pressure monitoring [3], partial discharge detection in transformers [4], in-cylinder pressure monitoring in engines [5], study of aerodynamics [6], etc. Pressure monitoring in many cases is required to operate at temperatures higher than 500 ˚C. As such, the sensors need to survive the high temperature conditions and have a low temperature cross sensitivity. In addition, pressure measurement sometimes needs to be performed in aqueous environments where the types and concentrations of the liquids may vary dramatically. Therefore, a good pressure sensor is also required to be insensitive to the changes in ambient media.

Diaphragm based fiber optic extrinsic Fabry-Perot interferometric (FPI) sensors are among the popular choices for pressure measurement due to their advantages of small size, high sensitivity, and fast response. A typical diaphragm based FPI sensor has a sealed cavity in which a cleaved optical fiber is brought in close proximity to a thin diaphragm. The optical reflections from the fiber endface and the diaphragm form an interference pattern that can be used to calculate the distance between the fiber and the diaphragm. When the ambient pressure changes, the diaphragm deforms its shape and consequently generates a change in the interference signal that can be correlated with the pressure change.

Early implementations of diaphragm based FPI sensors involved manually assembling and bonding a large-size diaphragm to an external cavity that was attached to an optical fiber [7, 8].

In later implementations, the FPI cavity was created directly on the optical fiber to reduce the sensor size. Direct creation of a micro FPI cavity on an optical fiber has been achieved by various methods including laser micromachining [9], selective etching of the fiber core [10], and photolithography patterning [11]. Attachment of the diaphragm to seal the cavity has been explored using different methods such as epoxy bonding [12], polymer dip-coating [13], thermal fusion and cleaving [14], electroplating of a metal film [15], and chemical vapor deposition of graphene [16], etc. Polymer diaphragms and epoxy bonding could not stand high temperatures. And the pressure ranges of polymer diaphragm sensors are relatively low because of its low Young's modulus. A diaphragm made from elastic polyurethane with 0.75 μm thickness has pressure range of 0–40 kPa [13]. In addition, the long-term reliability of the epoxy-bonded sensors was also a concern.

A fiber optic FPI pressure sensor with an all-glass structure has been reported for applications in high-temperature environments (up to 600 °C) [14]. With a radius of 37.5 μm and a diaphragm thickness of 5.85 μm, the sensor has a pressure limit of 10,000 psi (68,950 kPa). The sensor was made by fusion-splicing a short section of fused silica glass capillary tube between two optical fibers. The diaphragm was obtained by precisely cleaving one of the two optical fibers. However, the diaphragm thickness was limited to about 6 μm due to the controllability of cleaving. As a result, the pressure sensitivity was limited. Another issue associated with directly using a cleaved fiber as the diaphragm was that the interference signal was the contribution of three reflections: one from the endface of lead-in fiber and the other two from the two surfaces of the diaphragm. The three-beam interference induced multiplexed interference signals, adding difficulty to signal demodulation. In addition, the reflectivity at the

diaphragm outer surface was subject to ambient refractive index changes. As such, the sensor readings could be significantly influenced by the change in surrounding media.

In this project, we developed a fs laser micromachining method to fabricate thin diaphragm based fiber FPI sensors for pressure measurement at high temperatures. Fs laser is proven to be an efficient micromachining tool to fabricate many fiber inline devices. In our previous work, we reported using an fs laser fabricated to fabricate a fiber inline FPI with an open cavity [17] and a fiber inline Mach-Zehnder interferometer [18]. These devices have been shown useful for refractive index measurement, temperature sensing and strain monitoring. In this paper, we present a diaphragm based sealed cavity fiber FPI sensor fabricated by fs laser micromachining and arc fusion for pressure measurement. Using fs laser micromachining, the FPI cavity length can be made quite short to further reduce temperature sensitivity, and the diaphragm thickness can be controlled to meet specific requirements on pressure sensitivity and measurement range. Furthermore, the diaphragm outer surface can be roughened to minimize the influence of changes in the ambient media.

7.2 Sensor Principle and Fabrication

Figure 7-1 (a) schematically illustrates the structure of the sensor. To fabricate the sensor, a micro hole was first drilled into the cleaved endface of a single mode fiber (SMF) by fs laser micromachining. The inner surface of the laser-drilled micro hole had quasi-distributed structures of submicron sizes and a low optical reflectivity The hole-drilled SMF was then spliced to another SMF to form a sealed air cavity in between two fibers. Fusion splicer settings (arc duration, arc power, etc) were adjusted to avoid the collapsing of the hole. During fusion

splice, the rough structure of the micro hole surface was melted by the arc. As a result, the surface became smooth and the reflectivity increased. Precision fiber cleaving was applied to cut the fiber so that a thin piece of fiber was left to perform as the diaphragm. Finally the as-cleaved diaphragm was thinned and roughened by fs laser.

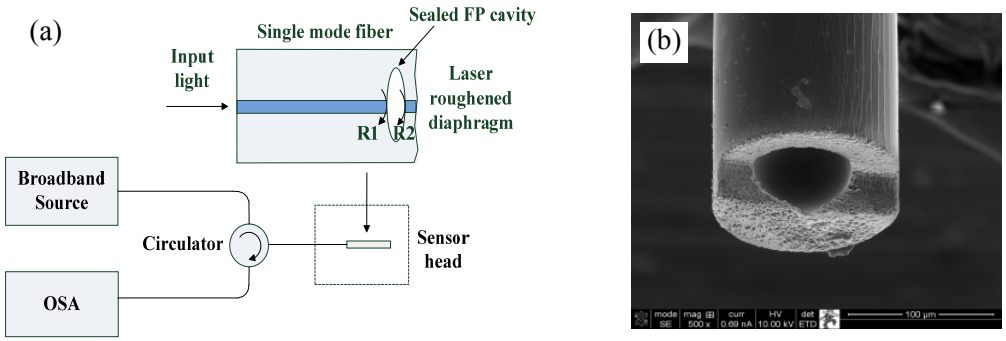

Figure 7-1. (a) Schematic of the pressure sensor, (b) SEM image of the cut out view of the sensor head

During fs laser micromachining, the sensor was mounted on a computer controlled high-precision 3D stage with a resolution of 0.1 μm. Light pulses generated by a regeneratively amplified Ti: Sapphire laser (Coherent RegA 9000, 200 fs pulse duration, 250 kHz repetition rate and 800 nm central wavelength) were focused onto the fiber endface or diaphragm surface through a microscope objective (20× magnification, 0.4 numerical aperture). The laser power could be changed by adjusting the laser beam optics, including a half-wave plate, a polarizer and several neutral density filters. The actual laser energy used for fabrication was approximately 0.4 μJ per pulse.

The diameter and depth of the hole could be varied flexibly. The diaphragm thinning process was also performed layer-by-layer with a step size of 0.5 μm. The fabrication was completed when preset depth scan was reached. Figure 7-1(b) shows the scanning electron microscopic

(SEM) image of a sensor head. For easy visualization, half of the sensor head was cut out using fs laser to expose the sealed hole and the diaphragm. This particular sensor had a cavity with the diameter of 70 μm and the length of 100 μm.

7.3 Tests and Results

A number of sensors were fabricated. The interference spectra of the fabricated sensors were acquired using a system shown in Figure 7-1(a). The system consisted of a broadband light source (Agilent 83437A), a fiber circulator (Thorlabs SM fiber optic circulator 6015-3) and an optical spectrum analyzer (OSA, Ando AQ6319). The optical transmission and reflection insertion losses of the circulator have been calibrated in the wavelength range of 1300 – 1700 nm.

Figure 7-2 (a) and (b) plot the interference fringes of a typical sensor before and after fs laser ablation in air and in water. The sensor had a cavity length of about 8 μm and a hole diameter of 75 μm. The cavity length was calculated to be 7.97 μm based on the interference fringes.

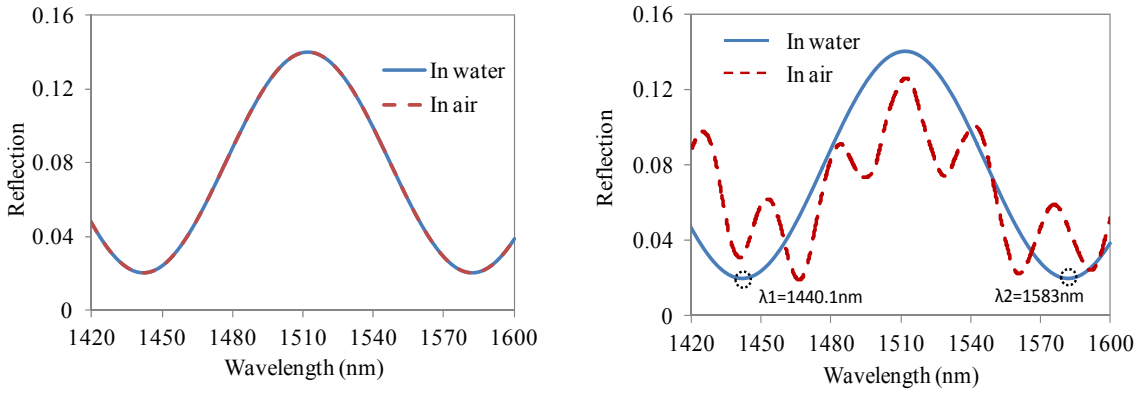

Figure 7-2. Typical interference spectra of the fiber FPI sensor in air and water. (a) Before laser ablation of the diaphragm, (b) After laser ablation of the diaphragm.

The as-cleaved diaphragm had a thickness of about 25 μm, measured by an optical measuring microscope (Nikon Measurescope UM-2). As shown in Figure 3-19(a), before laser ablation the sensor had a distorted spectrum, resulting from the superposition of three-beam interferences. In addition, when the surrounding medium changed from air to water, the fringes changed significantly, suggesting that the as-cleaved diaphragm would introduce measurement errors when the surrounding medium changes. The laser roughened diaphragm significantly reduced the reflection from the outer surface. Immersion of the sensor head into water did not incur any noticeable change to the interferogram, suggesting the immunity of the sensor to variations in surrounding media.

Here, we define the pressure sensitivity as the ratio between the center diaphragm deflection and the applied pressure. The pressure sensitivity is

$$S = \frac{3(1-\mu^2)a^4 P}{16Eh^3} \tag{7-1}$$

where a and h are the diaphragm radius and thickness (in μm), respectively. E and μ are Young's modulus and Poisson's ratio of the diaphragm material.

As the diaphragm deflects the FPI cavity length changes accordingly. The cavity length change can be calculated from wavelength shift according to the following equation

$$\Delta d = \frac{\Delta\lambda_v}{\lambda_v} d \tag{7-2}$$

where λ_v is the wavelength of a specific interference valley, $\Delta\lambda_v$ is the change in the center wavelength of that specific interference valley, Δd is the change in the cavity length, and d is the initial cavity length. Wavelength shift $\Delta\lambda_v$ was obtained by first applying curve fitting to experiment data, and then calculating the interference valley wavelength by setting the first order

derivative of the fit equation to zero. The sensitivity of this method depends on the wavelength measurement resolution, which is 0.05 nm for the OSA used in the experiments.

From Equations (7-1) and (7-2) the wavelength shift as a function of pressure can be written as

$$\Delta\lambda = \frac{3(1-\mu^2)\lambda_v R^4}{16Eh^3 d}\Delta P \tag{7-3}$$

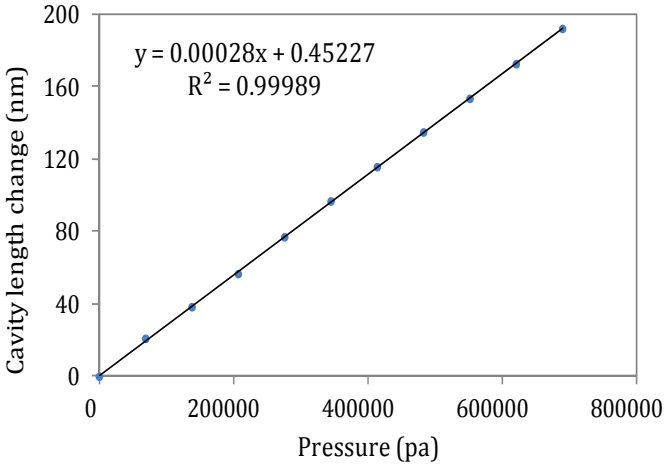

Figure 7-3. Pressure induced inteferogram shift of FPI sensor

Figure 7-3 shows the measurement results obtained from the sensor, where the changes in cavity length are plotted as a function of the applied pressure. Within the pressure range of 100 psi (6.895×10^5 Pa), the center of the diaphragm deflected linearly as the pressure changed. Based on the linear fitting curve, the sensitivity of the sensor was calculated to be 2.8×10^{-4} nm/Pa. Given a wavelength measurement resolution of 0.05 nm of the OSA, the resolution of the pressure sensor was estimated to 180 Pa. The diaphragm thickness could be calculated from measured sensitivity using Equation (7-1). The calculated diaphragm thickness was 2.6 μm, which was close to the target value after laser thinning.

A potential application of the developed sensor is in situ pressure monitoring in a high temperature environment. Minimizing the temperature dependence of the sensor becomes an important issue. To measure the temperature sensitivity, the sensor was placed in an electrical tubular furnace and heated from room temperature (20°C) to 700 °C, and the furnace temperature was then decreased from 700 ˚C to 20 ˚C. Measurements were performed both in temperature increase and decrease cycles. The largest difference between measurement results in the two cycles was 1%. Figure 7-4 plots the wavelength shift of the interferogram as a function of the ambient temperature. The sensor successfully survived at 700 °C and exhibited a linear response to temperature variation.

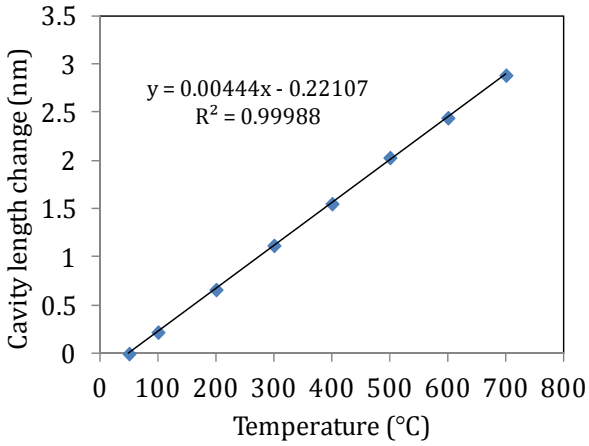

Figure 7-4. Sensor response to temperature changes

The sensor had a temperature sensitivity of 4.44×10^{-3} nm/°C based on the linear fitting curve in Figure 7-4. The air gap change was mainly induced by thermal expansion of the cavity, which was hosted inside fused silica fiber cladding with a coefficient of thermal expansion (CTE) of 5.5×10^{-7} /°C. Given that the sensor had a cavity length of 7.97 μm, the thermal expansion ratio was calculated to be 5.57×10^{-7} /°C, which was very close to the CTE of fused silica. The slightly larger temperature dependence of the sensor, in comparison with the CTE, could be caused by

the expansion of sealed air, which pushed the thin diaphragm outwards as the temperature increased. Nevertheless, the sensor had very small temperature dependence, suggesting low temperature cross-sensitivity in pressure measurement. According to the measurement results, the temperature-pressure cross sensitivity is found to be less than 15.86 Pa/°C.

The sensor was tested for measurement of the autogenic pressure of water vapor at high temperatures. The autogenic pressure is the pressure exerted by a vapor in thermodynamic equilibrium with its condensed phases (solid or liquid) at a given temperature in a closed system. According to reference [18], the saturation water vapor pressure is

$$P = P_0 \exp\left[24.921\left(1-\frac{T_0}{T}\right)\right]\left(\frac{T_0}{T}\right)^{5.06} \tag{7-5}$$

where P is the absolute vapor pressure, T is the temperature, $T_0 = 273.16$ K, $P_0 = 611.657$ Pa.

To perform the experiment, the sensor was sealed in a stainless steel tube, with part of the tube filled with water. The tube was placed in an electric oven and heated from room temperature (20 °C) to 200 °C. Measurements were performed three times at each pressure level. The largest difference among the three time measurements was 0.5%. Figure 3-5 plots the theoretical and measured pressures at different temperatures. The theoretical values were calculated by adding the result from Equation (3-11) and atmospheric pressure at room temperature. The measured values were obtained by measuring the wavelength shifts of the interferogram and converting them to pressure changes using the pressure sensitivity (2.8×10^{-4} nm/Pa) obtained from pressure testing (Figure 7-3).

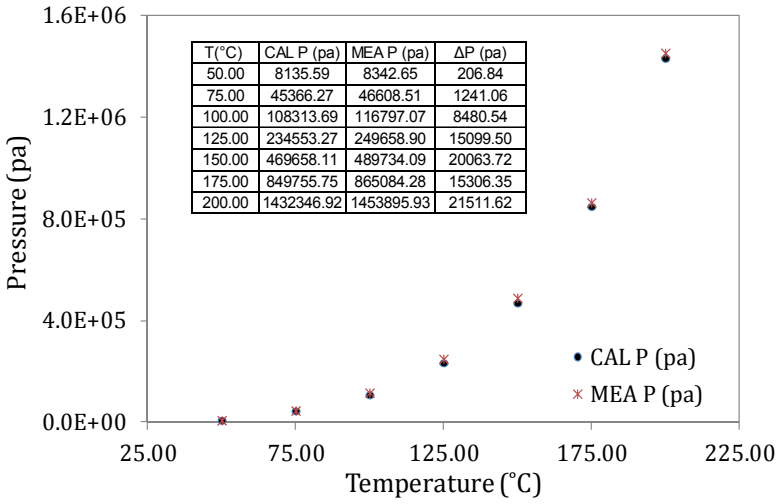

T(°C)	CAL P (pa)	MEA P (pa)	ΔP (pa)
50.00	8135.59	8342.65	206.84
75.00	45366.27	46608.51	1241.06
100.00	108313.69	116797.07	8480.54
125.00	234553.27	249658.90	15099.50
150.00	469658.11	489734.09	20063.72
175.00	849755.75	865084.28	15306.35
200.00	1432346.92	1453895.93	21511.62

Figure 7-5. Measured and calculated water vapor pressures at different temperatures. CAL P: theoretical pressure, MEA P: measured pressure, ΔP: difference of MEA P and CAL P

The sensor successfully survived the high-temperature and high-pressure conditions. The theoretical, experimental values and their difference are also listed in the inset table. In general, the measured pressures were in good agreement with the theoretical values, but the measured values were always larger than the theoretical values. In general, the difference became larger as temperature increased. We believe that the difference was mainly caused by the thermal expansion of the cavity, or in other words, the temperature cross-sensitivity of the device. Other error sources might include the inaccuracy of the model given in Equation (7-5), and imprecise measurements of the initial cavity length, pressure sensitivity, and temperature readings of the oven. Nevertheless, the experiment demonstrated that the feasibility of using the sensor to measure high pressure in a high temperature environment without temperature compensation.

7.4 Summary

In summary, a diaphragm-based miniature fiber optic FPI pressure sensor was fabricated by fs laser micromachining. The sensing head consists of a laser micromachined FPI air cavity and a fused silica diaphragm with its outer surface thinned and roughened by fs laser. The diaphragm thickness can be controlled to vary the sensitivity for pressure measurement. Thin diaphragms with a thickness of 2.6 μm are achievable. A pressure sensitivity of 2.8×10^{-4} nm/Pa and a resolution of 180 Pa were demonstrated. The sensors have been tested at high temperatures up to 700 °C, showing a linear response to temperature with low temperature sensitivity of 5.57×10^{-7}/°C, corresponding to a small pressure-temperature cross sensitivity less than 15.86 Pa/˚C. The sensor has also been demonstrated for measurement of autogenic pressures of water vapor up to 200 ˚C. Without temperature compensation, the pressure measurement results agreed well with those calculated based on the theoretical model. Compared with previously reported fiber-tip pressures sensors, the sensor presented here has less temperature cross-sensitivity. It is also insensitive to variations in ambient refractive index. The diaphragm thickness and diameter can be controlled with fs laser micromachining to adjust the sensitivity and measurement range. The sensor's pressure sensitivity is relatively low compared with sensors made of other diaphragm material such as polymer, but it has a larger pressure range and can work at higher temperature. The developed sensor is useful for pressure measurement in a high temperature harsh environment.

7.5 References

1. T. Zhu, D. Wu, M. Liu, and D. W. Duan, "In-line fiber optic interferometric sensors in single-mode fibers," Sensors **12**, 10430-10449 (2012).
2. C. E. Lee and H. F. Taylor, "Sensor for smart structures based on the Fabry Perot interferometer," in *Fiber Optic Smart Structures,* E. Udd. ed. (Wiley, New York, 1995), pp. 249-269.
3. S. H. Aref, H. Latifi, M. I. Zibaii, and M. Afshari, "Fiber optic Fabry–Perot pressure sensor with low sensitivity to temperature changes for downhole application," Optics Communications **269**, 322-330 (2007).
4. X. Wang, B. Li, Z. Xiao, S. H. Lee, H. Roman, O. L. Russo, K. K. Chin, and K. R. Farmer, "An ultra-sensitive optical MEMs sensor for partial discharge detection," J. Micromech. Microeng **15**, 521-527 (2005).
5. T. Bae, R. A. Atkins, H. F. Taylor, and W. N. Gibler, "Interferometric Fiber-Optic Sensor Embedded in a Spark Plug for In-Cylinder Pressure Measurement in Engines," Appl. Opt. **42**, 1003-1007 (2003).
6. M. J. Gander, W. N. Macpherson, J. S. Barton, R. L. Reuben, J. D. C. Jones, R. Stevens, K. S. Chana, S. J. Anderson, and T. V. Jones, "Embedded micromachined fibre optic Fabry-Perot pressure sensors in aerodynamics applications," IEEE Sensors J. **3**, 102-107 (2003).
7. J. Deng, H. Xiao, H. Huo, M. Luo, R. May, A. Wang, and Y. Liu, "Optical ber sensor-based detection of partial discharges in power transformers," Opt. Laser Technol. **33**, 305-311 (2001).
8. J. Zhou, S. Dasgupta, H. Kobayashi, J. M. Wolff, H. E. Jackson, and J. T. Boyd, "Optically interrogated MEMS pressure sensors for propulsion applications," Optical Engineering **40**, 598-604 (2001).
9. S. Watson, M. J. Gander, W. N. MacPherson, J. S. Barton, J. D. C. Jones, T. Klotzbuecher, T. Braune, J. Ott, and F. Schmitz, "Laser-machined fibers as Fabry-Perot pressure sensors," Appl. Opt. **45**, 5590-5596 (2006).
10. W. Wang, N. Wu, Y. Tian, C. Niezrecki, and X. Wang, "Miniature all-silica optical fiber pressure sensor with an ultrathin uniform diaphragm," Opt. Express **18**, 9006-9014 (2010).
11. H. Bae, L. Dunlap, J. Wong, and M. Yu, "Miniature Temperature Compensated Fabry-Perot

Pressure sensors created with Self-Aligned Polymer Photolithography Process," IEEE Sens. J. **12**, 1566-1572 (2012).

12. B. Yu, D. W. Kim, J. Deng, H. Xiao, and A. Wang, "Fiber Fabry-Perot Sensors for Detection of Partial Discharges in Power Transformers," Appl. Opt. **42**, 3241-3250 (2003).
13. E. Cibula and D. Đonlagic, "Miniature fiber-optic pressure sensor with a polymer diaphragm," Appl. Opt. **44**, 2736-2744 (2005).
14. X. Wang, J. Xu, Y. Zhu, K. L. Cooper, and A. Wang, "All-fused-silica miniature optical fiber tip pressure sensor," Opt. Lett. **31**, 885-887 (2006).
15. F. Xu, D. Ren, X. Shi, C. Li, W. Lu, L. Lu, L. Lu, and B. Yu, "High-sensitivity Fabry?Perot interferometric pressure sensor based on a nanothick silver diaphragm," Opt. Lett. **37**, 133-135 (2012).
16. J. Ma, W. Jin, H. L. Ho, and J. Y. Dai, "High-sensitivity fiber-tip pressure sensor with graphene diaphragm," Opt. Lett. **37**, 2493-2495 (2012).
17. T. Wei, Y. Han, H. L. Tsai, and H. Xiao, "Miniaturized fiber inline Fabry-Perot interferometer fabricated with a femtosecond laser," Optics letters **33**, 536-538 (2008).
18. D. Koutsoyiannis, "Clausius–Clapeyron equation and saturation vapour pressure: simple theory reconciled with practice," Eur. J. Phys. **33**, 295-305 (2012).

8. Hybrid EFPI/IFPI for Simultaneous Measurements of Temperature and Pressure

8.1 Introduction

Pressure and temperature are two important parameters in the well and reservoir down-hole monitoring. Accurate, continuous and real time data of pressure and temperature helps in the oil and reservoir management [1]. Sensors with dual-parameter sensing capability and survivability in the down-hole harsh environment are highly necessary in such applications. Fiber optic sensors, with advantages such as small size, low loss, high sensitivity, resistance to harsh environment and multiplexing capability, are good candidates for pressure and temperature down-hole monitoring.

In the past years, several types of fiber optic sensors have been demonstrated for pressure and temperature sensing. The major types include fiber Bragg Grating (FBG) for temperature or dual parameters measurement [2-5], diaphragm based Fabry-Perot interferometer (FPI) for pressure sensing [6, 7], long period fiber grating (LPFG) for temperature sensing [8], etc. An early reported type used a single FBG that was half encapsulated and the other half fixed in a polymer filled metal cylinder [2]. Because the resonance wavelength shift of the FBG is affected by both temperature and pressure, the cross sensitivity becomes an issue. Double FBG coated by a special polymer in a metal tube was later developed to discriminate between pressure and temperature [3]. FBGs in specialty fibers have also been proposed, e.g., FBGs in standard and grapefruit microstructure fibers (GMF) [9]. However, the ultraviolet laser induced FBG has a maximum temperature limit of around 200 ˚C. Recently, a combined pressure-temperature sensor consisting of two low-finesse Fabry-Perot resonators was reported [10]. This structure

provides potentials for high-temperature applications. However, the fabrication process involves HF etching which is hazardous.

In this project, we developed presents a new method for dual-parameter sensing using the cascaded intrinsic Fabry-Perot interferometer (IFPI) and extrinsic Fabry-Perot interferometer (EFPI) sensors. These sensors are fabricated using a femtosecond (fs) laser. The IFPI is constituted by a pair of fs laser-induced internal reflectors. The EFPI is positioned at the fiber tip consisting of fs laser thinned silica diaphragm and a sealed air cavity.

8.2 Sensing Mechanism and Device Fabrication

The proposed sensor consists of a pair of cascaded IFPI and EFPI, as shown in Figure 8-1(a). The IFPI is formed by two internal partial reflectors created by fs laser in the core of a single-mode fiber. It is sensitive to temperature due to the combination of the thermo-optic effect and thermal expansion of the fiber material. However, the IFPI is insensitive to pressure. The EFPI is located at the fiber tip, formed by the fiber endface and a thin silica diaphragm which deflects under pressure, providing pressure sensing function.

Sensor fabrication consists of the following steps. First, EFPI was fabricated at the tip of a single mode fiber. A section of hollow core silica capillary tube with outer diameter of 150 μm and inner diameter of 75 μm (TSP075150, Polymicro Inc.) was initially spliced to a standard single-mode fiber (Corning SMF-28e). Then the tube was cleaved at a distance (tens of micrometers) from the splice point with the help of a microscope. The tube was then spliced to another SMF to form a sealed air cavity sandwiched in two fibers. Precision fiber cleaving was applied to cut the fiber so that a thin piece of fiber was left to perform as a diaphragm. Finally

the as-cleaved diaphragm was thinned and roughened by a fs laser (Coherent RegA 9000, 200 fs pulse duration, 250 kHz repetition rate and 800 nm central wavelength). The fs laser micromachining method was described in detail in our previous publication. The fs laser fabrication method has several advantages, including precise control of the diaphragm thickness, immunity to the refractive index variations of the surrounding medium, and easy for signal processing, etc. Figure 8-1(d) shows the image of an EFPI fabricated using this method.

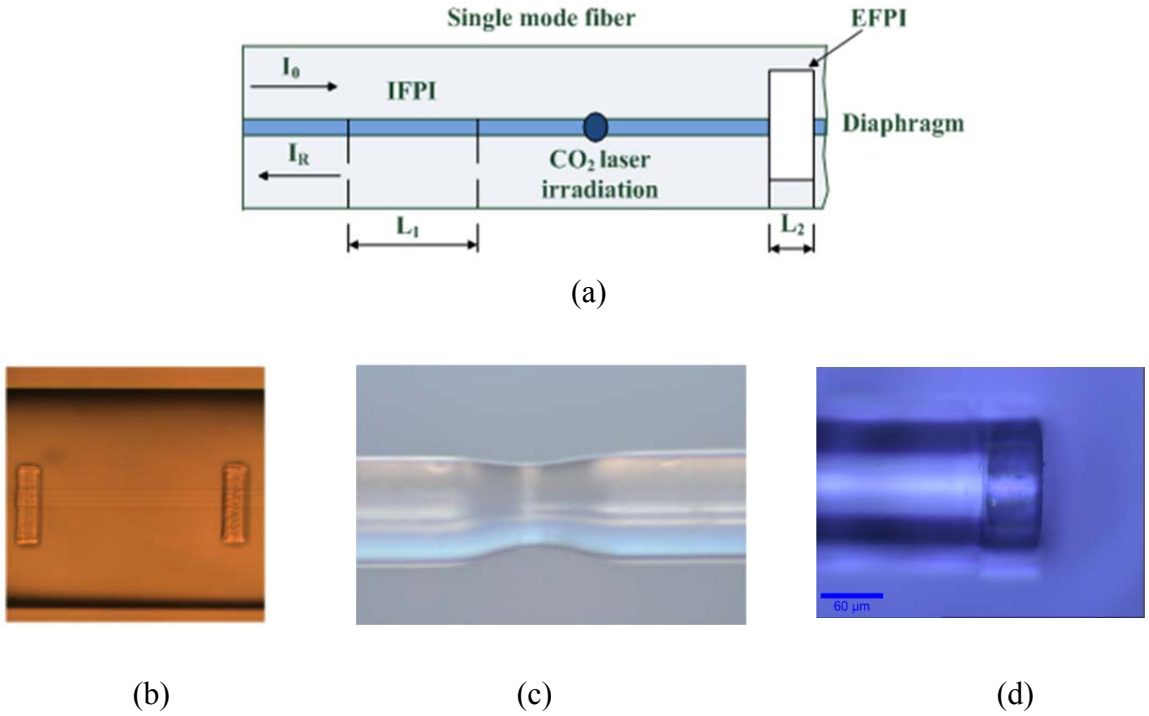

Figure 8-1. (a) Scheme of the proposed sensor (b) photo of IFPI (c) photo of CO2 laser irradiation point (d) photo of EFPI.

Next, an IFPI was fabricated at a short distance (~1 cm) away from the EFPI. It was created by inscribing two parallel lines in the fiber core with fs laser. A water immersion lens (Olympus UMPlanFL 20X) was used to focus the fs laser beam into the fiber core. Figure 8-1(b) shows the microscopic image of an IFPI. The two parallel lines in fiber core are clearly observed.

With the above fabrication procedure, an IFPI with a cavity length L_1 of a few hundred micrometers and an EFPI with a cavity length L_2 of tens of micrometers were successfully produced. L_1 was set to be significantly longer than L_2 to facilitate signal processing which will be discussed later.

The refractive index change in the fiber core induced by fs laser is very small (10^{-4} – 10^{-2}), therefore the reflectivity of the internal reflectors in an IFPI is far lower than the reflectivity of an air/glass interface in an EFPI (4%). Due to the unbalanced reflectivity, there is a difference of 20 to 30 dB in their intensity levels. The intensity level of the IFPI signal is so low that it can be hardly observed in the spectrum.

One method to balance the power levels of the IFPI and EFPI signals is to add a transmission loss between the IFPI and EFPI. In this paper, a CO_2 laser (SYNRAD, Inc.) with a free space wavelength of 10.6 μm was employed to heat the fiber to increase the transmission loss. A ZnSe cylindrical lens with a focal length of 50 mm was used to shape the CO_2 laser beam into a narrow line with a linewidth of about 220 μm. The CO_2 laser was controlled by a computer so that the output power and exposure duration could be accurately adjusted. During fabrication, the CO_2 laser heated the fiber and created a micro bend between EFPI and IFPI, as shown in Figure 8-1(c). An optical spectrum analyzer (Ando AQ 6319) was used to monitor the reflection spectrum. The power and duration time of the CO_2 laser was set to 12 W and 200 ms, and the irradiation process was repeated multiple times until an ideal spectrum was obtained.

The temperature sensitivity of a Fabry-Perot sensor is contributed by the thermo-optic and thermal-expansion effects,

$$K_T = (\alpha_{TO} + \alpha_{CTE})\lambda_v \tag{8-1}$$

where α_{TO} is the thermo-optic coefficient, α_{CTE} is the coefficient of thermal expansion, and λ_v is the wavelength of an interference valley. The typical values of the fused silica are 8.3×10^{-6} °C^{-1} and 5.5×10^{-7} °C^{-1}, respectively, so in an IFPI thermo-optic effect plays a major role in its temperature sensitivity. However, in an air cavity based EFPI, the thermo-expansion effect plays a dominant role.

The wavelength shift of an interference valley as a function of pressure is

$$\Delta\lambda = \lambda_v \frac{S}{L}\Delta P \tag{8-2}$$

where L is the EFPI cavity length, and ΔP is the pressure change. Therefore the pressure sensitivity coefficient $K_{P,EFPI}$ as a function of wavelength shift can be obtained.

When temperature and pressure are simultaneously applied, the wavelength shifts of the IFPI and EFPI can be expressed as

$$\Delta\lambda_{IFPI} = K_{P,IFPI} \times \Delta P + K_{T,IFPI} \times \Delta T \tag{8-3}$$

$$\Delta\lambda_{EFPI} = K_{P,EFPI} \times \Delta P + K_{T,EFPI} \times \Delta T \tag{8-4}$$

The temperature and pressure can be obtained by solving the following characteristic matrix

$$\begin{bmatrix} \Delta T \\ \Delta P \end{bmatrix} = \frac{1}{\Omega}\begin{pmatrix} K_{P,EFPI} & -K_{P,IFPI} \\ -K_{T,EFPI} & K_{T,IFPI} \end{pmatrix}\begin{bmatrix} \Delta_{\lambda,IFPI} \\ \Delta_{\lambda,EFPI} \end{bmatrix} \tag{8-5}$$

where $\Omega = K_{P,EFPI}K_{T,IFPI} - K_{T,EFPI}K_{P,IFPI}$.

The interference signals of the EFPI and IFPI sensors are multiplexed. The fast Fourier Transform (FFT) is a widely used method to demodulate multiplexed Fabry-Perot interferometer (FPI) signals. By performing the Fourier transform to the recorded interferogram, the optical

path difference (OPD) of each FPI can be resolved. The minimum detectable OPD change is given by

$$\Delta l = \frac{\pi}{\nu_E - \nu_S} \tag{8-6}$$

where ν_E and ν_S are the smallest and largest wavenumbers in the measurement range, respectively.

According to Equation (8-6), for a broadband light source with wavelength range from 1520 nm to 1620 nm, Δl is approximately 12 μm. Due to the low resolution, FFT is not suitable for signal demodulation when the cavity length change is small. Recently, a fast-Fourier-transform-based wavelength tracking method to demodulate multiplexed IFPI signals was proposed. This method uses band-pass filters to extract specific frequency components and transform them back to the wavelength domain, and then use wavelength tracking method to find the OPD change. As a result, the measurement accuracy has been significantly improved.

8.3 Experiments and Results

Figure 8-2 (a) plots the recorded spectrum of the multiplexed IFPI and EFPI sensors, and Figure 8-2 (b) plots the FFT of the spectrum. Two main frequency components with substantially different OPDs can be clearly identified, corresponding to the EFPI and IFPI, respectively. The OPD for IFPI is the refractive index of the fiber core (n = 1.4682) times the physical cavity length, so the cavity lengths of the EFPI and IFPI are calculated to be 62 μm and 680 μm, respectively.

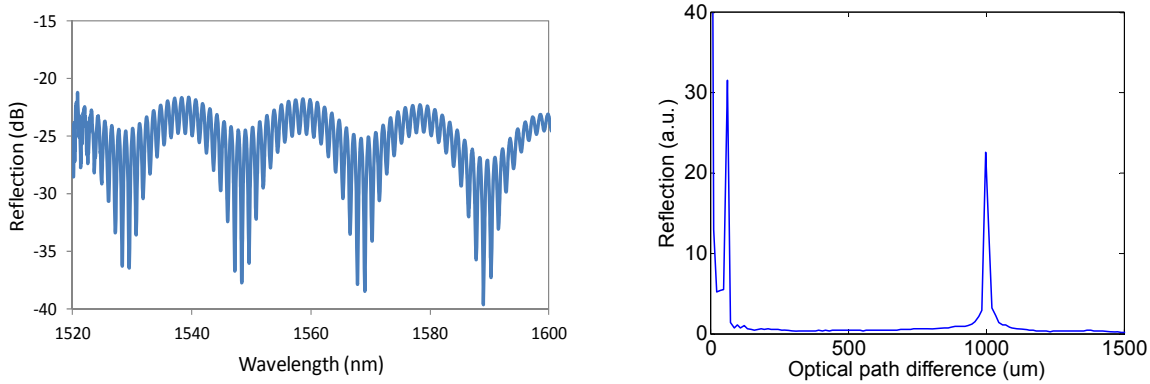

(a) (b)

Figure 8-2. (a) Interference spectrum of multiplexed EFPI and IFPI sensors, (b) FFT of the multiplexed sensor spectrum

Two Hamming-windowed digital filters were used to select each frequency component. After filtering, interference spectrum was reconstructed using an inverse FFT. Figure 8-3 (a) and (b) plot the reconstructed waveforms of the EFPI and IFPI, respectively.

Once the individual interferograms of the EFPI and IFPI were obtained, we can pick a specific interference valley in the reconstructed waveform as the tracking wavelength. Then the wavelength tracking method were used to obtain the wavelength shifts of the interferograms.

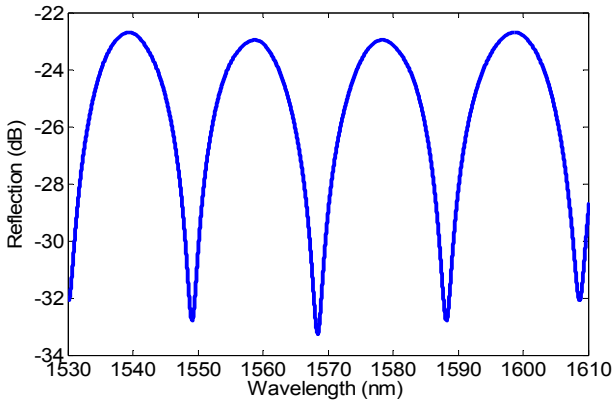

(a)

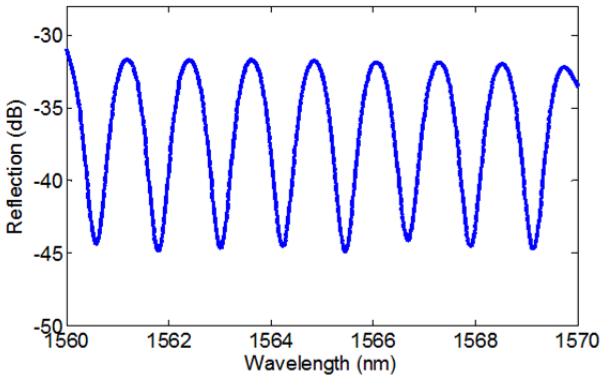

(b)

Figure 8-3. Reconstructed interferograms of (a) EFPI (b) IFPI

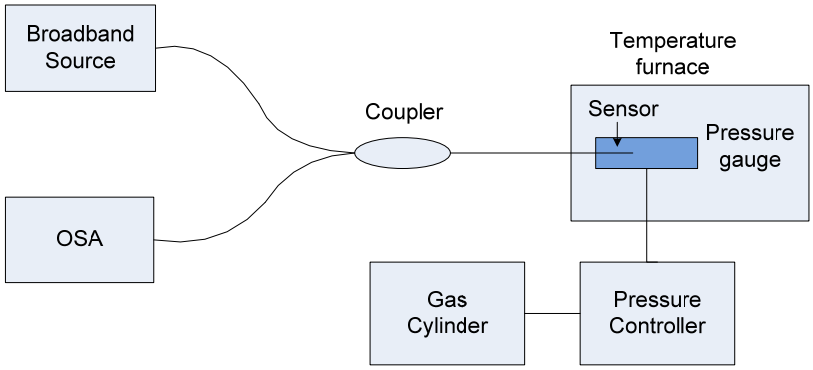

Figure 8-4. Experiment setup for sensor test

The experimental setup for sensor characterization is illustrated in Figure 8-4. The light from a 100 nm bandwidth ASE light source (BWC-ASE) was launched into the sensor via a 3-dB fiber coupler. The sensor was sealed in a Swagelok tube where the air pressure was supplied using a compressed Argon gas cylinder and controlled by a pressure controller (MKS640). The pressure controller/generator could provide a static pressure up to 6.895×10^5 Pa with a precision of ~0.5%. The Swagelok tube-sealed sensor was then placed in a programmable electrical furnace

(Lindberg/blue M) whose temperature could be varied from room temperature to 1100 °C. The sensor output signal was recorded using an optical spectrum analyzer.

First, the temperature and pressure sensitivities for the EFPI and IFPI sensors were calibrated. The calibration results are listed in Table 8-1. As we expected, the IFPI is primarily temperature sensitive but pressure insensitive. On the other hand, the EFPI is primarily pressure sensitive but temperature insensitive.

Table 8-1 Calibration results

Coefficient	$K_{T,EFPI}$	$K_{P,EFPI}$	$K_{T,IFPI}$	$K_{P,IFPI}$
Value	0.001 nm/°C	1×10^{-6} nm/Pa	0.0146 nm/°C	0

Next, the sensor was tested for simultaneous pressure and temperature measurements. The measurement procedure was described as follows. Given a constant temperature, the pressure was increased from 0 to 6.895×10^5 Pa at an increment of 1.379×10^5 Pa. Under a constant pressure, the temperature was set to increase from room temperature (20 °C) to 700 °C at an incrementing step of 50 °C.

Figure 8-5(a) shows the measured pressure results of the hybrid sensor at the temperatures of 20 °C, 400 °C and 700 °C. Figure 8-5(b) shows the measured temperature results of the hybrid sensor at different pressures of 0 Pa, 3.447×10^5 Pa, and 6.895×10^5 Pa. The temperature and pressure data were taken directly from the electrical furnace and the pressure controller readings, respectively. Linear approximation curves were added to show the linearity of the measurement results. As shown in Figure 8-5, the hybrid sensor successful decoupled the temperature and

pressure. The maximal measured discrepancy among individually measured pressures at three temperatures was 4×10^3 Pa, in the pressure range of 0 to 6.895×10^5 Pa. The maximal measured discrepancy among individually measured temperatures at three pressures was 0.8 °C, in the temperature range of 20 °C to 700 °C. The discrepancies were within the range of instrument uncertainties and the resolution limit of used optical spectrum analyzer.

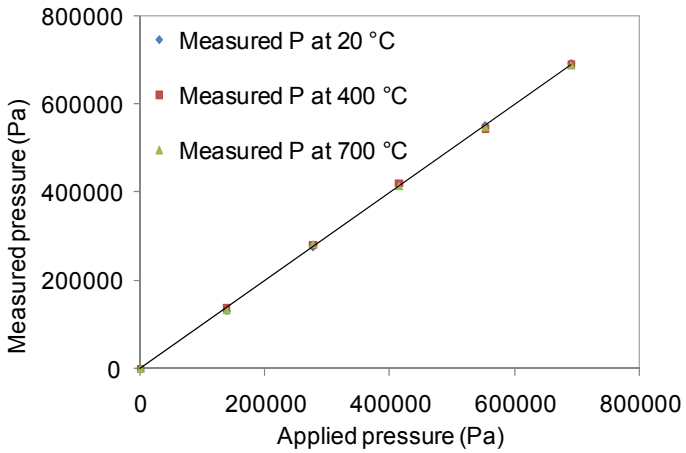

(a)

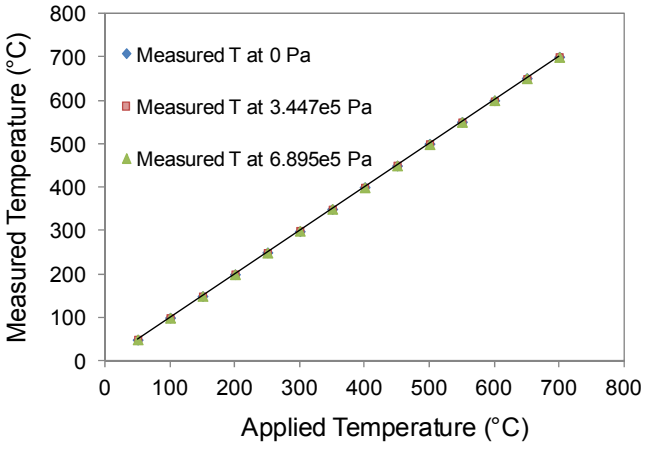

(b)

Figure 8-5. (a) Pressure measurement results under various temperatures (b) Temperature measurement results under various pressures.

8.4 Summary

In summary, we developed a miniature, all-fiber IFPI and EFPI hybrid sensor suitable for simultaneous measurement of temperature and pressure. The IFPI was fabricated using a fs laser to micromachine two reflectors inside the core of a singlemode fiber. The IFPI was primarily sensitive to temperature but intensitive to pressure variations. The EFPI was fabricated by fusion-spacing a fused silica capillary tube between two singlemode fibers and precision-cleaving of a fiber to form a thin diaphragm-sealed cavity. The diaphragm was further thinned by fs laser ablation which allowed for precise control of the diaphragm thickness and immunity to the refractive index variations of the surrounding medium. Because of the diaphragm sealed air-cavity structure, the EFPI is primarily sensitive to pressure but insensitive to temperature. A CO_2 laser was used for the creation of an attenuator to balance the reflected power levels of the two sensors for easy signal processing and sensor demultiplexing. The EFPI and IFPI were designed to have significant different OPDs and the multiplexed interference signals were demodulated using Fast Fourier transform based wavelength tracking method. The hybrid sensor was tested for simultaneous measurements of pressure and temperature in a temperature range from 20 to 700 °C and a pressure range from 0 to 6.895×10^5 Pa. The results showed complete decoupling between the pressure and temperature. The good linearity in the measurement range and the simultaneous measurement capability of the demonstrated sensor provide the potentials for down-hole monitoring in high temperature and pressure harsh environments.

8.4 References

1. G. Fusiek, P. Niewczas, and J. R. McDonald, "Design of a highly accurate optical sensor system for pressure and temperature monitoring in oil wells", in IEEE I2MTC 2009, Singapore, 574-578 (2009).

2. A. Sun, X. Q. Qiao, A. Jia, M. Li, and D. Z. Zhao, "Study of simultaneous measurement of temperature and pressure using double fiber Bragg gratings with polymer package," *Opt. Eng.* , **44**, 034402-034406 (2005).

3. Y. Liu, Z. Guo, Y. Zhang, K. S. Qiang, and X. Dong, "Simultaneous pressure and temperature measurement with polymer-coated fiber Bragg grating," *Electr. Lett.*, **36**, 564-566 (2000).

4. E. Chmielewska, W. Urbanczyk, and W. Bock, "Measurement of Pressure and Temperature Sensitivities of a Bragg Grating Imprinted in a Highly Birefringent Side-Hole Fiber," *Appl. Opt.*, **42**, 6284-6291 (2003).

5. T. Guo, X. Qiao, Z. Jia, Q. Zhao, and X. Dong, "Simultaneous measurement of temperature and pressure by a single fiber Bragg grating with a broadened reflection spectrum," *Appl. Opt.*, **45**, 2935-2939 (2005).

6. K. Bremer, E. Lewis, B. Moss, G. Leen, S. Lochmann, and I. Mueller, "Conception and preliminary evaluation of an optical fibre sensor for simultaneous measurement of pressure and temperature," in J. Phys.: Conf. Ser., Edinburgh, UK, 012016, (2006).

7. S. H. Aref, H. Latifi, M. I. Ziabii, and M. Afshari, "Fiber optic Fabry–Perot pressure sensor with low sensitivity to temperature changes for downhole application," *Opt. Commun*., **269**, 322-330, (2007).

8. Y. L. Wang, C. L. Yang, H. Y. C. Jan, G. R. Lin, J. C. Mau, M. Y. Fu, et al., "Simultaneous temperature and pressure measurement using a packaged FBG and LPG," in OptoeElectronics and Communications Conference (OECC), 2010 15th, 814-815, (2010).

9. C. Wu, Y. Zhang, and B. Guan, "Simultaneous Measurement of Temperature and Hydrostatic Pressure Using Bragg Gratings in Standard and Grapefruit Microstructured Fibers," *IEEE Sens. J.*, **11**, 489-492 (2011).

10. S. Pevec and D. Donlagic, "Miniature all-fiber Fabry-Perot sensor for simultaneous measurement of pressure and temperature," *Appl. Opt.*, **51**, 4536-41 (2012).

9. Microcavity High-Temperature Strain Sensors by fs Laser Micromachining

9.1 Introduction

Optical fiber-based sensors have gained wide application for strain monitoring due to their compact size, immunity from electromagnetic interference, multiplexing capabilities etc. thus offering an alternative to traditional electrical sensors and conventional pneumatic-based sensors [1-3]. Different types of optical fiber instruments like fiber Bragg grating sensors, extrinsic Fabry–Perot interferometric (EFPI) sensors, intrinsic Fabry–Perot interferometric (IFPI) sensors, long-period fiber grating sensors, and related hybrid combination sensors have been used for monitoring strain, stress, temperature, and pressure [3-7]. Temperature sensitivity and temperature maximums are important practical limitations for many of these sensors. For instance, the temperature sensitivity of Bragg grating and IFPI sensors are well known. The EFPI-type sensors are better suited for strain monitoring applications with high ambient temperatures as opposed to Bragg gratings and IFPI sensors. These rugged sensors have excellent noise-free performance and fatigue characteristics [8, 9].

The EFPI-type sensors are better suited for strain monitoring applications with high ambient temperatures as opposed to Bragg gratings and IFPI sensors. These rugged sensors have excellent noise-free performance and fatigue characteristics. [10] The most widely used method for realizing the EFPI sensor is by epoxying two pieces of fiber, with cleaved ends, inside a hollow tube (glass or ceramic) and controlling the separation distance between the two fiber ends. [11-15] In addition to the cumbersome fabrication process and the calibration issues related to controlling the cavity gap, this design has limited thermal performance due to the thermal

expansion of the tube and the temperature limitation of the epoxy, e.g., Loctite epoxy extra time pro (slow setting) is effective up to 150°C once cured. Alternative approaches with low temperature sensitivities have been demonstrated by splicing a hollow-core fiber between two sections of single-mode fiber, [16] by forming voids at splices between photonic crystal fiber and conventional singlemode fiber, [17-19] and by laser-machining micro-cavities into single-mode fiber. [20] The microcavity sensor in Ref. 20 provides easily reproducible characteristics, but it has an open cavity design that exposes the cavity to the environment. In particular, this open cavity limits embedded applications. An EFPI sensor can also be fabricated using wet chemical etching in which diluted hydrofluoric acid forms a cavity in the tip of a multimode fiber, and this cavity is fused with a single-mode fiber. [21] This latter EFPI alternative has good temperature characteristics, but it suffers from safety concerns during fabrication and from difficulty in controlling the etch, i.e., for calibrating the cavity length.

In this project, a microcavity EFPI strain sensor is fabricated using femtosecond (fs) laser micromachining to form the cavity and is self-enclosed with a fusion splice. This sensor is less bulky than a tube-based EFPI, the fs-laser processing is fast and the resulting cavity length is precisely controlled, and the performance is relatively temperature insensitive and is thermally stable. The sensor is capable of operating in high temperature applications. Fabrication, strain performance, and thermal effects are discussed.

9.2 Sensor Principle and Device Fabrication

The overall optical response for a Fabry–Perot cavity depends on multiple-beam interference in light transmitted and reflected from the two ends of the cavity. This periodic response is

modulated by the wavelength and optical path (gap) length. Figure 9-1 (a) shows a traditional EFPI design in which the cavity is formed between the end faces of optical fiber that are aligned with an epoxied capillary tube. In a strain sensor with an air gap of length d, the gauge length, i.e., the length of the sensing element, is approximately the tube length L. Figure 9-1 (b) shows the microcavity EFPI in which the cavity is formed in the fiber itself and a second fiber is fusion spliced to self-enclose the cavity. As a strain sensor with an air gap of length d, the gauge length is the cavity gap length d. The smaller gauge length allows the latter sensor to more closely approximate a point sensor. Also, the tube component causes the former design to be bulkier and to have a more complex fabrication than the microcavity design. Note that the exact gauge length and the initial gap length are more difficult to determine for the traditional design, hence calibration is an issue.

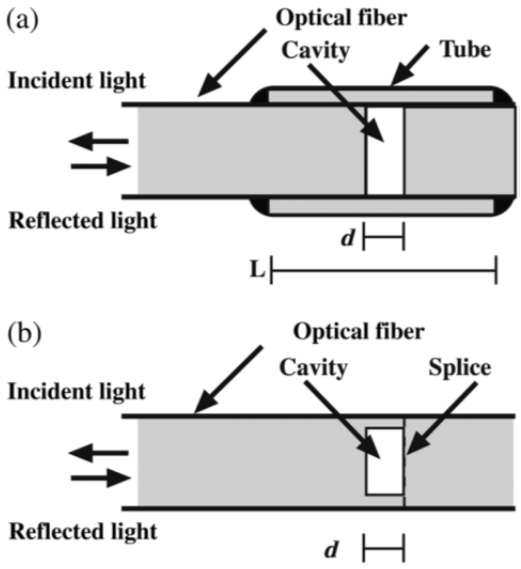

Figure 9-1. (a) Traditional tube-based extrinsic Fabry–Perot interferometric (EFPI) sensor and (b) microcavity EFPI sensor.

The EFPI response is dependent on any parameter changing the cavity optical path length. For the bare sensor with no applied strain, e.g., a sensor not attached to a structure to be measured, changes in ambient temperature T induces a Δd due to the thermal expansion of the silica fiber. Since the coefficient of thermal expansion (CTE) for silica (0.55×10^{-6}/°C) is small, this temperature dependence is minimal. Hence, the single-mode silica fiber EFPI is an ideal candidate for high temperature applications. The smaller gage length and the absence of epoxy reduce the influence of temperature on the microcavity EFPI performance.

Figure 9-2 shows the micromachining system with a fs laser. The single-mode fiber is cleaved and the fiber tip is aligned with a five-axis translation stage (resolution 1 μm). The fs laser is focused on the fiber tip and a cavity is precisely ablated as shown in Figure 3-30. The fs-laser system (maximum output of 1W) operates at a center wavelength of 800 nm with the repetition rate and pulse width of 250 kHz and 200 fs, respectively. The laser power used for fabrication was 0.4 μJ per pulse. The sensor fabrication is completed by fusion splicing another single-mode fiber. The resulting cavity is 65×65×35 μm^3.

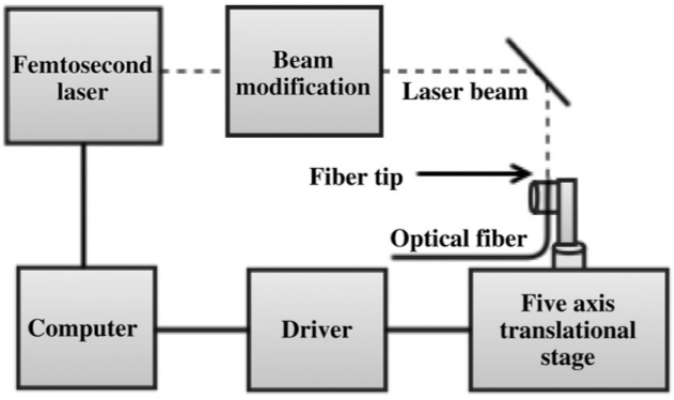

Figure 9-2. Block of the femtosecond-laser micromachining system.

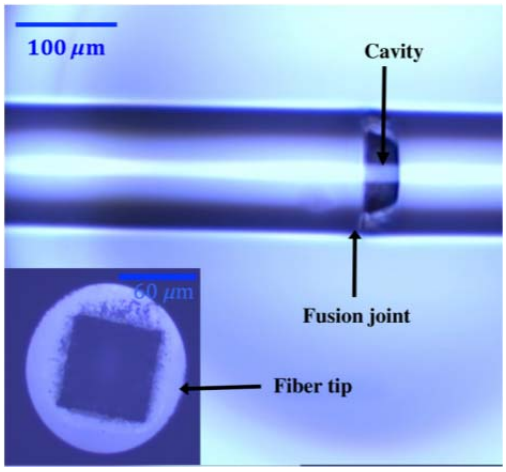

Figure 9-3. Confocal microscopic image of the microcavity (side view and tip view).

Figure 9-3 shows the instrumentation used for sensor testing. A 100-nm broadband source is the input, a 3-dB coupler sends the signal to the sensor and receives the reflected signal back, and an optical spectrum analyzer (OSA) then records the wavelength spectra. Figure 9-4 shows the spectra shift for an applied 500-με strain. Several microcavity EFPI sensors were fabricated with similar cavity lengths (~35 μm), fringe visibility (10 to 12 dB), and excess loss (4 to 6 dB) (The excess loss is the nonideal power drop, e.g., for destructive interference the return signal is −4 to −6 dB down from the ideal value of 0 dB).

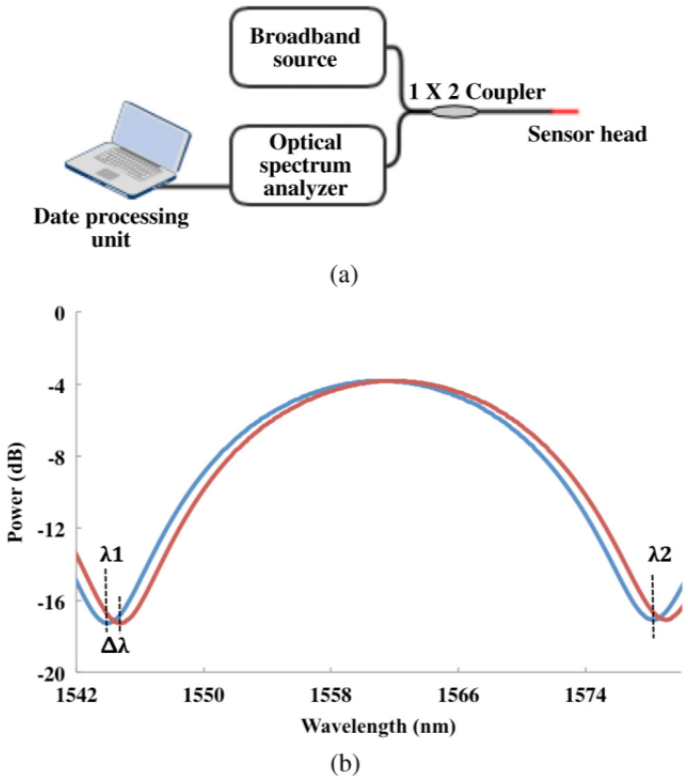

Figure 9-4. (a) Instrumentation for EFPI sensor testing and (b) wavelength spectra shift for an applied 500-με strain

9.3 Sensor Tests and Results

Figure 9-5 shows the strain-induced response of the microcavity sensor at room temperature. The wavelength spectra shift is plotted with respect to the applied strain. The sensor was fixed between two translational stages and axial strain was applied in steps of 100 με. The sensor response was linear with response slope of 1.5 pm/με. The strain was applied until the sensor broke at the fusion joint as verified under a microscope. The breaking point for the EFPI sensor was 3700 με approximately. The figure inset shows detailed performance for strains applied from 1000 through 1500 με.

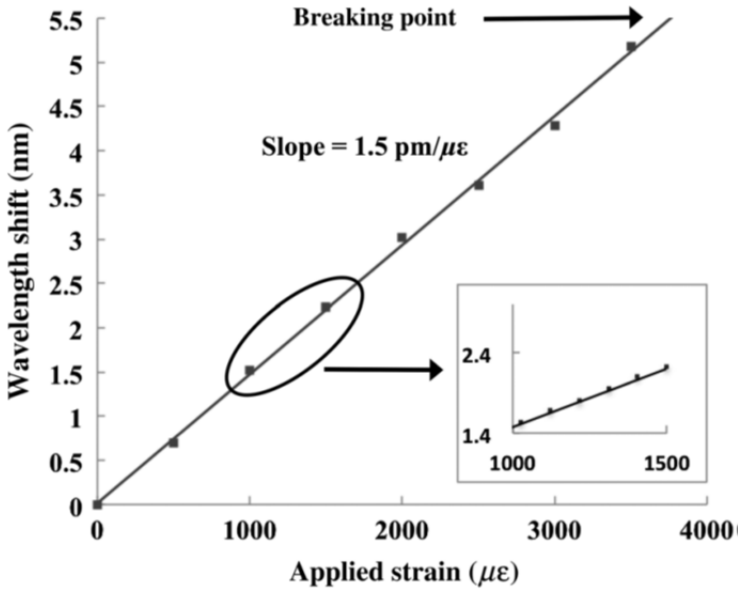

Figure 9-5. Wavelength spectra shift for applied strain at room temperature.

Figure 9-6 shows the temperature-induced wavelength shift with no applied strain. For the temperature testing, the sensor was placed inside a box furnace (Lindberg/Blue M). The temperature of the furnace was raised from 50°C to 800°C in steps of 50°C, and the resultant wavelength shift in the spectrum was recorded using the OSA. The results are plotted in terms of wavelength shift as well as the apparent strain.

The slopes of the experimental response for the EFPI sensor were 0.59 pm/°C and 0.37 με/°C for wavelength shift and apparent strain, respectively. The CTE of silica was calculated to be 0.715×10^{-6}/°C that is 1.3 times larger than that of the reference silica CTE of 0.55×10^{-6}/°C.

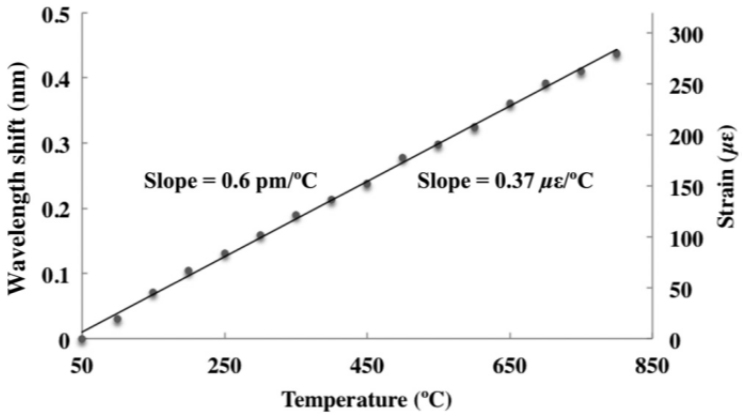

Figure 9-6. Temperature dependence of the wavelength spectra shift and the apparent strain.

The design's capability for handling high temperatures was also tested by keeping a second identical sensor at 650°C for 3 h. No change in the reflection spectrum was observed during this 3-h test. The sensor was then returned to room temperature and temperature-induced wavelength shift with no applied strain was again determined. The sensor survived the whole process without any deterioration in the performance, i.e., it had the same responses as given in Figure 9-6 for the sensor with no prior high temperature history.

9.4 Summary

In summary, a robust, compact EFPI strain sensor is demonstrated that is easy to fabricate and calibrate and that has a high operating temperature. A single fusion joint allows for better structural integrity and less complicated compared to traditional designs. The fs-laser fabrication results in well-controlled cavity for calibration. The wavelength shift with applied strain is linear up to a breaking point of about 3700 με. The sensor has a low cross sensitivity due to low thermal expansion of the silica glass, i.e., the wavelength shift with temperature is small up to at

least 800°C. The experimental CTE value was slightly higher than the reference value for silica. Ongoing work is examining the sensor performance for embedded applications in which the sensor must survive high-temperature fabrication processes and must monitor strain at elevated temperatures. Preliminary results show successful sensor operation and strain transfer while embedded in carbon fiber composite laminate plate. Overall, the microcavity EFPI is a good candidate for strain monitoring applications in high ambient temperatures.

9.5 References

1. E. Udd, "An overview of fiber-optic sensors," Rev. Sci. Instrum. 66(8), 4015–4030 (1995).
2. R. Kashyap, "Photosensitive optical fibers: devices and applications," Opt. Fiber Technol. 1(1), 17–34 (1994).
3. R. M. Measures, "Advances toward fiber optic based smart structures," Opt. Eng. 31(1), 34–47 (1992).
4. Y. Yu et al., "Fiber Bragg grating sensor for simultaneous measurement of displacement and temperature," Opt. Lett. 25(16), 1141–1143 (2000).
5. V. Bhatia et al., "Optical fiber extrinsic fabry-perot interferometric strain sensor for multiple strain state measurements," Proc. SPIE 2444, 115–126 (1995).
6. X. Wang et al., "All-fused-silica miniature optical fiber tip pressure sensor," Opt. Lett. 31(7), 885–887 (2006).
7. E. Cibula et al., "Miniature all-glass robust pressure sensor," Opt. Express 17(7), 5098–5106 (2009).
8. S. J. Mihailov, "Fiber Bragg grating sensors for harsh environments," Sensors 12(2), 1898–1918 (2012).
9. D. W. Kim et al., "Simultaneous measurement of refractive index and temperature based on a reflection mode long-period grating and an intrinsic fabry-perot interferometer sensor," Opt. Lett. 30(22), 3000–3002 (2005).
11. V. E. Zetterlind, III, S. E. Watkins, and M. Spoltman, "Fatigue testing of a composite

propeller blade using fiber-optic strain sensors," IEEE Sens. J. 3(4), 393–399 (2003).
12. T. Yoshino et al., "Fiber-optic Fabry-Perot interferometer and its sensor applications," IEEE J. Quantum Electron. 18(10), 1624–1633 (1982).
13. A. D. Kersey, D. A. Jackson, and M. Corke, "A simple fiber Fabry-Perot sensor," Opt. Commun. 45, 71–74 (1983).
14. D. Hogg et al., "Development of a fiber Fabry-Perot strain gauge," Proc. SPIE 1588, 300–307 (1991).
15. W. Zhao et al., "Geometric analysis of optical fiber EFPI sensor performance," Smart Mater. Struct. 7(6), 907–910 (1998).
16. Y. Huang et al., "An extrinsic Fabry–Perot interferometer-based large strain sensor with high resolution," Meas. Sci. Technol. 21(10), 10538 (2010).
17. J. Sirkis et al., "In-line fiber etalon (ILFE) fiber-optic strain sensors," J. Lightwave Technol. 13(7), 1256–1263 (1995).
18. J. Villatoro et al., "Photonic-crystal-fiber-enabled micro-Fabry-Perot interferometer," Opt. Lett. 34(16), 2441–2443 (2009).
19. F. C. Favero et al., "Fabry-Perot interferometers built by photonic crystal fiber pressurization during fusion splicing," Opt. Lett. 36(21),4191–4193 (2011).
20. F. C. Favero et al., "Spheroidal Fabry-Perot microcavities in optical fibers for high-sensitivity sensing," Opt. Express 20(7), 7112–7118 (2012).
21. Y. J. Rao et al., "Micro Fabry-Perot interferometers in silica fibers machined by femtosecond laser," Opt. Express 15(21), 14123–14128 (2007).
22. E. Cibula et al., "Miniature all-glass robust pressure sensor," Opt. Express 17(7), 5098–5106 (2009).

10. Fabry-Perot Fiber Optic Acoustic Sensors with Improved Directivity

10.1 Introduction

Fabry-Perot (FP) type fiber optic acoustic sensors are widely used to characterize ultrasound fields. Compared with Fiber Bragg Grating (FBG) and Michelson type acoustic sensors, fiber tip FP sensors have higher sensitivity, and their ultra-small probe structure facilitates measurement in limited space. Recently, FP acoustic sensors with different fabrication and assembly methods have been reported [1-5]. Much work has been done to achieve highly sensitive [3] and large bandwidth [6] acoustic sensors. Directional acoustic sensors are also being investigated by researchers; however, the FP type directional acoustic sensors are yet to be developed.

Directional acoustic sensors are preferred in applications requiring directional acoustic source information. Directivity is the sensor's response to acoustic wave incident on it from different directions. It depends on a number of factors, including acoustic frequency, sensor's active element radius, geometric structure, material and assembly method, etc. The directivity measurement of a FP fiber acoustic sensor shows the sensor has 45° monitoring range with an amplitude frequency fluctuation of 2.6 dB at 160 kHz [7]. The sensor directivity is quite low in this case, which is good for omni-directional measurement such as partial charge detection, but not suitable for directional measurement.

Directional acoustic sensor can be achieved with various structures. For example, a compact directional acoustic sensor was made from a two-fiber optical probe, a photodetector and a cylinder cantilever whose acoustically induced displacement modulates the light received by the photodetector [8]. Another example is a wavelength division multiplexing (WDM) underwater acoustic sensor two-fiber Bragg gratings (FBG) can detect the relative phase between two points

in the acoustic field and thereby determine the direction of the acoustic source [9]. One limitation of these structures is the sensor length is relatively long. We propose a method to improve directivity of FP acoustic sensor with ultra-small sensing part. The sensor head was encapsulated in a hollow glass tube coated with acoustically blocking wax film. The directivity of bare sensor was measured in comparison with packaged sensor.

10.2 Sensor Principle

Figure 10-1 shows the schematic diagram of the FP acoustic sensor structure and interrogation system. Light from a tunable laser is guided into the sensor through a circulator. The sensor head consists of an EFPI cavity formed by a lead-in single mode fiber, an air cavity and a thin fiber diaphragm. The sensor was fabricated by femtosecond laser and the procedure was described in detail in Section 4. The reflected signals (R_1 and R_2) from the two surfaces of EFPI are combined to generate an interference signal. A photodetector converts the optical signal to electrical signal and transmits the signal to an oscilloscope. When an acoustic wave impinges on the diaphragm, it deflects the diaphragm and changes the cavity length, therefore modulating the signal received by the oscilloscope.

The fundamental resonant frequency of such sensor in fluid is expressed as

$$f = \frac{1}{\sqrt{1+\beta}} \frac{\alpha h}{2\pi a^2} \sqrt{\frac{E}{12\omega(1-\mu^2)}} \tag{10-1}$$

$$\beta = 0.669 \frac{\omega_1 a}{\omega h} \tag{10-2}$$

where α is a constant defined by the vibration mode. For the fundamental vibration mode, α=10.21. a is the diaphragm radius, h is the diaphragm thickness, E and μ are Young's modulus and poisson's ratio of diaphragm material. ω is the specific weight of diaphragm material, and ω_1 is the specific weight of fluid surrounding the sensor.

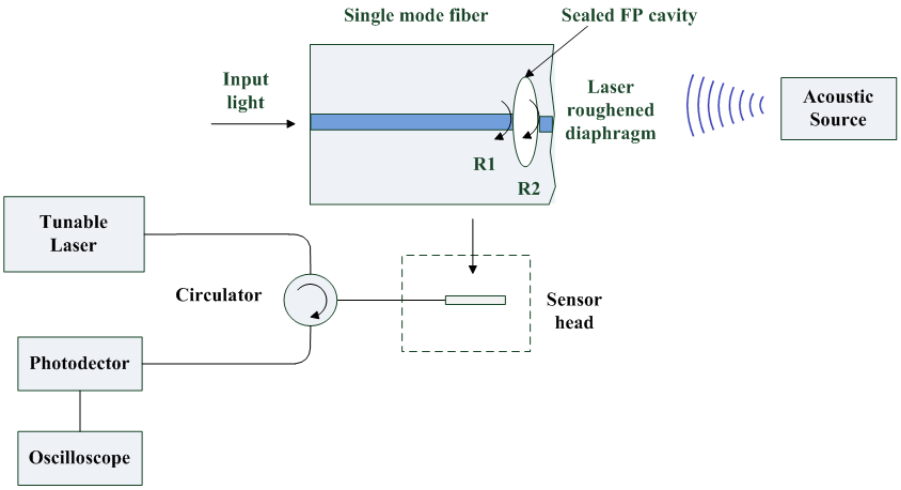

Figure 10-1. Diagram of acoustic sensor interrogation system

The directional response of FP acoustic sensor is usually modeled by circular piston model. In the case of rigid piston, the deflection of diaphragm can be written as

$$z(\theta) = z(0)\left(\frac{2J_1(ka\sin\theta)}{ka\sin\theta}\right) \tag{10-3}$$

where z(0) is the maximum diaphragm deflection at θ=0˚, k is the wave number, a is the diaphragm radius, and θ is the angle between fiber axis and incident wave.

Figure 10-2 shows the sensor packaging method to improve directivity. The sensor head was packaged in a hollow silica tube. The inner diameter of the tube was tapered to ~130 μm. The

tube was then coated with wax film by solidifying liquid wax uniformly at the surface of silica tube. Wax is a sound wave absorbing material like plastics and silicon rubbers. It was chosen as coating material because of its low cost and easy for operation. A short distance (tens of micro meters) was kept from the sensor diaphragm to the tube endface for sensor protection purpose. And finally epoxy was applied to bond the lead-in fiber to encapsulating tube.

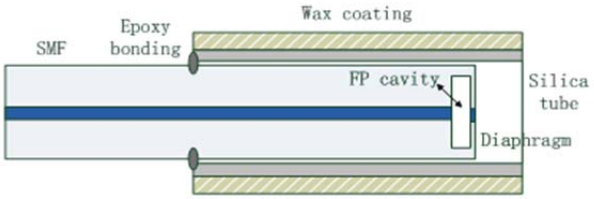

Figure 10-2. Sensor packaging schematic

Due to its acoustic absorbing property, the wax film absorbs incident acoustic waves on its surface. When the sensor was placed at $\theta=0^{\circ}$ to the acoustic source, no waves are absorbed. When angle θ increases, some waves will be absorbed by the wax film, therefore waves reaching the diaphragm become less, and the sensor becomes more directive.

10.3 Experiments and Results

Figure 10-3 shows the experiment setup for fiber optic hydrophone measurement. The measurement was carried out underwater in a water tank. An ultrasound transducer (Olympus V326-SU) driven by a high-voltage pulser/receiver (JSR Ultrasonic DPR300) was used as acoustic source. The transducer was mounted on a three-dimensional translation stage. A fiber acoustic sensor was fixed using a fiber holder (Newport FPH-S) with the fiber axis parallel to the transducer axis. A wavelength tunable laser used as light source, and its wavelength was tuned to

the Q-point in the sensor's interference spectrum to obtain maximum sensitivity. The sensor signal was converted to electrical signal using Tektronix P6073B O/E converter (DC-1.2 GHz), and then connected to Channel 1 in the oscilloscope (Tektronix DPO7254). The pulse-echo signal received by the pulser/receiver was connected to Channel 2 in the oscilloscope. And the internal trigger of the pulser/receiver was connected to oscilloscope as trigger signal. The signals were averaged 50 times to reduce white noise. To reduce sound reflections from the walls of water tank, acoustically absorbing plastic foams were attached to the inner walls.

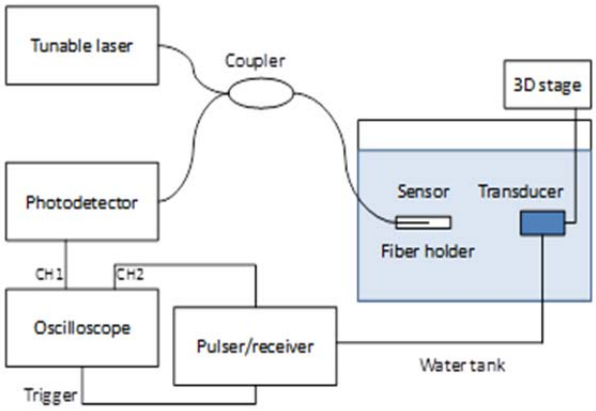

Figure 10-3. Fiber optic hydrophone measurement system

Figure 10-4 shows the typical time domain and frequency domain signals of the fiber optic hydrophone to pulsed ultrasound signal. The time domain signal is an exponentially decreasing ringing signal typical to the impulse response of a FP sensor. The fundamental resonant frequency f_0 of the sensor is ~6.2 MHz. The thickness and diameter of the sensor's diaphragm are set to be 5 μm and 70 μm respectively. Using Equations (3-18) and (3-19), we calculated f_0 to be 6.3 MHz, close to the measured result.

The frequency responses of the sensor at different incident angles were measured using the setup in Figure 10-5. The sensor was fixed in a fiber holder mounted on a rotation stage that can rotate 360° with a resolution of 1°. The tip of the sensor was placed one inch (focal length of the transducer) away from the ultrasound transducer. Angle between the transducer and sensor axis was controlled by the rotation stage.

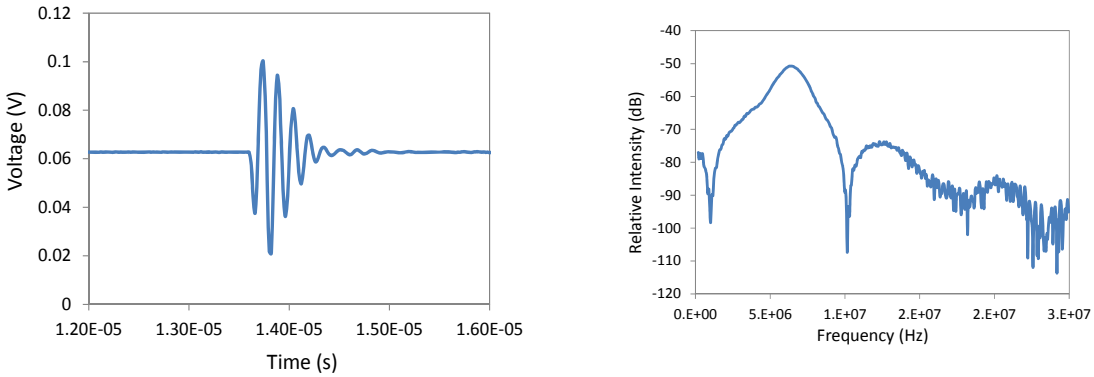

(a) (b)

Figure 10-4. (a) Time-domain response of the fiber hydrophone to transducer pulsed signal (b) Fourier transform of time-domain signal shown in (a)

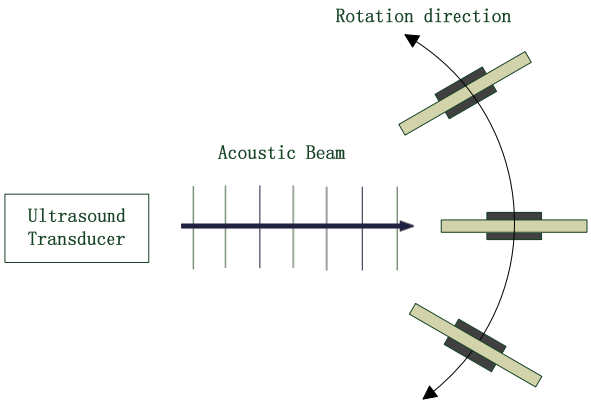

Figure 10-5. Experiment setup for directional response measurement

Figure 10-6 shows the amplitude frequency response of the sensor at different incident angles, from 0˚ to 90°. With the help of a three-dimensional stage, the sensor was aligned such that its tip remained at the same position when it was rotated. The directional response was obtained by measuring the sensor signal at each rotation angle, and taking fast Fourier Transform (FFT) of the signals. In the experiment, sensor signals were recorded every 10°. The result of rigid piston model at f=5 MHz is also plotted in Figure 10-7. From the figure it can be seen the curve of experiment data follows the same trend as rigid piston model, but the value is smaller than the model.

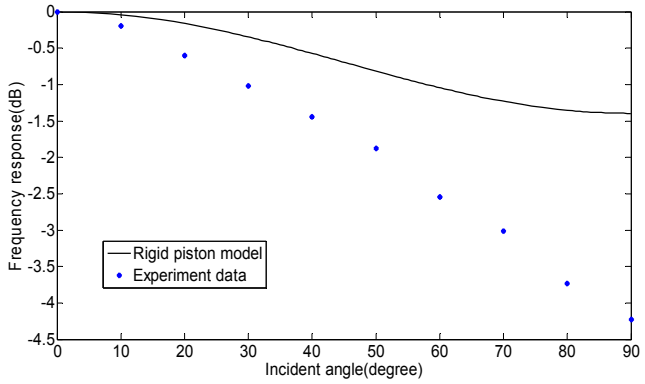

Figure 10-6. Directional response of bare sensor compared with rigid piston model

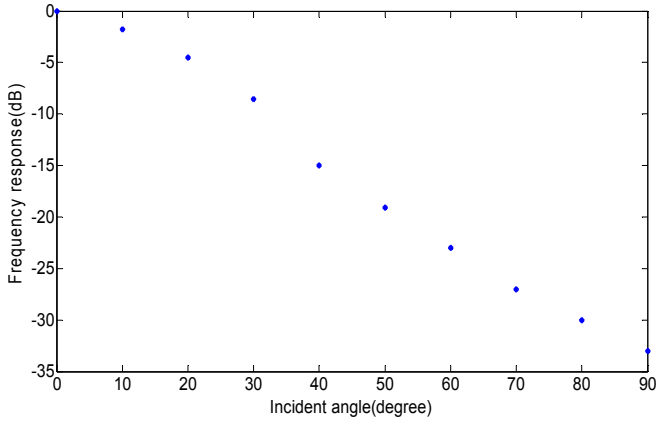

Figure 10-7. Directional response of the packaged sensor using the same setup.

From Figures 10-6 and 10-7, the amplitude of sensor's frequency response decreases much faster after packaging. The 3-dB bandwidth of frequency response changes from ~70˚ to ~8˚. It proves the function of sensor packaging to increase directivity.

10.4 Summary

In summary, a silica diaphragm Fabry Perot fiber optic acoustic sensor was fabricated and tested. Acoustic performance such as resonant frequency and directional response were investigated. The directivity of sensor increases after packaging in a wax film coated hollow tube. The packaging could also protect sensor head from damage. The assembly-free fiber optic sensor could be used for directional acoustic measurement in a high temperature environment.

10.5 References

1. P. Morris, H. Hurrell, A. Shaw, E. Zhang and P. Beard, "A Fabry–Pérot fiber-optic ultrasonic hydrophone for the simultaneous measurement of temperature and acoustic pressure," *J. Acoust. Soc. Am.* vol.125, no. 6, pp. 3611-22, Jun. 2009
2. B. T. Cox, E. Z. Zhang, J. G. Laufer and P.C. Beard, "Fabry Perot polymer film fiber-optic hydrophones and arrays for ultrasound field characterization," *Journal of Physics: Conference Series* 1 pp.32–37, 2004
3. J. Ma, H. Xuan, H. L. Ho, W. Jin, Y. Yang and S. Fan, "Fiber-Optic Fabry–Pérot Acoustic Sensor with Multilayer Graphene Diaphragm," *IEEE Photonics Technology Letters*, vol. 25, no. 10, pp. 932-935, May. 2013

4. W. Wang, N. Wu, Y. Tian, X. Wang, C. Niezrecki, and J. Chen, "Optical pressure/acoustic sensor with precise Fabry-Perot cavity length control using angle polished fiber," *Opt. Express* vol.17, no. 19, pp.16613-16618, Sep. 2009

5. J. Xu, X. Wang, K. Cooper, and A. Wang, "Miniature all-silica fiber optic pressure and acoustic sensors," *Opt. Lett.* vol. 30, pp. 3269-3271, Dec. 2005.

6. R. G. Minasamudram, "Optimization of wideband fiber optic hydrophone probe for ultrasound sensing applications," Ph.D dissertation, Dept. Elect. Eng. Drexel Univ., Philadelphia, PA, 2010.

7. L. Song, Z. Wang, K. Wang and K. L. Cooper, "Angular Dependence of the Frequency Response of an Extrinsic Fabry–Pérot Interferometric (EFPI) Fiber Acoustic Sensor for Partial Discharge Detection," *Journal of Lightwave Technology*, vol. 24, no. 9, pp. 2433-3438, Sep. 2006.

8. J. A. Bucaro, N. Lagakos, B. H. Houston, S. Dey, M. Zalalutdinov, "Compact directional acoustic sensor using a multi-fiber optical probe," *J. Acoust. Soc. Am*. vol.13, no.2, pp. 832-41, Feb. 2013.

9. N. Takahashi, K. Tetsumura, K. Imamura, S. Takahashi, "Fiber-Bragg-grating WDM underwater acoustic sensor with directivity," in *Proc. SPIE 3541,* 1998, pp. 18-26.

10. Y. Zhang, L. Yuan, A. Kaur, X. Lan, J. Huang and H. Xiao, "High temperature fiber optic Fabry-Perot interferometric pressure sensor fabricated by femtosecond laser," *Opt. Lett.,* to be published.

11. J. F. Krucker, "Rigid piston approximation for computing the transfer function and angular response of a fiber optic hydrophone, *Acoust. Soc. Am.* vol. 107, no. 4, pp. 1994-2003, 2000.

12. *Flat and Corrugated Diaphragm Design Handbook*, New York: Marcel Dekker, 1982, Ch. 12 and 17.

13. *Transmission Systems for Communications*, 3rd ed., Western Electric Co., Winston-Salem, NC, 1985, pp. 44–60.

14. H. J. Lee, S. S. Lee, Y. H. Lee, "Surface acoustic wave sensor system," U. S. Patent 20110068656, Mar. 24, 2011.

11. Optical Fiber Inline Microchannel Fabricated by fs laser

11.1 Introduction

Aiming to synergistically combine integrated optics and microfluidics, optofluidics based systems have attracted much research interest because of their unique advantages towards biological/chemical sensing applications [1]. In an optofluidic system, the liquid of interest is constrained and manipulated in a small geometry to interact with the optics. As such, the physical, chemical and biological properties of the liquid can be probed and analyzed effectively using optical means [2].

Most optofluidic systems have been constructed on a planar platform with microchannels in silica/polymetric materials and probed by a variety of optical methods, such as absorbance, fluorescence, refractometry, Raman-scattering, etc [3]. Objective lenses are commonly used to couple light into and out of the microfluidics [4]. However, the need of using a microscope to perform the optical alignment limits its field applicability. A number of efforts have been made to fabricate optical waveguides inside the substrate to confine and transport light in the substrate [5] or directly integrate optical fibers with the fluidics for excitation and probing [6]. However, the transmission efficiency of light coupling is still a challenge in most optofluidic configurations.

In addition to planar configurations, it has been suggested that the microfluidics can be directly fabricated on an optical fiber to form the so-called all-in-fiber optofluidics. The all-in-fiber configuration has the unique advantage of alignment free optics and improved robustness. Examples include the photonic crystal fibers (PCF) filled with functional fluids in their cladding air voids [7], the capillary-based optofluidic ring resonator (OFRR) with a microchannel for

sample delivery [8], and a miniaturized microchannel directly fabricated on a conventional optical fiber for light-fluid interaction [9]. While the PCF-based and OFRR-based optofluidic sensors utilize the evanescent fields to probe the fluid, the microchannel on a conventional fiber configuration allows a direct light passing-through of the liquid.

Recently, the femtosecond laser (fs) irradiation followed by chemical etching technique has been demonstrated as a powerful approach for fabricating optofluidic micro devices [10]. This technique offers great simplicity and flexibility to produce buried three-dimensional (3D) structures with high aspect ratios in transparent materials [11]. The etching rate of a laser-modified region was found to be two orders of magnitude higher than that of the unexposed region in silica materials. As a result, such hybrid technique has been adopted for fabrication of optofluidic devices in planar sample and optical fibers [9, 12].

In this project, we explored an all-in-fiber 3D optofluidic micro device fabricated by the femtosecond laser assisted chemical etching technique. To demonstrate the concept, we fabricated an all-in-fiber optofluidic device consisting of horizontal and vertical microchannels. The horizontal microchannel can be conceived as a Fabry-Perot (FP) cavity, while the vertical ones are the inlets/outlets to the cavity. In our previous work, the fs laser micromachined FP cavity has been used for various sensing applications such as refractive index (RI) [13] and pressure [14] measurement. It has been approved that the formed FP cavity is insensitive to the ambient temperature.

11.2 Sensing Mechanism and Device Fabrication

Figure 11-1 illustrates the schematic of the all-in-fiber optofluidic device, where a horizontal fluid-holding cavity is embedded in the center of a single-mode fiber and four vertical microchannels are punched through the fiber cladding to allow liquid access to the cavity. The device is fabricated in two steps: 1) irradiation of the selected regions (the rectangular cavity and vertical channels) with focused fs laser pulses; 2) selective etching of the laser modified zones using the hydrofluoric acid (HF) solution.

Optically, the horizontal cavity also functions as a FP cavity. The light propagates inside the fiber and reflects at the two air/silica endfaces of the cavity. The two reflections, which are denoted as I_1 and I_2, respectively, superimpose to generate an interference pattern.

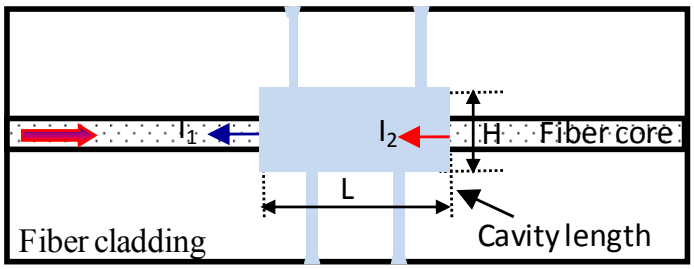

Figure 11-1. Schematic of the all-in-fiber optofluidic device.

The round-trip optical path difference (OPD) of the Fabry-Perot interferometer is given by:

$$OPD = 2n_{cavity}L \tag{11-1}$$

where n_{cavity} is the refractive index of the cavity medium; L is the cavity length. At the valleys of the interferogram in spectrum domain, the phase difference of the two reflected light beams satisfies the condition of coherently destructive interference,

$$\frac{4\pi n_{cavity} L}{\lambda_m} + \varphi_0 = (2m+1)\pi, \tag{11-2}$$

where m is an integer; λ_m is the wavelength of the m^{th} order interference valley. The distance between two adjacent minima of the spectrum, defined as free spectrum range (FSR) can then be expressed as,

$$FSR = \frac{\lambda^2}{2n_{cavity} L}, \tag{11-3}$$

Figure 11-2 shows the scheme of the Ti: Sapphire fs laser (Coherent, Inc.) micromachining system used for fabrication of the fiber inline Fabry-Perot interferometer. The central wavelength, pulse width and repetition rate of the laser were 800 nm, 200 fs and 250 kHz, respectively. The maximum output power of the laser was 1W.The actual power used for fabrication was controlled by adjusting the laser beam optics including a half-wave plate, a polarizer and several neutral density (ND) filters. The laser was switched on or off by electrically gating the internal clock. The actual laser energy used for fabrication was approximately 0.4 μJ per pulse.

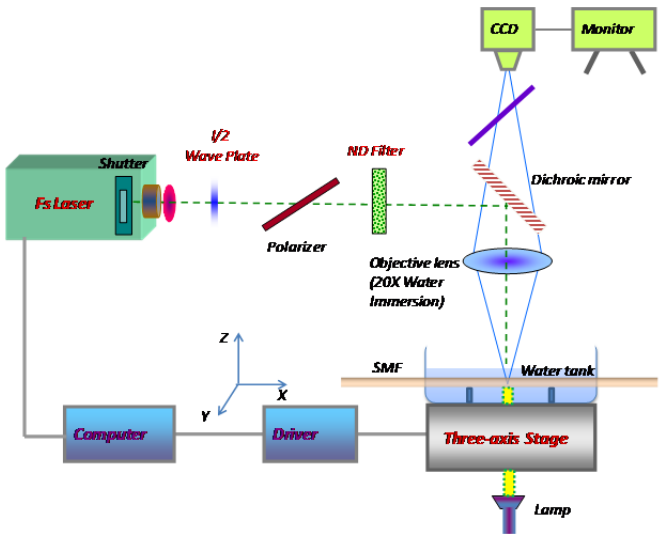

Figure 11-2. Scheme of the fs laser micromachining system.

A section of standard single-mode optical fiber (Corning SMF-28) with the core diameter of 8.2 μm was cleaned and clamped by two bare fiber holders (Newport 561-FH). A home-machined water tank was used for loading the fiber and filling with distilled water. The optical fiber and the fiber holders were placed inside a water-filled tank where they were all mounted on a high-precision, computer-controlled three-axial translation stage (Newport, Inc.) with a resolution of ± 0.1 μm. The fs laser beam was focused inside the optical fiber through a water immersion objective lens (Olympus UMPlanFL 20x) with a numerical aperture (NA) of 0.4. The spot size of the focused beam was about 1 μm. The velocities of the stages were all set at 100 μm/s.

In order to fabricate a high quality FPI cavity, the following steps were adopted in the fabrication process. Firstly, a rectangle region, which can cover the whole fiber core area, with the dimension of L×10 ×H μm was inscribed using fs irradiation from the bottom to the top (z direction), where L and H denote the length and height of the micro-cavity, respectively; Secondly, the irradiation position of the designable channels was chosen. The stage was translated along the fiber direction to locate the channel position, and the laser was focused right in the center of the fiber core. Then the stage was translated along the z direction to make sure the fs laser beam can irradiate a straight line along the z direction. After one side fabrication, the fiber was then rotated by 180° to allow the fabrication of the channels on the other side, following the same procedure as mentioned above; Finally, the sample was dipped into a HF solution with a concentration of 20 % for 10 minutes (cavity dimension dependent), following by cleaning in an ultrasonic bath filled with distilled water and drying in air. The microchannel with a built-in FPI cavity was formed ultimately.

Figure 11-3 (a) shows the microscope image of a fabricated all-in-fiber optofluidic device, where the cavity length *L* and the cavity height *H* are about 55 μm and 20 μm, respectively. Figure 11-3 (b) shows the top view of the device. The diameter of the vertical microchannels is about 5 μm.

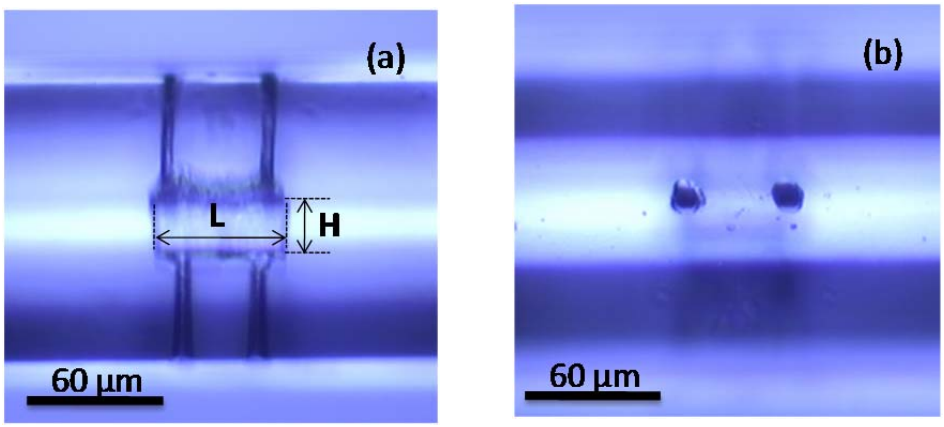

Figure 11-3. (a) Microscope image of the fabricated all-in-fiber optofluidic device with the FP cavity length of 55 μm and (b) top view of the fiber device.

11.3 Tests and Results

The fabricated all-in-fiber optofluidic device was interrogated using a broadband light source with wavelength range from 1520 nm to 1620 nm. A 3 dB fiber coupler was used to route the light into and out of the device. The interference spectrum was recorded by an optical spectral analyzer (OSA, AQ6319). Figure 11-4 shows the reflection spectra of the all-in-fiber optofluidic device with the FP cavity length of 35 μm and 55 μm, respectively. The FSRs of these two interferometers are 36 nm and 21 nm, respectively, which matched well with those calculated using Equation (11-2). The interference pattern with a fringe visibility of about 20 dB was

obtained with the cavity length of 55 μm, which is adequate for most sensing applications. The excess loss of the device was about 18 dB, which was mainly caused by the roughness of the cavity surfaces. To a certain extent, the surface quality can be improved by tuning the laser irradiation power, adjusting the concentration of HF solution and the etching time.

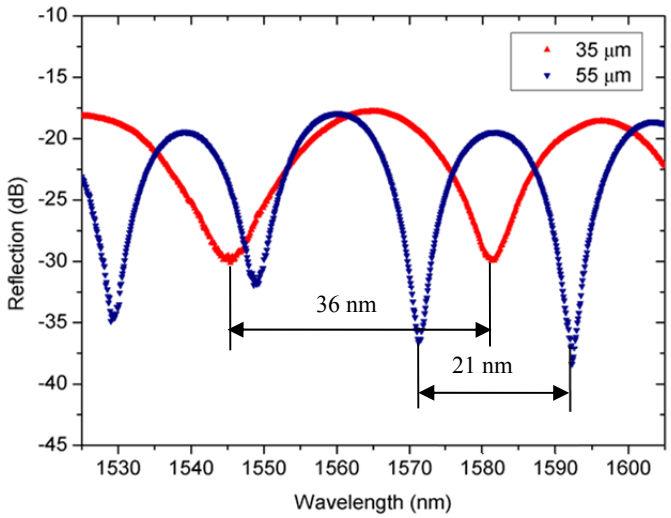

Figure 11-4. Reflection spectra of the all-in-fiber optofluidic devices with cavity lengths of 35 and 55 μm in air.

The all-in-fiber optofluidic device with a cavity length of 55 μm was tested for its capability of RI measurement at room temperature. The sensor probe was directly immerged into the sucrose solutions with different concentrations of 0.00, 1.00, 2.00, 3.00, 4.00, 5.00, 6.00, 7.00, 8.00 and 9.00 (unit: percentage). The corresponding RIs are 1.3333, 1.3344, 1.3359, 1.3373, 1.3388, 1.3403, 1.3418, 1.3433, 1.3448 and 1.3463, respectively. The ultrasonic bath was used to assist the liquid to flow into the embedded FP cavity during tests. The device was carefully cleaned using acetone, deionized water and dried after each measurement to ensure there was no residual liquid left within the cavity, indicated by the interference spectrum restored to its original in air.

Figure 11-5 (a) shows the interference spectra of all-in-fiber optofluidic device in the sucrose solutions at various concentrations of 0%, 2%, 4%, and 6%, respectively. As the RI increased, the interferogram shifted towards the long wavelength region (red shift). Figure 11-5 (b) plots the center wavelength of an interference valley (1567.6 nm) as a function of the RI of the liquid. Linear regression was used to fit the response curve and the slope of the fitted line was calculated as the RI sensitivity, which was estimated to be 1135.7 nm/RIU in the tested RI range.

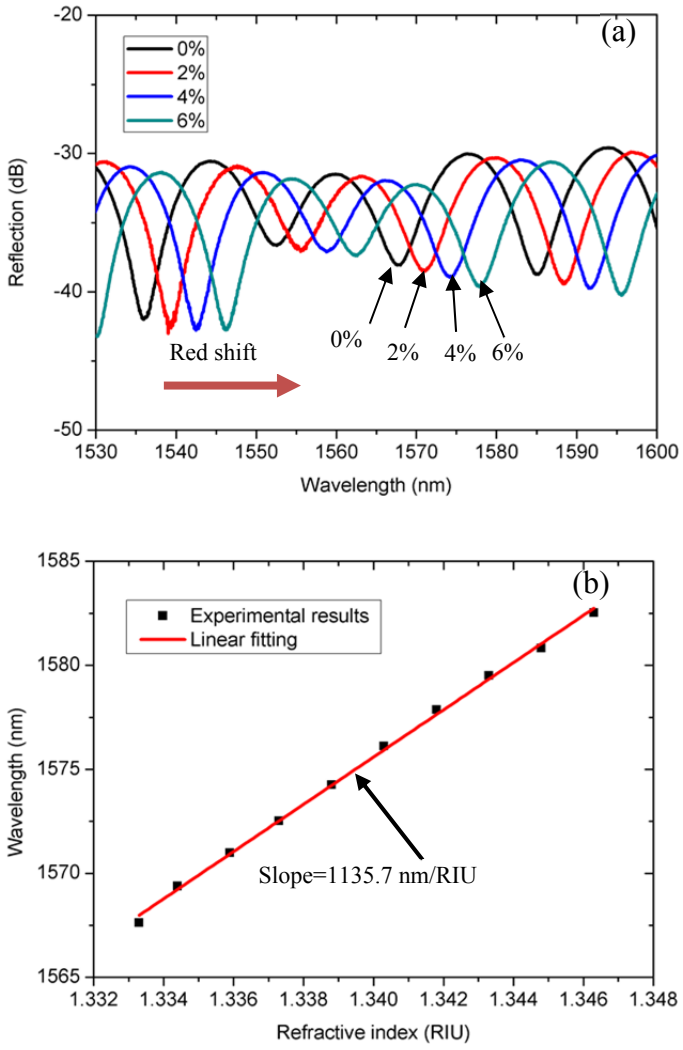

Figure 11-5. (a) Interference spectra and (b) center wavelength of an interference valley (1567.6 nm) of the all-in-fiber device in the sucrose solutions with different concentrations.

11.4 Summary

In summary, an all-in-fiber 3D optofluidic micro device was fabricated by fs laser irradiation assisted selective chemical etching. Horizontal and vertical microchannels can be flexibly created into an optical fiber to form a fluidic cavity with inlets/outlets. The fluidic cavity also functions as an optical FP cavity in which the filled liquid can be probed. This assembly-free micro device exhibited a high fringe visibility and demonstrated for measurement of the RI of the filling liquids. The proposed all-in-fiber optofluidic device is flexible in design, simple to fabricate, mechanically robust, and miniaturized in size, showing good potentials for chemical/biomedical sensing and integrated microfluidic applications. Because of the assembly-free structure, the developed sensor may also find applications in harsh environment sensing such as for gas analysis in the hot zones of various energy systems.

11.5 References

1. X. Fan and I. M. White, "Optofluidic microsystems for chemical and biological analysis," Nature photonics **5**, 591-597 (2011).

2. D. Psaltis, S. R. Quake, and C. Yang, "Developing optofluidic technology through the fusion of microfluidics and optics," Nature **442**, 381-386 (2006).

3. C. Monat, P. Domachuk, and B. Eggleton, "Integrated optofluidics: A new river of light," Nature photonics **1**, 106-114 (2007).

4. A. T. Woolley and R. A. Mathies, "Ultra-high-speed DNA fragment separations using microfabricated capillary array electrophoresis chips," Proceedings of the National Academy of Sciences **91**, 11348-11352 (1994).

5. R. Osellame, V. Maselli, R. M. Vazquez, R. Ramponi, and G. Cerullo, "Integration of optical waveguides and microfluidic channels both fabricated by femtosecond laser irradiation," Applied physics letters **90**, 231118-231118-231113 (2007).

6. P. Domachuk, I. Littler, M. Cronin-Golomb, and B. Eggleton, "Compact resonant integrated microfluidic refractometer," Applied physics letters **88**, 093513-093513-093513 (2006).

7. J. B. Jensen, L. H. Pedersen, P. E. Hoiby, L. B. Nielsen, T. P. Hansen, J. R. Folkenberg, J. Riishede, D. Noordegraaf, K. Nielsen, and A. Carlsen, "Photonic crystal fiber based evanescent-wave sensor for detection of biomolecules in aqueous solutions," Optics letters **29**, 1974-1976 (2004).

8. H. Zhu, I. M. White, J. D. Suter, M. Zourob, and X. Fan, "Opto-fluidic micro-ring resonator for sensitive label-free viral detection," Analyst **133**, 356-360 (2008).

9. Y. Lai, K. Zhou, L. Zhang, and I. Bennion, "Microchannels in conventional single-mode fibers," Optics letters **31**, 2559-2561 (2006).

10. R. Osellame, H. J. Hoekstra, G. Cerullo, and M. Pollnau, "Femtosecond laser microstructuring: an enabling tool for optofluidic lab-on-chips," Laser & Photonics Reviews **5**, 442-463 (2011).

11. Y. Bellouard, A. Said, M. Dugan, and P. Bado, "Fabrication of high-aspect ratio, micro-fluidic channels and tunnels using femtosecond laser pulses and chemical etching," Optics Express **12**, 2120-2129 (2004).

12. A. Crespi, Y. Gu, B. Ngamsom, H. J. Hoekstra, C. Dongre, M. Pollnau, R. Ramponi, H. H. van den Vlekkert, P. Watts, and G. Cerullo, "Three-dimensional Mach-Zehnder interferometer in a microfluidic chip for spatially-resolved label-free detection," Lab on a Chip **10**, 1167-1173 (2010).

13. T. Wei, Y. Han, Y. Li, H.-L. Tsai, and H. Xiao, "Temperature-insensitive miniaturized fiber inline Fabry-Perot interferometer for highly sensitive refractive index measurement," Optics Express **16**, 5764-5769 (2008).

14. Y. Zhang, L. Yuan, X. Lan, A. Kaur, J. Huang, and H. Xiao, "High-temperature fiber-optic Fabry–Perot interferometric pressure sensor fabricated by femtosecond laser," Optics letters **38**, 4609-4612 (2013).

12. Optical Fiber Polarization Devices Fabricated by fs laser

12.1 Introduction

Control of the state of polarization (SOP) of light waves, especially in optical fibers, is essential in a variety of applications, such as optical communications [1], networking, spectroscopy, microscopy [2], and sensing [3]. However, the vast majority polarization controlling devices (e.g., wave plates and polarizers) used in existing fiber optic systems are still based on bulk-optic components. These bulk-optic devices have to be interfaced with optical fibers through collimators and pigtails. This not only increases the cost of implementation but also compromises the robustness of the system. It is highly desired that the waveplates and polarizers can be implemented in an all-fiber form, preferably in a standard singlemode fiber, with minimum insertion loss and desirable performance.

High birefringence (Hi-Bi) or polarization maintaining (PM) optical fibers (e.g., panda, bow-tie or elliptical core) have a consistent built-in birefringence and can be used to fabricate an all-fiber waveplate. The amount of phase retardance depends on the fiber birefringence and the length of the fiber. For example, PM fiber based inline waveplates have been demonstrated using precise cleaving and controlled splicing [5]. However, it is hard to control the exact length of the PM fiber during cleaving and fusion splicing. It has also been reported that an anisotropic photonic crystal fiber (PCF) can be highly birefringent [6]. A large amount of birefringence can be generated by deforming an air-holed photonic crystal fiber from its side, introducing an ellipticity in both the core and the air holes [7]. The amount of birefringence can be controlled by the degree of compression. However, in addition to the difficulty in the practical implementation

of such a large deformation, PCFs are expensive, difficult to splice, and could be lossy when heavily deformed [8].

All-fiber polarizers have also been reported by various researchers over the years. Examples include the in-fiber polarizers based on the side-polished or D-shape fibers coated with optical absorbing materials on the flat side [9, 10], the in-fiber polarizer based on mechanically microbending a Hi-Bi fiber [11], the photonic crystal fiber in-line polarizer based on an LPFG fabricated using CO_2 laser irradiations [12], and the in-fiber polarizer based on tilted fiber Bragg gratings (FBG) [13]. These reported devices have shown good extinction ratios but also a number of shortcomings such as poor mechanical robustness, large insertion loss, narrow bandwidth, and high implementation cost.

The latest advancements in high power femtosecond (fs) laser technology have opened a new opportunity to fabricate various optical devices and sensors in solid transparent materials including optical fibers [14-19]. It has reported that fs laser irradiations can generate birefringence in transparent materials [20, 21]. Recently, it was reported that a FBG could be written by a fs laser to generate a high birefringence [23]. However, direct radiations of fs laser pulses onto the fiber core may bring in larger insertion loss to the in-fiber polarization devices. Furthermore, the FBG based device worked only within a narrow spectral width.

In this paper, we report a new technique to generate stress-induced birefringence in a singlemode optical fiber (Corning SMF-28) by creating two parallel stress rods along the fiber core using an fs laser. The position and size of the fs laser induced stress rods were optimized to minimize the insertion loss. By controlling the total length of the stress rods, the amount of polarization birefringence could be precisely controlled to fabricate waveplates of desired

retardance. Polarization dependent LPFGs were fabricated by introducing periodic stress rods inside the singlemode fiber. The fabricated LPFGs had a polarization dependent loss exceeding 25 dB at the peak resonance band, showing the promise of being used as an in-fiber polarizer.

12.2 Device Principle and Fabrication

It is well known that mechanical stresses produce additional refractive index change in optical materials because of the photoelastic effect. As a fact, commercially available Panda and Bow-tie PM fibers are fabricated by intentionally implanting axial stress rods along the fiber. The stress rods introduce asymmetric index profile in the cross section of the fiber, resulting in a systematic linear birefringence along the fiber.

Based on the similar principle, we can use fs laser micromachining to create distributed cuboid stress patterns in the cladding region of a singlemode optical fiber and produce controlled birefringence along the fiber. As shown in Figure 1, each pair of fs laser ablated patterns are in parallel and very close to the fiber core. The two ablated patterns create certain amount of normal stresses to the fiber core. Because the ablated patterns are asymmetric radially in the cross section, it is expected that an asymmetric index profile is created within the fiber, which shall result in a birefringence to the light propagating along the fiber.

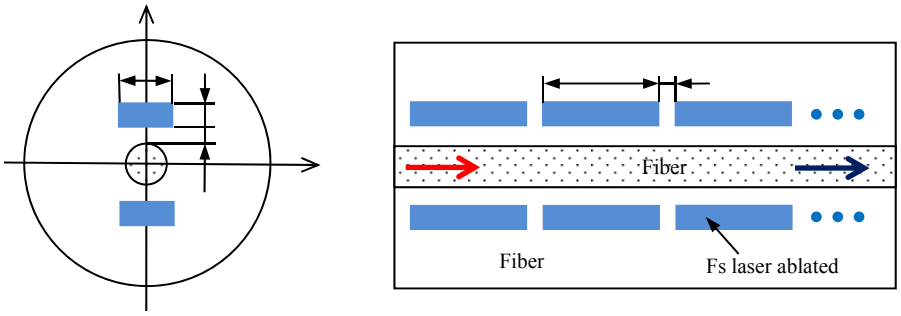

Figure 12-1. Schematic illustration of stress regions created by fs laser micromachining inside an optical fiber.

The length, width, and height of each cuboid stress region are denoted as L_1, W and H, respectively. The distance between each two adjacent regions and the offset between the region and the fiber core are L_2 and D, respectively. The amount of birefringence will depend on the amount of stress or the distance (*D*) between the ablated region and the fiber core. A smaller *D* usually results in a large stress but may also cause larger light loss.

The laser ablation induced birefringence allows us to fabricate in-fiber waveplates of desired polarization rotations. As shown in Figure 12-1(b), each pair of laser-ablated regions produces a small amount of rotation in polarization. As the number of pairs increases, the total amount of polarization rotation will increase correspondingly. The amount of polarization rotation can thus be controlled to fabricate waveplates of any desired polarization rotations.

The ability to precise control the birefringence of a singlemode fiber at specific locations also allows us to fabricate an in-fiber polarizer. As illustrated in Figure 12-2, the fs laser induced stress patterns are aligned periodically along the axial direction. Because of the stress-induced birefringence, the grating will have split resonance. As a result, the resonances of the orthogonal two polarizations happen at different wavelengths. The device can be used as an inline fiber polarizer.

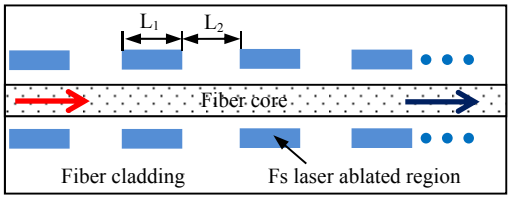

Figure 12-2. Schematic illustration of an optical fiber inline polarizer based on fs laser micromachining of a polarization dependent long period grating.

12.3 Experiments, Results and Discussions

Figure 12-3 shows the experimental setup for fabrication of in-fiber polarization devices using fs laser irradiation technique. A standard single-mode optical fiber was buffer-stripped in fabricating regions, carefully cleaned using acetone and then clamped by two bare fiber holders (Newport 561-FH). A water-filled tank with breaks in double sides, which can let the optical fiber go through, was used in all experiments. Also, distilled water was added in the tank. The optical fiber, the fiber holders and the water-filled tank were all mounted on a high-precision, computer-controlled three-axial translation stage (Newport, Inc.) with a resolution of 0.1 μm. The fs laser beam was focused inside the optical fiber through a water immersion objective lens (Olympus UMPlanFL 20x) with a numerical aperture (NA) of 0.4. The spot size of the focused beam was about 1 μm. The scanning velocity of the stage was set at 100 μm/s. The actual laser energy used for fabrication was 0.4 ~ 0.5 μJ per pulse. Two types of in-situ monitoring systems were used to monitor the performance of the polarization devices during the micromachining process, as shown in Fig. 2. For the quarter waveplate fabrication, the polarization states monitoring system (Type 1) consists of a tunable laser, an external polarization controller and a lightwave polarization analyzer (Agilent, 8509B). While for the LPFG-based polarizer fabrication, the interrogation system (Type 2) can be substituted to a broadband source (1300-1700 nm), a commercial fiber inline polarizer, a polarization controller, and an optical spectral analyzer (AQ6319).

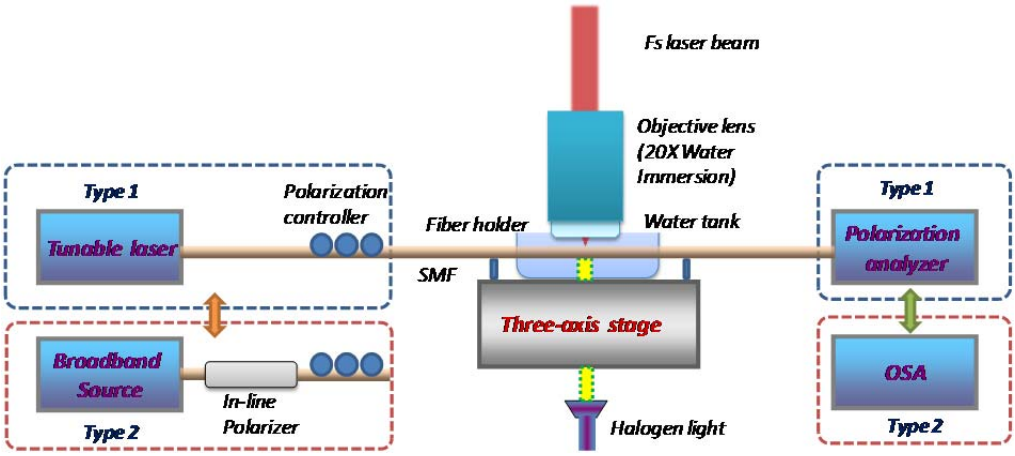

Figure 12-3. The experiment setup for fabrication of in-fiber polarization devices using fs laser irradiation technique. Two types of interrogation systems can be substituted for different cases.

To obtain a high-quality quarter waveplate, the following steps were adopted: Firstly, the wavelength and the output power of the tunable laser were set at 1550 nm and 0 dBm, respectively and a reference polarization state was set at the +45° or -45° linear polarization in the equator with respect to the Stokes vectors of 0.00, 1.00, 0.00 or 0.00, -1.00, 0.00, respectively, by tuning the external polarization controller; Then, a series of symmetric cuboid stress regions with the dimension of $L_1 \times H \times D_1$ μm were fabricated in-order and all the regions were irradiated sequentially from the bottom to the top to avoid focusing through previously modified regions. During the irradiation process, the distance L_2 and the offset D_2 were tuned gradually until the tradeoff between the insertion loss and the polarization state trace displayed on the Poincaré sphere was found; Finally, polarization states were recorded after each two stress region pairs and the fabrication was stopped after the ultimate polarization state was just located at right or left circular polarization in the poles with respect to the Stokes vectors of 0.00, 0.00, 1.00 or 0.00, 0.00, -1.00, respectively.

In another example, the transmission spectra of in-fiber polarizer based on LPFG can be monitored via Type 2 in-situ monitoring system. One can easily vary the resonant wavelength of this device by tuning the spatial period (L_1+L_2) of the grating. The fabrication was stopped after the largest attenuation peak (might be the critical coupling point) was occurred in the wavelength range of 1500-1600 nm.

The separation between two adjacent stress regions is necessary because of two reasons. First, there is a stringent requirement on the relative position between the ablated region and the fiber core. As such, realignment is necessary after the stage travels the limited traveling range in which the alignment between the laser beam and the fiber can be maintained accurately.

12.3.1 In-fiber quarter waveplate

Figure 12-4 shows the microscopic image of the fs laser induced stress patterns inside and optical fiber. The dimension of single cuboid stress region was about 100×10×20 μm, whose height H is much larger than the diameter of the fiber core. Larger height of the regions shall guarantee that the stress region pairs can generate identical effect on the fiber core and the appropriate width of the stress region will provide enough stress-induced birefringence effect during the irradiation process.

The offset $D_2$was a significant impact factor with respect to the final result as well. Table 1 shows three experimental results during the optimization process. Based on the results from Table 12-1, we can easily come to a conclusion that the smaller the offset D_2 is, the larger the relative transmission loss ($P_{relative}$=$P_{circular}$-P_{linear}, where P means the real time intensity obtained from the power meter) will be obtained. In addition, larger offset will increase the number of

stress region pairs and then influence the ultimate length of the polarization controlled optical device. In our experiment, the offset D_2 was set at 10 μm.

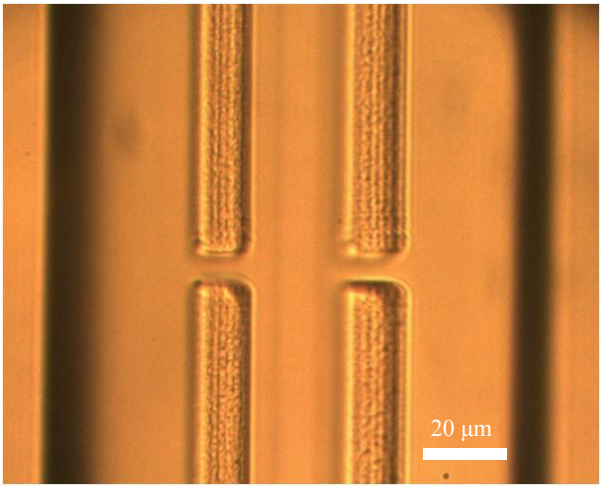

Figure 12-4. Microscopic images of two stress region pairs (top view) of in-fiber quarter waveplate.

Table 14-1. Experimental results during the optimization process

The offset D_2 (μm)	The relative transmission loss P (dB)	NO. of stress region pairs
2	11.36	9
5	4.35	13
10	0.19	16

To get a better trace along the longitude of the Poincaré sphere, the relationship between the distance L_2 and the stress region length L_1 might be an issue due to the limitation of the fabrication process. The trace will evidently deviate from the longitude of the Poincaré sphere when we increase the length of the stress region. In addition, appropriate distance L_2 between two adjacent cuboid stress regions will improve the feasibility and controllability to readily realize the *in-situ* monitoring during the fabrication process. After tradeoff budgeting, the distance L_2 and the stress region length L_1 were set at 10 μm and 100 μm, respectively.

The ultimate number of stress region pairs is 16. The fabrication sequence (first left then right or first right then left) can be fine-tuned during the whole process to control the trace of polarization states from the Poincaré sphere. According to the results obtained from the power meter, the transmission loss was changed from -14.51 dBm at the +45° linear polarization to -14.70 dBm at the circular polarization, therefore, the relative transmission loss was about 0.19 dB as we expected. When the fabrication process was terminated, the polarization dependent loss (PDL) of this in-fiber quarter waveplate was only 0.214 dB detected from the lightwave polarization analyzer.

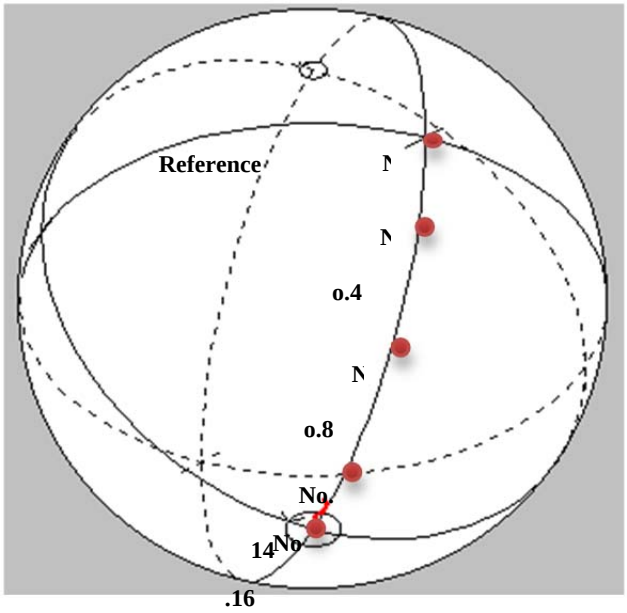

Figure 12-5. The characteristic five stress region pair positions of the polarization states onto the Poincarésphere:No.0 means the reference point and No. 4, 8, 14, 16 indicate the other four characteristic stress region pair positions of the polarization states during the fabrication process.

Figure 12-5 shows the characteristic positions of polarization states on the Poincaré sphere. The reference point represents the starting point with respect to the polarization state of the +45°

linear polarization with the Stokes vector of (0.00, 1.00, 0.00). The other four characteristic stress region pair positions (No.4, No.8, No.14, No.16) are also marked, corresponding to the Stokes vectors of (0.00, 0.97, -0.21), (0.01, 0.79, -0.60), (0.01, 0.30, -0.94) and (0.00, 0.00, -0.99), respectively. Additionally, the marked positions along the longitude of the Poincaré sphere indicate that the polarization states can be precisely controlled and gradually changed during the fs irradiation process.

Based on the experimental results from Figure 12-5, the final polarization state of the fiber core changed gradually from the +45°linear polarization to the left circular polarization, and a quarter-waveplate was formed ultimately. The stress-induced birefringence β of the fiber core can also be given as:

$$\beta d = \pm \frac{\lambda}{4} \tag{12-1}$$

where λ is the optical wavelength from the tunable laser and d is the effective length of the quarter-waveplate determined by:

$$d = \sum_{i=1}^{n} L_1 \quad \text{(n=1, 2, 3...)} \tag{12-2}$$

In our experiments, the optical wavelength λ was set at 1550 nm, and the effective length d = $n \times L_1 = 16 \times 100$ μm= 1600 μm. Based on the Equations (12-1) and (12-2), the value of stress-induced birefringence β is approximately 2.42×10^{-4}. Compared with the values of conventional polarization maintaining single-mode fibers (PMFs) [24, 25], such as panda (3.1×10^{-4}) and bow-tie (3.8×10^{-4}), the values are close to each other, which represents that using fs laser irradiation technique can also obtain highly stress-induced birefringence without doping other materials

with different thermal-expansion coefficient (CTE). The highly stress-induced birefringence value indicate that the polarization state of the incident light has a $\pi/2$ phase delay between the two orthogonal electromagnetic components due to the stress-optic effect generated from the cuboid stress regions fabricated by the fs laser irradiation. As such, the trace changed from the equator (reference point) to the pole along the longitude of the Poincaré sphere was obtained by precisely controlling the effective dimensions of the cuboid stress regions besides the fiber core, as shown in Figure 12-5.

12.3.2 In-fiber polarizer based on LPFG

According to the results shown in the quarter waveplate, the in-fiber stress-induced birefringence can be obtained by precisely control of the dimension and relative position of the cuboid stress regions along the fiber core via fs laser irradiation technique. However, when it comes to the LPFG fabrication, the grating length (~ 4-5 cm) is much larger than the effective length of quarter waveplate, thus, the issue of time consuming needs to be fully considered in this case.

Figure 12-6 shows the microscopic image of one stress region pair of the in-fiber polarizer based on LPFG. In order to save the fabricating time, the height H was decreased to ~3 μm forming by the non-circular shape of the focused laser beam and the width D_1 was set at 4 μm. Each region can be considered as a single-layer cuboid stress region. The offset D_2, yielding to the insertion loss, was set at 8 μm. The laser energy was increased to 0.5 μJ to guarantee the sufficient stress-induced effect to the fiber core. After fine-tuning the fabrication parameters of the stress region pairs, the desired transmission spectra were observed eventually.

The fabricated in-fiber polarizer was interrogated using Type 2 *in-situ* monitoring system. Figure 12-7 shows the transmission spectra of the fabricated LPFGs with increasing stress region pairs, which indicates a 6th order LPFG with ~1.3dB insertion loss was obtained after irradiating 100 pairs of stress region. The grating period (L1+L2) of the LPFG was set at 460 μm.

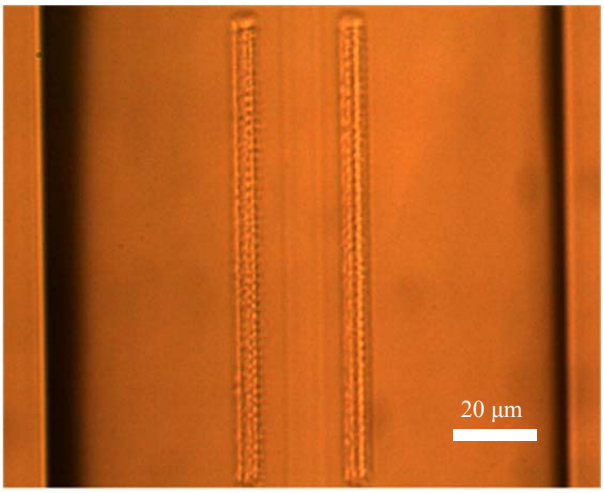

Figure 12-6. Microscopic image of one stress region pair (top view) of in-fiber polarizer based on LPFG.

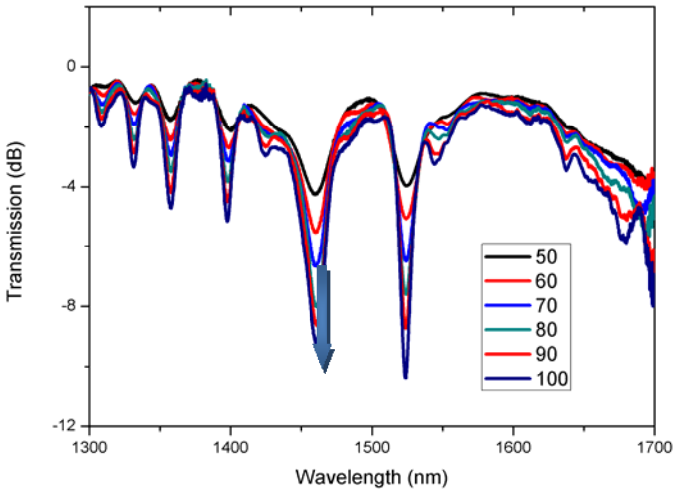

Figure 12-7. The transmission spectra of the in-fiber polarizer based on LPFG in different number of stress region pairs. The blue arrow indicates the trend of finding the critical coupling point of the proposed device in water.

When the fabrication was terminated, the external polarization controller was twisted a little bit to find the critical coupling point. In our experiment, the largest fringe visibility of ~22 dB at the wavelength of 1525 nm was obtained at polarization state 1(P1) in water. We believed that the difference between the fringes at attenuation peak before and after twisting the polarization controller might be contributed to the misalignment of each stress region pairs during the fabrication process. Continually twisting the polarization controller will find the smallest fringe visibility (almost flat) at the same operating wavelength, which is marked as polarization state 2 (P2) in water, as shown in Figure 12-8 (a).

The polarization performance of the in-fiber polarizer was also investigated when placed it in air, as shown in Figure 12-8 (b). The largest fringe visibility of attenuation peak in one polarization state (P1) is about 25 dB, which is nearly the same as the limit of the commercial fiber inline polarizer (~26 dB). In addition, the whole spectra in two polarization states (P1 and P2) shifted towards the long wavelength region (red shift) due to the decreasing refractive index of the surrounding medium, as shown in Figure 12-8 (c) and (d).

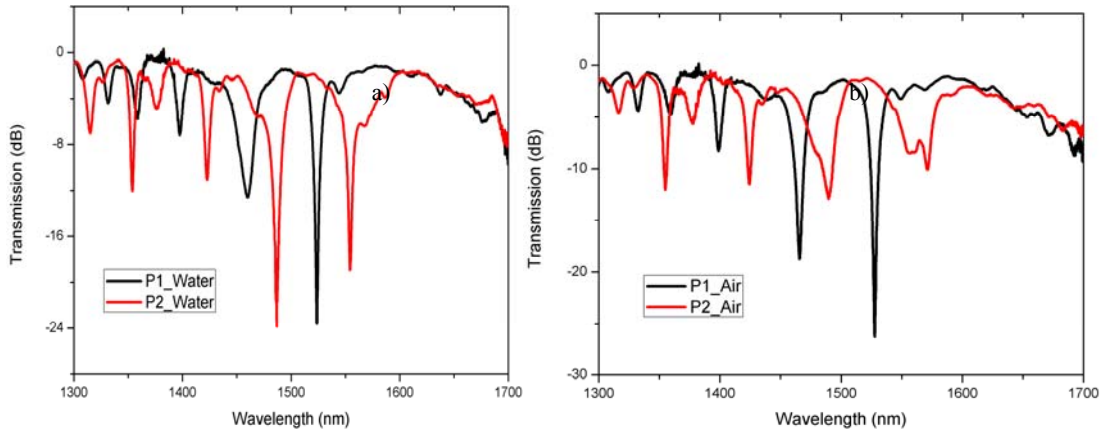

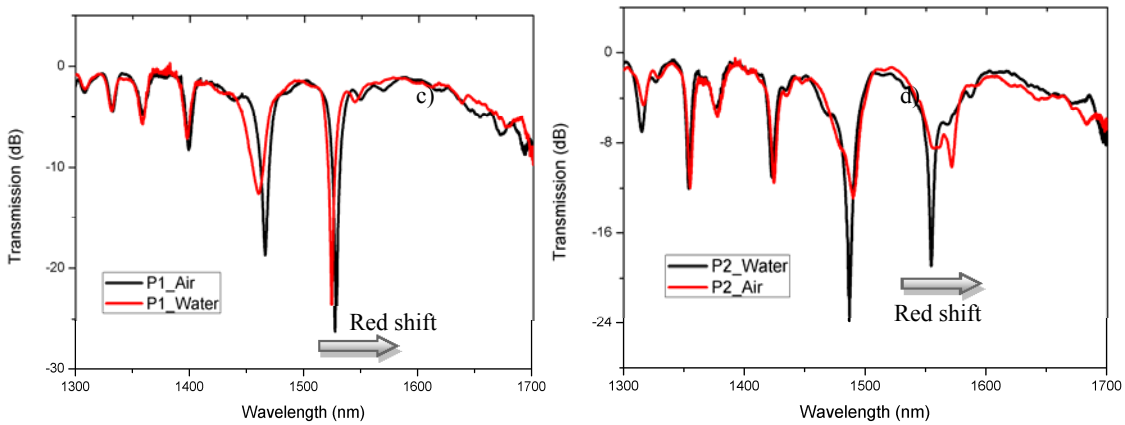

Figure 12-8. The transmission spectra of in-fiber polarizer based on LPFG at two characteristic points in different surrounding mediums: (a) Only in water; (b) only in air; (c) P1 in water and air; (d) P2 in water and air.

Figure 12-9 shows the polarization extinction ratio (PER) of the in-fiber polarizer based on LPFG in different surrounding mediums (water and air). Obviously, the largest PER of the proposed device placed in air is about 25 dB at the operating wavelength of 1527.8 nm.

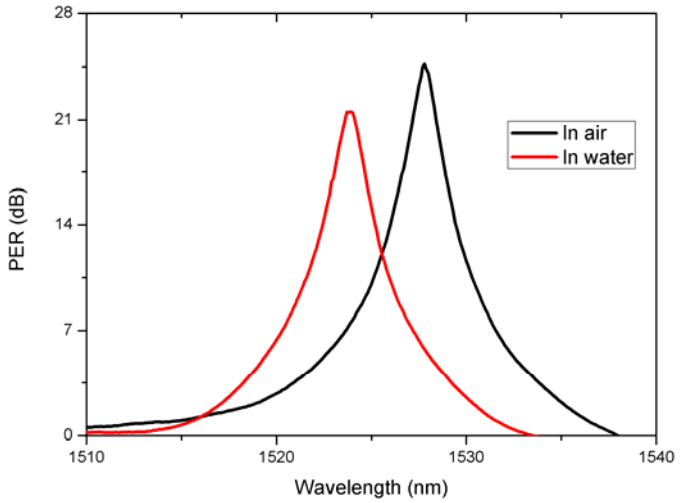

Figure 12-9. The polarization extinction ratio (PER) of the in-fiber polarizer based on LPFG in different surrounding mediums (water and air).

12.4 Summary

Two in-fiber stress-induced birefringent polarization devices are fabricated by fs irradiation a series of cuboid stress regions on both sides along the fiber core. The polarization controlled trace can be optimized by precise control of the dimensions and relative alignment of the rectangular stress regions. The structure robustness and the insertion loss are also improved, which is contributed by the precision controller during the fabrication process. The high value of stress-induced birefringence indicates the capability of polarization controlled optical devices fabricated by fs laser. In addition, the in-fiber polarizer based on LPFG was also obtained using fs laser micromachining. The polarization extinction ratio of 25 dB at operating wavelength of 1527.8 nm was observed, which exhibits the capability of polarization devices fabrication using precisely fs laser technique. As a result, the in-fiber polarization devices are expected to provide a potential solution for micro-photonics polarization maintaining applications.

12.5 References

1. B. R. Acharya, L. Möller, K. W. Baldwin, R. A. MacHarrie, R. A. Stepnoski, C. C. Huang, R. Pindak, and J. A. Rogers, "In-line liquid-crystal microcell wave plates and their application for high-speed, reset-free polarization mode dispersion compensation in 40-Gbit/s systems," Applied optics 42, 5407-5412 (2003).
2. T. Lacoste, T. Huser, R. Prioli, and H. Heinzelmann, "Contrast enhancement using polarization-modulation scanning near-field optical microscopy (PM-SNOM)," Ultramicroscopy 71, 333-340 (1998).
3. R. A. Bergh, H. C. Lefevre, and H. J. Shaw, "An overview of fiber-optic gyroscopes," Journal of lightwave technology 2, 91-107 (1984).

4. M. Born and E. Wolf, Principles of optics: electromagnetic theory of propagation, interference and diffraction of light (CUP Archive, 1999).
5. R. Zhang, H. Lu, Y. Liu, X. Mao, H. Wei, J. Li, and J. Guo, "Polarization-maintaining photonic crystal fiber based quarter waveplate for temperature stability improvement of fiber optic current sensor," Journal of Modern Optics 60, 963-969 (2013).
6. L. Zhang and C. Yang, "Photonic crystal fibers with squeezed hexagonal lattice," Optics express 12, 2371-2376 (2004).
7. F. Beltrán-Mejía, G. Chesini, E. Silvestre, A. K. George, J. Knight, and C. M. Cordeiro, "Ultrahigh-birefringent squeezed lattice photonic crystal fiber with rotated elliptical air holes," Optics letters 35, 544-546 (2010).
8. H. Xuan, W. Jin, M. Zhang, J. Ju, and Y. Liao, "In-fiber polarimeters based on hollow-core photonic bandgap fibers," Optics express 17, 13246-13254 (2009).
9. S.-P. Ma and S.-M. Tseng, "High-performance side-polished fibers and applications as liquid crystal clad fiber polarizers," Lightwave Technology, Journal of 15, 1554-1558 (1997).
10. R. Dyott, J. Bello, and V. Handerek, "Indium-coated D-shaped-fiber polarizer," Optics letters 12, 287-289 (1987).
11. A. Wang, V. Arya, M. H. Nasta, K. A. Murphy, and R. O. Claus, "Optical fiber polarizer based on highly birefringent single-mode fiber," Optics letters 20, 279-281 (1995).
12. Y. Wang, L. Xiao, D. Wang, and W. Jin, "In-fiber polarizer based on a long-period fiber grating written on photonic crystal fiber," Optics letters 32, 1035-1037 (2007).
13. K. Zhou, X. Chen, A. G. Simpson, L. Zhang, and I. Bennion, "High Extinction Ratio In-Fiber Polarizer Based on a 45o-Tilted Fiber Bragg Grating," in Optical Fiber Communication Conference, (Optical Society of America, 2005), OME22.
14. R. R. Gattass and E. Mazur, "Femtosecond laser micromachining in transparent materials," Nature photonics 2, 219-225 (2008).
15. L. Yuan, T. Wei, Q. Han, H. Wang, J. Huang, L. Jiang, and H. Xiao, "Fiber inline Michelson interferometer fabricated by a femtosecond laser," Optics letters 37, 4489-4491 (2012).

16. T. Wei, Y. Han, Y. Li, H.-L. Tsai, and H. Xiao, "Temperature-insensitive miniaturized fiber inline Fabry-Perot interferometer for highly sensitive refractive index measurement," Optics express 16, 5764-5769 (2008).

17. Y. Zhang, L. Yuan, X. Lan, A. Kaur, J. Huang, and H. Xiao, "High-temperature fiber-optic Fabry–Perot interferometric pressure sensor fabricated by femtosecond laser," Optics letters 38, 4609-4612 (2013).

18. Y. Kondo, K. Nouchi, T. Mitsuyu, M. Watanabe, P. G. Kazansky, and K. Hirao, "Fabrication of long-period fiber gratings by focused irradiation of infrared femtosecond laser pulses," Optics letters 24, 646-648 (1999).

19. X. Fang, C. Liao, and D. Wang, "Femtosecond laser fabricated fiber Bragg grating in microfiber for refractive index sensing," Optics letters 35, 1007-1009 (2010).

20. S. Gross, M. J. Withford, and A. Fuerbach, "Direct femtosecond laser written waveguides in bulk Ti3+: Sapphire," in SPIE LASE, (International Society for Optics and Photonics, 2010), 75890U-75890U-75898.

21. L. A. Fernandes, J. R. Grenier, P. R. Herman, J. S. Aitchison, and P. V. Marques, "Stress induced birefringence tuning in femtosecond laser fabricated waveguides in fused silica," Optics express 20, 24103-24114 (2012).

22. H. Xuan, J. Ju, and W. Jin, "Highly birefringent optical microfibers," Optics express 18, 3828-3839 (2010).

23. K. Chah, D. Kinet, M. Wuilpart, P. Mégret, and C. Caucheteur, "Femtosecond-laser-induced highly birefringent Bragg gratings in standard optical fiber," Optics letters 38, 594-596 (2013).

24. T. Hosaka, Y. Sasaki, J. Noda, and M. Horiguchi, "Low-loss and low-crosstalk polarisation-maintaining optical fibres," Electronics Letters 21, 920-921 (1985).

13. Sapphire Fiber SERS Probe Fabricated by fs Laser

13.1 Introduction

Surface-enhanced Raman scattering (SERS) has attracted substantial interests in recent years [1], [2] because of its unique capability of molecular identification. The concept has also been implemented on optical fibers, resulting in miniaturized SERS probes for various sensing applications [3], [4]. A variety of techniques have been developed in the past for fabrication of fiber optic SERS probes, including metal coating of roughened endface with mechanical means [5], metallic nanoparticle deposition[6], bio-imprint aided fabrication [7], metal coating on a fiber taper [8], and femtosecond (fs) laser micromachining [9], [10]. Methods have also been investigated to improve the sensitivity of fiber SERS probes. For example, Gu et al. reported a "sandwiched" fiber SERS probe configuration by the combination of depositing silver nanoparticle on fiber endface and adding suspended silver colloids in the solution to be measured [11]. Lucottiet al. reported enhanced SERS signals using a double-tapered fiber tip geometry obtained by two-fold etching [12].

A fiber optic SERS probe is preferred to operate in a reflection configuration in which the excitation and detection are on the same side. In addition, the probe is desired to have an enough lead length for convenient installation or insertion. However, the reported SERS probes were mostly made using doped-silica glass fibers, which have a broad and strong Raman scattering in the spectral range of 100-1100 cm^{-1} [13]. As the lead length of the probe increases, the fiber background Raman scattering may accumulate and over shadow the weak Raman signal to be detected. For this reason, Hartly et al. limited the fiber length to about 25 mm when they compared the performance of the SERS probes made of different silica fibers [14]. Various types

of optical fibers have been proposed to reduce the background Raman scattering, including the low-OH fused silica fiber [15], solid-core [16] and hollow-core [17] photonic crystal fibers, and the single-crystal sapphire fiber [15,18]. Unlike silica glass materials, single crystal sapphire has narrow and isolated Raman peaks. When used as a waveguide for excitation and collection of Raman signals, a sapphire fiber has the advantages of low background Raman scattering and high collection efficiency as a result of its very large numerical aperture. It is worth noting that the background Raman of the sapphire fiber strongly depends on the purity of the material. In [14], a broad background Raman band was observed in a sapphire fiber purchased from Saphikon and made by the edge-defined film-fed growth (EFG) method. The authors attributed the broad background Raman band to the fluorescence caused by crystalline impurities in the sapphire fiber. On the other hand in [18], the background Raman bands of the sapphire fiber (made by MicroMaterials, Inc.) were found to be weak and narrow. The MicroMaterials sapphire fiber was made by the laser-heated pedestal-growth (LHPG) method.

In this project, we fabricated and compared three types of fibers for construction of SERS probes that operate in a reflection configuration, including the fused silica singlemode fiber (SMF), fused silica multimode fiber (MMF) and single crystal sapphire fiber. The probes are made by fs laser ablations of nanostructures on the endface and subsequent costing of silver thin film by chemical plating.

13.2 Fabrication of the SERS Probe

An unclad, single crystal sapphire fiber (MicroMaterials, Inc. SF75-50) with a diameter of 75 μm was chosen for the experiment. Before the fs ablation process, a piece of SCSF with a length of 20 cm was precisely polished on both endfaces. The polishing process was performed by a

wheel polisher (Ultrapol-1200, Ultra Tec) using diamond lapping films. The rotation speed of polishing plate was set to be 40 rpm (rounds per minute). Two types of diamond lapping films were used: a lapping film with 3 μm grain size was first used to flat the sapphire fiber endfaces, and then a lapping film of 0.1 μm grain size was used for fine polishing.

Two different types of silica fibers with the same length (20 cm) as the sapphire fiber were also prepared for the purpose of comparison, including a SMF (Corning, SMF-28), and a MMF (Corning, infinicor 300) with the core and cladding diameters of 62.5 and 125 μm, respectively. The endfaces of the silica fibers were cleaved and cleaned carefully in acetone and distilled water.

A home-integrated fs laser micromachining system was used to fabricate microstructures on the endface of the fibers. The central wavelength, pulse width and repetition rate of the fs laser (Coherent, Inc.) were 800 nm, 200 fs and 250 kHz, respectively. The maximum output power of the fs laser was approximately 1 W. The laser was switched on or off by electrically gating the internal clock. The laser pulse energy was attenuated through a half-wave plate and a polarizer to less than 0.5 W. Several neutral density (ND) filters were applied to reduce the pulse energy to desirable values before the objective lens (Zeiss EC Epiplan20X) with a numerical aperture (NA) of 0.4. The attenuated laser beam was focused onto the endface of the fiber. The fiber was vertically mounted on a computer-controlled three-axis translation stage (Newport, Inc.) with a resolution of 0.1 μm. The scanning velocity was set to be 200 μm/s and the actual laser energy used was approximately 0.5 μJ per pulse. The fs laser beam spot size was about 1 μm in diameter.

During fabrication, the fs laser beam scanned through the fiber endface line by line. The spacing between two adjacent lines was 1 μm and the distance between two neighboring points

was also 1μm. It took less than 30 seconds to cover the entire sapphire fiber endface with a diameter of 75 μm. The ablated fiber endface was then chemical plated with nanometer size silver particles, whose formation process could be referred to [9].

13.2 Raman Signal Test

Figure 13-1 shows the schematic of the experimental setup for Raman signal test. A Raman spectroscopy system (Alpha 300s, WITec) was used to acquire the Raman signal. The fiber probe to be tested was mounted under the microscope. Because the sapphire fiber is uncladded, only a small portion (about 3 mm in length) of the fiber was taped to the fiber holder to minimize the extra optical loss. The excitation light was coupled into the fiber probe from its polished or cleaved endface using an objective lens (Zeiss EC Epiplan 20X) with a numerical aperture (NA) of 0.4. The other endface of the fiber had SERS active structures and was immersed in the liquid solution. The laser beam propagated through the fiber to excite the Raman signal at the SERS active endface. Part of the excited SERS signal was captured by the fiber, travelled backwards and was collected by the objective lens for recording and analysis.

The background Raman scatterings of the sapphire fiber and the silica fibers were first measured using the system. The lengths of all fibers were 20 cm and their endfaces were either fine-polished (sapphire fiber) or cleaved (silica fibers). During background Raman scattering measurements, the far ends of the fibers were placed in air.

The three types of SERS probes were evaluated using an aqueous Rhodamine 6G (R6G) solution with a concentration of 10^{-7} M diluted in distilled water mixed with a 10mM NaCl solution [9]. In all experiments, the wavelength and the power of the excitation laser were 532 nm and 30 mW, respectively. The integration time was 2 seconds.

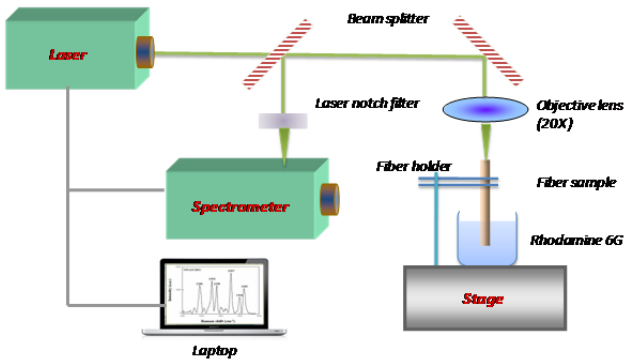

Figure 13-1. Schematic of the setup for characterization of the background Raman scattering of the fibers and the performance of the SERS probes

13.3 Results and Discussion

Figures 13-2 (a) and (b) show the scanning electron microscopic (SEM) images of the fs laser ablated sapphire fiber endface. A magnified image of the square area in Fig. 2 (a) is shown in Fig. 2 (b). The laser ablation created a roughened surface with quasi-uniformly distributed features with an average size of several hundred nanometers. We believe that the surface ripples were removed under the large laser fluence and the quasi-uniformly distributed subsurface structures was exposed [19]. The SERS performance strongly depends on the surface morphology, which can be varied by tuning the laser parameters such as the pulse energy, repetition rate, wavelength, spot size, scan speed, etc.

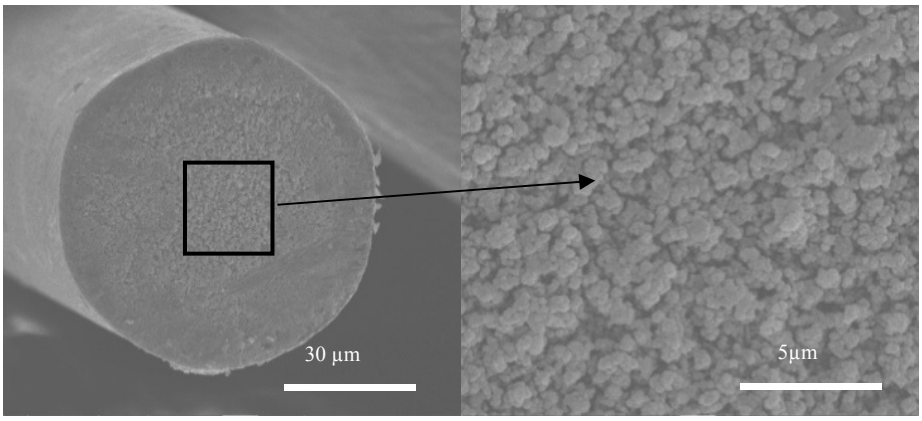

(a) (b)

Figure 13-2. SEM images of fs laser-ablated sapphire fiber endface, (a) the fiber tip and (b) surface profile.

The background Raman scattering spectra of the singlemode, multimode and sapphire fibers in air are plotted in Figure 13-3. The intensities of the background Raman signal were quite different. The MMF had the largest intensity because of its large NA and core diameter. The background Raman signal of the SMF was also strong. The sapphire fiber had the weakest intensity. In addition, the silica fibers had a broad background Raman spectra peaked at the frequency of about 430 cm^{-1} with a long tail into the high frequency region. However, the sapphire fiber had several isolated narrow peaks as shown in the inset of Figure 13-3. The weak and isolated background Raman scattering of the sapphire fiber makes it a good choice to construct a reflection based Raman probe.

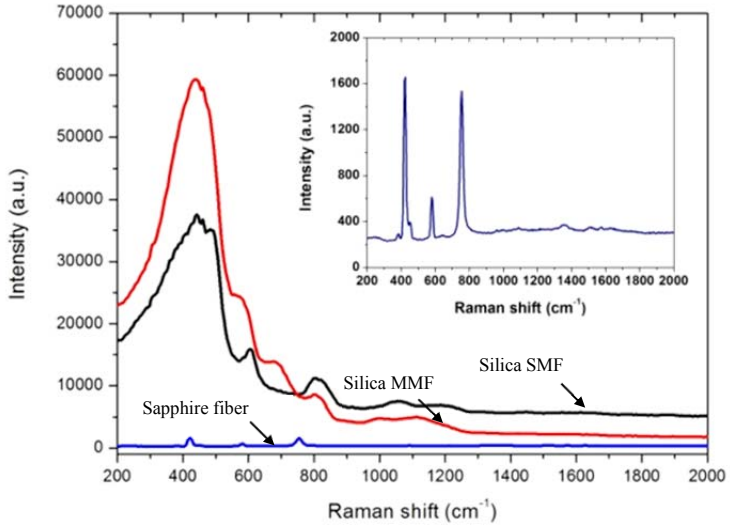

Figure 13-3. Background Raman spectra of two silica fibers (SMF and MMF) and a sapphire fiber (all 20 cm in length) in air; Inset: enlarged background Raman spectrum of the sapphire fiber.

The laser-ablated fiber endfaces were coated with silver nanoparticles by chemical plating. The lead lengths of the three fiber probes were all 20 cm. The SERS performance of the probes was tested by immersing the silver coated endfaces into a R6G solution (10^{-7} M concentration). The SERS spectra of the R6G solution obtained by the three fiber probes are shown in Fig. 4, where the Raman fingerprint signals of the R6G solution are superpositioned on the Raman background spectra of the fibers. Both the silica fiber probes have shown strong and broad Raman background peaks around 430 cm^{-1}. The sapphire probe has a much weaker background Raman.

For better comparison, we normalized the Raman spectra with respect to their highest intensities as shown in the insert of Figure 13-4.The sapphire fiber had the highest contrast with high-quality Raman signatures whose intensities were almost as strong as the background. The MMF probe had recognizable signatures but their strengths were much weaker than the

background Raman of the fiber. The SMF probe did not pick up any identifiable R6G Raman signal. We believe this is because the SMF had a much smaller core size, and so was the SERS active area at its tip, compared with the MMF and sapphire fibers. The contributions from these differences may become more pronounced as the fiber length increases.

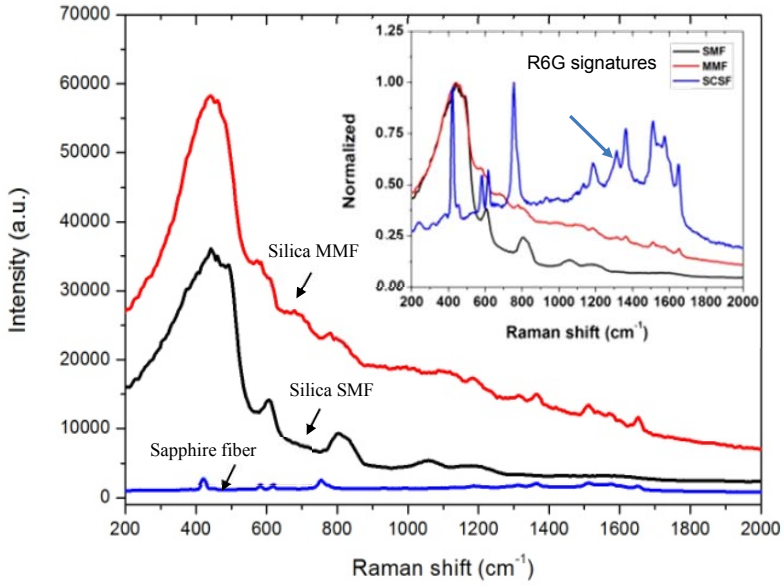

Figure 13-4. Raman spectra of R6G solution with a concentration of 10^{-7} M. Inset: normalized Raman spectra with respect to their highest intensities.

13.5 Summary

To summarize, three types of fibers were compared for construction of reflection-based SERS probes including the singlemode and multimode silica fibers and the single-crystal sapphire fiber. Fs laser micromachining was used to ablate nanometer structures on the endface of the fiber and silver chemical plating was performed to make the laser-ablated endface SERS active. Compared with the strong and broad Raman background scattering of the silica singlemode and multimode fibers, the background Raman scattering of the sapphire fiber was weak and narrow, making it useful for construction of SERS probes operating in a reflection

configuration. When tested using a low concentration (10^{-7}) R6G solution, the sapphire fiber SERS probe showed a good performance. In contrast, the silica SMF probe did not pick up any recognizable Raman signature and the silica MMF probe had a strong background Raman peak that overwhelmed the R6G signals. Operating in an attractive reflection-based configuration, the sapphire fiber SERS probe fabricated by fs laser ablations may find applications for detection and identification of biological/chemical species.

13.6 References

1. J. Kneipp, H. Kneipp, and K. Kneipp, "SERS—a single-molecule and nanoscale tool for bioanalytics," *Chemical Society Reviews,* vol. 37, pp. 1052-1060, 2008.
2. G. McNay, D. Eustace, W. E. Smith, K. Faulds, and D. Graham, "Surface-enhanced Raman scattering (SERS) and surface-enhanced resonance Raman scattering (SERRS): a review of applications," *Applied Spectroscopy,* vol. 65, pp. 825-837, 2011.
3. C. L. Haynes, A. D. McFarland, and R. P. V. Duyne, "Surface-enhanced Raman spectroscopy," *Analytical Chemistry,* vol. 77, pp. 338 A-346 A, 2005.
4. P. Stoddart and D. White, "Optical fibre SERS sensors," *Analytical and bioanalytical chemistry,* vol. 394, pp. 1761-1774, 2009.
5. C. Viets and W. Hill, "Comparison of fibre-optic SERS sensors with differently prepared tips," *Sensors and Actuators B: Chemical,* vol. 51, pp. 92-99, 1998.
6. X. Zheng, D. Guo, Y. Shao, S. Jia, S. Xu, B. Zhao, W. Xu, C. Corredor, and J. R. Lombardi, "Photochemical modification of an optical fiber tip with a silver nanoparticle film: a SERS chemical sensor," *Langmuir,* vol. 24, pp. 4394-4398, 2008.
7. G. Kostovski, D. J. White, A. Mitchell, M. W. Austin, and P. R. Stoddart, "Nanoimprinted optical fibres: Biotemplated nanostructures for SERS sensing," *Biosensors and Bioelectronics,* vol. 24, pp. 1531-1535, 2009.
8. A. Lucotti and G. Zerbi, "Fiber-optic SERS sensor with optimized geometry," *Sensors and Actuators B: Chemical,* vol. 121, pp. 356-364, 2007.

9. X. Lan, Y. Han, T. Wei, Y. Zhang, L. Jiang, H.-L. Tsai, and H. Xiao, "Surface-enhanced Raman-scattering fiber probe fabricated by femtosecond laser," *Optics letters,* vol. 34, pp. 2285-2287, 2009.

10. X. Ma, H. Huo, W. Wang, Y. Tian, N. Wu, C. Guthy, M. Shen, and X. Wang, "Surface-enhanced Raman scattering sensor on an optical fiber probe fabricated with a femtosecond laser," *Sensors,* vol. 10, pp. 11064-11071, 2010.

11. C. Shi, H. Yan, C. Gu, D. Ghosh, L. Seballos, S. Chen, J. Z. Zhang, and B. Chen, "A double substrate ``sandwich" structure for fiber surface enhanced Raman scattering detection," *Applied Physics Letters,* vol. 92, pp. 103107-3, 2008.

12. A. Lucotti, A. Pesapane, and G. Zerbi, "Use of a Geometry Optimized Fiber-Optic Surface-Enhanced Raman Scattering Sensor in Trace Detection," *Appl. Spectrosc.,* vol. 61, pp. 260-268, 2007.

13. R. L. McCreery, *Raman spectroscopy for chemical analysis* vol. 225: Wiley. com, 2005.

14. J. S. Hartley, S. Juodkazis, and P. R. Stoddart, "Optical fibers for miniaturized surface-enhanced Raman-scattering probes," Applied Optics, vol. 52, pp. 8388-8393, 2013.

15. M. G. Shim and B. C. Wilson, "Development of an in vivo Raman spectroscopic system for diagnostic applications," *Journal of Raman spectroscopy,* vol. 28, pp. 131-142, 1997.

16. D. Pristinski and H. Du, "Solid-core photonic crystal fiber as a Raman spectroscopy platform with a silica core as an internal reference," *Optics letters,* vol. 31, pp. 3246-3248, 2006.

17. S. O. Konorov, C. J. Addison, H. G. Schulze, R. F. Turner, and M. W. Blades, "Hollow-core photonic crystal fiber-optic probes for Raman spectroscopy," *Optics letters,* vol. 31, pp. 1911-1913, 2006.

18. C. Raml, X. He, M. Han, D. R. Alexander, and Y. Lu, "Raman spectroscopy based on a single-crystal sapphire fiber," *Optics letters,* vol. 36, pp. 1287-1289, 2011.

19. R. Buividas, L. Rosa, R. Šliupas, T. Kudrius, G. Šlekys, V. Datsyuk and S. Juodkazis, "Mechanism of fine ripple formation on surfaces of (semi)transparent materials via a half-wavelength cavity feedback," Nanotechnology, vol. 22, pp. 055304, 2011.

14. SERS Substrates Fabricated by fs Laser

14.1 Introduction

Supported by this project, we have also developed various surface enhanced Raman substrates (SERS) on both silicon and silica planar substrates using fs laser fabrication technique. In this report, we only take the flat silicon substrate as an example, please refer to the references for SERS substrates based on other types of materials. This example is chosen because of the one-step process to fabricate high-quality SERS substrate through fs laser directly ablation in the aqueous solution of silver nitrate. Parametric studies were conducted for the different concentrations of aqueous silver nitrate solutions and scanning speeds. The enhancement factor of the SERS is found to be higher than 10^9.

Since the surface-enhanced Raman scattering (SERS) was discovered [1,2], it has been widely employed for molecular detection due to its capabilities of providing simultaneously the structural [3] and quantitative information [4,5] as well as strong signal enhancements up to 10^{14} for single molecular detections [6]. The strength of enhancement depends on the exciting wavelength and properties of the metal nanostructures which affect the interaction between the electromagnetic (EM) field and the nanostructures when plasmon propagates at their surfaces. Since the enhancement factors (EFs) depend on the properties of the metal nanostructures, such as the surface morphology, categories of metals, and chemical environment of the nanostructures, a variety of approaches have been developed to fabricate SERS substrates for high EFs, including the electrochemically roughened electrodes, aggregates of colloidal gold or silver particles, and nanolithography [7].

Metal nanocomponents can be synthesized by chemical-reduction [8] or photoreduction [9] from metal salts into different types of formations such as nanoparticles [10], nanoplates [11], and nanowires [12]. Employing the photoreduction mechanism to synthesize metal particles has been demonstrated in glass [13], polymer matrix [14] and solutions [10]. SERS measurements can be conducted directly in the produced metal colloids or on the solid substrates immobilized with synthesized metal nanoparticles by chemical methods or directly on the deposited nanoparticles by physical methods. The photoreduction process produces metal colloids as well as 2D or 3D microstructures on a solid support [15]. The light source used to reduce metal cations can be a lamp-based white light [10], a nanosecond laser [16], or a femtosecond (fs) laser [14,15].

Fs laser micromachining has attracted much attention due to the unique properties of minimum thermal damage as the pulse duration is shorter than the thermalization time, and the phenomenon of multiphoton absorption leading tothe benefit of machining dielectrics inside the bulk material [17]. Fs laser micromachining in dielectric materials opens a window of opportunity to fabricate functional microdevicesdirectly [18] or indirectly [19]. Recently, periodic micro/nano-structures generated by fs laser irradiations on silicon wafers were demonstrated [20]. Their unique optical property of high absorbability in a wide range of wavelengths (visible light to IR) can be very important for optical detectors to enhance the optical-electric efficiency and the effective wavelength range [21,22]. Furthermore, the periodic surface morphology, after depositing metal particles on the surface, was used as the SERS substrate [23].

In this Section, we report an efficient approach to fabricate SERS substrates which provide high EFs. A combined process of material ablation, particle synthesis, and particle deposition

were achieved by fs laser micromachining of silicon wafers in aqueous solutions of silver nitrate. A high EF of 10^9 was obtained for the synthesized silver nanoparticles on the substrate using Rhodamine 6G (R6G) as analyte molecules at the excitation wavelength of 632.8 nm.

14.2 Fabrication Methods

Sample preparation: Silicon wafer substrates were cleaned in an ultrasonic bath with acetone for 10 minutes and then rinsed by de-ionized water. The cleaned substrates were dipped into 2 ml diluted aqueous solutions of silver nitrate with different concentrations from 1 M to 1 mM contained in an open plastic vessel. The fs laser pulses were focused onto the sample via a 10 × objective lens (NA = 0.3) with a spot size of about 3.3 μm and the samples were translated by the motion stage during the line-by-line machining process. The pulse energy was adjusted to 27 nJ which corresponds to about 0.3 J/cm2. The scanning pitch was set as 1 μm and the scanning speed was varied from 0.5 mm/min to 10 mm/min which correspond to the number of laser pulses deposited on a unit area (NLPDUA) from about 400 to 20. Note for the scanning speed V (with the unit of mm/min), the NLPDUA = (60 × 3.3) / V, where 3.3 is the laser spot size with the unit of μm. After the machining process, the samples were rinsed in de-ionized water to clean up the excess silver nitrate solution. The morphology and composition of the produced nanostructures were examined using scanning electron microscopy (SEM) and energy dispersed spectrum (EDS) respectively.

Evaluation of nanostructures: First, the silicon wafer was machined by fs laser pulses in de-ionized water at different scanning speeds and the resulting surface morphology images are illustrated in Figure 14-1. It is seen, at high scanning speeds, 10 mm/min [Figure 14-1 (a)] and 5 mm/min [Figure 14-1 (b)], the morphology of the roughened surface seems rather random. At the

scanning speed of 2 mm/min [Figure 14-1 (c)], the grating-like periodic nanostructures start to appear but they are not completely developed. At high scanning speeds, 1 mm/min and 0.5 mm/min, the nanostructures have been completely developed and the period is independent of the scanning speed. Compared with the period of the structures machined in air, the structure period machined in water is smaller which reveals a smoother surface in the large scale. Besides the grating-like structures, no apparent nanoparticle is observed in this case of machining in de-ionized water.

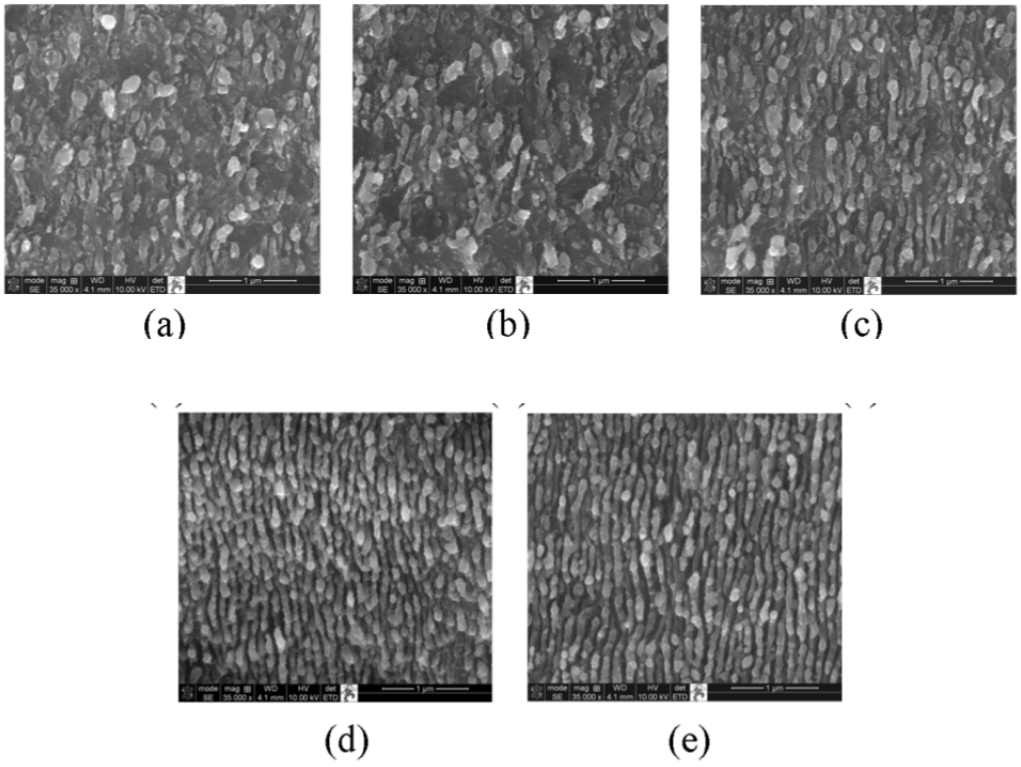

Figure 14-1. Surface morphologies of the machined silicon wafer substrates in de-ionized water with scanning speeds of (a) 10 mm/min, (b) 5 mm/min, (c) 2 mm/min, (d) 1 mm/min, and (e) 0.5mm/min

Figure 14-2 shows the surface morphologies of silicon substrates machined in 0.1 M aqueous solutions of silver nitrate at different scanning speeds ranging from 10 mm/min to 0.5 mm/min.

When the sample was machined in the aqueous solutions of silver nitrate with different scanning speeds, nanoparticles attached to the machined surface are clearly seen as compared to Figure 13-2. The number of attached nanoparticles increases with the decreasing of scanning speed (increasing of NLPDUA). In Figure 14-2 (a) and (b), the periodic structures are not fully developed yet due to the high scanning speeds (low NLPDUA) and only a few nanoparticles on the surface can be seen. In Figure 14-2 (c) to (e), the particle density significantly increases once the scanning speed is slower than 2 mm/min (NLPDUA = 100).

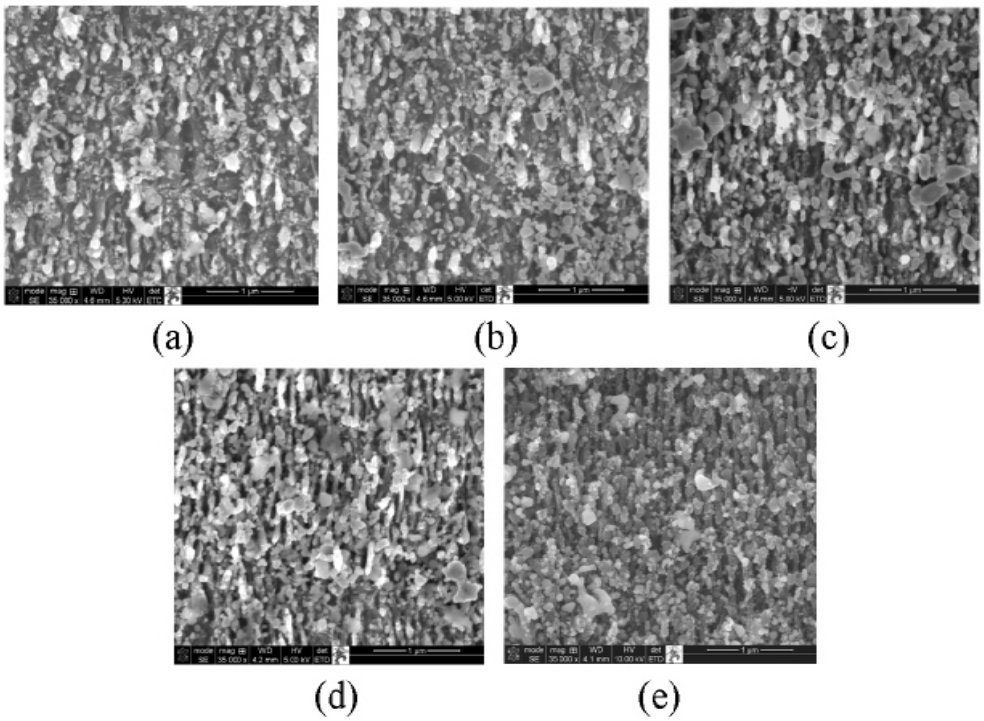

Figure 14-2. Surface morphologies of the machined silicon wafer substrates in 0.1 M silver nitrate solutions with different scanning speeds. (a) 10 mm/min. (b) 5 mm/min. (c) 2 mm/min. (d) 1 mm/min. (e) 0.5 mm/min

In order to identify the compositions of the nanoparticles, the EDS chemical composition mapping was taken as shown in Figure 14-3. Figure 14-3 (a) reveals the mapping area and Figure

14-3 (b) and Figure 14-3 (c) show, respectively, the silver mapping and silicon mapping. The composition of the deposited nanoparticles was proven to be silver. The particle size ranges from tens of nm to hundreds of nm which is evaluated from the enlarged SEM images. From the SEM images, the synthesized nanoparticles reside on the machined surface as well as on the valleys of the grating-like nanostructures. The nanoparticles in the valleys form multilayer nanoparticle clusters, which leads to higher EFs as compared to single layer structures. Furthermore, the format of nanoparticles on the machined surface appears to be particle aggregations. These aggregation structures are also proven to cause higher EFs due to the creation of "hot spots" with strong EM field enhancements in the nanogap between particles in the aggregations.

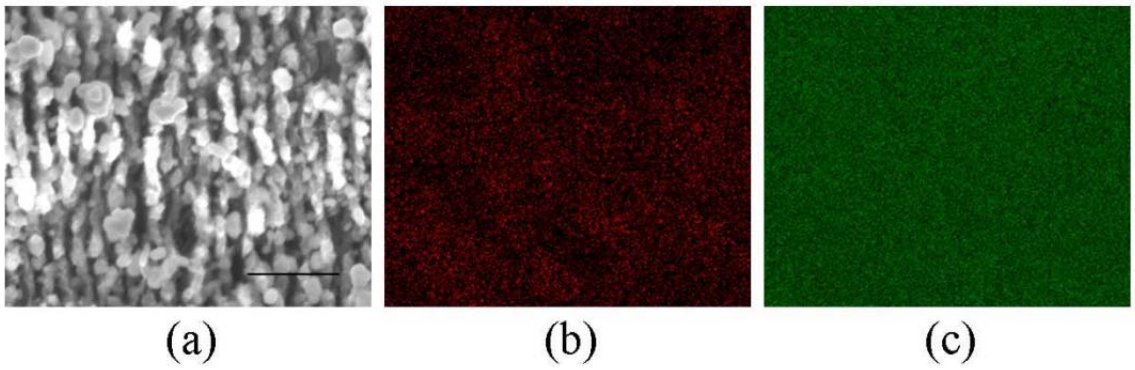

Figure 14-3. EDS mapping of the sample machined in 0.1 M silver nitrate solutions at a scanning speed of 1 mm/min. (a**)** SEM image of the mapping area. The scale bar is 500 nm. **(**b**)** silver mapping, (c**)** silicon mapping.

Figure 14-4 shows the surface morphologies of the machined silicon wafer substrates in 1 mM, 10 mM, 0.1 M, and 1 M silver nitrate solutions with the same scanning speed of 0.5 mm/min. For low concentration, 1 mM [Figure 14-4 (a)], silver particles are still being developed and the particle density attached to the nanostructure is relative low. When the concentration of the silver nitrate solution increases, the particle density increases as Figure 3-

6(b). However, there is not much difference in particle density between 0.1 M [Figure 14-4 (c)] and 1 M [Figure 14-4 (d)]. In other words, the particle density appears to reach saturation when the concentration is higher than 0.1 M.

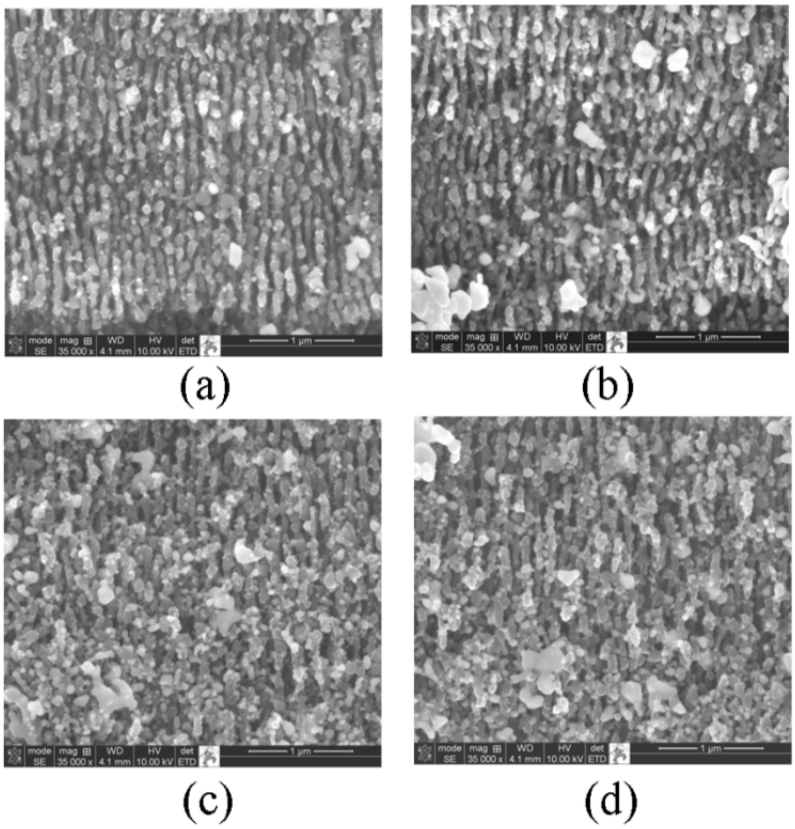

Figure 14-4. Surface morphologies of the machined silicon wafer substrates in different concentrations of silver nitrate solutions with a scanning speed of 0.5 mm/min. (a) 1 mM. (b) 10 mM. (c) 0.1 M. (d) 1 M

14.3 Tests and Results

Parametric study*:* The fs laser pulse energy has dual functions; one is to ablate the substrate to become grating like nanostructures and the other is to reduce the Ag^{+} cations in the silver

nitrate solution to Ag atoms by photoreduction mechanism which will attach to the nanostructures. Hence, the entire process is a combination of material ablation and the subsequent photoreduction and particle deposition. Apparently, the laser energy density must be greater than the damage threshold of the substrate in order to ablate it. The first several laser pulses will ablate the material until the ablation is saturated, i.e., no additional ablation occurs, then, the subsequent laser pulses will produce silver nanoparticles. Before the ablation saturation is reached, some nanoparticles may be produced, they would be ablated by the subsequent laser pulses. Figure 14-5 illustrates the relation of SERS intensity (610 cm^{-1}) and NLPDUA at various concentrations of silver nitrate solutions. In the low concentrations (1 mM and 10 mM), the increase of NLPDUA does not lead to an apparent increase of SERS intensity. Hence, a higher concentration of silver nitrate solutions is required to increase the population of nanoparticles.

As it takes time to photoreduce the Ag^{+} cations, the laser scanning speed must be slow enough (i.e., the NLPDUA must be high enough) allowing time for the photoreduction to occur and for the formation of nanoparticles. As shown in Figure 14-5, for the concentration at 0.1 M, the high scanning speeds at 10 mm/min and 5 mm/min, which correspond, respectively, to 20 and 40 of NLPDUA, the SERS intensities are relative low. This is because there is not enough time for the formation of nanoparticles. In contrast, if the scanning speed is below 2 mm/min (NLPDUA = 100), the SERS intensity arises significantly. Hence, there exists a threshold scanning speed which depends on the concentration of the solution and the laser pulse energy to generate nanoparticles. For the 1 M concentration of silver nitrate solutions, the scanning speed has to be below 1 mm/min to observe the apparent signal enhancement. During the machining process in the 1 M silver nitrate solutions, it was observed that a large amount of reduced silver particles in the solution causes the solution to become locally semi-opaque. As a result, the fs

laser pulse energy would be scattered or absorbed by the dense particles in the solution reducing the effective fluence to arrive at the substrate surface and, thus, more laser pulses are required to achieve the ablation saturation and to generate nanoparticles on the surface of the nanostructures which leads to the lag of SERS intensity increase at 1 mm/min. Note the SERS intensities for 0.1 M and 1 M at NLPDUA = 400 are very close to each other which is consistent with the discussion in Figure 14-5 that their surface morphologies are very similar and the nanoparticle density has reached saturation at 0.1 M.

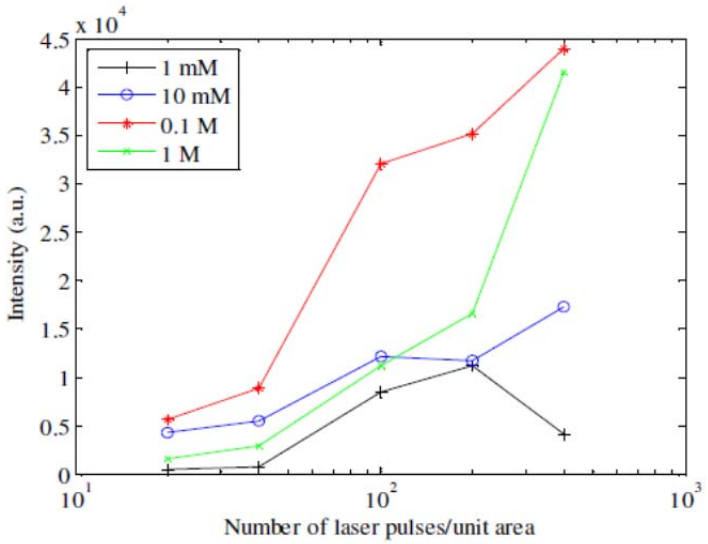

Figure 14-5. SERS intensity vs. NLPDUA in different concentrations of silver nitrate solutions

Estimation of enhancement factor: The black line and blue line in Figure 14-6 show, respectively, the measured SERS spectra of 10^{-7} M R6G in the area inside (black) and outside (blue) of the machined region in the 0.1 M silver nitrate solutions. It is seen the SERS spectra in the machined area is very strong, while it is almost zero outside of the machined area. The strong signal enhancement by the deposited silver nanoparticles is evident. The red line and green line in Figure 14-6 show, respectively, the normal Raman spectra of 10^{-3} M R6G on the sample

machined in de-ionized water (red) and its magnified spectrum (green). For SERS and normal Raman spectra, the exciting He-Ne laser powers are, respectively, 0.17 mW and 17 mW, and the accumulating times are, respectively, 0.5 s, 10 s. In the normal Raman spectrum of 10^{-3} M R6G on the sample machined in de-ionized water, weak R6G signals are seen in the magnified spectrum (green line), except a strong sharp peak at 520 cm^{-1} and a broad peak from 950 cm^{-1} to 1000 cm^{-1}. The results indicate the silicon substrate is observed due to the high exciting laser power and long accumulating time. However, the signal of silicon is unapparent in the SERS spectra due to the existence of strong signal enhancement in the adsorbent R6G molecules which is several orders of magnitude greater than the Raman signal of silicon. In order to quantify the performance of the SERS substrate, the SERS signals of 10^{-7} M R6G measured on the sample that was machined in the 0.1 M silver nitrate solution are compared to the normal Raman signals of 10^{-3} M R6G measured on the sample that was machined in de-ionized water. Both samples were machined at the same scanning speed of 1 mm/min. The commonly accepted EF is defined by Equation (14-1).

$$EF=\frac{I_{SERS}N_{nR}}{I_{nR}N_{SERS}} \tag{14-1}$$

where I_{nR} and I_{SERS} are the normal Raman and SERS intensities in the unit of $mW^{-1}s^{-1}$, respectively. N_{nR} and N_{SERS} represent the number of molecules probed in the reference sample and on the SERS substrate, respectively.

Due to rough surface morphology of the nanostructures with and without silver nanoparticles, the number of adsorbent molecules is difficult to measure accurately. Thus, two comparable samples were machined, respectively, in water and in the silver nitrate solution to generate the same (or very similar) surface roughness. Assuming the effective surface areas of both

nanostructures are identical and there is no specific binding between the analyte and the sample surface, the number of adsorbent molecules on the surface is proportional to the concentration of the analyte solution in which the sample was dipped. Using Equation (14-1) and the aforementioned assumptions and conditions, the EFs at Raman peaks 610 cm^{-1}, 1310 cm^{-1}, 1360 cm^{-1}, and 1510 cm^{-1} are, respectively, 1.3×10^9, 1.1×10^9, 1.3×10^9 and 1.7×10^9, which demonstrates the high sensitivity for SERS measurements with a low R6G concentration.

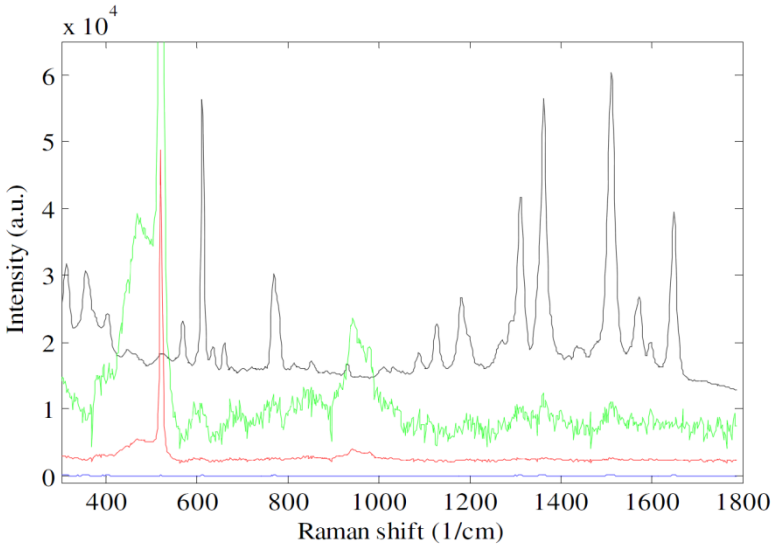

Figure 14-6. SERS and Raman spectra. Black: SERS spectrum of 10^{-7} M R6G measured in the area machined by fs laser in the 0.1 M silver nitrate solution. blue: SERS spectrum of 10^{-7} M R6G measured in the un-machined area. red: Raman spectrum of 10^{-3} M R6G measured in the area machined by fs laser in the de-ionized water. green: magnified (10 ×) Raman spectrum of 10^{-3} M R6G measured in the area machined by fs laser in the de-ionized water.

14.3 Summary

By fs laser machining of silicon wafer in the aqueous solutions of silver nitric under a suitable concentration and laser scanning speed, the generation of grating-like nanostructures and

the subsequent formation of silver nanoparticles on the nanostructures were simultaneously accomplished. The one-step fabrication of SERS substrates with high enhancement factors of 10^9 were demonstrated. The selective laser patterning approach provides the opportunity of directly fabricating SERS active substrates in a functional micro device or chip.

14.4 References

1. M. Fleischmann, P. J. Hendra, and A. J. McQuillan, "Raman spectra of pyridine adsorbed at a silver electrode," Chem. Phys. Lett. **26**(2), 163–166 (1974).
2. D. L. Jeanmaire, and R. P. Van Duyne, "Surface raman spectroelectrochemistry Part I. Heterocyclic, aromatic, and aliphatic amines adsorbed on the anodized silver electrode," J. Electroanal. Chem. **84**(1), 1–20 (1977).
3. C. Fang, A. Agarwal, K. D. Buddharaju, N. M. Khalid, S. M. Salim, E. Widjaja, M. V. Garland, N. Balasubramanian, and D. L. Kwong, "DNA detection using nanostructured SERS substrates with Rhodamine B as Raman label," Biosens. Bioelectron. **24**(2), 216–221 (2008).
4. P. Measor, L. Seballos, D. Yin, J. Z. Zhang, E. J. Lunt, A. R. Hawkins, and H. Schmidt, "On-chip surfaceenhanced Raman scattering detection using integrated liquid-core waveguide," Appl. Phys. Lett. **90**(21), 211107 (2007).
5. L. Su, C. J. Rowlands, and S. R. Elliott, "Nanostructures fabricated in chalcogenide glass for use as surfaceenhanced Raman scattering substrates," Opt. Lett. **34**(11), 1645–1647 (2009).
6. K. Kneipp, Y. Wang, H. Kneipp, L. T. Perelman, I. Itzkan, R. R. Dasari, and M. S. Feld, "Single Molecule Detection Using Surface-Enhanced Raman Scattering (SERS)," Phys. Rev. Lett. **78**(9), 1667–1670 (1997).
7. R. J. C. Brown, and J. T. Milton, "Nanostructures and nanostructured substrates for surface-enhanced Raman scattering (SERS)," J. Raman Spectrosc. **39**(10), 1313–1326 (2008).
8. P. C. Lee, and D. Meisel, "Adsorption and surface-enhanced Raman of dyes on silver and gold sols," J. Phys. Chem. **86**(17), 3391–3395 (1982).
9. H. Hada, Y. Yonezawa, A. Yoshida, and A. Kurakake, "Photoreduction of silver ion aqueous and alcoholic solutions," J. Phys. Chem. **80**(25), 2728–2731 (1976).

10. R. Sato-Berrú, R. Redón, A. Vázquez-Olmos, and J. M. Saniger, "Silver nanoparticles synthesized by direct photoreduction of metal salts. Application in surface-enhanced Raman spectroscopy," J. Raman Spectrosc. **40**(4), 376–380 (2009).
11. X. Tian, K. Chen, and G. Cao, "Seedless, surfactantless photoreduction synthesis of silver nanoplates," Mater. Lett. **60**(6), 828–830 (2006).
12. H. T. Tung, I. G. Chen, J. M. Song, and C. W. Yen, "Thermally assisted photoreduction of vertical silver nanowires," J. Mater. Chem. **19**(16), 2386–2391 (2009).
13. Z. Zhou, J. Xu, Y. Cheng, Z. Xu, K. Sugioka, and K. Midorikawa, "Surface-enhanced Raman scattering substrate fabricated by femtosecond laser direct writing," Jpn. J. Appl. Phys. **47**(1), 189–192 (2008).
14. S. Maruo, and T. Saeki, "Femtosecond laser direct writing of metallic microstructures by photoreduction of silver nitrate in a polymer matrix," Opt. Express **16**(2), 1174–1179 (2008).
15. A. Ishikawa, T. Tanaka, and S. Kawata, "Improvement in the reduction of silver ions in aqueous solution using two-photon sensitive dye," Appl. Phys. Lett. **89**(11), 113102 (2006).
16. S. J. Henley, and S. R. P. Silva, "Laser direct write of silver nanoparticles from solution onto glass substrates for surface-enhanced Raman spectroscopy," Appl. Phys. Lett. **91**(2), 023107 (2007).
17. R. R. Gattass, and E. Mazur, "Femtosecond laser micromachining in transparent material," Nat. Photonics **2**(4), 219–225 (2008).
18. T. Wei, Y. Han, H. L. Tsai, and H. Xiao, "Miniaturized fiber inline Fabry-Perot interferometer fabricated with a femtosecond laser," Opt. Lett. **33**(6), 536–538 (2008).
19. C. H. Lin, L. Jiang, H. Xiao, Y. H. Chai, S. J. Chen, and H. L. Tsai, "Fabry-Perot interferometer embedded in a glass chip fabricated by femtosecond laser," Opt. Lett. **34**(16), 2408–2410 (2009).
20. J. Bonse, S. Baudach, J. Krüger, W. Kautek, and M. Lenzner, "Femtosecond laser ablation of siliconmodification thresholds and morphology," Appl. Phys., A Mater. Sci. Process. **74**(1), 19–25 (2002).
21. C. H. Crouch, J. E. Carey, M. Shen, E. Mazur, and F. Y. Genin, "Infrared absorption by sulfur-doped silicon formed by femtosecond laser irradiation," Appl. Phys., A Mater. Sci. Process. **79**, 1635–1641 (2004).
22. Z. Huang, J. E. Carey, M. Liu, X. Guo, E. Mazur, and J. C. Campbell, "Microstructured

silicon photodetector," Appl. Phys. Lett. **89**(3), 033506 (2006).

23. E. D. Diebold, N. H. Mack, S. K. Doorn, and E. Mazur, "Femtosecond laser-nanostructured substrates for surface-enhanced Raman scattering," Langmuir **25**(3), 1790–1794 (2009).
24. M. Futamata, and Y. Maruyama, "Electromagnetic and chemical interaction between Ag nanoparticles and adsorbed rhodamine molecules in surface-enhanced Raman scattering," Anal. Bioanal. Chem. **388**(1), 89–102 (2007).
25. Y. Han, C. H. Lin, H. Xiao, and H. L. Tsai, "Femtosecond laser-induced silicon surface morphology in water confinement," Microsyst. Technol. **15**(7), 1045–1049 (2009).
26. T. Kondo, K. Nishio, and H. Masuda, "Surface-enhanced Raman scattering in multilayered Au nanoparticles in anodic porous alumina matrix," Appl. Phys. Express **2**, 032001 (2009).
27. I.W. Sztainbuch, "The effects of Au aggregate morphology on surface-enhanced Raman scattering enhancement," J. Chem. Phys. **125**(12), 124707 (2006).
28. P. A. Temple, and C. E. Hathaway, "Multiphonon Raman spectrum of silicon," Phys. Rev. B **7**(8), 3685–3697 (1973).
29. R. P. Van Duyne, J. C. Hulteen, and D. A. Treichel, "Atomic force microscopy and surface-enhanced Raman spectroscopy. 1. Ag island films and Ag film over polymer nanosphere surface supported on glass," J. Chem. Phys. **99**(3), 2101–2115 (1993).
30. G. L. Liu, and L. P. Lee, "Nanowell surface enhanced Raman scattering arrays fabricated by soft-lithography for label-free biomolecular detections in integrated microfluidics," Appl. Phys. Lett. **87**(7), 074101 (2005).

15. Measurement of RI change of optical fiber core induced by fs laser

15.1 Introduction

Recent advancement in ultrafast femtosecond pulse laser technology has opened a new window of opportunity for one-step without additional assembly fabrication of micro- and even nanoscale photonic structures in various solid materials.1,2 A femtosecond laser beam can be focused into a transparent object, creating localized optical features at the focal point on the surface or inside the solid material.

Various miniaturized optical devices have been demonstrated using femtosecond lasers. Compared with other fabrication methods, the femtosecond-laser-based technique has the unique feature of fabricating 3-D microstructures with great flexibility. Femtosecond-laser-based fabrication of optical devices can be either destructive or nondestructive. In a destructive fabrication, the femtosecond laser ablation effect is directly used to sculpture solid materials into desired 3-D shapes.

Optical device examples include microlenses,3 microfluidic channels,4 fiber inline Fabry-Perot interferometers,5,6 and optical switches.7 Destructive fabrication is above the material ablation threshold. Nondestructive fabrication, called subablation fabrication, is below the material ablation threshold. Although the point at which absorbed laser energy is not sufficient to break the bonds between molecules of a material, the short-pulse lasers cause nearsurface thermal stresses, which can lead to a wide variety of micromechanical responses.8,9 In a nondestructive way, femtosecond laser irradiations can induce the refractive index in optical materials.10–12 As a result, optical waveguides,13,14 gratings,15,16 and directional couplers17 have been demonstrated, for instance, fiber Bragg gratings and long-period fiber Bragg gratings.

The amount of refractive index variation induced by femtosecond laser exposure inside the photonic device is one of the most critical variables that determine the characteristic of the target structure, such as fiber Bragg grating. Quite a few research groups study laser induced refractive index change in different materials. However, up until now, although femtosecond-laser-induced refractive index change on bulk fused silicon has been studied, no precise measurement has been conducted toward this parameter in optical fiber.

This work mainly focuses on the measurement method of femtosecond-laser-induced refractive index change in the optical fiber core. Assisted by the most recently developed femtosecond laser fabricated fiber inline Fabry-Perot interferometer (FPI), the refractive index change can be calculated by the optical length change measured in fiber inline FPI. Since the fiber inline FPI was fabricated on the optical fiber in one step, together with the fact that the refractive index measurement was carried out on the same device, the whole experiment was integrated on the same structure by one-time assembly, which further improved the measurement accuracy.

15.2 Measurement Platform Fabrication

Figure 15-1 shows the optical image of the fabricated fiber inline FPI device. The device was fabricated for an optical fiber (Corning SMF-28] by femtosecond laser micromachining following the procedures reported previously.5 The cavity length was about 40 μm as estimated from the optical image. The depth of micronotch was around 72 μm, just passing the fiber core. The cavity was made 5 mm to the end of the cleaved fiber tip. The background loss of this particular device was about 20 dB. This device can be considered as a combination of two FPIs. The femtosecond laser ablated notch section is the extrinsic Fabry-Perot interferometer (EFPI),

while the following fiber segment to the end of the fiber tip is the intrinsic Fabry-Perot interferometer (IFPI). The EFPI corresponds to interference spectra with a period of around 40 nm, and the IFPI has that of around 0.15 nm. In this experiment, the IFPI was used as the measuring device, and the IFPI signal is relatively independent from that of EFPI as a result of the huge scale difference between the interference spectra. With femtosecond laser scanning close to the IFPI cavity, the shift of IFPI interference can be detected due to the refractive index change in the fiber core.

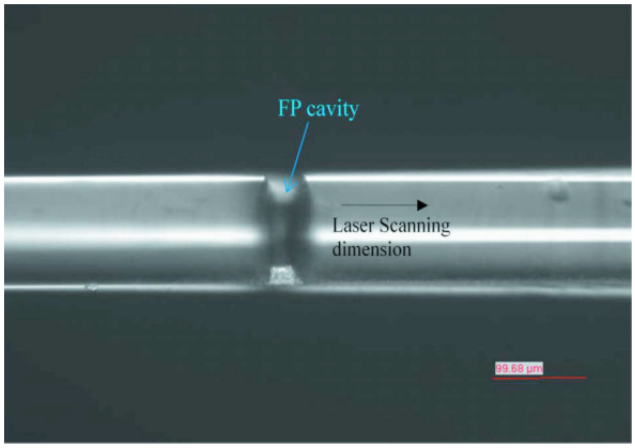

Figure 15-1. Microscopic optical image of the fabricated fiber inline FPI device.

15.3 Principle and Theory

The refractive change can be measured using a fiber inline FPI as schematically shown in Figure 15-2. The IFPI section serves as an interferometer, in which the reflections at the two endfaces, coupling back to the lead in fiber through the femtosecond ablated notch (EFPI section), superimposed to form an interference signal at the optical power meter (HP8163). By stepping the tunable laser through its available wavelength range and coordinating the signal detection at the power meter using a computer, the interference spectrum of the IFPI can thus be

recorded. When exposed to femtosecond laser irradiations, the IFFPI section at the end of the fiber tip changes its refractive index, resulting in a phase shift in the interference signal. The femtosecond laser-induced fiber refractive index change can thus be calculated based on the amount of phase shift after laser irradiation.

Assuming that the two reflected lights from the IFPI section have the intensities of I_1 and I_2, respectively, the interference signal I_i generated by these two reflections is given by:

$$I_i = I_1 + I_2 + 2\sqrt{I_1 I_2}\cos\left[\frac{4\pi}{\lambda}(OL) + \phi_0\right] \tag{15-1}$$

where OL is the optical length of IFPI, defined as the product of length and the refractive index of the core; ϕ_0 is the initial phase of the interference; and λ is the optical wavelength in vacuum.

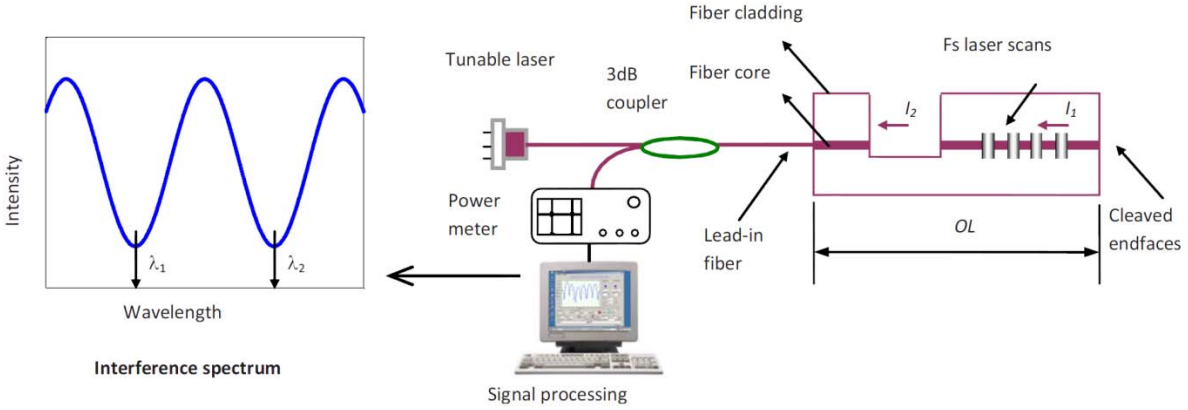

Figure 15-2. System schematic of the setup for measurement of fs laser irradiation induced refractive change inside an optial fiber core using a fiber inline FPI.

As shown in Figure 15-2, the two adjacent valleys at λ_1 and λ_2 in the interference spectrum have a phase difference of 2π, that is:

$$\left(\frac{4\pi}{\lambda_1}OL\right)-\left(\frac{4\pi}{\lambda_2}OL\right)=2\pi \tag{15-2}$$

Therefore, the initial optical length of the IFPI section can be calculated using the following equation:

$$OL=\frac{\lambda_1\lambda_2}{2(\lambda_1-\lambda_2)}. \tag{15-3}$$

Since the device is fixed under a tension-free circumstance, and the IFFPI section is considerably short (about 5mm), the change in optical length is mainly caused by the laser irradiation-induced refractive index change inside the fiber core. For multiple-point laser irradiations at different locations, the accumulated change in optical path is given by

$$\Delta OL=m\cdot(\Delta OL_{\text{single}})=m\cdot(\Delta n\cdot W) \tag{15-4}$$

where m is the total number of laser irradiations, Δn is the refractive index change, and W is the width of one femtosecond laser exposure scan.

When the change in optical path length is small enough that the phase shift is less than 2π, the phase ambiguity issue can be avoided. The relative optical length change can be calculated based on the spectral shift of the interferogram at the featured points such as the peak, valley, and center of the interference fringes, given by

$$\Delta OL = \frac{\Delta\lambda_1}{\lambda_1} OL \tag{15-5}$$

Combining Equations (15-4) and (15-5), one finds the refractive index change:

$$\Delta n = \frac{1}{mW} \frac{\Delta\lambda_1}{\lambda_1} OL \tag{15-6}$$

In the experiments, the laser pulse energy was tunable. An alternative way of calculating the refractive index change is directly based on Equation (15-4), in which the change in optical length is a linear function of the number of laser exposures, and the slope of the line is linearly proportional to Δn. Experimentally, one can measure the optical length change after a various number of laser exposures, and curve-fit the measurement results into a line. The slope of the fitted line can thus be used to calculate Δn. This method uses multiple data points in calculation and can effectively reduce measurement uncertainty.

15.4 Experiments and Results

The experiment was carried out on a home-integrated femtosecond laser 3-D micromachining system. The repetition rate, center wavelength, and pulse width of the femtosecond laser (Legend-F, Coherent, Incorporated), were 1 kHz, 800 nm, and 80 fs, respectively. The maximum output power of the femtosecond laser was approximately 1 W. A combination of a half-wave plate and a polarizer was used to reduce the laser power to 20 mW in the first place, and then several neutral density filters were applied to further reduce the laser pulse energy to desired values of 0.5, 0.8, and 1 μJ, based on different experimental conditions. The attenuated laser beam was directed into objective lenses (Olympus UMPLFL 20X) with a

numerical aperture (NA) of 0.45, and was focused at the center of the IFPI section. Each time, with the help of a five-axis motion stage (Aerotech, Incorporated), providing 1 μm resolution, a block (20×15×15 μm^3) was scanned covering the fiber core potion with a width of 20 μm, defined as one femtosecond laser exposure scan. We altered the distance between the single laser scans, as the experiment went along, to avoid the grating effect, which might disturb the interference signal.

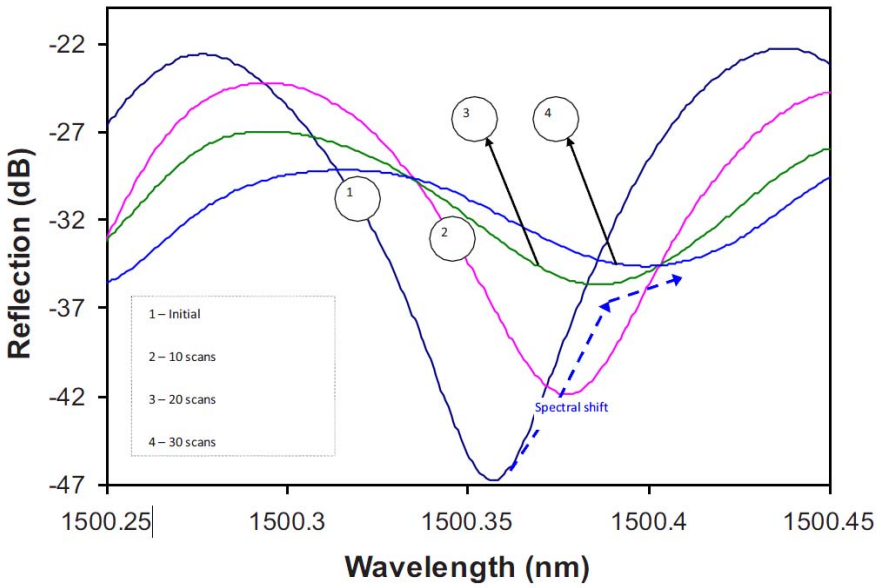

Figure 15-3. Changes of the interferograms as the number of laser scans increases.

Figure 15-3 shows the initial interference spectrum and those after 10, 20, and 30-fs laser scans with laser pulse energy of 0.8 μJ. The large fringe visibility—the ratio of the size or amplitude of oscillations to the sum of the powers of the individual waves—indicated the high quality of the interference signals. Since each laser scan induced a small amount of energy loss, the fringe visibility of the interference signal reduced as the number of laser exposures increased.

This is still an open topic; some groups employed the Kramers-Kronig relations to explain laser pulse properties and refractive index change.18,19

The interference spectrum shifts to the short wavelength as the number of laser scans increases. By tracing the interferogram shift, we calculated the changes of optical length based on Equation 15-4. The results, as a function of the number of laser scans, are plotted in Figure 15-4, where the measured data points fit nicely into a line with a slope of 6.9 nm per fs laser scan. The induced Δn was 3.45×10^{-4} based on Equation 15-4.

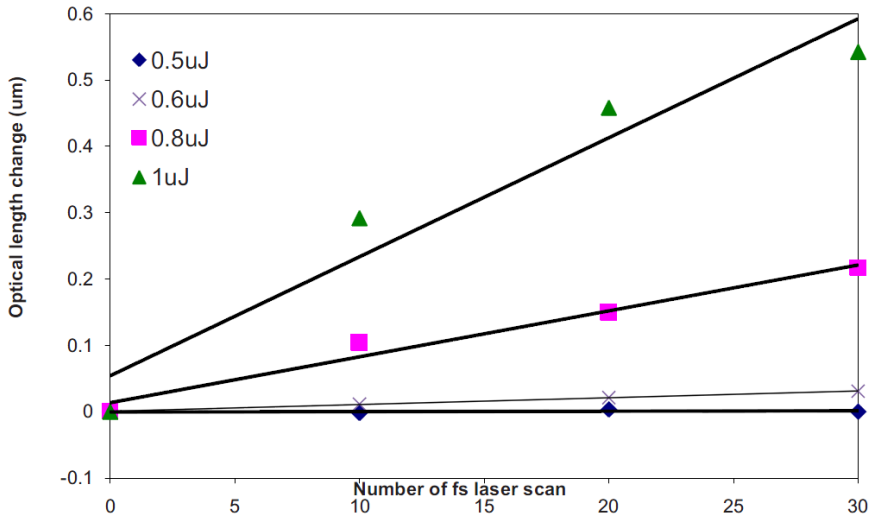

Figure 15-4. Change in fiber optical length versus numbers of the laser scans

To investigate the induced refractive index at alternative laser pulse energy, we repeated the previous experiments by varying the femtosecond laser pulse energy by adding or dropping ND filters. Figure 15-4 shows the change in fiber optical length as a function of the number of the laser scans with different pulse energy of 0.5, 0.6, 0.8, and 1 μJ. For comparison, the refractive changes induced by different pulse energy are 2.5×10^{-6}, 2.78×10^{-5}, 3.45×10^{-4}, and 8.95×10^{-4},

respectively. Obviously, the refractive index change induced by 0.5 μJ, approximately the refractive index modification threshold for fusion silicon ablation, is ignorable. The experiment revealed that pulse energy less than the refractive index modification threshold cannot produce an observable refractive index change, which we believe is because smaller pulse energy below the threshold is not able to significantly change the material thermal stresses, inducing refractive index modification. Still, it is an open issue that needs further verification and investigation.

15.5 Summary

We demonstrate a fiber inline IFPI-based measurement method to investigate the femtosecond-laser-induced refractive index change in an optical fiber core. The femtosecond-laser-induced refractive index change is found to be 2.5×10^{-6}, 2.78×10^{-5}, 3.45×10^{-4}, and 8.95×10^{-4}, at different pulse energy levels 0.5, 0.6, 0.8, and 1 μJ, respectively. We believe accurate refractive index change values can help develop and design nondestructive femtosecond laser fabricated photonic devices.

15.6 References

1. R. R. Gattass and E. Mazur, "Femtosecond laser micromachining in transparent materials," Nat. Photonics 2(4), 219–225 (2008).
2. M. Lenzner, J. Krüger, S. Sartania, Z. Cheng, C. Spielmann, G. Mourou, W. Kautek, and F. Krausz, "Femtosecond optical breakdown in dielectrics," Phys. Rev. Lett. 80(18), 4076–4079 (1998).
3. Y. Cheng, H. L. Tsai, K. Sugioka, and K. Midorikawa, "Fabrication of 3D microoptical lenses in photosensitive glass using femtosecond laser micromachining," Appl. Phys. A 85(1), 11–14 (2006).

4. Y. Cheng, K. Sugioka, and K. Midorikawa, “Microfluidic laser embedded in glass by three-dimensional femtosecond laser microprocessing,”
1. Opt. Lett. 29(17), 2007–2009 (2004).
5. T. Wei, Y. Han, H. L. Tsai, and H. Xiao, “Miniaturized fiber inline Fabry-Perot interferometer fabricated with a femtosecond laser,” Opt.
2. Lett. 33(6), 536–538 (2008).
6. T. Wei, Y. Li, Y. Han, H. L. Tsai, and H. Xiao, “Temperature insensitive miniaturized fiber inline Fabry-Perot interferometer for highly sensitive refractive index measurement,” Opt. Express 16(8), 5764–5769 (2008).
7. H. Y. Zheng, H. Liu, S. Wan, G. C. Lim, S. Nikumb, and Q. Chen, “Ultrashort pulse laser micromachined microchannels and their application in an optical switch,” Int. J. Adv. Manuf. Technol. 27(9–10), 925–929 (2006).
8. J. Kruger, H. Niino, and A. Yabe, “Investigation of excimer laser ablation threshold of polymers using a microphone,” Appl. Surf. Sci. 197–198, 800–804 (2002).
9. A. Baum, P. Scully, M. Basanta, C. Thomas, P. Fielden, and N. Goddard, “Photochemistry of refractive index structures in polymethylmethacrylate_ by femtosecond laser irradiation,” Opt. Lett. 32(2), 190–192 (2007).
10. M. Kamata and M. Obara, “Control of the refractive index change in fused silica glasses induced by a loosely focused femtosecond laser,” Appl. Phys. 78(1), 85–88 (2004).
11. F. Vega, J. Armengol, V. Diez-Blanco, J. Siegel, J. Solis, B. Barcones, A. Pérez-Rodríguez, and P. Loza-Alvarez, “Mechanisms of refractive index modification during femtosecond laser writing of waveguides in alkaline lead-oxide silicate glass,” Appl. Phys. Lett. 87(2), 1–3 (2005).
12. A. Zoubir, M. Richardson, L. Canioni, A. Brocas, and L. Sarger, “Optical properties of infrared femtosecond laser-modified fused silica and application to waveguide fabrication,” J. Opt. Soc. Am. B 22(10), 2138–2143 (2005).
13. K. M. Davis, K. Miura, N. Sugimoto, and K. Hirao, “Writing waveguides in glass with a femtosecond laser,” Opt. Lett. 21(21), 1729–1731 (1996).
14. S. Nolte, M. Will, J. Burghoff, and A. Tuennermann, “Femtosecond waveguide writing: a new avenue to three-dimensional integrated optics,” Appl. Phys. A 77(1), 109–111 (2003).
15. A. Martinez, M. Dubov, I. Khrushchev, and I. Bennion, “Direct writing of fiber Bragg

gratings by femtosecond laser," Electron. Lett. 40(19), 1170–1172 (2004).

16. Y. Kondo, K. Nouchi, T. Mitsuyu, M. Watanabe, P. G. Kazansky, and K. Hirao, "Fabrication of long-period fiber gratings by focused irradiation of infrared femtosecond laser pulses," Opt. Lett. 24(10), 646–648 (1999).
17. A. M. Streltsov and N. F. Borrelli, "Fabrication and analysis of a directional coupler written in glass by nanojoule femtosecond laser pulses," Opt. Lett. 26(1), 42–43 (2001).
18. K. Peiponen, V. Lucarini, E. Vartiainen, and J. Saarinen, "Kramers-Kronig relations and sum rules of negative refractive index media," Eur. Phys. J. B 41, 61–65 (2004).
19. H. Nishiyama, J. Nishii, M. Mizoshiri, and Y. Hirata, "Microlens arrays of high-refractive-index glass fabricated by femtosecond laser lithography," Appl. Surf. Sci. 255, 9750–9753 (2009).

16. Fiber Sensor based on a Radio Frequency MZI

16.1 Introduction

Optical fiber sensors are well known for their advantages, such as small size, light weight, immunity to electromagnetic interference, resistance to chemical corrosion, and high temperature survivability [1]. Also, as a transmission line, optical fiber is supreme in terms of transmission loss and cost in comparison with its analog, coaxial cable in the radio frequency (RF) domain. These unique features position optical fiber sensors to fulfill the needs of a wide range of sensing tasks. In general, the interrogation techniques of optical fiber sensors are conducted using optical instruments, such as an optical powermeter and an optical spectrum analyzer.

Interestingly, researchers have demonstrated the possibility to interrogate optical fiber sensors in the RF domain. Until now, most of the reported techniques focus on active sensing devices. The main idea is to generate two signals at slightly different wavelengths in the optical domain and measure their beat frequency in the RF domain.

One successful example is by tracing the beat frequency between two polarization states in a distributed feedback laser constructed by a section of active fiber and two identical fiber Bragg gratings [2]. It has been reported that such a configuration can be used to measure temperature [3], strain [4], acoustic waves [5], etc. Another example is by using the beat frequency of the longitudinal modes in a fiber laser to measure the optical path length of the laser cavity, which varies as a function of ambient temperature [6], strain [7], and vibration [8]. In both examples, the spectral information is converted from the optical domain to the RF domain. As a result, an electronic signal spectrum analyzer can be used to replace an optical spectrum analyzer to interrogate the fiber sensor.

On the other hand, optical fiber devices have been explored to create microwave photonic (MWP) processors, including filters [9], signal generators [10], mixers [11], etc. It is proven that the photonic signal processing offers wide bandwidth operation, high resolution, and low noise performance [12]. These unique features stem mainly from the intrinsic excellent properties of optical fiber delay lines. Inspired by the MWP processors, different from previously reported active RF optical fiber sensors, we propose a passive optical fiber sensor that can be interrogated using RF instruments. An optical fiber RF Mach–Zehnder interferometer (MZI) with one reference arm and one sensing arm was demonstrated to measure temperature changes. The interference pattern of the RF-MZI sensor shifts to lower frequencies as temperature increases.

16.2 System Configuration and Results

Figure 16-1 is the schematic of the RF-MZI sensor and the instrumentation to acquire the signal. A cw laser at 1541.7 nm (Agilent 81651A) is amplitude modulated by an electro-optic modulator (EOM, Agere 2623N). The EOM is driven by port 1 of a network analyzer (NWA, HP 8753es). The modulated light is then fed into a 3 dB coupler to be split into two optical fiber arms. Both arms can be considered as optical fiber delay lines; the upper arm with a length of 0.52 m serves as the reference arm, while the lower one with a much longer length serves as the sensing arm. The second 3 dB coupler is used to merge the signal from both optical fiber arms. The two 3 dB couplers, together with the reference and the sensing delay line arms, form the passive RF-MZI structure. The output light from the RF-MZI is injected into a photodiode (PD, Agilent 83440d), which converts the light signal into an RF analog signal. Port 2 of the NWA is connected to the PD to receive the converted RF signal, where an RF amplifier is used to provide gain to the signal to help the output RF signal reach the sensitivity limit of the NWA.

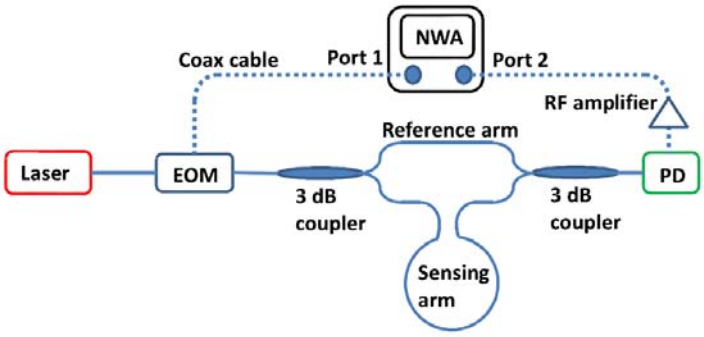

Figure 16-1. Schematic of RF-MZI sensor and instrumentation for interrogation (dotted lines are coaxial cable and solid lines are optical fiber link).

The NWA sweeps the frequency at a fixed voltage level at port 1 and records the transmitted voltage in correspondence to each frequency step at port 2. The interference pattern of the RF-MZI is achieved by plotting the magnitude of the voltage transmission coefficient (S_{21}), which is defined as the ratio between output voltage and input voltage of the NWA with respect to frequency. The magnitude of the transmission coefficient of the RF-MZI can be expressed as

$$|S_{21}| = G\cos(2\pi f \Delta\tau_d) \tag{16-1}$$

where f is the swept frequency, $\Delta\tau_d$ is the optical fiber delay difference between the sensing arm and the reference arm, and G describes the transmission efficiency along the wave path, including the RF-to-light-signal conversion efficiency of the EOM, the light-to-RF-signal conversion efficiency of the PD, the gain of the RF amplifier, and the loss of the coaxial cable and the fiber couplers.

Equation (16-1) shows that $|S_{21}|$ follows a sinusoidal trend, which is also known as the interference pattern of the RF-MZI. The delay line difference can be written as

$$\Delta\tau_d = \frac{n_{\text{eff}}(L_{\text{sen}} - L_{\text{ref}})}{c} \tag{16-2}$$

where n_{eff} is the effective refractive index of the singlemode optical fiber and c is the speed of light, L_{ref} is the physical length of the referencing arm, and L_{sen} is the length of the sensing arm.

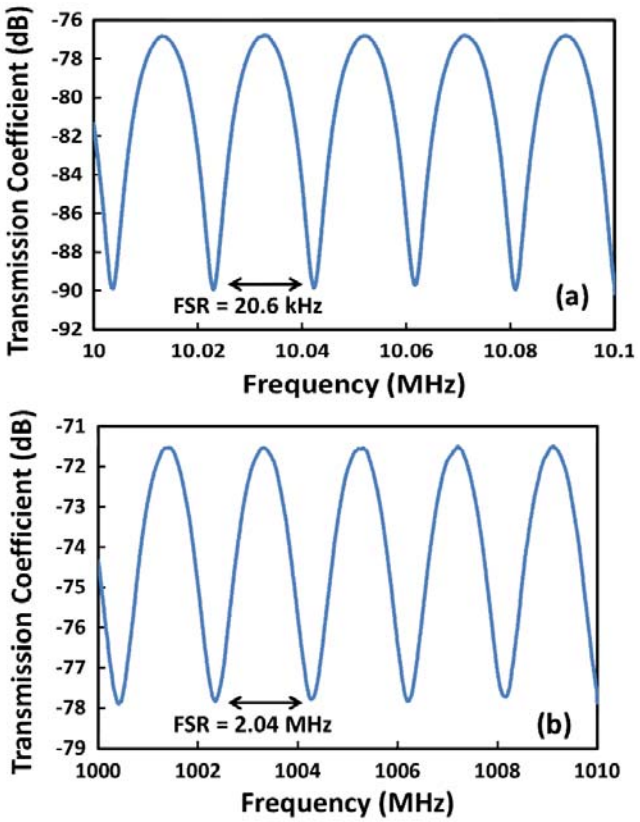

Figure 16-2. Transmission coefficient of RF-MZI sensor when (a) the sensing arm is 10 km and (b) the sensing arm is 100 m.

Figure 16-2 plots the interference pattern of the RF-MZI with two very different sensing arm lengths, 10 km and 100 m. The resolution bandwidth is set at 30 Hz and the total number of sampling points is set to be 1601 for both cases. The bandwidth of the RF-MZI with the 10 km sensing arm is 10–10.1 MHz, while the bandwidth of the one with 100 m is 1000–1010 MHz. In

both cases, one sweep of the NWA takes less than 1 s. The frequency at the minima on the interference spectrum is defined as the resonant frequency (f_{res}) of the RFMZI, which can be predicted by the following equation [13]:

$$f_{\text{res}} = (2k+1)\frac{c}{2n_{\text{eff}}(L_{\text{sen}} - L_{\text{ref}})} \tag{16-3}$$

where k = 0; 1; 2…is the harmonic order of resonant frequencies. Thus, the free spectrum range (FSR), defined as the frequency span between two consecutive resonant frequencies, is given by

$$\text{FSR} = \frac{c}{n_{\text{eff}}(L_{\text{sen}} - L_{\text{ref}})} \tag{16-4}$$

By applying the fiber parameter n_{eff}= 1.46 in Equation (16-4), the FSR calculated for the 10 km sensing arm is 20.6 kHz, while the one with the 100 m sensing arm is 2.04 MHz. In both cases, the predicated FSR matched well with the experimental results marked in Figure 16-2.

The sensing mechanism of the RF-MZI is based on tracking the shift of the resonant frequency. Given the optical path length of the reference arm of an RF-MZI is unchanged, the variation of the sensing arm, including both neff and Lsen, results in a frequency shift of the resonant frequency.

To test the sensing function of the RF-MZI, a temperature test was performed on the RF-MZI with a sensing arm of 10 km. The sensing arm was placed in an electrical oven (Yamato DX300). Two small pieces of the sensing arm, with a total length of 0.43 m, stick out of the oven to splice to the couplers. It is worth noting that the measured temperature affects only the portion of the

sensing arm inside the oven, defined as the effective length. The sensitivity decreases when the sensing arm reduces its effective length. The test temperature ranged from 25°C to 70 °C with a step of 5 °C. We waited for around 15 min after the oven reached each desired temperature point to give enough time for the oven to stabilize. Two resonant frequencies, 10.0232 and 100.0853 MHz at room temperature, were used for temperature sensing in this experiment. A fourth-order polynomial fit was applied to the measured data near the resonant frequency to smooth the curve by reducing the ripple effect during the measurement. The resonant frequency was determined after curve fitting. Both resonant frequencies shifted to lower frequency as the temperature increased. This phenomenon indicates that the optical path in the sensing arm increases as temperature rises, which agrees with the previously reported results using an active fiber sensor [6].

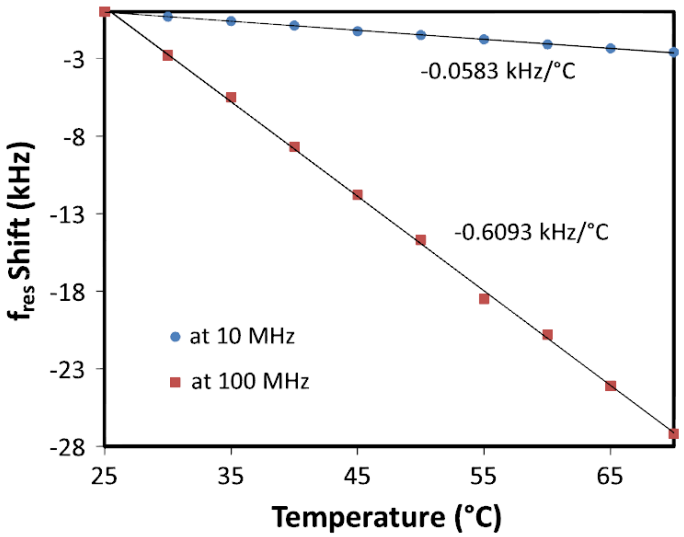

Figure 16-3. Resonant frequency shift as a function of temperature of a RF-MZI with a 10 km sensing arm: resonant frequency at 10 MHz and resonant frequency at 100 MHz.

Figure 16-3 plots the resonant frequency shift as a function of temperature. The resonant frequency shift is inversely linear proportional to the temperature. In addition, the sensitivity of the resonant frequency at around 10 MHz is −0.0583 kHz/°C, while at around 100 MHz, the sensitivity is −0.6093 kHz/°C, which is approximately 10 times that of the resonant frequency at 10 MHz. Equation (16-4) suggests that the higher-order resonant frequency is associated with a larger frequency shift in response to certain optical path changes in the sensing arm, which explains the increased sensitivity at higher frequencies. Also, the sensitivity is linearly proportional to the resonant frequency under observation. However, in real applications, higher sensitivity may generate a frequency shift that is larger than the FSR, which would result in an ambiguity issue, similar to those interferometric sensors in the optical domain [14]. For example, in this experiment, a total temperature change of 45 °C produces a resonant frequency shift of ~28 kHz, which surpasses its FSR (20.6 kHz). As a result, it is impossible to differentiate the observation resonant frequency and the consecutive resonant frequency with a smaller harmonic order.

The second temperature test was applied on the RFMZI with a 100 m sensing arm. Sufficient time was given for the oven to fully cool down after the first temperature test. The resonant frequency to be monitored was set at ~1002.3 MHz. By repeating the same experimental procedure, a sensitivity of −6.1 kHz/°C was achieved, which agreed well with the predicated value of −6.093 kHz/°C. Also, the total temperature variation generated a frequency shift of 274.5 kHz, which was within the FSR (2.04 MHz) of this sensor. In addition, the 100 m sensing arm is much easier to handle than the 10 km one, which makes it a better solution in this case.

Just like a regular optical fiber MZI, the RF-MZI is sensitive to polarization drift and instability of the reference arm. The polarization of the two interfering beams may drift randomly due to alterations in the residual birefringence of the fiber caused by minor variations in temperature or position of the fiber, resulting in unpredicted phase shift. Also, the instability due to minor temperature or position variation in the reference arm may lead to unpredictable phase shift. The undesirable phase shifts restrict the sensor performance in terms of minimum detectable temperature change, as well as measurement accuracy. To evaluate the measurement instability, the interference spectrum of the 100 m sensing arm RFMZI was taken every 3 s under room temperature with a total number of 1000. By tracing the frequency at one minima position in the interference spectra, we calculated that the frequency standard deviation is 0.252 kHz, corresponding to a temperature change of approximately 0.4 °C.

16.3 Summary

To summarize, we developed and demonstrated a passive optical fiber RF-MZI for sensing applications. An RF modulated laser source was injected into an optical fiber MZI and the interference signal was collected by a PD and analyzed in the RF domain. High-quality interference patterns were observed in the RF domain by sweeping the modulation frequency using an NWA. The proposed RFMZI was demonstrated for temperature sensing. The resonant frequency shifted to lower frequency as temperature increased. In addition, the sensitivity, observation resonant frequency range, and the length of the sensing arm are discussed.

16.4 References

1. A. D. Kersey, M. A. Davis, H. J. Patrick, M. Le Blanc, K. P. Koo, C. G. Askins, M. A. Putnam, and E. J. Friebele, J. Lightwave Technol. 15, 1442 (1997).
2. J. T. Kringlebotn, W. H. Loh, and R. I. Laming, Opt. Lett. 21, 1869 (1996).
3. A. C. L. Wong, D. Chen, H. J. Wang, W. H. Chung, H. Y. Tam, C. Lu, and B. O. Guan, Meas. Sci. Technol. 22, 045202 (2011).
4. Y. Zhang, B. O. Guan, and H. Y. Tam, Opt. Commun. 281, 4619 (2008).
5. T. Guo, A. C. L. Wong, W. S. Liu, B. O. Guan, C. Lu, and H. Y. Tam, Opt. Express 19, 2485 (2011).
6. Z. Yin, L. Gao, S. Liu, L. Zhang, F. Wu, L. Chen, and X. Chen, J. Lightwave Technol. 28, 3403 (2010).
7. S. Liu, R. Gu, L. Gao, Z. Yin, L. Zhang, X. Chen, and J. Cheng, Opt. Eng. 50, 054401 (2011).
8. L. Gao, S. Liu, Z. Yin, L. Zhang, L. Chen, and X. Chen, IEEE Photon. Technol. Lett. 23, 18 (2011).
9. J. Capmany, B. Ortega, and D. Pastor, J. Lightwave Technol. 24, 201 (2006).
10. R. A. Minasian, IEEE Trans. Microwave Theory Tech. 54, 832 (2006).
11. C. K. Sun, R. J. Orazi, and S. A. Pappert, IEEE Photon. Technol. Lett. 8, 154 (1996).
12. K. Wilner and A. P. van den Heuvel, Proc. IEEE 64, 805 (1976).
13. A. H. Quoc and S. Tedjini, IEEE Microwave Guided Wave Lett. 4, 183 (1994).
14. A. Wang, H. Xiao, J. Wang, Z. Wang, W. Zhao, and R. G. May, J. Lightwave Technol. 19, 1495 (2001).

17. Optical Carrier Microwave Interferometer: Theories

17.1 Introduction

Optical interferometry has been widely used for accurate measurement of various physical, chemical and biological quantities by encoding the information of interest into the propagation delay between the optical beams. The principle has been implemented into various sensors and found a many important applications in various scientific and engineering fields. Although optical interferometers have many well-known advantages (e.g., high resolution), they have also shown certain disadvantages such as the stringent requirements on surface qualify and fabrication precision, difficulty to be multiplexed, and strong dependence on the material and geometry of the optical waveguides. As a result, optical interferometers have limited field applications despite their wide usage in laboratory conditions and controlled environments.

Governed by the same electromagnetic theories, microwave and optics have many characteristics in common but significant differences in properties and applications. Two microwave beams can also be coherently superimposed to generate an interference pattern similar to two optical beams. Due to the large wavelength (low frequency) of microwave, the size of a microwave interferometer is larger than that of an optical interferometer. Construction of a microwave interferometer thus does not necessarily require a manufacturing accuracy as high as that required by an optical interferometer. In addition, the stringent requirements on optical waveguides (e.g., geometry, dispersion, modal and material characteristics) for making an optical interferometer can be relieved significantly in a microwave interferometer. However, microwaves cannot transmit over a long distance because of the large loss of the waveguide (e.g., a coaxial cable). A promising effort is to bring the strengths from both microwave and optics

together by combining microwave and optics. This combination, which is called **microwave photonics**, is already widely used in optical communication and related broadband wireless access network areas. The success of microwave-photonics in telecommunications intrigued us to explore the possibility of combining microwave and photonics for sensing applications.

17.2 Novel Concept AND Modeling of OCMI

The essence of OCMI is to read an optical interferometer in microwave domain as described in Figure 17-1. The light from an optical broadband source is intensity modulated by a microwave signal, and sent into an optical interferometer whose output is recorded by a high-speed photodetector. The optical detection is synchronized at the modulation frequency.

Simplified Condition: For simplicity we assume two-beam interference with equal amplitude. The complex amplitudes of the two intensity-modulated optical waves are given by

$$\begin{aligned} E_1(t, L_{O1}) &= A\sqrt{1 + M\cos\left[\Omega\left(t + \frac{W + L_{O1}}{c}\right)\right]} \cdot \exp\left[-j\omega\left(t + \frac{L_{O1}}{c}\right)\right] \\ E_2(t, L_{O2}) &= A\sqrt{1 + M\cos\left[\Omega\left(t + \frac{W + L_{O2}}{c}\right)\right]} \cdot \exp\left[-j\omega\left(t + \frac{L_{O2}}{c}\right)\right] \end{aligned} \tag{17-1}$$

where t is the time; A and M are the amplitudes of the optical carrier and microwave envelope, respectively; ω and Ω are the optical and microwave angular frequencies, respectively; c is the speed of light in vacuum; W is the electrical length of the common microwave path; L_{O1} and L_{O2} are the two optical path lengths, respectively. The power of the superimposed optical waves is thus given by

$$|E|^2 = |E_1 + E_2|^2 = 2A^2 + 2A^2 M \cos\left[\Omega\frac{L_{O1} - L_{O2}}{2c}\right]\cos\left[\Omega\left(t + \frac{2W + L_{O1} + L_{O2}}{2c}\right)\right]$$
$$+2A^2\sqrt{\left\{1 + M\cos\left[\Omega\left(t + \frac{W + L_{O1}}{c}\right)\right]\right\}\left\{1 + M\cos\left[\Omega\left(t + \frac{W + L_{O2}}{c}\right)\right]\right\}}\cdot\int_{\omega_{min}}^{\omega_{max}}\cos\left(\omega\frac{L_{O1} - L_{O2}}{c}\right)d\omega$$

Microwave term

Optical term

(17-2)

where ω_{min} and ω_{max} are the minimum and maximum frequencies of the light source, respectively.

The detected signal given in Eq. (17-2) includes three terms: the DC, microwave and optical terms. When the $OPD = L_{O1} - L_{O2}$ is sufficiently larger than the coherence length of the optical source, the integral term of the optical contribution approaches zero. The synchronized detection at the microwave frequency eliminates the DC term to provide the amplitude and phase of the microwave signal in Eq. (17-2). By scanning the frequency, the microwave amplitude and phase spectra can be acquired as shown in Figure 17-1 (a) and (b). The microwave amplitude spectrum (i.e., microwave interferogram) can be analyzed to determine the OPD and/or its changes for the purpose of sensing. In addition, the microwave phase is a function of the total length (i.e., the summation of the electric and optical lengths) between the microwave source and detector. As shown in Figure 17-1(c), the Fourier transform of the complex microwave spectrum provides the propagation delays of the two paths, which can be used to determine the location of the interferometer.

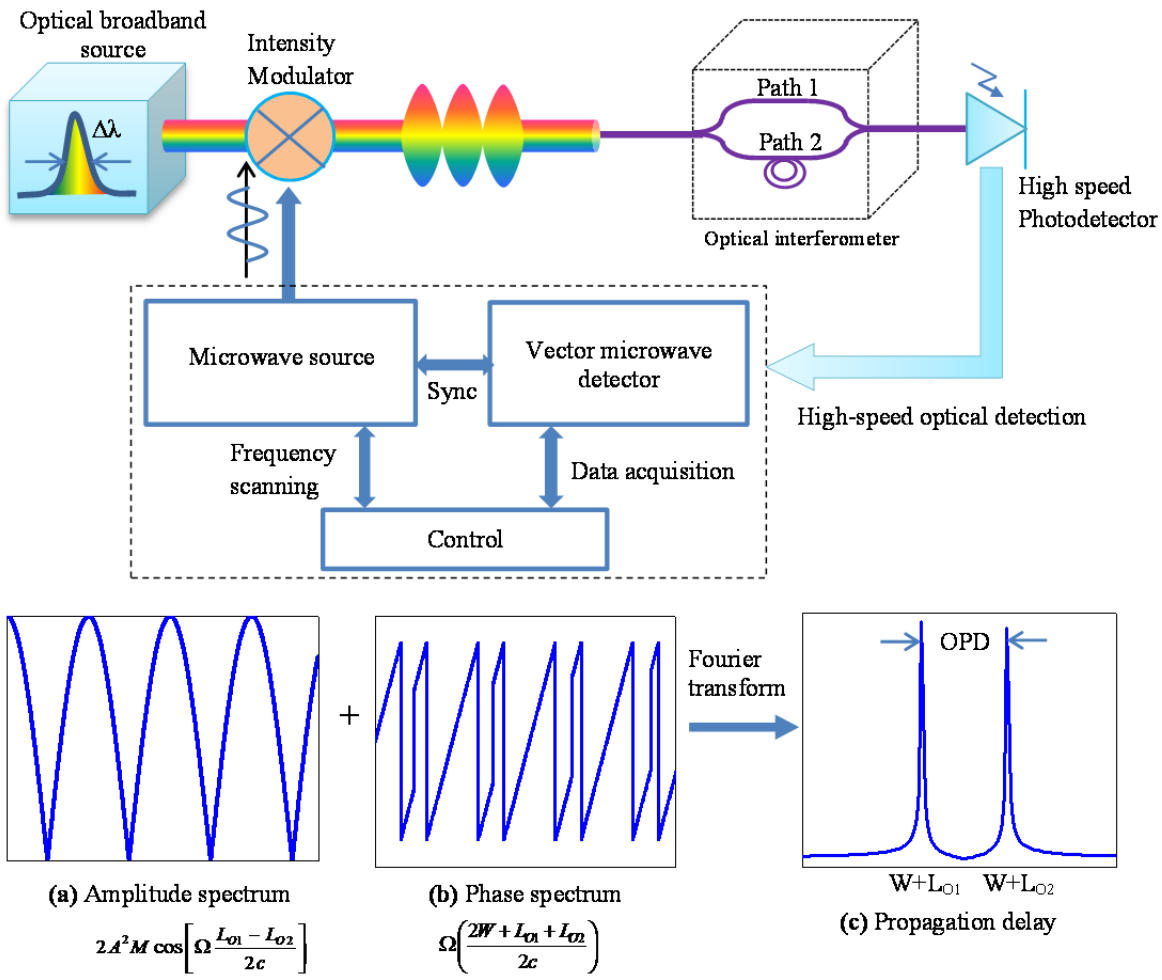

Figure 17-1. Conceptual illustration of the optical carrier based microwave interferometry. The light from an optical broadband source is intensity modulated by a microwave signal, and sent into an optical interferometer whose output is recorded by a high-speed photodetector. The optical detection is synchronized at the modulation frequency. By scanning the frequency, the microwave amplitude spectrum (a) and phase spectrum (b) are acquired. The Fourier transform of the microwave complex spectrum shows the propagation delays of the two paths (c).

General Condition: The modeling of OCMI under general condition is shown as follows:

Assume a polarized optical wave given by:

$$\begin{aligned}\vec{E}_o &= E_o^x \vec{a}_x + E_o^y \vec{a}_y \\ &= A^x \exp\left\{-j\left[\omega t + \varphi^x\right]\right\}\vec{a}_x + A^y \exp\left\{-j\left[\omega t + \varphi^y\right]\right\}\vec{a}_y\end{aligned} \tag{17-3}$$

where, t is the time; E_o^x and E_o^y are electric fields in the x and y directions, respectively; A^x and A^y are the amplitudes and φ^x and φ^y are the phases of the corresponding electric fields, respectively; ω is the angular optical frequency; $\vec{a}_x$ and $\vec{a}_y$ are the unit vectors along x and y directions, respectively.

The microwave signal used to modulate the optical wave is given by:

$$s(t) = M\cos\left(\Omega t + \phi\right) \tag{17-4}$$

where M is the amplitude, Ω is the angular frequency, and ϕ is the phase.

The electric field of the light wave modulated by the microwave becomes:

$$\vec{E} = m^x(t)E_o^x\vec{a}_x + m^y(t)E_o^y\vec{a}_y \tag{17-5}$$

where $m^x(t)$ and $m^y(t)$ are the amplitude modulation terms, given by

$$\begin{aligned}m^x(t) &= \sqrt{1 + h^x s(t)} = \sqrt{1 + h^x M\cos\left(\Omega t + \phi\right)} \\ m^y(t) &= \sqrt{1 + h^y s(t)} = \sqrt{1 + h^y M\cos\left(\Omega t + \phi\right)}\end{aligned} \tag{17-6}$$

where h^x and h^y are the modulation index in the x and y direction, respectively. Note that the microwave modulations may be different in the x and y directions.

The microwave modulated light is split into two optical paths. These two light waves propagate through different paths (z_1 and z_2), excite different optical modes, experience different

polarization evolutions (φ^x and φ^y), and eventually superimpose to generate the interference signal.

The complex electric field amplitudes of the two microwave-modulated light waves propagating in the i-*th* mode are given by

$$\begin{aligned}\vec{E}_{1,i}(t,z_1) &= E_{1,i}^x(t,z_1)\vec{a}_x + E_{1,i}^y(t,z_1)\vec{a}_y \\ &= m_{1,i}^x(t,z_1)E_{o1,i}^x(t,z_1)\vec{a}_x + m_{1,i}^y(t,z_1)E_{o1,i}^y(t,z_1)\vec{a}_y \\ \vec{E}_{2,i}(t,z_2) &= E_{2,i}^x(t,z_2)\vec{a}_x + E_{2,i}^y(t,z_2)\vec{a}_y \\ &= m_{2,i}^x(t,z_2)E_{o2,i}^x(t,z_2)\vec{a}_x + m_{2,i}^y(t,z_2)E_{o2,i}^y(t,z_2)\vec{a}_y\end{aligned} \tag{17-7}$$

Note that in Equation (17-7), both the optical and microwave components are functions of their corresponding optical path lengths.

The optical components (i.e., electric fields of the *i-th* optical mode in the *x* and *y* directions) in Equation (17-7) are given by

$$\begin{aligned}E_{o1,i}^x(t,z_1) &= A_{1,i}^x \exp\left\{-j\left[\omega\left(t+\frac{z_1 n_{eff,i}}{c}\right)+\varphi_{1,i}^x\right]\right\} \\ E_{o1,i}^y(t,z_1) &= A_{1,i}^y \exp\left\{-j\left[\omega\left(t+\frac{z_1 n_{eff,i}}{c}\right)+\varphi_{1,i}^y\right]\right\} \\ E_{o2,i}^x(t,z_2) &= A_{2,i}^x \exp\left\{-j\left[\omega\left(t+\frac{z_2 n_{eff,i}}{c}\right)+\varphi_{2,i}^x\right]\right\} \\ E_{o2,i}^y(t,z_2) &= A_{2,i}^y \exp\left\{-j\left[\omega\left(t+\frac{z_2 n_{eff,i}}{c}\right)+\varphi_{2,i}^y\right]\right\}\end{aligned} \tag{17-8}$$

where $A_{1,i}^x$, $A_{1,i}^y$, $A_{2,i}^x$, $A_{2,i}^y$ are the electric field amplitudes of the optical waves; c is the speed of light in vacuum; z_1 and z_2 are the lengths of the two optical paths, respectively; $n_{eff,i}$ is the

effective refractive index of the *i-th* optical mode; $\varphi_{1,i}^{x}$, $\varphi_{1,i}^{y}$, $\varphi_{2,i}^{x}$, $\varphi_{2,i}^{y}$ are the polarization phase terms.

The microwave amplitude modulation terms in Equation (17-7) are

$$
\begin{aligned}
m_{1,i}^{x}(t,z_1) &= \sqrt{1+h^{x}M\cos\left[\Omega\left(t+\frac{W}{c}+\frac{z_1 n_{eff,i}}{c}\right)+\frac{\Omega}{\omega}\varphi_{1,i}^{x}\right]} \approx \sqrt{1+h^{x}M\cos\left[\Omega\left(t+\frac{W}{c}+\frac{z_1 n_{eff,i}}{c}\right)\right]} \\
m_{1,i}^{y}(t,z_1) &= \sqrt{1+h^{y}M\cos\left[\Omega\left(t+\frac{W}{c}+\frac{z_1 n_{eff,i}}{c}\right)+\frac{\Omega}{\omega}\varphi_{1,i}^{y}\right]} \approx \sqrt{1+h^{y}M\cos\left[\Omega\left(t+\frac{W}{c}+\frac{z_1 n_{eff,i}}{c}\right)\right]} \\
m_{2,i}^{x}(t,z_2) &= \sqrt{1+h^{x}M\cos\left[\Omega\left(t+\frac{W}{c}+\frac{z_2 n_{eff,i}}{c}\right)+\frac{\Omega}{\omega}\varphi_{2,i}^{x}\right]} \approx \sqrt{1+h^{x}M\cos\left[\Omega\left(t+\frac{W}{c}+\frac{z_2 n_{eff,i}}{c}\right)\right]} \\
m_{2,i}^{y}(t,z_2) &= \sqrt{1+h^{y}M\cos\left[\Omega\left(t+\frac{W}{c}+\frac{z_2 n_{eff,i}}{c}\right)+\frac{\Omega}{\omega}\varphi_{2,i}^{y}\right]} \approx \sqrt{1+h^{y}M\cos\left[\Omega\left(t+\frac{W}{c}+\frac{z_2 n_{eff,i}}{c}\right)\right]}
\end{aligned}
\tag{17-9}
$$

where the microwave envelopes include two delay terms. The first is the delay associated with the common electrical length (W) of microwave system and this delay is the same for all the paths. The second delay term is the contributions from the optical propagation delays along the different optical paths. It is interesting to notice that the polarization phase contributions are reduced by a factor of ω/Ω, becoming negligible because ω is at least 5 orders magnitude larger than Ω. As such, the variations in optical polarization have very little influence on the microwave signals.

Assume that the optical source has a spectrum width from ω_{min} and ω_{max}, the total optical power of the superimposed optical waves of all modes is thus given by

$$\left|\vec{E}_{total}\right|^2 = \left|E^x_{total}\right|^2 + \left|E^y_{total}\right|^2$$
$$= \int_{\omega_{\min}}^{\omega_{\max}} \left|\sum_{i=1}^{N}\left(E^x_{1,i} + E^x_{2,i}\right)\right|^2 d\omega + \int_{\omega_{\min}}^{\omega_{\max}} \left|\sum_{i=1}^{N}\left(E^y_{1,i} + E^y_{2,i}\right)\right|^2 d\omega \tag{17-10}$$

where N is the total number of optical modes.

The total optical power in *x* direction can be further derived as follow,

$$\left|E^x_{total}\right|^2 = \sum_{i=1}^{N}\left(E^x_{1,i}E^{x*}_{1,i}\right) + \sum_{i=1}^{N}\left(E^x_{2,i}E^{x*}_{2,i}\right) + \int_{\omega_{\min}}^{\omega_{\max}}\left[\sum_{i=1}^{N}\left(E^x_{1,i}E^{x*}_{2,i}\right) + \sum_{i=1}^{N}\left(E^{x*}_{1,i}E^x_{2,i}\right)\right]d\omega \tag{17-11}$$

where the first two terms are the self-products and the last two terms are the cross-products.

Let's first examine the cross-products in Equation (17-11)

$$\int_{\omega_{\min}}^{\omega_{\max}}\left[\sum_{i=1}^{N}\left(E^x_{1,i}E^{x*}_{2,i}\right) + \sum_{i=1}^{N}\left(E^{x*}_{1,i}E^x_{2,i}\right)\right]d\omega$$
$$= \sum_{i=1}^{N}\left\{m^x_{1,i}A^x_{1,i}m^x_{2,i}A^x_{2,i}\int_{\omega_{\min}}^{\omega_{\max}}\left\{2\cos\left[\frac{\omega}{c}(z_1 - z_2)n_{eff,i} + \left(\varphi^x_{1,i} - \varphi^x_{2,i}\right)\right]\right\}d\omega\right\} \tag{17-12}$$

It is interesting to notice that the cross-product terms is the optical interference signal similar to a conventional all-optical interferometer. In the OCMI, the optical path difference (OPD) is chosen to be sufficiently larger than the coherence length of the optical source, i.e., $(z_1 - z_2)n_{eff,i} >> \frac{2\pi c}{\omega_{\max} - \omega_{\min}}$. As a result, the integral term in Equation (17-12) approaches zero. The optical variations (e.g., variations in polarization states and modal interferences) commonly seen in an all-optical interferometer have much reduced influences on the OMCI. In our experimental OCMI system, we used a light source with a spectral width of 50 nm at the center wavelength of about 1550 nm, whose coherence length was about 48 μm. A typical OCMI has

an OPD of a few centimeters that is much larger than the coherence length of a broadband light source.

Let's examine the self-product terms in Equation (17-11)

$$\begin{aligned}
&\sum_{i=1}^{N}\left(E_{1,i}^{x}E_{1,i}^{x*}\right)+\sum_{i=1}^{N}\left(E_{2,i}^{x}E_{2,i}^{x*}\right)\\
&=\sum_{i=1}^{N}\left[\left(A_{1,i}^{x}\right)^{2}+\left(A_{2,i}^{x}\right)^{2}\right]+\sum_{i=1}^{N}h^{x}M\left\{\left(A_{1,i}^{x}\right)^{2}\cos\left[\Omega\left(t+\frac{W+z_1n_{eff,i}}{c}\right)\right]+\left(A_{2,i}^{x}\right)^{2}\cos\left[\Omega\left(t+\frac{W+z_2n_{eff,i}}{c}\right)\right]\right\}\\
&=\sum_{i=1}^{N}\left[\left(A_{1,i}^{x}\right)^{2}+\left(A_{2,i}^{x}\right)^{2}\right]+A^{x}\cos\left(\Omega t+\Phi^{x}\right)
\end{aligned} \tag{17-13}$$

Equation (17-13) is easy to calculate using the Phasor method. As such, we have

$$A^{x}=\sqrt{\sum_{i,j}^{N}A_{eff,i}^{x}A_{eff,j}^{x}\cos\left(\phi_{eff,i}^{x}-\phi_{eff,j}^{x}\right)} \tag{17-14}$$

$$\Phi^{x}=\arctan\left[\frac{\sum_{i}^{N}A_{eff,i}^{x}\sin\left(\phi_{eff,i}^{x}\right)}{\sum_{i}^{N}A_{eff,i}^{x}\cos\left(\phi_{eff,i}^{x}\right)}\right],\qquad \Phi^{x}\in\{-\pi,\ \pi\} \tag{17-15}$$

and

$$A_{eff,i}^{x}=h^{x}M\sqrt{\left(A_{1,i}^{x}\right)^{4}+\left(A_{2,i}^{x}\right)^{4}+2\left(A_{1,i}^{x}A_{2,i}^{x}\right)^{2}\cos\left[\Omega\frac{n_{eff,i}^{x}}{c}\left(z_1-z_2\right)\right]} \tag{17-16}$$

$$\phi_{eff,i}^{x}=\arctan\left\{\frac{\left(A_{1,i}^{x}\right)^{2}\sin\left[\Omega\left(\frac{W}{c}+\frac{z_1n_{eff,i}}{c}\right)\right]+\left(A_{2,i}^{x}\right)^{2}\sin\left[\Omega\left(\frac{W}{c}+\frac{z_2n_{eff,i}}{c}\right)\right]}{\left(A_{1,i}^{x}\right)^{2}\cos\left[\Omega\left(\frac{W}{c}+\frac{z_1n_{eff,i}}{c}\right)\right]+\left(A_{2,i}^{x}\right)^{2}\cos\left[\Omega\left(\frac{W}{c}+\frac{z_2n_{eff,i}}{c}\right)\right]}\right\},\qquad \phi_{eff,i}^{x}\in\{-\pi,\ \pi\} \tag{17-17}$$

Similarly, the total optical power in *y* direction is found to be

$$\left|E^{y}_{total}\right|^2 = \sum_{i=1}^{N}\left[\left(A^{y}_{1,i}\right)^2 + \left(A^{y}_{2,i}\right)^2\right] + A^{y}\cos\left(\Omega t + \Phi^{y}\right) \tag{17-18}$$

where

$$A^{y} = \sqrt{\sum_{i,j}^{N} A^{y}_{eff,i} A^{y}_{eff,j} \cos\left(\phi^{y}_{eff,i} - \phi^{y}_{eff,j}\right)} \tag{17-19}$$

$$\Phi^{y} = \arctan\left[\frac{\sum_{i}^{N} A^{y}_{eff,i}\sin\left(\phi^{y}_{eff,i}\right)}{\sum_{i}^{N} A^{y}_{eff,i}\cos\left(\phi^{y}_{eff,i}\right)}\right], \qquad \Phi^{y} \in \{-\pi,\ \pi\} \tag{17-20}$$

$$A^{y}_{eff,i} = h^{y} M \sqrt{\left(A^{y}_{1,i}\right)^4 + \left(A^{y}_{2,i}\right)^4 + 2\left(A^{y}_{1,i}A^{y}_{2,i}\right)^2 \cos\left[\Omega\frac{n^{y}_{eff,i}}{c}\left(z_1 - z_2\right)\right]} \tag{17-21}$$

$$\phi^{y}_{eff,i} = \arctan\left\{\frac{\left(A^{y}_{1,i}\right)^2 \sin\left[\Omega\left(\frac{W}{c} + \frac{z_1 n_{eff,i}}{c}\right)\right] + \left(A^{y}_{2,i}\right)^2 \sin\left[\Omega\left(\frac{W}{c} + \frac{z_2 n_{eff,i}}{c}\right)\right]}{\left(A^{y}_{1,i}\right)^2 \cos\left[\Omega\left(\frac{W}{c} + \frac{z_1 n_{eff,i}}{c}\right)\right] + \left(A^{y}_{2,i}\right)^2 \cos\left[\Omega\left(\frac{W}{c} + \frac{z_2 n_{eff,i}}{c}\right)\right]}\right\}, \qquad \phi^{y}_{eff,i} \in \{-\pi,\ \pi\} \tag{17-22}$$

The OCMI uses synchronized detection to eliminate the DC term in Equation (17-13) and (17-18) and record only the amplitude and phase of the microwave signal at the microwave frequency Ω. As a result, the total signal after optoelectronic conversion (with an optical gain of *g*) and synchronized microwave detection is found by summing the powers in *x* and *y* directions, given by

$$\begin{aligned} S &= g\left[A^x \cos\left(\Omega t + \Phi^x\right) + A^y \cos\left(\Omega t + \Phi^y\right)\right] \\ &= A\cos\left(\Omega t + \Phi\right) \end{aligned} \tag{17-23}$$

where

$$A = g\sqrt{\left(A^x\right)^2 + \left(A^y\right)^2 + 2A^x A^y \cos\left(\Phi^x - \Phi^y\right)} \tag{17-24}$$

$$\Phi = \arctan\left[\frac{A^x \sin\left(\Phi^x\right) + A^y \sin\left(\Phi^y\right)}{A^x \cos\left(\Phi^x\right) + A^y \cos\left(\Phi^y\right)}\right], \qquad \Phi \in \{-\pi,\ \pi\} \tag{17-25}$$

17.3 Simulations and Results

The Microwave interferogram – the amplitude and phase spectra: Numerical simulations were performed to understand Equation (17-23) and study the amplitude and phase of the signal as functions of the optical parameters.

First, let's examine the case of a singlemode fiber (SMF) based OCMI. Assume the fiber used is Corning SMF-28e with the effective refractive index of the core of n_{eff} = 1.468 according to the datasheet from the manufacturer. The optical power is equally split into the two paths. The lengths of the two optical paths are z_1 = 0.1 m and z_2 = 0.2 m, respectively. The common electric length is W = 1 m. The two polarization states are evenly excited. Based on the assumption, the microwave signal in Equation (5-23) becomes

$$\begin{aligned} S &= 2A^2 gM \cos\left[\Omega\frac{z_1 - z_2}{2c} n_{eff}\right]\cos\left[\Omega\left(t + \frac{2W + \left(z_1 + z_2\right)n_{eff}}{2c}\right)\right] \\ &= 2A^2 gM \cos\left[\Omega\frac{OPD}{2c}\right]\cos\left[\Omega\left(t + \frac{2W + \left(z_1 + z_2\right)n_{eff}}{2c}\right)\right] \end{aligned} \tag{17-26}$$

where $OPD = |L_{01} - L_{02}| = |(z_1 - z_2) n_{eff}|$. L_{o1} *and* L_{o2} are the optical path lengths of the two optical paths, respectively.

Equation (17-26) indicates that the amplitude of the signal varies as a sinusoidal function of the microwave frequency and OPD, and the phase of the microwave signal is a function of the summation of the electric and optical lengths. Figure 17-2 shows the simulated microwave amplitude and phase spectra of the OCMI in the frequency range of 0 – 6 GHz. The free spectral range (FSR) of the spectrum is a function of the OPD, given by

$$FSR = \frac{c}{OPD}$$

Similar to an optical interference spectrum, the microwave amplitude spectrum in the OCMI can be used to find the optical path difference of an interferometer. It can also be used to find the change in OPD based on the interference fringe shift.

By applying complex Fourier transform of the signal shown in Equation (17-22), one can find the propagation delays of the microwave signal. As shown in Figure 17-2 (c), the common electric length (W) and the two optical path lengths can be clearly identified, allowing the OCMI to locate the position of the interferometer and enabling its unique capability of distributed sensing.

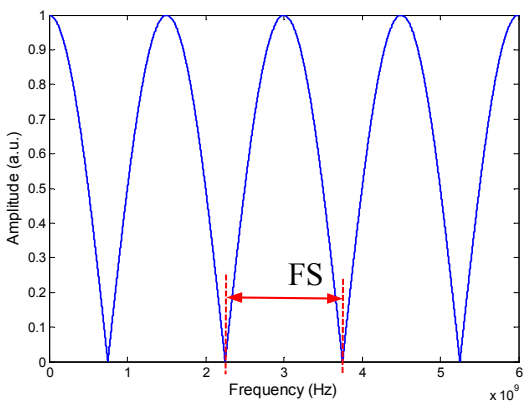

(a) Amplitude spectrum

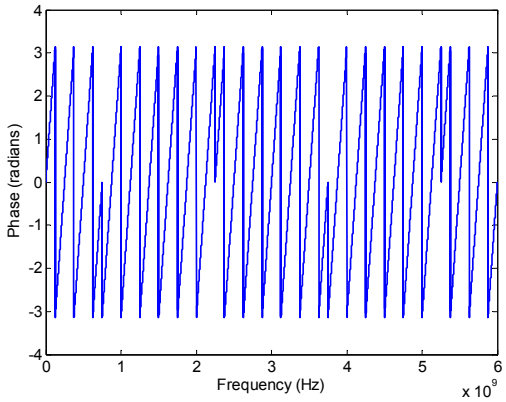

(b) Phase spectrum

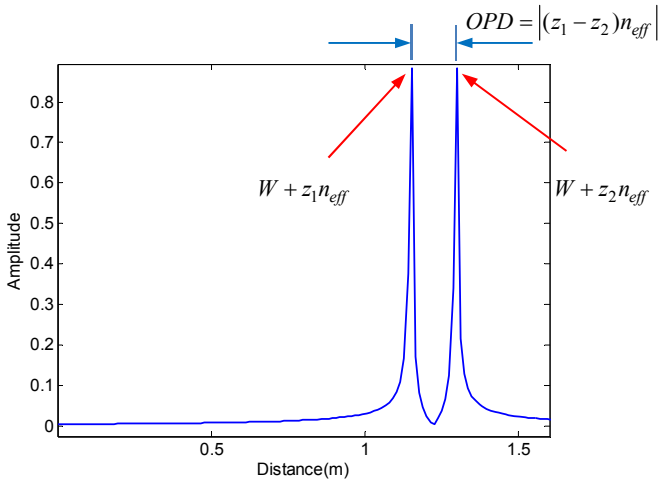

(c) Delay diagram

Figure 17-2. Simulation of an OCMI implemented using single-mode fibers. The optical power is equally split into the two paths. The lengths of the two optical paths are z_1 = 0.1 m and z_2 = 0.2 m, respectively. The common electric length is W = 1 m. (a) Amplitude spectrum (i.e., interferogram), (b) Phase spectrum, (c) Delay diagram obtained by applying complex Fourier transform on the amplitude and phase spectra.

The multimodal influences: The influence of multiple optical modes on the OCMI signal is clearly shown in Equations (17-14) and (17-19), where the effective refractive indices of the optical modes are different. In addition, the multimodal influences also depend on the lengths of propagation (z_1 and z_2). In essence, the multimodal dispersion generates phase differences among the different optical modes and reduces the fringe visibility of the interferogram.

In reality, the number of modes excited inside the fiber strongly depends on how the light is coupled into the fiber. In addition, the optical power usually is not evenly distributed among the various modes. The detailed analysis is quite involved. Here for the purposes of gaining a qualitative understanding of the multimodal influences, we simplify the case by assuming that all optical modes are evenly excited and the power is evenly distributed among them.

The number of modes supported in a multimode optical fiber can be estimated by $N_m \approx \frac{V^2}{2}$ for a step-index fiber and $N_m \approx \frac{V^2}{4}$ for a graded-index fiber. V is the normalized frequency, given by $V = \frac{2\pi a}{\lambda}\sqrt{n_{core}{}^2 - n_{clad}{}^2}$. The effective refractive index n_{eff} of a guided mode in a multimode fiber is bounded between the core and cladding refractive indices. That is $n_{core} < n_{eff} < n_{clad}$, where n_{core} and n_{clad} are the refractive index of the core and cladding, respectively. The actual effective index range ($\delta n_{eff} = n_{eff,\max} - n_{eff,\min}$) of the multimode fiber can be estimated based on the group delay of the optical fiber, given by

$$\delta t_{SI} = \frac{L\delta n_{eff,SI}}{c} \approx \frac{L\Delta}{c} \cdot \frac{n_{core}^2}{n_{clad}}, \text{ for a step-index multimode fiber,} \qquad (17\text{-}27)$$

and

$$\delta t_{GI} = \frac{L\delta n_{eff,GI}}{c} \approx \frac{L}{8c}\Delta^2 \cdot n_{core}$$, for a graded-index multimode fiber (17-28)

where $\Delta = \left(n_{core} - n_{clad}\right)/n_{core}$ is the index difference between the core and cladding, $\Delta << 1$; L is the length of the fiber. The ranges of the effective indices of the modes supported in multimode fibers are thus found to be

$$\delta n_{eff,SI} \approx \Delta \cdot n_{core}$$ for a step-index multimode fiber, (17-29)

and

$$\Delta n_{eff,GI} \approx \Delta^2 \cdot n_{core}/8$$ for a graded-index multimode fiber. (17-30)

Simulations were performed to study the multimodal influence on OCMIs and its dependence on the fiber type and length. Figure 17-3 shows the simulated interferograms of an OCMI implemented using a step-index multimode fiber. The step-index multimode fiber had core and cladding diameters of 62.5 and 12.5μm, respectively. The refractive index of the core is n_{core} = 1.488, and the index difference is Δ = 0.01. Based on Equation (17-29), the maximum effective refractive index difference is found to be $\delta n_{eff,SI} = 0.01 n_{core}$. The lengths of the two optical beams varied but their difference was kept the same ($z_1 - z_2$ = 0.2 m). It is noticed that the contrast of the interferogram reduces as the optical length increases, indicating that the multimodal influence is accumulative along the fiber length. In addition, the contrast reduction becomes more noticeable in the high frequency region. The peak-to-peak value at 3 GHz and 10 m fiber length reduces by half compared with that at 1 m fiber length. It is anticipated that the fringes may completely disappear when the length exceeds a certain value.

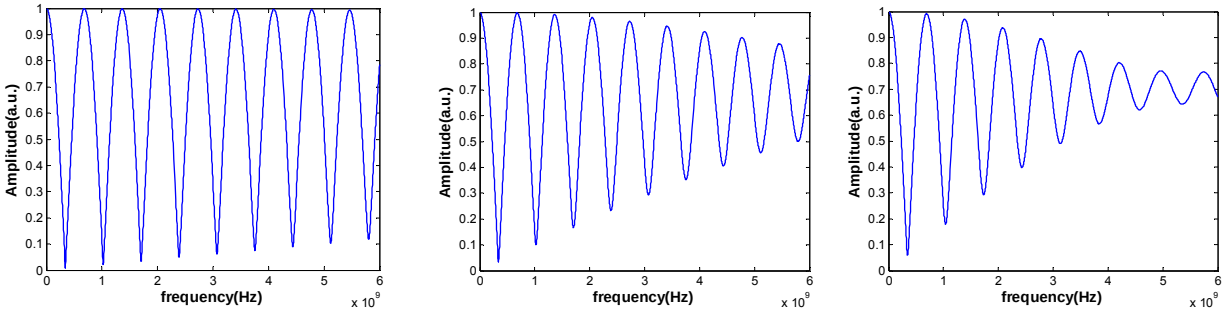

(a) z_1 = 1 m, z_2 = 1.3 (b) z_1 = 5 m, z_2 = 5.3 (c) z_1 = 10 m,

Figure 17-3. Simulation of an OCMI implemented using step-index multimode fibers. All optical modes are equally excited. The core and cladding diameters of the fiber are 62.5 and 125 μm, respectively. The refractive index of the core is n_{core} = 1.488, and the index difference is Δ = 0.01. The common electric length is W = 1. (a) Amplitude spectrum when z_1=1 m and z_2=1.3 m. (b) Amplitude spectrum when z_1=5 m and z_2=5.3 m. (c) Amplitude spectrum when z_1=10 m and z_2=10.3 m.

Figure 17-4 shows the simulated interferograms of an OCMI implemented using a graded-index multimode fiber with core and cladding diameters of 62.5 and 12.5 μm, respectively. The common electric length is W = 1. The refractive index of the core is n_{core} = 1.488, and the index difference is Δ = 0.02. Based on Equation (5-30), the maximum effective refractive index difference is found to be $\delta n_{eff,GI} = 7.4\times10^{-5} n_{core}$ which is significantly smaller than that of a step-index multimode fiber. As shown in Figure 5-4, the contrast of the interferograms reduces slowly as the fiber length increases. The peak-to-peak value around 3 GHz reduces by half after propagating through 1 km of graded-index fiber. In comparison, it only takes 10 m step-index multimode fiber to decrease by half from its original peak-to-peak value.

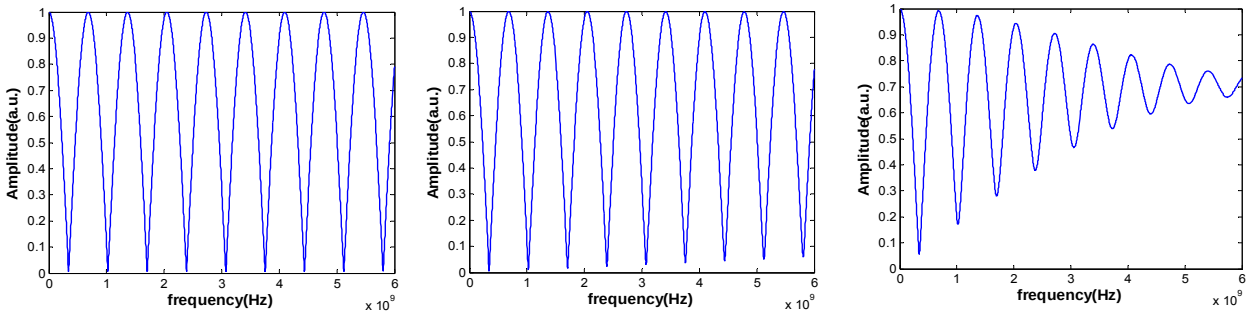

(a) z_1=10 m, z_2=10.3 (b) z_1=100 m, (c) z_1=1000 m,

Figure 17-4. Simulation of an OCMI implemented using graded-index multimode fibers. All optical modes are equally excited. The core and cladding diameters of the fiber are 62.5 and 125 μm, respectively. The refractive index of the core is n_{core} = 1.488, and the index difference is $\Delta = 0.02$. The common electric length is $W = 1$. (a) Amplitude spectrum when z_1=10 m and z_2=10.3 m. (b) Amplitude spectrum when z_1=100 m and z_2=100.3 m. (c) Amplitude spectrum when z_1=1000 m and z_2=1,000.3 m.

The simulation results indicate that OCMI can be implemented using multimode fibers. However, the modal dispersions will lower the quality of the interferogram by decreasing the contrast of the fringes. The larger the modal dispersion is, the lower the fringe contrast becomes. The dispersion effect is also accumulative along the fiber length. The contrast decreases as the length of the multimode fiber increases.

17.4 Typical System Implementation

While there are many ways to implement the OCMI concept, Figure 17-5 illustrates an example system configuration where a microwave vector network analyzer (VNA) is used as the microwave source and signal detector. A broadband light source with the bandwidth of 50 nm is intensity modulated using an electro-optic modulator (EOM) driven by the microwave signal

from the Port 1 of a VNA (HP 8753es). The VNA output is DC-biased and amplified to achieve a high modulation index. The modulated light is then sent into an FOI (or FOIs) whose outputs are detected by a high speed photodetector.

For a reflection type FOI (e.g., a Fabry-Perot or Michelson interferometer), a fiber circulator is used to route the input light into and the output signal out of the FOI (solid lines in Figure 17-5(b)). For a transmission type FOI (e.g., a Mach-Zhender interferometer), its output is directly connected to the photodetector (dashed lines in Figure 17-5(c)). An optional erbium doped fiber amplifier (EDFA) can be used for additional signal amplification. After DC-filtering and RF amplification, the photodetector output is connected to the Port 2 of the VNA, where the amplitude and phase of the signal are extracted. By sweeping the VNA frequency, the microwave spectrum of the interferometer is obtained.

Figure 17-5 only shows the main components that are required to construct a typical OCMI system. In practical applications, many supporting components may need to be added to the system for performance enhancement. These components may include RF amplifiers, RF filters, optical amplifiers, optical filters, DC bias filters, optical circulators, RF circulators, and transimpedance amplifiers. These components can be used to enhance the optical or RF signals at certain point of the microwave-photonic system while suppress the noises.

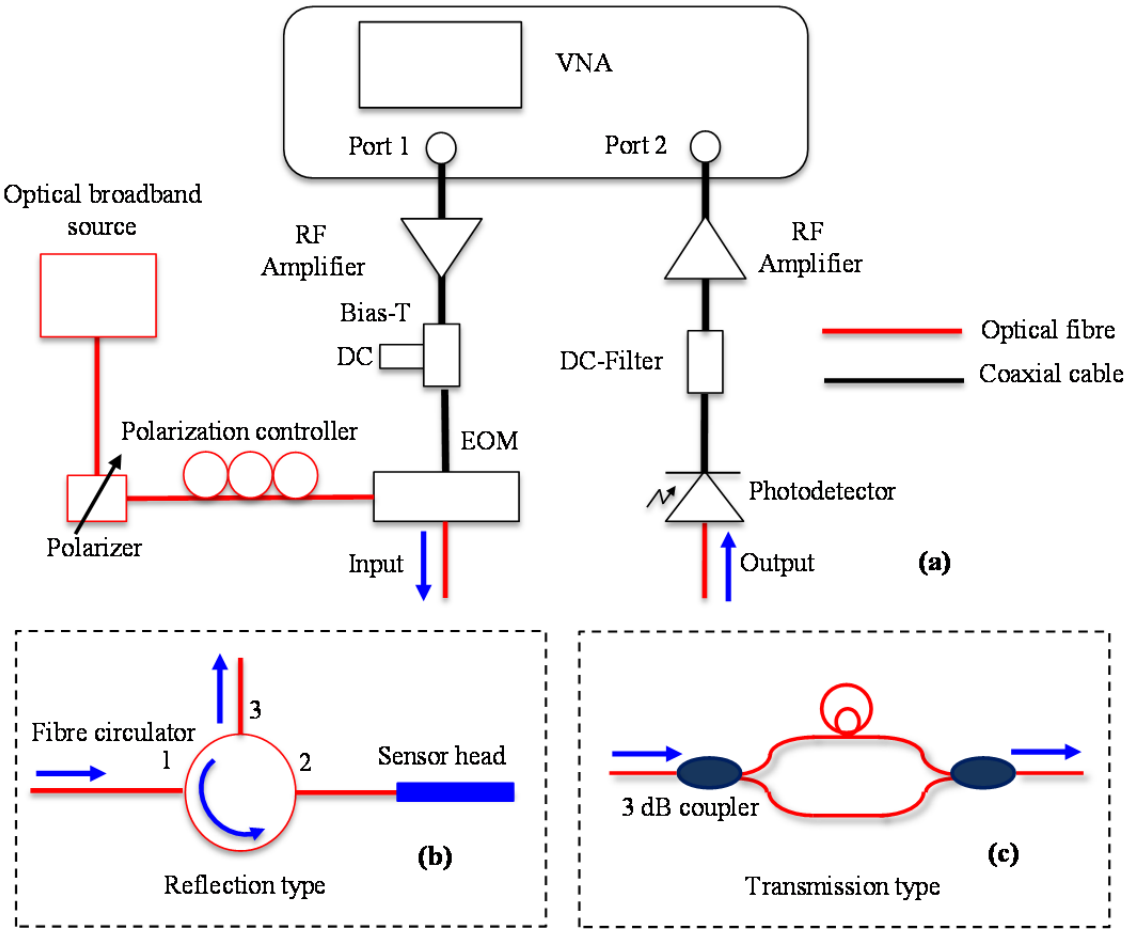

Figure 17-5. Schematic of the OCMI system used to support proof-of-concept experiments. A broadband light source (bandwidth ~50 nm) is intensity-modulated using an electro-optic modulator (EOM) driven by the microwave output (DC-biased and amplified) from Port 1 of a VNA (HP 8753es). The output from the FOI is detected by a photodetector whose signal, after DC-filtering and RF amplification, is recorded at Port 2 where the amplitude and phase of the signal are extracted. By sweeping the VNA frequency, the microwave spectrum of the interferometer is obtained (i.e., the S21 of the VNA). (a) For a reflection type FOI (e.g., Michelson or Fabry-Perot), a fiber circulator is used to route the optical input and output. (b) For a transmission type FOI (e.g., Mach-Zehnder), its output is directly connected to the photodetector.

18. Optical Carrier Microwave Interferometer: Prove the Concept

18.1 Introduction

Optical carrier microwave interferometer (OCMI) is a powerful concept that has the potential to provide the revolutionary solutions for many challenging sensor needs. The essence of OCMI is to read optical interferometers using microwave. As such, it combines the advantages from both optics and microwave. When used for sensing, it inherits the advantages of optical interferometry such as small size, light weight, low signal loss, remote operation and immunity to EMI. Meanwhile, by constructing the interference in microwave domain, the OCMI has many unique advantages that are unachievable by conventional optical interferometry, including:

1) High measurement resolution: OCMI uses coherent detection in which the modulation, detection and demodulation are all synchronized to the same microwave frequency. As a result, OCMI has a higher SNR comparing with the traditional all-optical interferometers that use DC detection. In addition, the measurement of distance change is based on tracking the spectral shift of the interferogram. As such, the measurement resolution is expected to be high.

2) Distributed sensing with spatial continuity and reconfigurable gauge length: Time-resolved reflections can be easily obtained by complex Fourier transform of the microwave signals with phase and amplitude information. Distributed sensing can be achieved with spatial continuity by taking consecutive measurement between two adjacent reflectors. In addition, the gauge length can be varied by taking measurement between two arbitrary reflectors.

3) Insensitivity to the types of optical waveguides. The differences in optics (e.g., dispersion and modal interference) have little influences on the microwave signal. As such, multimode waveguides (e.g., POFs) can be used to construct OCMI for distributed sensing.

4) Insensitivity to optical polarizations. In OCMI, the interference is a result of coherent superposition of the microwave envelops. As such, OCMI does not have the polarization fading issue commonly faced by all-optical interferometers.

5) Relieved fabrication requirements. In order to obtain a high-quality interference signal, the surface smoothness of the reflectors needs to be smaller than 1/20 of the wavelength. The wavelength of microwave is much larger than that of an optical wave. In a sense, currently available micromachining techniques can easily satisfy the precision requirements of OCMI.

To prove these advantages, we have conducted a number of experiments using various optical fibers including singlemode, multimode, uncladded, polymer and sapphire fibers. We will provide some examples in this Section to serve the proof-of-concept purposes. Other detailed experiments and results will be provided in the following sections.

18.1 OCMI Concept using Singlemode Fibers

In principle, the OCMI concept can be implemented in most types of FOIs. Two types of commonly-used FOIs are selected to demonstrate the concept. Figure 18-1 (a) shows a Mach-Zehnder FOI implemented using SMFs (Corning SMF-28e) with a length difference of 18.10 cm. Figure 18-1 (b) shows the microwave interferogram in the frequency range of 0 – 3.5 GHz. The fringes are clean with a visibility exceeding 45 dB. The free spectral range (FSR) was found to be 1.125 GHz. Based on Equation (17-2), the OPD was found to be 26.67 cm. Using the effective refractive index of the fiber core of 1.468, the length difference was calculated to be 18.16 cm, which agreed well with the value measured by the caliper. An optical fiber polarization controller was inserted in Path 1 to test the polarization dependence. As shown in

Figure 18-1 (c), the interferogram showed very little dependence on the polarization, with a maximum variation of 0.12 dB at the interference peak.

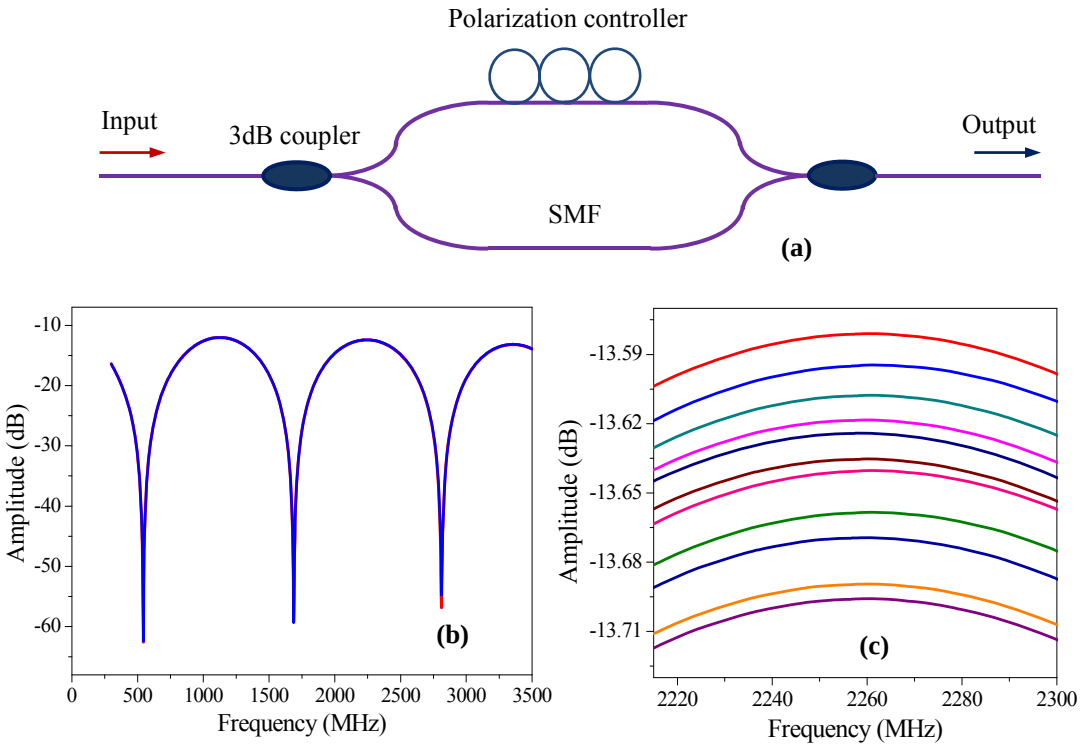

Figure 18-1. (a) Schematic of a Mach-Zehnder OCMI implemented using SMFs (Corning SMF28e). (b) Microwave interferogram of the Mach-Zehnder OCMI showing a visibility exceeding 45 dB. Using the effective refractive index of the fiber core of 1.468, the length difference was calculated to be 18.16 cm, which agreed well with the value (18.10 cm) measured by the caliper. (c) Variation of an interference peak at different polarization states. A maximum intensity variation of 0.12 dB was observed at all polarization states.

In addition to the high signal quality, large fringe visibility and easy implementation, the most significant advantages of the OCMI based singlemode fiber sensor is its polarization insensitivity. It has been well-known that singlemode fiber interferometers are sensitive the polarization variations during its deployment and applications. This is commonly referred to as

the polarization fading issue. That is the fringe visibility varied significantly as the polarization states of the two interfering arms change. When the two polarizations match each other, the fringe visibility becomes the highest. However, when the two polarizations are orthogonal, the visibility becomes lowest (zero). In real applications, it is very difficult to control the polarization state of the light propagating inside a single mode fiber. As a result, conventional single mode fiber based Mach-Zehnder or Michelson interferometers have been found very limited usages. The COMI concept effectively overcomes the polarization fading issue and therefore shall find many applications using the well-established fiber optic Mach-Zehnder and Michelson interferometers.

18.2 OCMI Concept using Multimode Fibers

In many applications multimode fibers are preferred because of their large numerical aperture and easy light coupling. Other situations may prefer multimode optical fibers such as polymer optical fibers and sapphire fibers because of the superior mechanical or thermal properties of these specialty fibers. For example, a polymer optical fiber is preferred in structural health monitoring because of its large core diameter and large axial strain capability. A sapphire optical fiber is preferred in high temperature applications because of its high melting point. Unfortunately, multimode optical fibers cannot be used to build interferometers due to their large modal dispersions. There are many optical modes inside a multimode fiber. These models have different propagation constants. As a result, the light traveling in a multimode fiber loses its coherence after traveling through a multimode fiber of a certain distance. On the other hand, we know that interferometers have very high sensitivity when used as sensors. A challenging

question is that can we build interferometers using multimode fibers? The OCMI concept may provide an answer for this challenging question.

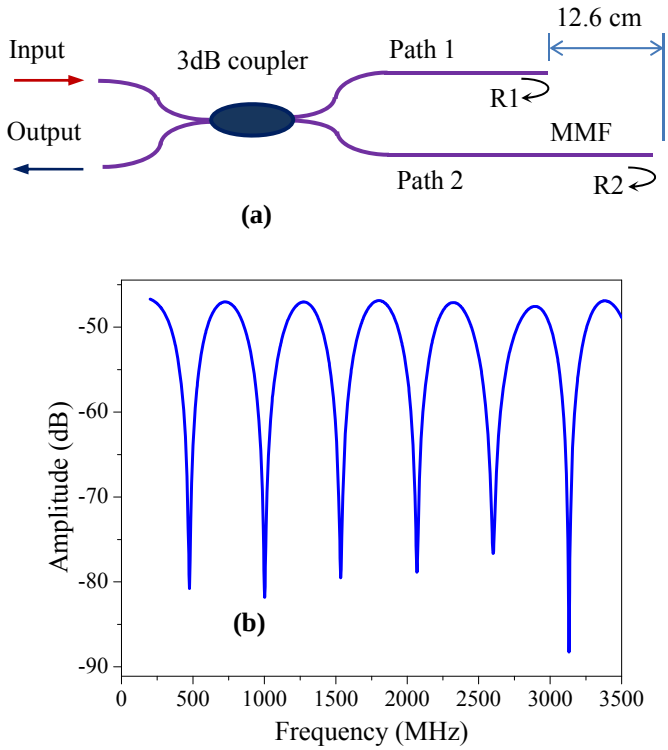

Figure 18-2. (a) Schematic of a Michelson OCMI implemented using graded index MMFs (Corning, InfiniCor-300). (b) Microwave interferogram of the Michelson OCMI, showing a visibility exceeding 40 dB and a FSR of 798 MHz. Using the fibre core effective index of 1.488 at 1550 nm, the path difference was found to be 12.61 cm, in excellent agreement with the value (12.40 cm) measured by the caliper.

The OCMI concept has been validated using a multimode fiber (MMF, Corning InfiniCor-300, with 50 and 125 μm in core and cladding diameter, respectively) Michelson interferometer as shown in Figure 18-2 (a). The acquired microwave interferogram (Figure 18-2 (b)) has an excellent quality with a visibility over 40 dB. The FSR is 798 MHz. Using the fiber core

effective index of 1.488 at 1550 nm, the path difference was found to be 12.61 cm, in excellent agreement with the value (12.40 cm) measured by the caliper. The experiment results prove that the OCMI concept is insensitive to multimodal influences and can be conveniently implemented using various MMFs.

18.3 Strain Measurement using a SMF Fabry-Perot OCMI

A SMF extrinsic Fabry-Perot interferometer (EFPI) OCMI was constructed as schematically shown in the inset of Figure 18-3 (b). The EFPI had a cavity length (i.e., the distance between the two reflectors) of about 2 m with both ends cleaved. The lead-in fiber was angle cleaved to eliminate its own reflection and connected to the EFPI sensor using a capillary tube. A high quality microwave interferogram was obtained, with fringe visibilities exceeding 40 dB and a FSR of about 40 MHz. The long interferometer was tested as a strain sensor. Figure 18-3 (a) shows the interference fringes at different applied axial strains. The fringe moved towards the low frequency regime as the strain increased, indicating the optical length of the interferometer increased correspondingly. Figure 18-3 (b) plots the frequency shift as a function of the applied strain at a step of 100 με. The frequency shift varied with the applied strain linearly with a slope of -2.37 kHz/με. This monotonic, linear relation clearly demonstrated the potential of using the OCMI for strain sensing.

One of the challenges in strain sensor development is that limited choice of gauge length. The OCMI has the advantages of flexible gauge length ranging from a few centimeters to several tens of meters. For example, in structural health monitoring, it is highly desired to have sensors

that can cover structural components of different dimensions. The OCMI shall provide an excellent solution for such demands.

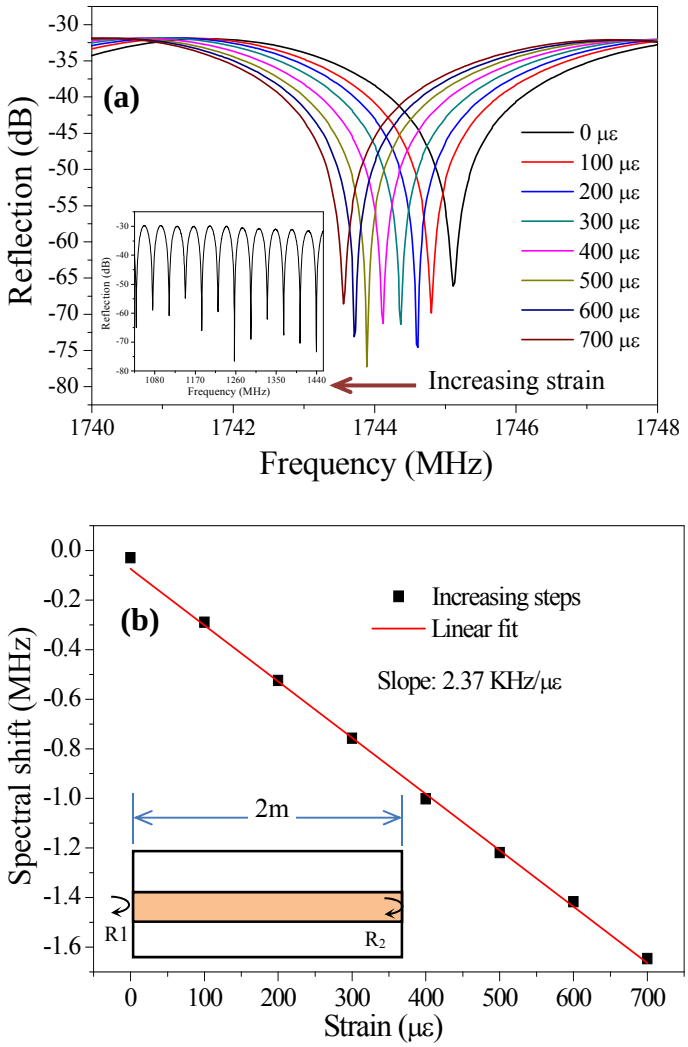

Figure 18-3. SMF extrinsic Fabry-Perot OCMI for strain sensing. (a) Zoom-in microwave interferograms under various applied axial strain (inset: interferogram observed in the frequency range of 1 - 1.5 GHz, (b) Spectral shift as a function of applied strain (inset: schematic of the Fabry-Perot interferometer with a length of 2 m).

18.4 Temperature measurement using a SMF Michelson OCMI

The OCMI concept has been validated for temperature sensing using a SMF based Michelson interferometer with a fiber length difference of 0.31 m. Figure 18-4 (a) shows one interference fringe valley at different temperatures from 50 to 900 °C at an increment of 50 °C. The fringe moved towards the low frequency regime as the temperature increased, indicating the optical length of the interferometer increased correspondingly. Figure 18-4(b) plots the frequency shift of the interference valley as a function of temperature. The frequency shift varied with temperature almost linearly with a slope of -35 kHz/°C. This monotonic, linear relation clearly demonstrated the capability of using the OCMI system for temperature sensing.

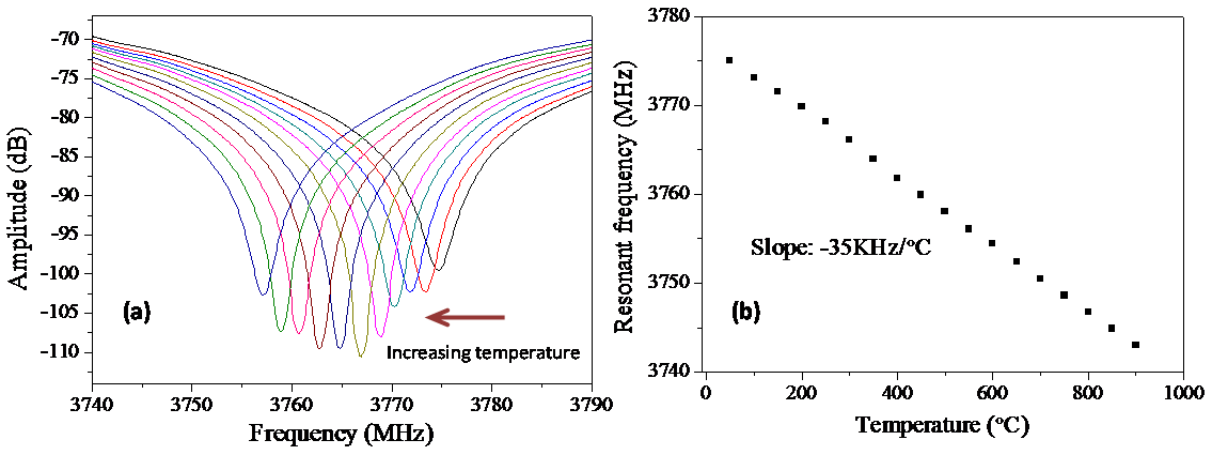

Figure 18-4. SMF Michelson OCMI for temperature sensing. (a) Zoom-in microwave interferograms at various temperatures from 50 to 900°C at an increment of 50°C. The interference fringe shifted towards low frequency region indicating the increases of the optical path difference as the temperature increased. (b) Spectral shift as a function of temperature. The slope shows a temperature sensitivity of -35 kHz/°C.

19. Optical Carrier Microwave Interferometer: Distributed Sensing

19.1 Introduction

In the past few decades, optical fibers have been widely used for various sensing applications due to their low loss, light weight, immunity to electromagnetic interference (EMI), and resistance to corrosion [1]. One of the most attractive features of optical fiber sensing is its capability of measurement of spatially distributed parameters. In general, optical fiber based distributed sensing can be implemented either by multiplexing a large number of discrete sensors to form a spatially-distributed measurement network or by sending a pulsed signal to probe the spatially-resolved information as a function of time-of-arrival.

In multiplexed sensing, or the so-called quasi-distributed sensing, many discrete sensors are cascaded in series along a single optical fiber. The signals of the sensors are unambiguously demodulated either in time or frequency domain. For example, fiber Bragg gratings (FBGs) have been cascaded along a single fiber for multiplexed sensing. The cascaded FBGs can have different Bragg wavelengths so that their spectral shifts can be unambiguously determined [2, 3]. Thousands of weakly reflecting FBGs can also be made of the same resonant wavelength and interrogated using either optical time domain reflectormetry (OTDR) [4] or optical frequency domain reflectometry (OFDR) [5]. In addition to FBGs, fiber optic interferometers (FOIs) can also be multiplexed [6]. For example, fiber Fabry-Perot interferometers (FPIs) of different cavity lengths have been multiplexed onto a single fiber. Identification of the cascaded FPIs can be achieved by Fourier transform of the optical interferogram in the spectral domain to obtain their individual optical path differences [7, 8]. Recently, it has been demonstrated that cascaded FPIs with the same or similar cavity lengths can be discriminated using microwave assisted separation

and reconstruction of the individual optical interferograms in the spectrum domain [9]. One unique feature of the multiplexed sensing is that each point sensor along the optical fiber can be flexibly encoded to measure different physical, chemical and biological quantities [10, 11]. However, the current multiplexed sensing techniques were still quasi-distributed or spatially interrupted, only providing discrete sampling of the space, leaving dark zones among the sensors.

Spatially continuous measurement can be achieved by collecting the back-scattered signals generated by the elastic (e.g., Rayleigh) [12, 13] or inelastic (e.g., Brillouin or Raman) [14-16] scatterings along the fiber. Optical probing and collection of these back-scattered have been done in the time domain through OTDR [17] or in the frequency domain using OFDR [18]. The unique advantage of the scattering based distributed sensing is the spatial continuity (no dark-zones). For example, long-range spatially continuous Brillouin optical time-domain analysis (BOTDA) measurement systems has been demonstrated using both methods [19, 20]. Another advantage of the back-scattering based distributed sensing is that it does not necessarily require extra modifications to the optical fiber, making it possible to cover a long measurement distance (e.g., tens of kilometers). Most of the quantitative measurements based on scattering have been performed using singlemode fibers. The back-scattered signals in an optical fiber are mainly sensitive to strain and temperature.

Recently, we demonstrated a new concept of optical carrier based microwave interferometry (OCMI) [21] inspired by the research advancements in microwave photonics [22, 23]. By interrogating optical interferometers in microwave domain, the OCMI concept integrates the strengths of optics and microwave, providing several unique features that are particularly advantageous for sensing application. These features include low dependent on the types of

optical waveguides, insensitive to variations in optical polarizations, high signal quality, relieved fabrication requirements, and the potential capability for distributed sensing.

Here, we studied using the OCMI technique for spatially continuous distributed sensing. Intrinsic FPIs formed by cascaded weak reflectors in an optical fiber are used for the purpose of demonstration. It is expected that the proposed technique can also be used for multiplexing other types of fiber interferometers. Distributed strain sensing is used as an example in this paper. However, we believe that the interferometry based system can be easily modified for distributed measurement of other physical, chemical and biological parameters.

19.2 Concept of Distributed Sensing Based on Cascaded OCMI-FPIs

Figure 19-1 illustrates the fundamental concept of the spatially continuous distributed sensing technique using cascaded inline OCMI-FPIs. The essence of OCMI is to read an optical interferometer in microwave domain as described in [21].

As shown in Figure 19-1, the light from a broadband optical source is intensity-modulated by a microwave signal whose frequency can be scanned via computer control. The microwave-modulated light, where the optical is the carrier and the microwave is the envelope, is then sent into (via a fiber optic circulator) an optical fiber with cascaded weak reflectors. The optical reflections travel backwards, pass the fiber circulator and are detected by a high-speed photodetector. The optical detection is synchronized with the microwave frequency by a phase lock loop (PLL) so that the amplitude and phase of the reflected signal can be resolved. After scanning the microwave frequency through the entire available range, the reflection spectrum (with both amplitude and phase) is obtained.

The inverse complex Fourier transform of the reflection spectrum provides the time-resolved discrete reflections along the optical fiber. A time gating function with two opening windows is then applied to the time series so as to "cut out" two arbitrary reflections (e.g., Γ_i and Γ_j in Fig. 1) while suppressing other values to zero. These two reflections are then Fourier transformed back to frequency domain to reconstruct a microwave interferogram, which can be used to find the optical path difference (OPD) between the two reflectors (e.g., d_{ij}). The change in the OPD between these two reflectors (e.g., Δd_{ij}) can be calculated based on the frequency shift of the microwave interferogram.

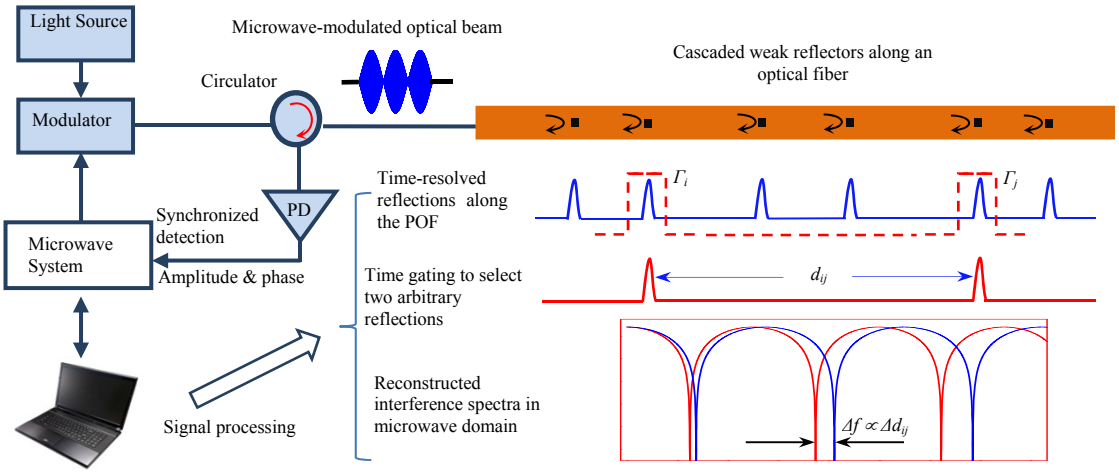

Figure 19-1. Schematic illustration of the fundamental concept of the spatially continuous distributed sensing using cascaded FPIs. The segmentation is achieved by implementing a time-gating function with two windows to isolate two arbitrary reflections (e.g., Γ_i and Γ_j) for reconstruction of the microwave interferogram, whose spectral shift is proportional to the length change of the segment between the i-*th* and j-*th* reflectors (i.e., Δd_{ij}).

Because any two reflectors can be chosen to form an OCMI interferogram, spatially continuous distributed sensing can be realized by consecutively selecting two adjacent reflectors along the cable. In addition, the base length of the interferometer can be varied by choosing any

two arbitrary reflectors (e.g., select 2 and 5 and suppress the other reflectors). As such, the gauge length can be flexibly reconfigured during measurement.

19.3 Modeling and simulations

Let's start with an optical wave in the form of

$$E_o = A\exp\left\{-j\left[\omega t + \varphi\right]\right\} \tag{19-1}$$

where, t is the time; E_o is the electric field; A is the amplitude; φ is the phase; ω is the angular optical frequency.

The microwave signal used to modulate the optical wave is given by

$$s(t) = M\cos\left(\Omega t + \phi\right) \tag{19-2}$$

where M is the amplitude of the modulation, which falls in the range of 0 to 1, Ω is the microwave angular frequency, and ϕ is the phase.

The electric field of the light wave modulated by the microwave becomes

$$E = m(t)E_o \tag{19-3}$$

where *m(t)* is the amplitude modulation term, given by

$$m(t) = \sqrt{1+s(t)} = \sqrt{1+M\cos\left(\Omega t + \phi\right)} \tag{19-4}$$

The microwave-modulated light, in which the optical is the carrier and the microwave is the envelope, is then sent into an optical fiber with cascaded reflectors. The reflection of each reflector can be designed to be weak enough so that the light can be transmitted over many

sensors and the multiple reflections are negligible. The electric field of the total reflected light wave is given by

$$E_{total} = \sum_{i=1}^{N} E_i(t, z_i) = \sum_{i=1}^{N} m_i(t, z_i) E_{o,i}(t, z_i) \tag{19-5}$$

where N is the total number of the reflectors. z_i represents the location of the i-*th* reflector. Note that in Equation (19-5), both the optical and microwave components are functions of the locations (z_i) of the reflectors.

The optical component (i.e., the electric field of the i-*th* optical reflection) in Equation (5) is given by

$$E_{o,i}(t, z_i) = \Gamma_i A \exp\left\{-j\left[\omega\left(t + \frac{2z_i n}{c}\right)\right]\right\} \tag{6}$$

where Γ_i is the amplitude reflection coefficient of the i-*th* reflector seen by the photodetector; c is the speed of light in vacuum; n is the effective refractive index.

The microwave amplitude modulation term in Equation (19-5) is

$$m(t, z_i) = \sqrt{1 + M\cos\left[\Omega\left(t + \frac{W}{c} + \frac{2z_i n}{c}\right)\right]} \tag{19-7}$$

where the microwave envelopes include two delay terms. The first is the delay associated with the common electrical length (W) of the microwave system and this delay is the same for all the paths. The second delay term is the contribution from the optical propagation delays at different reflectors.

For simplicity, let's assume that the broadband optical source has a rectangular shaped spectrum in the frequency range from ω_{min} to ω_{max}. The total power of the superimposed optical waves of all the reflections is given by

$$\begin{aligned}\left|E_{total}\right|^2 &= \frac{1}{\Delta\omega}\int_{\omega_{\min}}^{\omega_{\max}}\left|\sum_{i=1}^{N}E_i\left(t,z_i\right)\right|^2 d\omega \\ &= \frac{1}{\Delta\omega}\left(\int_{\omega_{\min}}^{\omega_{\max}}\sum_{i=1}^{N}\left|E\left(t,z_i\right)\right|^2 d\omega + \int_{\omega_{\min}}^{\omega_{\max}}\sum_{i=1,j=1,i\neq j}^{N}\left[E\left(t,z_i\right)E^*\left(t,z_j\right)+E^*\left(t,z_i\right)E\left(t,z_j\right)\right]d\omega\right)\end{aligned} \tag{19-8}$$

where the first integral is the self-product term and the second integral is the cross-product term, and $\Delta\omega = \omega_{\max} - \omega_{\min}$.

Let's first examine the cross-product term in Equation (19-8)

$$\begin{aligned}&\frac{1}{\Delta\omega}\int_{\omega_{\min}}^{\omega_{\max}}\sum_{i=1,j=1,i\neq j}^{N}\left[E\left(t,z_i\right)E^*\left(t,z_j\right)+E^*\left(t,z_i\right)E\left(t,z_j\right)\right]d\omega \\ &= \frac{2}{\Delta\omega}\sum_{i=1,j=1,i\neq j}^{N}m\left(t,z_i\right)m\left(t,z_j\right)\Gamma_i\Gamma_j A^2\int_{\omega_{\min}}^{\omega_{\max}}\left\{\cos\left[\frac{2\omega}{c}\left(z_1-z_2\right)n\right]\right\}d\omega\end{aligned} \tag{19-9}$$

It is interesting to notice that the cross-product term is the optical interference signal similar to a conventional all-optical interferometer. In the OCMI, the optical path difference (OPD) is chosen to be sufficiently larger than the coherence length of the optical source, i.e., $\left(z_1-z_2\right)n >> c/\Delta\omega$. Under this condition, the integral term in Equation (19-9) approaches zero. In our experimental OCMI system, we used a light source with a spectral width of 50 nm at the center wavelength of about 1550 nm, whose coherence length was about 48 μm. A typical OCMI has an OPD of a few centimeters that is much larger than the coherence length of a broadband

light source. As a result, the contribution from pure optical interference as depicted in Equation (19-9) is negligible in a typical OCMI system.

The self-product term in Equation (19-8) is found to be

$$\frac{1}{\Delta\omega}\int_{\omega_{\min}}^{\omega_{\max}}\sum_{i=1}^{N}\left|E\left(t,z_i\right)\right|^2 d\omega=\sum_{i=1}^{N}\Gamma_i^2A^2+\sum_{i=1}^{N}\Gamma_i^2A^2M\cos\left[\Omega\left(t+\frac{W}{c}+\frac{2z_in}{c}\right)\right] \qquad (19\text{-}10)$$

which includes a DC term and the summation of a series of sinusoids at the microwave frequency of Ω.

The OCMI system uses synchronized detection to eliminate the DC term (first term) and record the amplitude and phase of the microwave signal (second term) in Equation (19-10). As a result, the total signal after optoelectronic conversion by the photodetector (with a gain of g) and synchronized microwave detection is given by

$$S=A_{eff}\cos\left(\Omega t+\Phi_{eff}\right) \qquad (19\text{-}11)$$

In Equation (19-11), A_{eff} and Φ_{eff} are the amplitude and phase of the microwave signal, respectively.

$$A_{eff}=g\sqrt{\sum_{i,j}^{N}A_{eff,i}A_{eff,j}\cos\left(\phi_{eff,i}-\phi_{eff,j}\right)}$$

$$\Phi_{eff}=\arctan\left[\frac{\sum_{i}^{N}\Gamma_i^2\sin\left[\Omega\left(\frac{W}{c}+\frac{2z_in}{c}\right)\right]}{\sum_{i,j}^{N}\Gamma_i^2\cos\left[\Omega\left(\frac{W}{c}+\frac{2z_in}{c}\right)\right]}\right],\qquad \Phi_{eff}\in\{-\pi,\ \pi\}$$

where

$$A_{eff,i} = \Gamma_i^2 A^2 M \ ,$$

$$A_{eff,j} = \Gamma_j^2 A^2 M$$

$$\phi_{eff,i} = \Gamma_i^2 A^2 M \left(\frac{W}{c} + \frac{2 z_i n}{c} \right)$$

$$\phi_{eff,j} = \Gamma_j^2 A^2 M \left(\frac{W}{c} + \frac{2 z_j n}{c} \right)$$

After scanning the microwave frequency through the entire available range (from Ω_{min} to Ω_{max}), the complex microwave reflection spectrum (with both amplitude and phase) is obtained. By applying a complex and inverse Fourier-transform to the microwave spectrum, a series of cardinal sine functions are obtained at discrete reflectors, given by:

$$\begin{aligned} \mathrm{X}(t) &= \frac{1}{2\pi} \int_{\Omega_{\min}}^{\Omega_{\max}} S \exp(j\Omega t)\, d\Omega \\ &= \frac{1}{2\pi} \int_{\Omega_{\min}}^{\Omega_{\max}} \sum_{i=1}^{N} \Gamma_i^2 A^2 M \cos\left[\Omega \left(t + \frac{W}{c} + \frac{2 z_i n}{c} \right) \right] \exp(j\Omega t)\, d\Omega \\ &= \sum_{i=1}^{N} \Gamma_i^2 A^2 M \left| \mathrm{sinc}\left[(\Omega_{\max} - \Omega_{\min})(t + \tau_i) \right] \right| \end{aligned} \tag{19-12}$$

where $\tau_i = \frac{W}{c} + \frac{2 z_i n}{c}$ is the propagation delay of the signal corresponding to the *i-th* reflector.

In Equation (19-12), the maximum amplitudes of the discrete sinc functions are proportional to the reflectivity of the cascaded reflectors. In addition, Equation (19-12) also provides the location information of the reflectors along the optical fiber. The peaks of the sinc functions are at the specific reflector locations (z_i) that can be found when the delays (τ_i) are determined. The frequency bandwidth (Ω_{max} -Ω_{min}) determines the spatial resolution, i.e., the minimum distance

between two adjacent reflectors to avoid an overlap of the two pulses in the time domain. The larger the microwave bandwidth, the narrower is the pulse width (sinc function) in time domain and the higher is the spatial resolution.

A time gating function with two windows is then applied to time domain signal given in Equation (19-12) so as to isolate two arbitrary reflections. The gate functions could be designed to have different shapes such as rectangular, Hanning, Turkey, etc. Here we generalize the gate function as *g(t)*. The time domain signal after applying a gate function is thus given by *X(t)g(t)*. The gated signal is then Fourier transformed back to the frequency domain to reconstruct the microwave interferogram, which can be used to find the optical distance between the two reflectors (e.g., d_{ij}). The reconstructed OCMI-FPI interferogram is thus given by

$$S_{OCMI} = S * G(\Omega)\exp(-i\Omega\tau_0) \tag{19-13}$$

where *G(Ω)* is the inverse Fourier transform of the gate function *g(t)*; τ_0 is the time delay of the gate function. As shown in Equation (19-13), the reconstructed microwave FPI interferogram in spectrum domain is in essence a convolution of the microwave signal *S* and *G(Ω)*. Here we define the optical path difference (OPD) of the OCMI-FPI is

$$OPD = d_{ij} = \left|2\left(z_i - z_j\right)n\right| \tag{19-14}$$

The free spectral range (FSR) of the reconstructed interference spectrum is a function of the OPD, given by

$$FSR = \frac{c}{OPD} \tag{19-15}$$

Similar to an optical interference spectrum, the microwave amplitude spectrum in the reconstructed OMCI-FPI can be used to find the OPD of an interferometer. It can also be used to find the change in OPD based on the interference fringe shift.

Numerical simulations were performed to gain an intuitive understanding of using the OCMI technique for distributed sensing. In the simulation, the fiber used was a Corning SMF-28e singlemode fiber with the effective refractive index of the core of 1.468 according to the datasheet from the manufacturer. The microwave frequency was chosen to be in the range of 0-6 GHz with 20000 equally-spaced sampling points. 8 weak reflectors with equal reflectivity of 1% were implanted in the fiber at the discrete locations of 0.30, 0.40, 0.60, 0.75, 0.80, 0.90, 1.20, 1.60 m, respectively. The common electrical length of the microwave system was chosen to be 0.20 m.

Figures 19-2 (a) and (b) plot the calculated amplitude (A_{eff}) and phase (Φ_{eff}) spectra based on Equation (11). Figure 19-2 (c) and (d) plot the calculated results based on Equations (19-12) and (13), respectively. As shown in Figure 19-2(c), the 8 reflectors can be clearly identified at the corresponding locations. A Hanning window function was applied to the time-domain signal shown in Figure 19-2(c) to cut out a section including the 4^{th} and 5^{th} reflectors. The center of the Hhanning window was located at the center between the two reflectors and the width of the window was chosen to be 1.22 ns. The cut-out section of the time-domain signal was then Fourier transformed back into the frequency domain as shown in Figure 19-2(d), where an interferogram can be clearly identified. The reconstructed interferogram is the result of the microwave interference of the two reflected signals at the 4^{th} and 5^{th} reflectors. The FSR was found to be 1.005 GHz, which matched well with that calculated based on Equation (19-15).

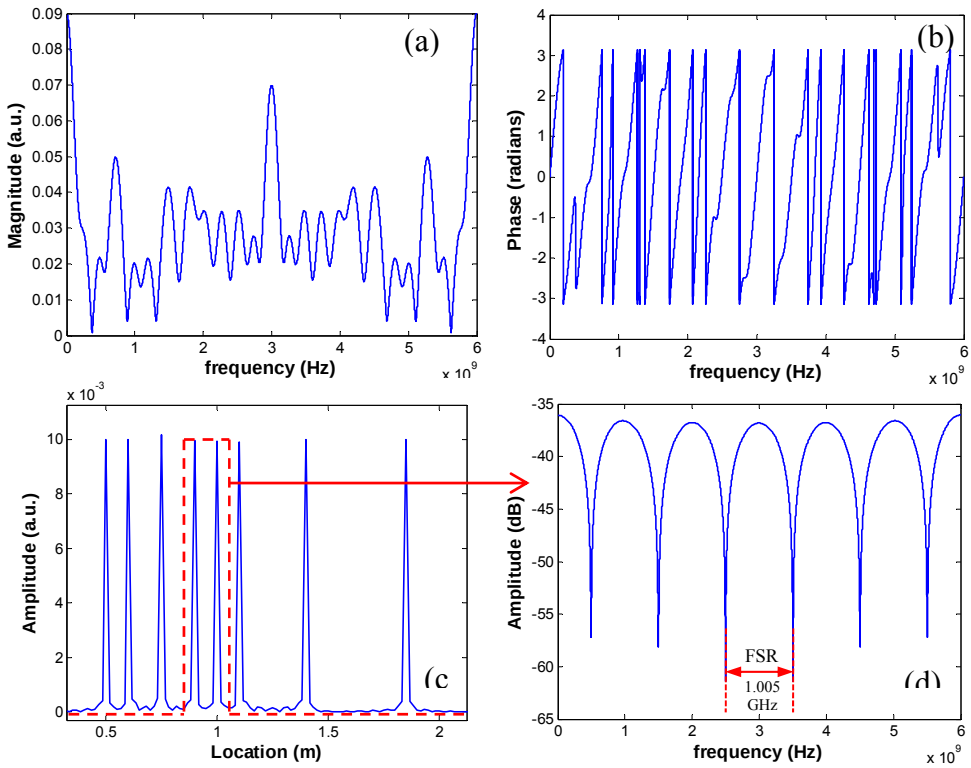

Figure 19-2. Simulation of 8 reflectors along a single-mode fiber. The optical reflectivity is equally distributed. The locations of the reflectors are 0.5, 0.6, 0.8, 0.9, 1, 1.1, 1.4, 1.8m, respectively. (a) Calculated amplitude spectrum (A_{eff}) based on Eq. 19-11. (b) Calculated phase spectrum (Φ_{eff}) based on Eq. 19-11. (c) Calculated time/spatial domain result based on Eq. 19-12. (d) Calculated microwave interferogram of the 4th and 5th reflectors based on Eq. 19-13.

In a similar way, any two reflectors can be cut out by applying a proper windowing function. In essence, the two cut-out reflectors and the fiber section between them defines a low-finesse fiber intrinsic FPI whose interferogram can be reconstructed in the frequency domain. The reconstructed microwave interferogram can be processed to find its OPD or changes in OPD for sensing applications. The location of the cut-out FPI is also known because the positions of the two reflectors can be found in the time-domain. Spatially continuous distributed sensing can be realized by consecutively selecting two adjacent reflectors along the optical fiber. In addition,

any two arbitrary reflectors on the optical fiber can be selected to construct the interferometer. As such, the gauge length can be flexibly reconfigured during measurement.

19.4 Experimental demonstration

According to the aforementioned modeling and simulation results, the OCMI interferogram of any two reflectors can be unambiguously reconstructed for spatially continuous distributed sensing. To validate the proposed concept, we designed two experiments based on cascaded optical fiber FPIs.

19.4.1 System implementation

While there are many ways to implement the OCMI concept, Figure 19-3 illustrates an example system configuration where a microwave vector network analyzer (VNA) is used as the microwave source and signal detector. A broadband light source with the bandwidth of 50 nm is intensity modulated using an electro-optic modulator (EOM) driven by the microwave signal from the Port 1 of a VNA (HP 8753es). The VNA output is DC-biased and amplified to achieve a high modulation index. A fiber circulator is used to route the modulated light into and the output signal out of the distributed fiber optic Fabry-Perot interferometers. An optional erbium doped fiber amplifier (EDFA) can be used for additional signal amplification if needed. After DC-filtering and RF amplification, the photodetector output is connected to the Port 2 of the VNA, where the amplitude and phase of the signal are extracted. By sweeping the VNA frequency, the microwave spectrum (i.e., the S21 of the VNA) of the interferometer is obtained.

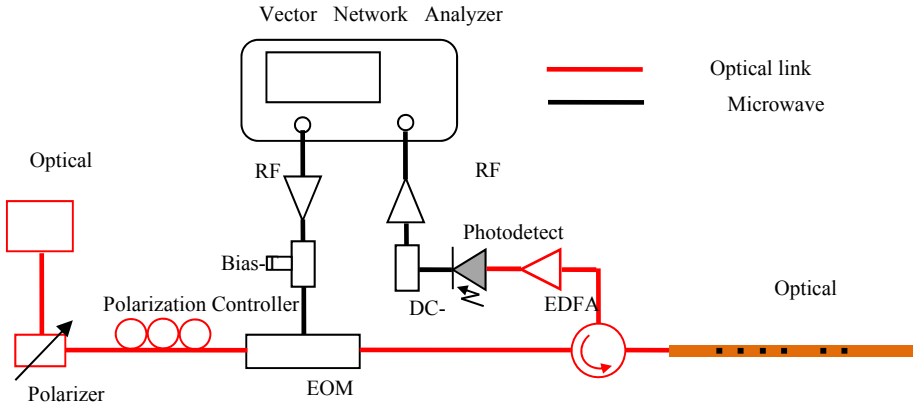

Figure 19-3. Schematic of the OCMI system used to support proof-of-concept experiments. A broadband light source (bandwidth ≈ 50 nm) is intensity-modulated using an electro-optic modulator (EOM) driven by the microwave output (DC-biased and amplified) from Port 1 of a VNA (HP 8753es). The output from the fiber interferometer is detected by a photodetector whose signal, after DC-filtering and RF amplification, is recorded at Port 2 where the amplitude and phase of the signal are extracted. By sweeping the VNA frequency, the microwave spectrum of the interferometer is obtained (i.e., the S21 of the VNA).

19.4.2 Strain measurement using OCMI-FPIs

As shown in Figure 19-4(a), 6 weak reflectors were implemented on a singlemode fiber (SMF-28e) by intentionally misaligning the fibers during fusion splicing. The 6 reflectors divided the entire fiber into 5 measurement sections of different lengths as schematically shown in Figure. The sensors were interrogated using the OCMI system described in Figure 19-3. The microwave interference spectrum of the distributed sensors was first acquired and then complex inverse Fourier transformed to obtain the time resolved reflections along the optical fiber as shown in Figure 19-4(b), where the 6 reflections can be clearly identified at the time intervals matching the section lengths. Using a time gating window, we isolated the two reflectors defining Section 19.3 and reconstructed its microwave interferogram by complex Fourier

transform as shown in Figure 19-4(c), where interference fringes are clean with the visibility exceeding 25 dB, indicating excellent signal quality. Distributed sensing capability was tested by applying axial strains to Section 3 only. Figure 19-3(d) plots the 3D view of the frequency shift of the interferogram as a function of the applied strain, where the frequency decreases linearly as the strain increases. In contrast, the other sections were left unstressed. As a result, no frequency shifts were observed along the fiber outside Section 3. As shown in Figure 19-4(e), the FPI defined by Section 19.3 had a linear response to the applied axial strain with a sensitivity of 2.26 KHz/με.

It is worth noting that the reflectors created by fiber misalignments had large losses. As a result, the reflections were not even and their amplitudes dropped quickly. A reflector with controlled reflectivity and negligible losses is needed so that better fringe visibilities can be obtained for each section and the number of reflectors can be significantly increased (thus a much longer monitoring span). Nevertheless, the experiment results clearly show the capability of using OCMI-FPI for strain sensing and the capability of locating the spatial position of the interferometer using the OCMI technique.

19.4.3 Spatially continuous measurement of distributed strains

We also experimentally validated the spatially continuous distributed sensing capability using cascaded optical fiber intrinsic Fabry-Perot interferometers (IFPI) as illustrated in Figure 19-5(a), where 10 weak reflectors were inscribed inside the core of a SMF using femtosecond (fs) laser micromachining. The fs laser is a regeneratively amplified Ti: Sapphire laser (Coherent, Inc.). The central wavelength, pulse width and repetition rate of the laser are 800 nm, 180 fs and 250 kHz, respectively. The maximum output power of the laser is 1 W. The actual power used

for fabrication was controlled by adjusting the laser beam optics. The laser operation is fully controlled by a computer. A microscopic video system is included in the system to observe the fabrication process in real time.

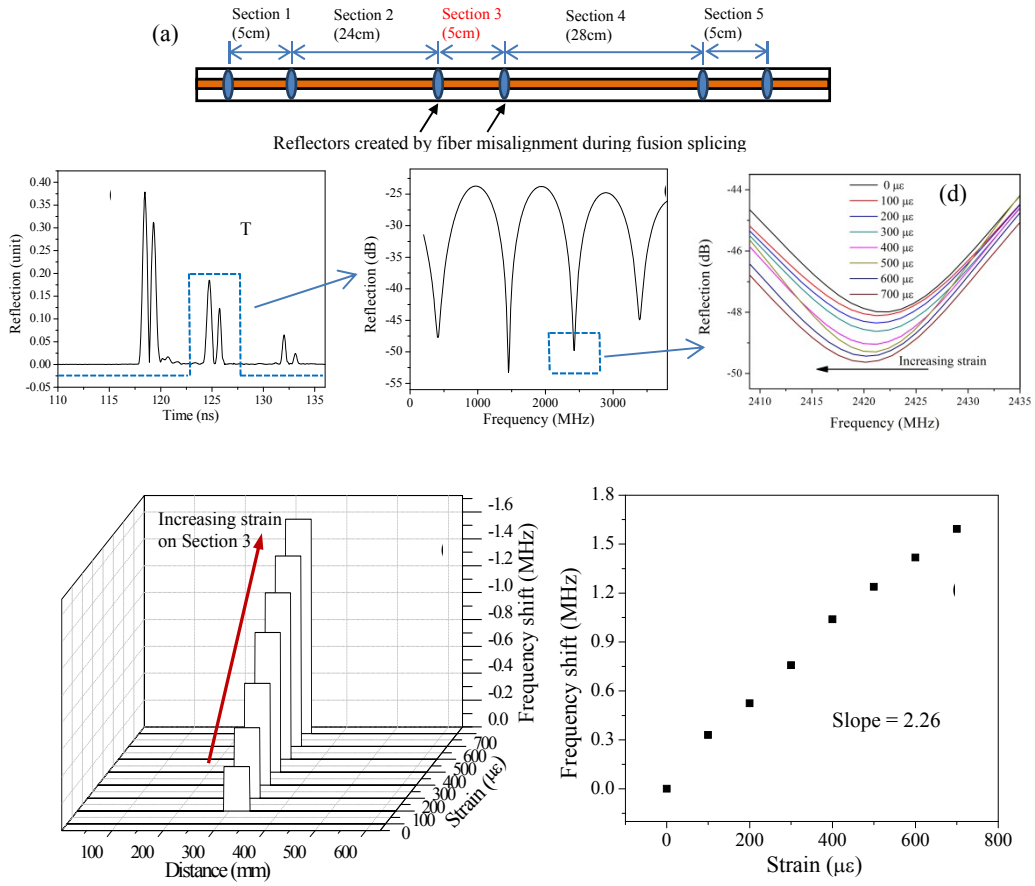

Figure 19-4. Validation of the distributed sensing capability of OCMI. (a) SMF distributed sensors with 6 reflectors implanted to divide the entire length into 5 sections, (b) Time resolved reflections along the optical fiber and time gating window to isolate Section 3, (c) Reconstructed microwave interferogram of Section 3, (d) Zoomed interference spectra at different strains, (e) 3D view of the distributed OCMI fiber sensor in response to axial strains applied to Section 3 only, and (f) Frequency shift as a function of the applied strain.

During fabrication, the lens and fiber were immersed in deionized water. The focused fs laser beam penetrated into the fiber and ablated a small cuboid shape with the dimension of 5 μm × 30

μm × 20 μm in the fiber core as shown in Figure 19-4(f). The typical reflectivity of such a structure was about -45 dB and the loss was about 0.02 dB measured by an optical power meter. The weak reflectivity and very small loss allow us to cascade many reflectors along a fiber, enabling distributed sensing over a long distance.

The reflectors divided the fiber into 9 consecutive measurement sections. Each section was an IFPI with a length of about 12 cm. The IFPI sensors were epoxied on the surface of an aluminum cantilever beam with its length, width, and thickness of 1,250, 80, and 9.10 mm, respectively. One side of the beam was clamped in a vice. The other side was pushed by a micro-actuator to bend the beam and apply strain to the attached sensors. The distance between the clamp and the micro-actuator was 1.14 m. As the cantilever beam deflected, the amounts of axial strain seen by the IFPI sensors were different. The mathematical model of the cantilever beam used to calculate the strain distribution can be found in [24].

The complex microwave spectrum (amplitude and phase spectrum) of the distributed sensors was first acquired as shown in Figure 19-5(b) and (c). Then complex inverse Fourier transform was performed to obtain the distance-resolved reflections along the fiber as shown in Figure 19-4(d), where the 10 reflections can be clearly identified and their separations match the corresponding section lengths. Using a Hanning window, we isolated the two reflectors defining Section 8 and reconstructed a microwave interferogram by applying complex Fourier transform to the window-gated data. As shown in Fig. 5(e), the reconstructed interferogram is clean and has a visibility exceeding 25 dB.

The deflections of the aluminum plate were increased at a step of 5 cm, measured by a caliper. As the strain increased, the interferogram of each IFPI shifted correspondingly, as shown

in Figure 19-5(e). By tracking the frequency shift of the individual interferogram, the changes in OPDs (thus the physical lengths) were calculated for all the consecutive sections. The strain value of each section was calculated by dividing the physical length change with respect to its initial length calculated based on the FSR of the interferogram. Figure 19-5(e) shows the measured strains (black dots) of various sections along the cantilever beam at the deflections of 5, 10 and 15 cm, respectively. The measurement data agreed well with the statics model predictions, i.e., the mesh grids in Figure 19-5(g). The strain increased at the location that was closer to the clamped end of the beam. The strain also increased at the same location as the deflection increased.

In our preliminary OCMI system, the microwave bandwidth was about 6 GHz, which provided a theoretical spatial resolution of about 3 cm. The pulses shown in Figure 19-5(d) indicated no obverse overlap for the reflectors separated by about 12 cm. Given that modern microwave instrumentation can easily reach 50 GHz bandwidth, the spatial resolution can be as high as a few millimeters.

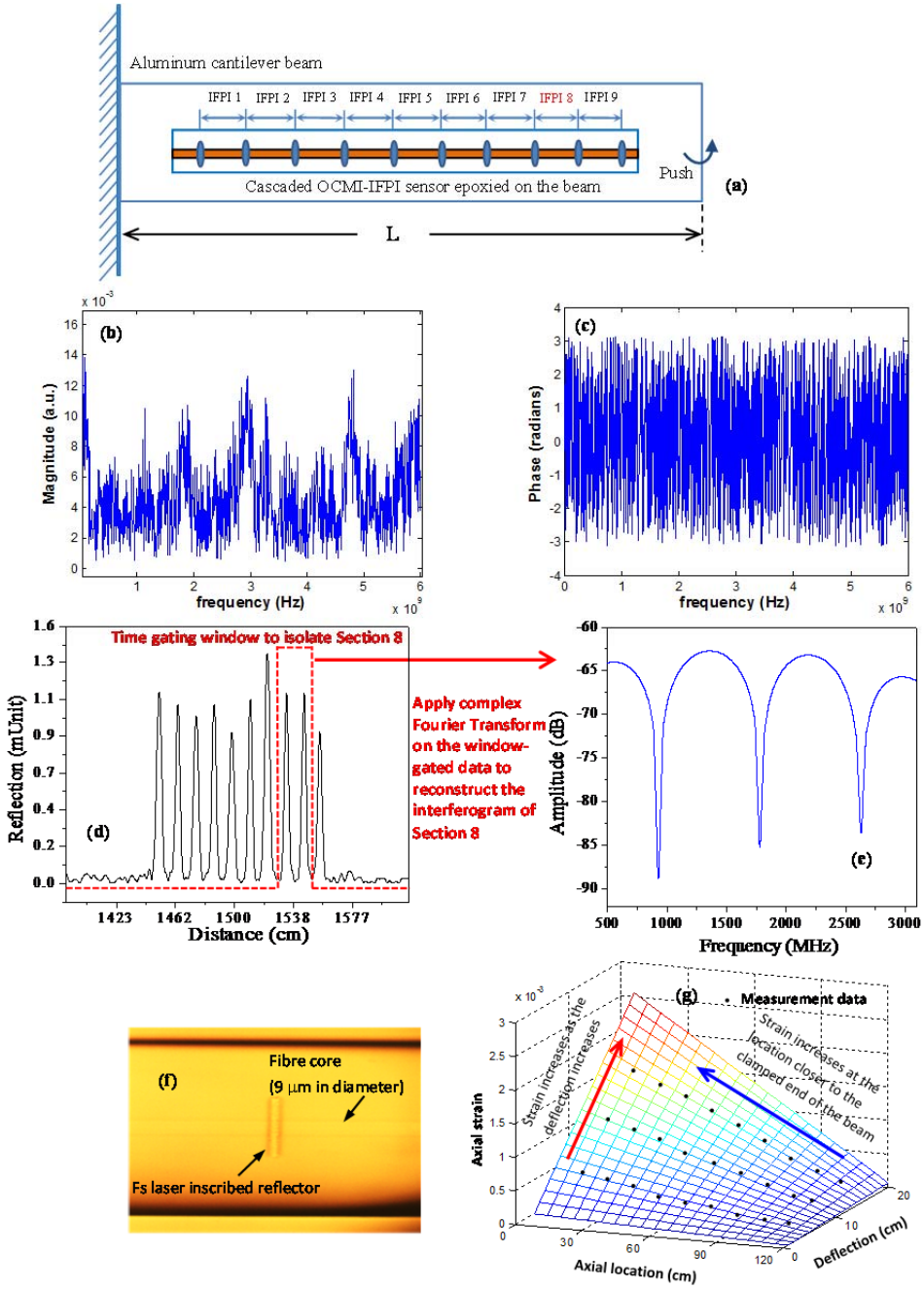

Figure 19-5. (a) Schematic illustration of the experiment setup to validate the distributed strain sensing capability of OCMI. (b) Amplitude spectrum and (c) phase spectrum of the distributed sensor systems. (d) Time/distance resolved reflections along the optical fiber where the 10 weak reflections can be clearly identified with excellent SNR. (e) Reconstructed microwave interferogram of Section 8. (f) Confocal microscopic image of a weak reflector fabricated by femtosecond laser micromachining. Using water immersion fabrication, the focused fs laser beam penetrated into the fiber and ablated a

very small region inside the fiber core. The reflector has a typical reflectivity of about -45 dB and a typical loss of about 0.02 dB. (g) Measured strain distribution at the different sections along the beam under different amounts of deflections. The strain increased at the location that was closer to the clamped end of the beam. The strain also increased at the same location as the deflection increased.

19.5 Summary

In conclusion, a new distributed fiber optic sensing technique using optical carrier based microwave interferometry was developed. Many optical interferometers with the same or different optical path differences are interrogated in the microwave domain and their locations can be unambiguously determined. The concept is demonstrated using cascaded weak optical reflectors along a single optical fiber, where any two arbitrary reflectors are paired to define a low-finesse Fabry-Perot interferometer. Spatially continuous (i.e., no dark zone), fully distributed strain measurement was used as an example to demonstrate the capability of the proposed concept. The spatial resolution is inversely proportional to the microwave bandwidth. With a microwave bandwidth of 6 GHz, the spatial resolution can reach 3 cm. Although distributed strain measurement using cascaded FPIs was used as a demonstration, the proposed concept may also be implemented on other types of waveguide or free-space interferometers. In addition to strain measurements, it can also be flexibly designed to measure other physical, chemical and biological quantities by encoding the parameters to be measured into the OPDs of the interferometers. As presented in [21], by reading the fiber optic interferometers in microwave domain, the system offers many unique features including high signal quality, relieved requirement on fabrication, low dependence on the types of optical waveguide, and insensitivity

to the variations of polarization. It is also envisioned that the proposed technique could be implemented in special optical fibers (e.g., multimode, single crystal sapphire and polymer fibers), optical waveguides and free space. The new distributed sensing concept may enable many important applications that are long-desired but currently unavailable.

19.6 References

1. K. Grattan and T. Sun, "Fiber optic sensor technology: an overview," Sensors and Actuators A: Physical **82**, 40-61 (2000).
2. A.D. Kersey, T. Berkoff, and W. Morey, "Multiplexed fiber Bragg grating strain-sensor system with a fiber Fabry–Perot wavelength filter," Optics Letters **18**, 1370-1372 (1993).
3. K. O. Hill and G. Meltz, "Fiber Bragg grating technology fundamentals and overview," Journal of Lightwave Technology **15**, 1263-1276 (1997).
4. Y. Wang, J. Gong, B. Dong, W. Bi, and A. Wang, "A quasi-distributed sensing network with time-division-multiplexed fiber Bragg gratings," IEEE Photonics Technology Letters **23**, 70-72 (2011).
5. A.A. Childers, M. E. Froggatt, S. G. Allison, T. C. Moore Sr, D. A. Hare, C. F. Batten, and D. C. Jegley, "Use of 3000 Bragg grating strain sensors distributed on four 8-m optical fibers during static load tests of a composite structure," in SPIE's 8th Annual International Symposium on Smart Structures and Materials, (International Society for Optics and Photonics, 2001), 133-142.
6. J. L. Brooks, R. H. Wentworth, R. C. Youngquist, M. Tur, B. Y. Kim, and H. Shaw, "Coherence multiplexing of fiber-optic interferometric sensors," Journal of Lightwave Technology **3**, 1062-1072 (1985).
7. J. Wang, B. Dong, E. Lally, J. Gong, M. Han, and A. Wang, "Multiplexed high temperature sensing with sapphire fiber air gap-based extrinsic Fabry–Perot interferometers," Optics Letters **35**, 619-621 (2010).

8. F. Shen and A. Wang, "Frequency-estimation-based signal-processing algorithm for white-light optical fiber Fabry-Perot interferometers," Applied Optics **44**, 5206-5214 (2005).

9. J. Huang, L. Hua, X. Lan, T. Wei, and H. Xiao, "Microwave assisted reconstruction of optical interferograms for distributed fiber optic sensing," Optics Express **21**, 18152-18159 (2013).

10. A. Sutapun, M. Tabib-Azar, and A. Kazemi, "Pd-coated elastooptic fiber optic Bragg grating sensors for multiplexed hydrogen sensing," Sensors and Actuators B: Chemical **60**, 27-34 (1999).

11. L. Chen, T. Li, C. C. Chan, R. Menon, P. Balamurali, M. Shaillender, B. Neu, X. Ang, P. Zu, and W. Wong, "Chitosan based fiber-optic Fabry–Perot humidity sensor," Sensors and Actuators B: Chemical **169**, 167-172 (2012).

12. M. Froggatt and J. Moore, "High-spatial-resolution distributed strain measurement in optical fiber with Rayleigh scatter," Applied Optics **37**, 1735-1740 (1998).

13. Y. Koyamada, M. Imahama, K. Kubota, and K. Hogari, "Fiber-optic distributed strain and temperature sensing with very high measurand resolution over long range using coherent OTDR," Journal of Lightwave Technology **27**, 1142-1146 (2009).

14. X. Bao, J. Dhliwayo, N. Heron, D. J. Webb, and D. A. Jackson, "Experimental and theoretical studies on a distributed temperature sensor based on Brillouin scattering," Lightwave Technology, Journal of **13**, 1340-1348 (1995).

15. J. Dakin, D. Pratt, G. Bibby, and J. Ross, "Distributed optical fibre Raman temperature sensor using a semiconductor light source and detector," Electronics Letters **21**, 569-570 (1985).

16. M. N. Alahbabi, Y. T. Cho, and T. P. Newson, "150-km-range distributed temperature sensor based on coherent detection of spontaneous Brillouin backscatter and in-line Raman amplification," JOSA B **22**, 1321-1324 (2005).

17. K. Shimizu, T. Horiguchi, Y. Koyamada, and T. Kurashima, "Coherent self-heterodyne Brillouin OTDR for measurement of Brillouin frequency shift distribution in optical fibers," Lightwave Technology, Journal of **12**, 730-736 (1994).

18. W. Eickhoff and R. Ulrich, "Optical frequency domain reflectometry in single-mode fiber," Applied Physics Letters **39**, 693-695 (1981).

19. M. A. Soto, G. Bolognini, F. Di Pasquale, and L. Thévenaz, "Simplex-coded BOTDA fiber sensor with 1 m spatial resolution over a 50 km range," Optics Letters **35**, 259-261 (2010).

20. Y. Dong, L. Chen, and X. Bao, "Time-division multiplexing-based BOTDA over 100km sensing length," Optics Letters **36**, 277-279 (2011).

21. J. Huang, X. Lan, H. Wang, L. Yuan and H. Xiao, "Optical carrier-based microwave interferometers for sensing application," Proc. SPIE 9098, 90980H (2014).

22. J. Capmany and D. Novak, "Microwave photonics combines two worlds," Nature Photonics **1**, 319-330 (2007).

23. J. Yao, "Microwave photonics," Lightwave Technology, Journal of **27**, 314-335 (2009).

24. K. Bisshopp and D. Drucker, "Large deflection of cantilever beams," Quarterly of Applied Mathematics **3** (1945).

20. High Temperature Sensor Testing System Design

20.1 Testing Capabilities

To support the evaluation and testing of the developed high temperature sensors and instrumentation systems, a high temperature sensor testing system has been established in the PI's lab at Clemson University. The system has been successfully used to test the various developed high temperature sensors and instrumentation. In addition, the testing system has been used to evaluate the sensor packaging design and implementation.

Figure 20-1 shows the block diagram of the sensor test system. The system includes the following seven functional units.

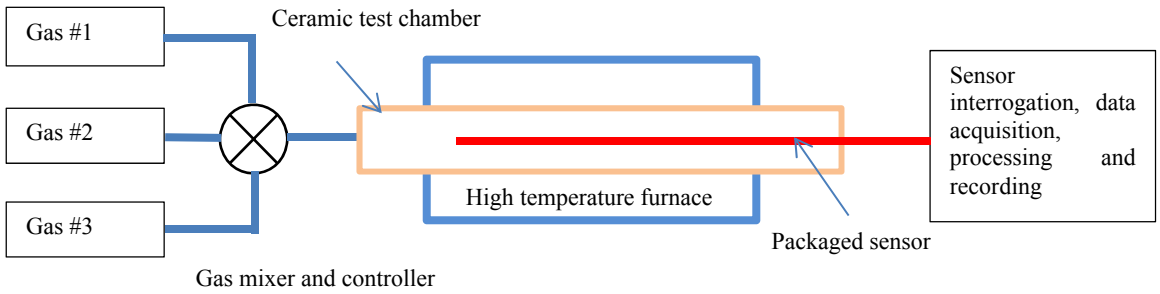

Figure 20-1. Block diagram of the sensor testing system

The developed sensor testing system has the following testing capabilities and functions:

Capabilities

1) Temperature survivability the packaged sapphire sensor up to 1450°C.

2) The temperature sensitivity of the packaged sapphire sensor upto 1450°C.

3) The temperature measurement resolution of the packaged sapphire sensor upto 1450°C.

4) The temperature measurement accuracy of the packaged sapphire sensor upto 1450°C.

5) The stability of the packaged sapphire temperature sensors at high temperatures (1450°C) for an extended period of time of 300 hours and longer.

System functions

1) A electrical furnace to provide a high temperature capability upto 1600℃.

2) Gas suppliers and regulator/controller to provide different gas environment at high temperatures.

3) A Ceramic test chamber to provide the high temperature and high pressure testing environment.

4) A sensor insertion port for installation of the packaged sapphire sensors to be installed into the test chamber.

5) Automated sensor interrogation, signal processing and recording.

20.2 Sensor Testing System Implementation

High Temperature Furnace: A 1730 Series high temperature furnace was purchased from CM Furnace Company and fully assembled in our lab. It is a high temperature horizontal tube furnace with double wall construction to allow rapid temperature heating as well as keeping the outside skin temperature lower and cooling the terminals of the heating elements. The furnace has a maximum continuous operating temperature of 1700 ^{o}C in air, providing us the required high temperature characterization capability.

To protect the fragile heating elements from damage during transportation process and package their furnace and controlling system, the CM furnace system was delivered unassembled. We installed the whole furnace system by assembling the heating elements, thermocouples, power wires and extensions from furnace to the control system, positioning the ceramic posts into the tube furnace, and connecting the water sealed models on the post terminals through solid state cooling/chilling system. Figure 20-2 shows the fully assembled furnace, which has passed the inspection by the university safety department.

Back side Front side

Figure 20-2. Images (back and front views) of the new, fully assembled CM 1730 furnace system, showing the furnace, controller, chilling system, connected heating elements, thermo couples, extension wires, power transformer and ceramic post.

Gas composition system: The pressured air is provided by three gas cylinders (N_2, O_2, and CO_2) with a maximum pressure of 800 psi. The pressured airs from the cylinders are separated regulated, mixed by a three-way mixer and then pressure-controlled to feed the high temperature chamber. By varying the flow rate of the individual gas stream, the gas compositions inside the test chamber can be changed to study the sensor dependence on the gas composition changes. Specifically, we are interested in the oxygen rich environment and its influences on the sensor

outputs. The system is also designed to test the sensor long term stability in different gas compositions.

Integrated sensor testing system: Figure 20-3 shows the photograph of the desk-top sensor interrogation system where an large size desk-top VNA is used. In field tests, the large size VNA will be replaced by a portable VNA. A computer program has also been developed for automated sensor logging.

Figure 20-4 shows the photograph of the packaged sapphire fiber sensor placed inside the high temperature furnace. The long stainless steel tube is used to protect the fiber leads. The sapphire sensor is placed in the ceramic portion and inserted into the high temperature furnace. The gas cylinders and regulation system are used to change the gas compositions inside the test chamber.

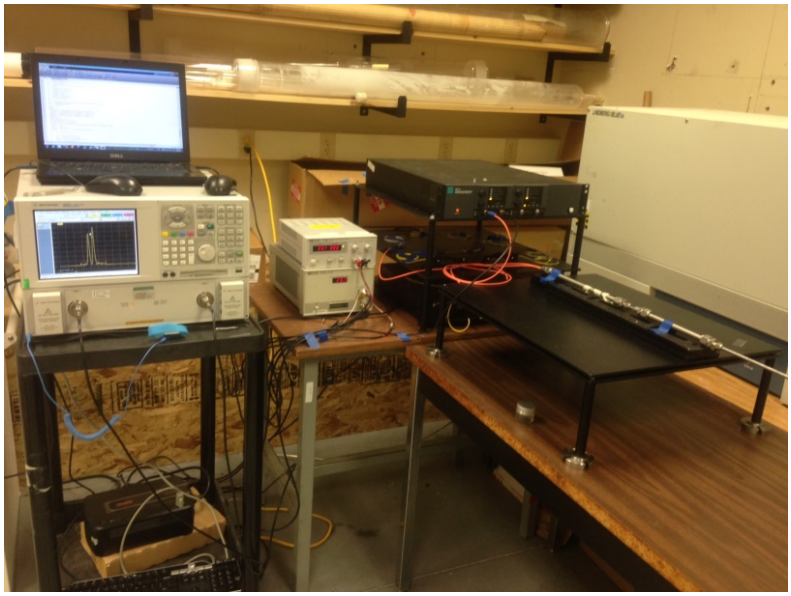

Figure 20-3. Photograph of the integrated automated sensor interrogation system.

Figure 20-4. Photograph of packaged sapphire fiber sensor inserted inside the high temperature furnace.

20.3 Evaluation of the Sensor Testing System

Single mode fiber Michelson interferometer based OCMI sensors have been used to evaluate the developed sensor testing system as well as the performance of the instrumentation system.

Figure 20-5 (a) shows the schematic construction of a SMF Michelson interferometer with a length difference of 29 cm. The MI first splits light into two paths by a 2x2 optical coupler. The two light beams travels along a distance and are reflected back by two reflectors inserted into the two paths. The two reflected beams are then recombined at the coupler. The superposition of the two beams results in an interference signal that is a function of the optical path difference (OPD) between the two different paths. The time resolved reflections from two endfaces of these fibers are shown in Figure 20-5 (b), and the reflection intensities from two endfaces are very close to each other. Figure 20-5 (c) plots the microwave interference spectrum from this SMF Michelson interferometer. The fringe visibility is 30~40 dB showing an excellent signal to noise ratio (SNR). There are many methods to create the reflection mirrors, and we directly use the two endfaces of SMF fibers as reflectors. It is worth noting that there are two factors impacting the quality of interference signal: one is the magnitude of reflected intensities and the other is the relative difference between two reflected intensities. To obtain a high quality interference spectrum, the two reflection light intensities should be very close to each other, while the magnitudes should be relatively strong.

The singlemode fiber based COMI Michelson interferometer was packaged into a ceramic tube with an inner diameter of 0.5 mm. The ceramic tube was inserted into a programmable tube furnace for high temperature sensing characterization, as shown in Figure 20-6. A vector network analyzer was used to record the interference signals. The intermediate frequency bandwidth (IFBW) and the sampling point of the VNA were set to be 100 Hz and 1600, respectively.

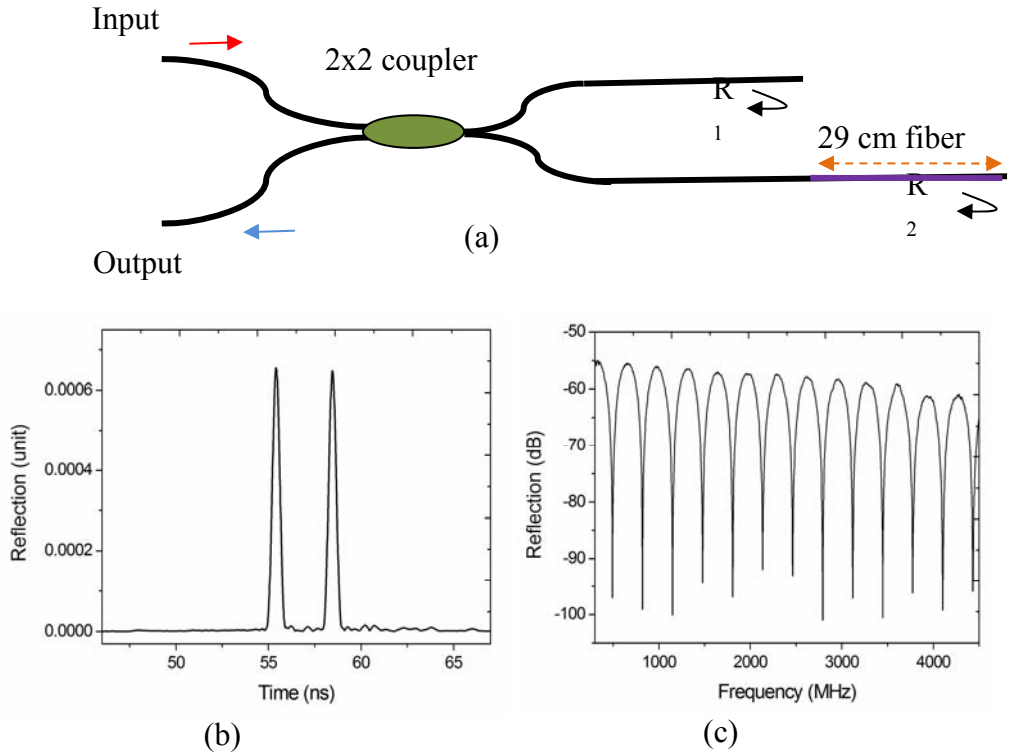

Figure 20-5. The schematic and the spectrum from OCMI based Michelson interferometer using single mode fiber.

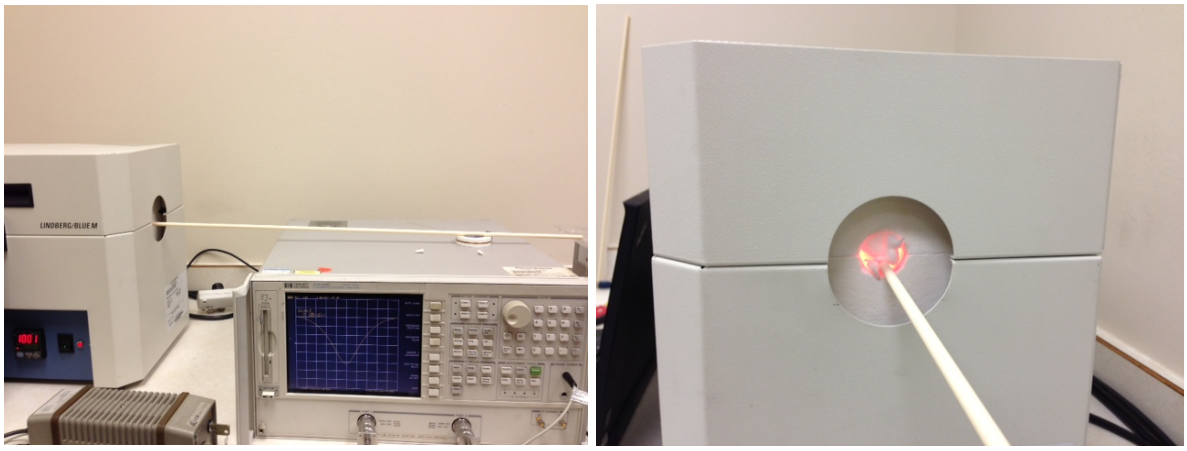

Figure 20-6. Pictures of experimental setup using the sapphire optical fiber based OCMI-Michelson interferometer

The stability of SMF Michelson interferometer was characterized by programming the tube furnace stay at specific temperature points for certain longer time period. In our test, we set the temperature increase speed as 100 ^{o}C per 15 minutes, and the dwelling time at each specific temperature was 80 minutes in the temperature increase process. For temperature decreasing process, due to much longer recovery time is needed for lower temperature, the temperature decrease speed was set at 100 ^{o} C per 30 minutes for 400 and 300 ^{o}C and dwelling time at 200 ^{o}C was set to 120 minutes to fully stabilize the temperature in tube furnace. Some abrupt temperature changes are due to the limited programmable steps from our tube furnace and 100 ^{o} C spectra was not taken due to too long waiting time needed.

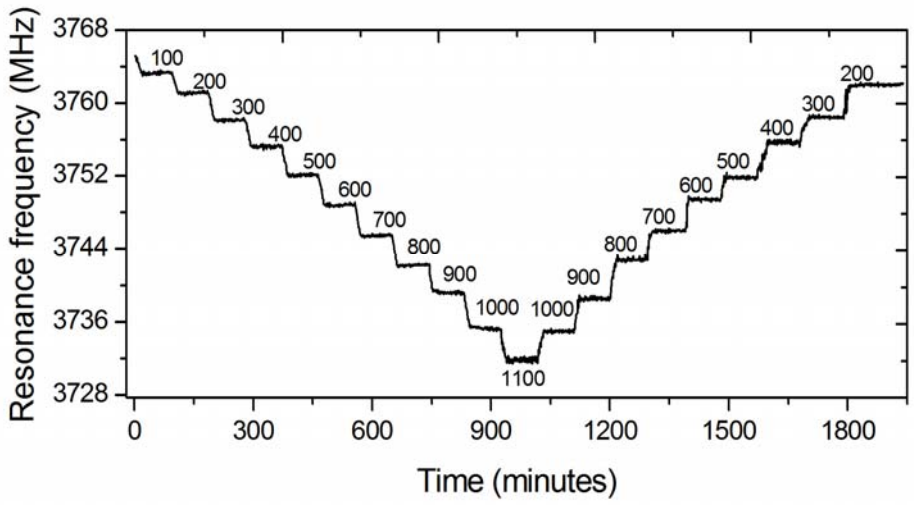

Figure 20-7. Stability test of OCMI based optical fiber Michelson interferometer at different temperatures (100 ~ 1100 ^{o} C).

Figure 20-7 shows the stability test results of OCMI Michelson interferometer (MI2) in the whole temperature increasing and decreasing procedure. The spectrum bottom values were recorded after each circle of frequency scan, and temperature increasing, decreasing and

stabilizing process can be easily and clearly distinguished from each other in this figure. Based on the experimental data, the sensor stability can be characterized by reading the frequency variation values. It is estimated that the temperature variation range is around $\pm 3 \sim \pm 10\ ^{o}C$ in the whole test process, demonstrating OCMI Michelson interferometer has high stability even under very high temperature environment.

The reversibility of OCMI Michelson interferometer was characterized by recording and comparing the resonance frequency shifts during temperature increasing and decreasing process. The experimental data was acquired from Michelson interferometer 1, with maximum temperature reaching 900 ^{o}C and the processed results were plotted in Figure 20-8.

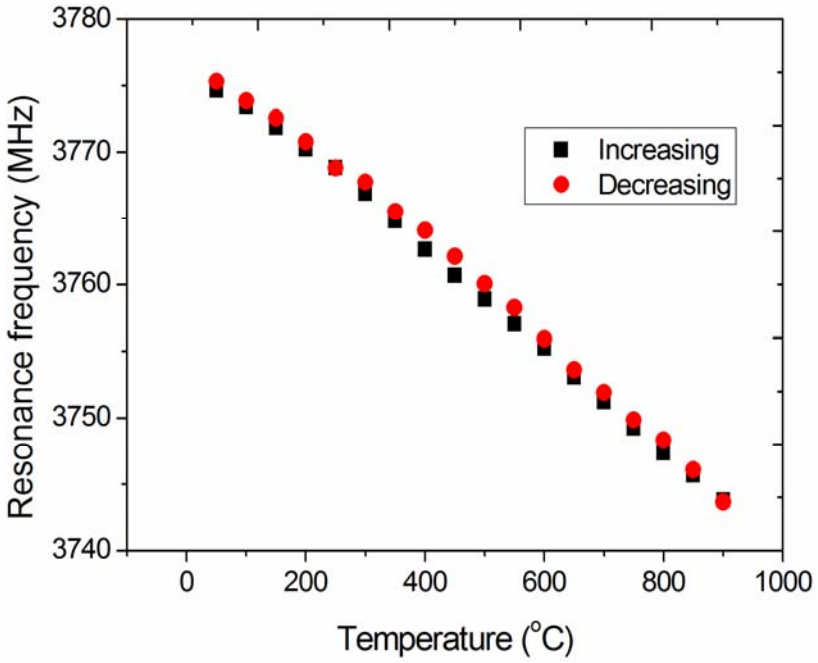

Figure 20-8. Repeatability test of temperature-induced resonant frequency shifts with OCMI based optical fiber Michelson interferometer.

This OCMI Michelson interferometer was firstly tested at temperature increasing condition, and before the temperature was decreased, this device was kept under 900 ^{o}C for 24 hours, with resonance frequency shifted a little bit to smaller frequency region. Basically, the recorded decreasing temperatures matched well with those taken at increasing procedure, meaning good reversibility can be realized using this temperature sensor, and no obvious optical hysteresis was obtained.

21. Sapphire Fiber Cladding Using Polymeric Precursor Method

21.1 Introduction

High temperature sensors capable of in-situ monitoring physical and chemical properties of gases are needed in the emerging advanced fossil fuel power plants for process control and optimization to improve energy efficiency and emission reduction [1]. Sapphire (i.e. α-phase Al_2O_3) optical fibers are promising candidates for constructing high temperature fiber optic sensors (FOSs) to meet such harsh environment analytical needs [2] because of their very high melting point (~2050^{o}C) and outstanding chemical resistances and mechanical strength at high temperature [3,4]. Pure sapphire crystals also possess excellent optical transparency over a broad spectrum covering UV to infrared (IR) wavelengths. Unfortunately, commercially available sapphire fiber waveguides are not cladded due to limitations associated with the manufacturing processes based on melting-crystallization mechanism. The uncladded sapphire fibers suffer severe losses of transmitting light intensity and interference from the environment due to the very large difference of refractive index between sapphire and the surrounding gas as well as surface scattering [5,6]. In addition, without the cladding protection, the sapphire fiber core will be quickly damaged when it directly contacts the dusty fossil fuel gases at very high temperatures. Therefore, the realization of high temperature sapphire FOS depends on the development of appropriate sapphire fiber cladding to improve the waveguide efficiency and provide fiber surface protection [7].

For applications in high temperature fossil energy production processes, such as coal-gasification and combustion, the sapphire fiber cladding material must meet several basic requirements, including a refractive index slightly smaller than that of the sapphire fiber, long-

term thermochemical stability on sapphire, inertness in oxidizing and reducing atmospheres, and coefficient of thermal expansion (CTE) close to sapphire. In the open literature, attempts have been made on developing sapphire claddings using refractory materials such as polycrystalline alumina (Al_2O_3), metal niobium, silicon carbide (SiC), and zirconia (ZrO_2) [3]. These materials have major issues of chemical or structural instabilities at high temperatures. Because of the identical chemical composition, polycrystalline alumina can readily incorporate into the sapphire phase that causes the cladding/core interface to disappear. The silicon carbide and metal cladding layers readily react in high temperature oxidizing atmospheres [8]. The zirconia cladding layer is generally ineffective for improving the waveguide efficiency because it has refractive index greater than sapphire; also zirconia experiences monoclinic-to-tetragonal phase transition at ~1000^{o}C accompanied by large volume changes which can induce structural damage in the cladding or the fiber core [9].

Spinel $MgAl_2O_4$ is a well-known refractory ceramic material with a high malting point of ~2135^{o}C [10] and a CTE (~8.1×10^{-6} $^{o}C^{-1}$ [11]) similar to that of sapphire (α-Al_2O_3, CTE ≈ 7.5×10^{-6} $^{o}C^{-1}$) [12]. The refractive index of $MgAl_2O_4$ single crystal is about 1.716 at λ = 600 nm ($dn/d\lambda$ = 0.0612 um^{-1}), which is slightly smaller than the index of sapphire single crystal (n = 1.769 at λ = 600 nm, $dn/d\lambda$ = 0.0588 um^{-1}). These basic properties of spinel $MgAl_2O_4$ are desirable for sapphire fiber cladding. The $MgAl_2O_4$ also possesses excellent chemical resistance not only in high temperature oxidizing and reducing atmospheres but also in acidic and basic environments [10]. Spinel claddings have been recently fabricated on ϕ400μm sapphire optical fibers through direct reaction between a pre-coated thick MgO or MgO/$MgAl_2O_4$ layer with the sapphire core at very high temperatures (>1500^{o}C) for a short time [13]. The spinel-cladded sapphire fibers were able to drastically reduce the numerical aperture (NA) and improve the

transmission light intensity. However, the chemical compositions of these spinel claddings were not equilibrated in the high temperature reaction process that could limit their thermochemical stability as inter-diffusion and reaction between MgO and Al_2O_3 will continue at high temperatures [13,14].

In this work, we synthesized the spinel $MgAl_2O_4$ thin film cladding on ϕ75μm sapphire fiber by a relatively low temperature process for potential high temperatures applications. The MgO-α-Al_2O_3 phase diagram contains two phase-equilibrium regimes which share a boundary of spinel phase [15]. The spinel phase at this boundary has an MgO/Al_2O_3 molar ratio ($R_{MgO/Al2O3}$) of ~1.0 which remains almost constant at temperatures up to ~1250°C. Below 1250°C, when $R_{MgO/Al2O3}$ of the entire specimen (including the coated film and sapphire substrate) is smaller than 1.0, a final equilibrium state will be reached between a $MgAl_2O_4$ ($R_{MgO/Al2O3}$ ~1.0) phase and a nearly pure α-Al_2O_3 phase; in contrast, when the overall $R_{MgO/Al2O3}$ is greater than 1.0, the system will reach an equilibrium state between an alumina-doped MgO phase and a spinel $MgAl_2O_4$ phase ($R_{MgO/Al2O3}$ ~1.0). The hypothesis of this research is that, a spinel $MgAl_2O_4$ thin film with $R_{MgO/Al2O3}$ of 1.0 can be chemically stable on the sapphire substrate at temperatures up to 1250°C because the compositions of the spinel and sapphire phases are already the same as or very close to the values of their thermodynamic equilibrium state.

Spinel $MgAl_2O_4$ materials have been synthesized by various techniques such as solid state reaction, spray drying, citrate precipitation, and sol-gel methods [10]. However, these conventional methods are ineffective for coating spinel thin films on the sapphire fibers because they employ extremely high temperature (1700-1900°C) for solid state reactions to form uniform spinel phase and for film densification to achieve sufficient refractive index. In addition, directly coating uniform inorganic solid precursor or spinel particle layer on the micron-sized cylindrical

surface is technically challenging. Here, a facile polymeric precursor based approach was used to synthesize the spinel thin film on the sapphire fiber. The polymeric precursor-based fabrication process involves the synthesis of a liquid phase metal ion chelated polyethylene glycol (M-PEG), coating of the M-PEG on the substrate surface, and conversion of the M-PEG precursor coating into a ceramic thin film by firing in air at relatively low temperatures (<800^{o}C) [16,17]. The liquid polymeric precursor is particularly convenient for coating thin films on small size substrates with complicated geometries. More importantly, this synthesis method avoids thermal treatments at extreme temperatures for the formation of dense and uniform metal oxide solutions because the constituting metal ions are mixed at molecular level with precisely controlled atomic ratio in the precursor [18,19].

21.2 Experimental Procedures

The polymeric precursor was prepared by acid-catalyzed polymerization of an aqueous solution containing ethylene glycol and metal ions with predetermined molar ratios. The general reaction process of the formation of M-PEG is shown below [16]. The metal ions (M) involved this work include Al^{3+} and Mg^{2+}.

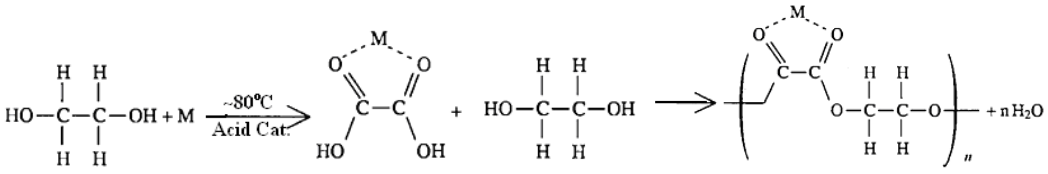

The basic procedures for the polymeric precursor synthesis, precursor film coating on sapphire wafers and optical fibers are similar to those described in our previous publications [17,19]. The starting aqueous solution for synthesizing the Al^{3+} and Mg^{2+} chelated PEG (Al+Mg-PEG) contained 0.02 mol of metal ions, 20 ml DI water, 0.02 mol glycine (used as pH buffer),

and 40 ml ethylene glycol (EG). The Al^{3+}/Mg^{2+} molar ratio in the solution was 2:1 which was obtained by dissolving 0.0133 moles of $Al(NO_3)_3 \cdot 9H_2O$ (Aldrich, 99.997%) and 0.0067 moles of $Mg(NO_3)_2 \cdot 6H_2O$ (Fluka, ≥99.0%). The polymerization was conducted at 80ºC for 144 h in a 125-ml glass flask which was placed in a gravity convection oven with its mouth open for water removal. After completing the polymerization process, the flask was sealed and cooled naturally to room temperature before being used for film coating.

The Al+Mg-PEG precursor film was coated on the single crystal sapphire fiber (<001> orientation, Micromaterials Inc.) which was 10-cm-long and 75-μm in diameter (ϕ75-μm). The polymer precursor coating was obtained by sliding a droplet of the viscous liquid M-PEG over the horizontally suspended sapphire fiber. The droplet was manually pulled by a brush tip moving back and forth along the fiber for 5 times at a speed of about 1~2 cm/s. The precursor film-coated fibers were dried in an oven at 120°C for overnight to remove water and residual volatile organics and then fired at 700 ºC in air for 90 min. The heating and cooling rates used in the firing process were 5°C/min. This three-step solid oxide film synthesis cycle, i.e. precursor film coating, drying, and firing, was repeated for multiple times to achieve desired thickness of the final oxide film.

The metal oxide thin films were also coated on single crystal sapphire wafers (<001> orientation, 2.5cm×2.5cm, Crystal Systems, MA) for studying the film microstructural, material stability, and optical refractive index. The precursor film was coated on the sapphire wafer by a programmable two-stage spin coater. The spin-coating program included an initial step of 18-second spinning at 500 rpm and a second step of 40-second spinning at 2100 rpm. The precursor-coated substrates were dried and then fired under conditions similar to those used for coating the fibers, namely drying at 120°C and then firing at 700°C for 90 min with heating and cooling rates

of 5°C/min. Multiple cycles of precursor film coating, drying, and firing was employed to achieve certain film thicknesses. In addition, powdery samples of the metal oxide materials were also prepared by drying and rapidly firing thick layers (~2 mm) of the polymeric precursor placed in large ceramic crucibles.

The polymer precursor samples were tested by Attenuated Total Reflectance (ATR; with diamond crystal) Fourier transform infrared spectroscopy (FTIR; Nicolet 7600, Thermo Scientific) in a wavenumber range of 400 ~ 4000 cm^{-1}. The pure polyethylene glycol (PEG) and ethylene glycol (EG) monomer were used as blank samples which were also tested by ATR-FTIR for comparison. The crystal phase, morphology, and chemical compositions of the synthesized metal oxide powders and films were characterized by X-ray diffraction (XRD; PANalytical X'Pert Pro diffractometer, CuKα 1.54060Å radiation, Bragg–Brentano θ-2θ), scanning electron microscopy (SEM; FEI XL-30 System, accelerating voltage 10 – 15 kV), and energy-dispersive spectroscopy (EDS; EDAX Corp., d=10mm and accelerating potential 15 keV). The refractive index (n) was measured for the films coated on sapphire wafers by ellipsometry (Woollam VASE32 ellipsometer) in a visible wavelength range of 500 – 900 nm. To investigate the thermochemical stability of the $MgAl_2O_4$ film on sapphire substrate, the samples were annealed for extended periods of time at 1000°C, 1200°C and 1300°C, respectively. The annealed samples were examined by XRD, SEM, and EDS line scanning to observe changes in crystal phase, microstructure, $MgAl_2O_4$/sapphire interface, and metal ion distribution across interface.

The effect of $MgAl_2O_4$ thin film on waveguide effectiveness of the sapphire fiber was evaluated by comparing the numerical aperture (NA = $sin(\theta)$) of the fibers with and without the $MgAl_2O_4$ coating. The apparatus for NA measurement is schematically shown in Figure 21-1. The light input to the sapphire fiber was introduced by a single mode fiber (SMF, NA=0.14,

Corning SMF-28e) which was connected to a tunable laser source. The SMF was placed on a high precision rotation stage so that the angle of input to the sapphire fiber could be varied to cover all possible excitation conditions. The output light from the other end of the sapphire fiber was received by a multimode fiber (MMF, NA=0.22, Fiberguide 105/125Y) which was connected to a photo detector (Newport 818-IR) and a power meter (Newport 2831-C). The NA measurements were performed with the distance between the light source SMF and sapphire fiber endface fixed at 2 mm, 4 mm, and 10 mm, respectively. The excitation SMF was rotated step-by-step at a small angle (θ) of 0.5^{o} or 1^{o} for each step.

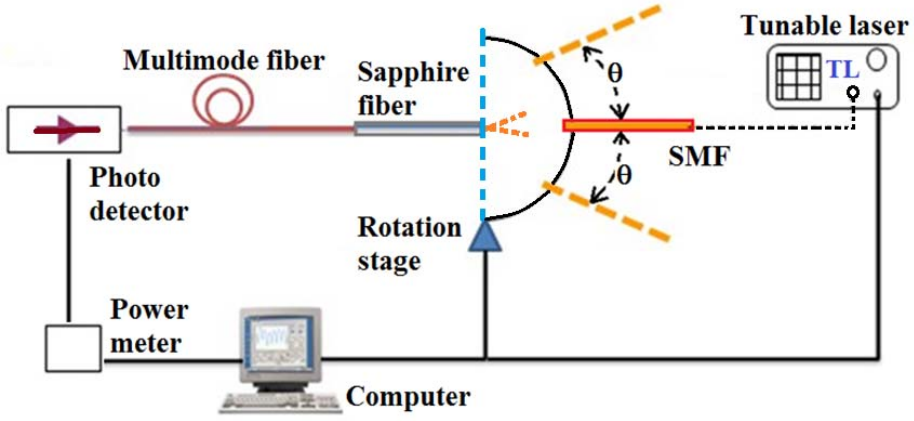

Figure 21-1. Schematics showing the apparatus for NA measurement.

21.3 Results and Discussion

The formation of the metal ion chelated polymer precursor is critical to achieving uniform metal oxide solid solution at relatively low firing temperatures. Figure 21-2 shows the FTIR spectra of the EG, PEG, and Al+Mg-PEG. The absorption peaks at ~1752 cm^{-1} and ~1632 cm^{-1} (*v*C=O), which were observed for the Al+Mg-PEG sample but not for PEG and EG, indicate the

presence of C=O double bonds resulted from metal chelates in the Al+Mg-PEG molecules [15]. Comparing with the spectrum of PEG, the new absorption peaks for Al+Mg-PEG at about 835 cm^{-1} and 925 cm^{-1} also indicate the existence of weak bonding between metal and oxygen in the chelate structure [17,20]. The results of FTIR measurements prove that the metal ions were effectively chelated onto the PEG chain.

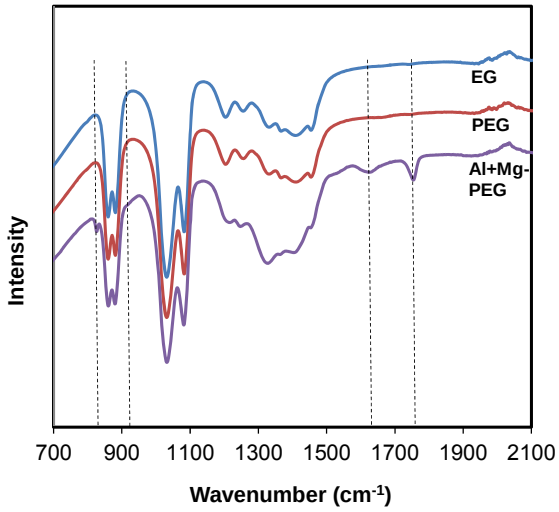

Figure 21-2. FTIR spectra of the Al+Mg-PEG precursor, metal-free PEG, and EG monomer.

Powdery samples of the solid oxide obtained by firing the Al+Mg-PEG precursor were examined by XRD to confirm the formation of spinel $MgAl_2O_4$. The solid oxide powders were fired in air for 20 h at 700°C, 1000°C, 1200°C, and 1400°C, respectively. The samples fired at 700, 1000, 1200, and 1400°C are denoted as P700, P1000, P1200, and P1400, respectively. The XRD patterns of all these samples are shown in Figure 21-3 where the standard XRD pattern of pure spinel $MgAl_2O_4$ powder (PDF-00-021-1152, JCPDS) is also included for comparison. The perfect match of 2θ positions of the XRD peaks between the spinel $MgAl_2O_4$ standard and

powder samples confirms that spinel phase was formed after firing at the low temperature of 700°C. The formation of spinel $MgAl_2O_4$ at such a low firing temperature was due to the molecular level mixing of the chelated Al^{3+} and Mg^{2+} ions on the polymer chain that instantly produces a uniform $MgO\text{-}Al_2O_3$ solid solution upon combustion of the polymer backbone [16,19]. Also, the fast firing process of the thin precursor film creates a large number of molecular oxides that leads to rapid nucleation and formation of $MgAl_2O_4$ nanocrystallites. The low intensity and broad XRD peaks of the spinel particles obtained at 700°C are characteristic of nanocrystalline microstructures. As the firing temperature increased, the XRD peak intensity increased and the peak broadness decreased because of the growth of grain size by sintering effect.

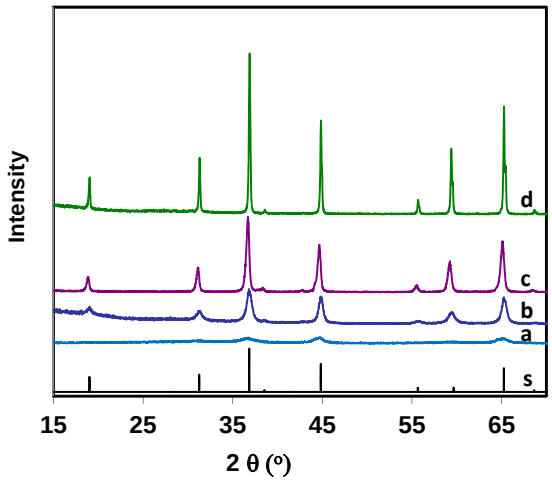

Figure 21-3. XRD patterns of the metal oxide powders obtained by firing the Al+Mg-PEG precursor at different temperatures (a: P700; b: P1000; c: P1200; d: P1400; s: standard cubic spinel $MgAl_2O_4$).

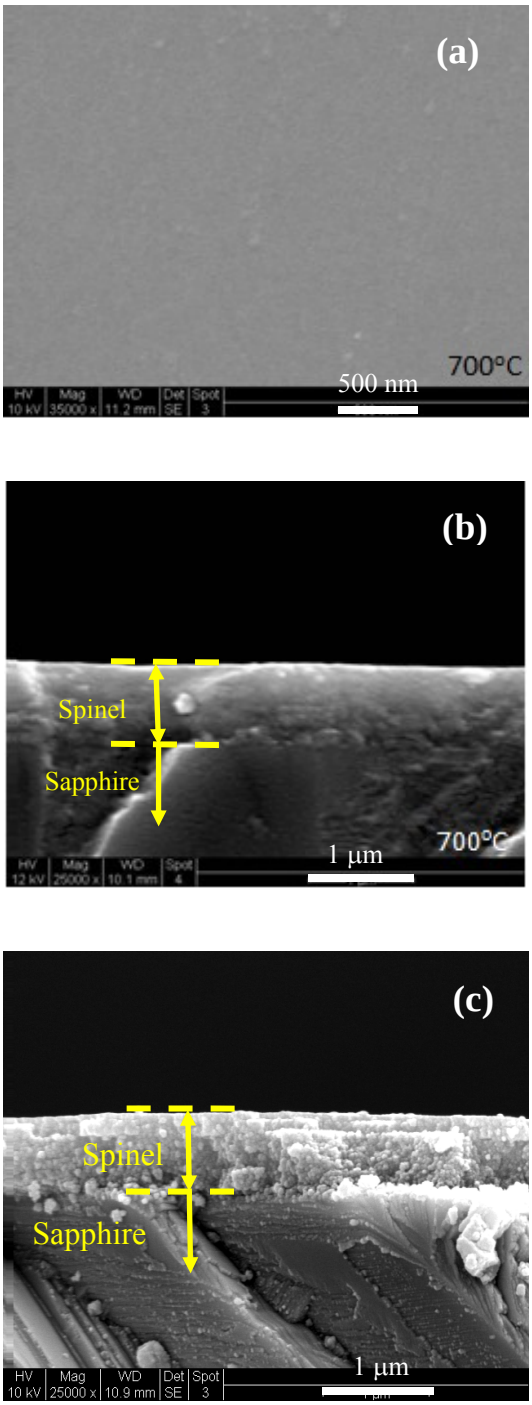

Figure 21-4. SEM images of the spinel films on sapphire substrates obtained by firing the precursor films at 700°C for 90 min (a: spinel film surface; b: cross-section of the $MgAl_2O_4$-coated sapphire wafer; c: cross-section of the $MgAl_2O_4$-coated sapphire fiber).

The $MgAl_2O_4$ films were coated on the sapphire wafers by 40 cycles of precursor spin-coating, drying, and firing process. The $MgAl_2O_4$ films on the 10-cm long sapphire fibers were obtained by 25 cycles of brush-coating, drying and firing process. The $MgAl_2O_4$ films on both the sapphire wafers and fibers were initially obtained by firing the precursor films at 700^{o}C in air for 90 min. Figure 21-4 shows the SEM images of the spinel films on the sapphire wafer and fiber. Although the numbers of coating cycles were different, the films on the wafer and fiber had similar thicknesses of ~ 800 nm because the thickness of the resultant oxide film obtained by a single spin-coating cycle (~20 nm per coating cycle) was much smaller than that of the film obtained by a single cycle of brush coating (30 – 35 nm per coating cycle).

The sapphire wafer-supported films obtained by 90-min of firing at 700^{o}C (denoted as Sp-700) were further annealed in air for 168 h at temperatures of 1000^{o}C (denoted as Sp-1000) and 1200^{o}C (denoted as Sp-1200), respectively. Figure 21-5 presents the cross-sectional SEM images of the Sp-1000 and Sp-1200 samples. As can be seen in the SEM pictures, both films had clearly defined interfaces between the $MgAl_2O_4$ film and sapphire substrate. By comparing the textures of the film cross-sections shown in the SEM images, it is quite obvious that the sample film Sp-1200 is more densified and has larger grain size than Sp-1000.

The $MgAl_2O_4$ film coated sapphire wafers, including Sp-700, Sp-1000, and Sp-1200, were also examined by XRD. The XRD patterns of these samples are shown in Figure 6 in comparison with the spectra of standard spinel $MgAl_2O_4$ powders and sapphire wafer (<001> orientation). The XRD patterns of all three samples show the characteristic peaks of $MgAl_2O_4$ and sapphire substrate without appreciable new peaks.

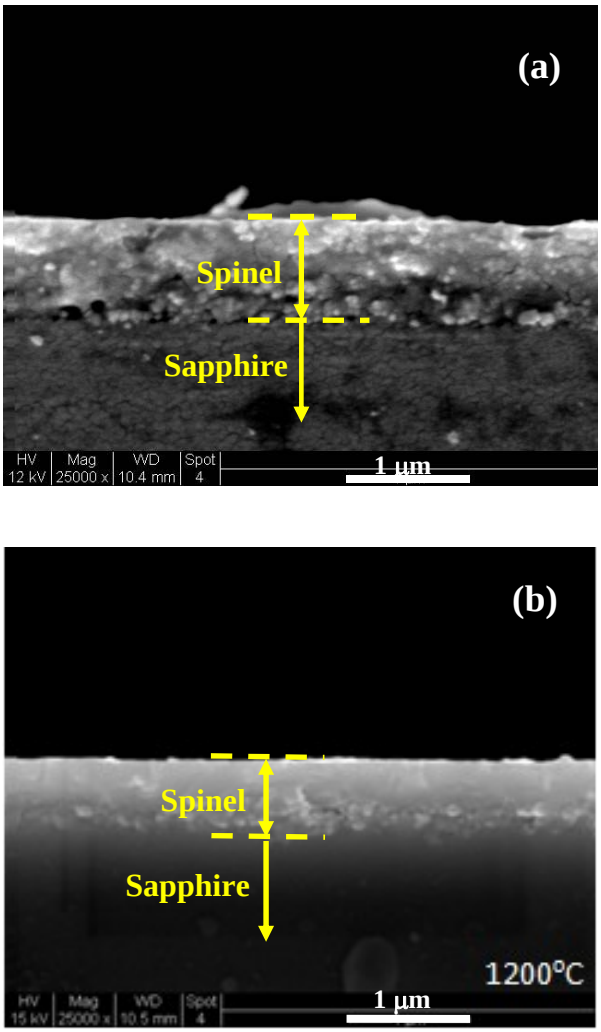

Figure 21-5. The cross-sectional SEM images of the $MgAl_2O_4$ films on sapphire wafers after 168 h of annealing at (a) 1000oC (Sp-10000 and (b) 1200°C (Sp-1200).

For the spinel peaks, the intensity increased while the broadness decreased as the annealing temperature increased because of the grain growth caused by sintering effects. A Sp-1200 sample was further annealed at 1200°C for additional 672 h. The SEM picture of the cross-section of this further annealed $MgAl_2O_4$ film (not shown) was not visibly different from the image of the original Sp-1200 shown in Figure 21-5 (b). EDS line scanning was performed for the Sp-1200 after the 672-h annealing process. The line canning started from surface of the $MgAl_2O_4$ film and ended deep inside the sapphire substrate. The results of EDS line scanning along the film

thickness are presented in Figure 21-7. As can be seen in Figure 21-7, the Mg^{2+} was observed only within the thickness of the $MgAl_2O_4$ film, confirming that solid state diffusion of Mg^{2+} into the sapphire substrate was not appreciable during the long-time annealing at 1200°C. The extraordinary thermochemical stability of the $MgAl_2O_4$ coating on the sapphire surface was obtained because the spinel film had a pre-made composition (i.e. $R_{MgO/Al2O3} \approx 1.0$) that is the same as or very close to that required for establishing equilibrium state with the sapphire (α-Al_2O_3) phase at temperatures up to 1250°C. Because at phase equilibrium state, there is no driving force for net ion transfer or element redistribution across the interface of the two phases, the $MgAl_2O_4$ film is able to achieve long-term stability at <1250°C.

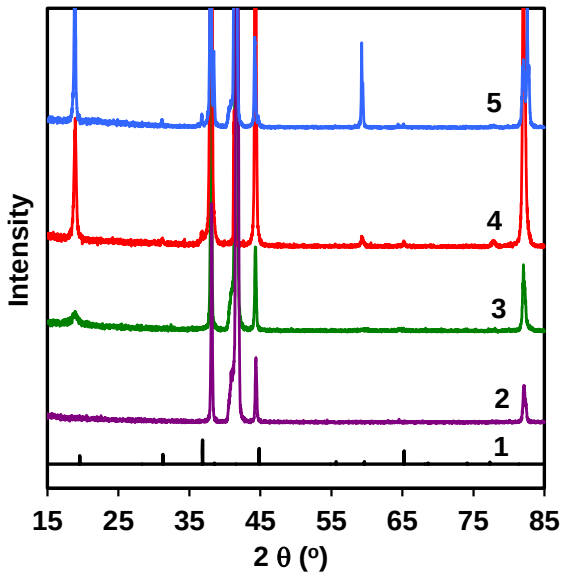

Figure 21-6. XRD patterns of the sapphire wafer-supported spinel films annealed at different temperatures (1: standard of spinel $MgAl_2O_4$; 2: sapphire substrate; 3: Sp-700; 4: Sp-1000; and 5: Sp-1200).

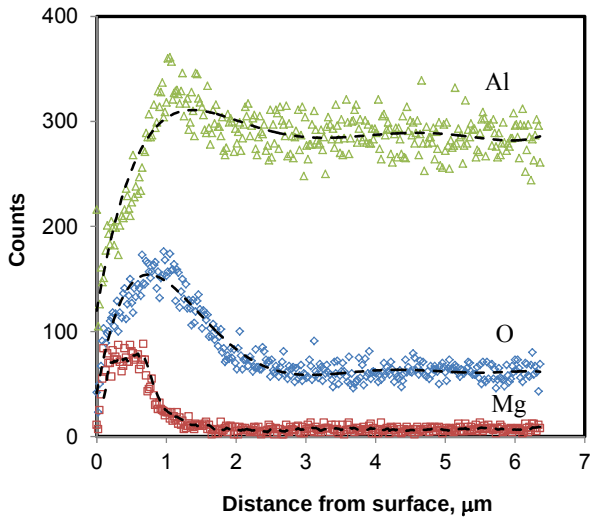

Figure 21-7. Results of EDS line scanning along the $MgAl_2O_4$ film thickness for Sp-1200 after further annealing at 1200°C for 678 h.

According to the MgO-Al_2O_3 binary phase diagram shown in Figure 21-8 [21], the equilibrium composition of the spinel phase and the mass distribution between the two phases will change rapidly when temperature exceeds 1250°C. When the compositions change to reach a new equilibrium state at a higher temperature (>1250°C), $R_{MgO/Al2O3}$ in the spinel film becomes less than 1.0 as a results of Mg^{2+} and Al^{3+} diffusion across the interface. Therefore, such a change of equilibrium compoistion at >1250°C is expected to make the spinel/sapphire interface disappear because of the solid state reaction at the interface. To study the morphological change of the sapphire supported $MgAl_2O_4$ film at >1250°C, a 2.5cm×2.5cm Sp-700 sample was cut into two pieces which were then annealed at 1300°C for 24 h and 48 h, respectively. The cross sections of the two films were examined by SEM as shown in Figure 21-9. The spinel-sapphire two-layer structure remained distinguishable after being annealed at 1300°C for 24 h but became completely undistinguishable after 48 h of annealing at 1300°C. These observations prove that spinel $MgAl_2O_4$ is thermodynamically unstable on the sapphire surface at >1250°C. Based on the

results of the current study, it can be concluded that the spinel $MgAl_2O_4$ film (with $R_{MgO/Al2O3}$ ~1.0) can maintain long-term stability on the sapphire substrate below 1250°C but becomes thermodynamically unstable when temperature exceeds 1250°C.

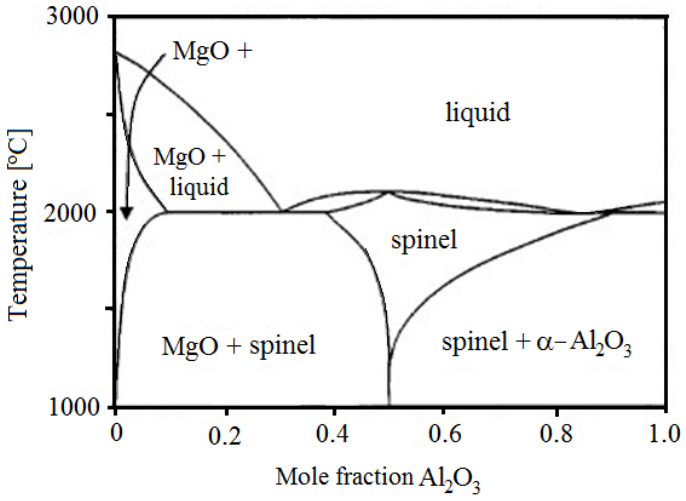

Figure 21-8. Phase diagram of the MgO-α-Al_2O_3 binary system [21].

The refractive indices of the sapphire wafer-supported spinel films fired at 700°C (Sp-700), 1000°C (Sp-1000) and 1200°C (Sp-1200) were measured by ellipsometry in a wavelength range of 500 ~ 900 nm. The results of the ellipsometric measurements are shown in Figure 10. The refractive index of the spinel film increased with increasing the annealing temperature because of the enhanced densification of the $MgAl_2O_4$ film at higher temperatures. The refractive indices of the films annealed at 1000°C and 1200°C for 168 h were close to the value of single crystal spinel. For example, at λ = 600 nm, the refractive indices of Sp-1000 and Sp-1200 were 1.611 (i.e. ~94.9% of the single crystal value) and 1.660 (~96.8% of single crystal value), respectively. The refractive indices of the Sp-1000 and Sp-1200 are slightly smaller than the sapphire single index (n = 1.769 at λ = 600 nm) that makes them optically suitable for sapphire fiber cladding. The Sp-700 had a refractive index value of 1.522 at λ = 600 nm (88.7% of the single crystal

index) that is significantly smaller than that of the sapphire single crystal. Thus, the $MgAl_2O_4$ film fired at 700°C may be inappropriate for high temperature sapphire fiber cladding because the film density will inevitably increase to cause large changes in its index at application temperatures higher than 700°C.

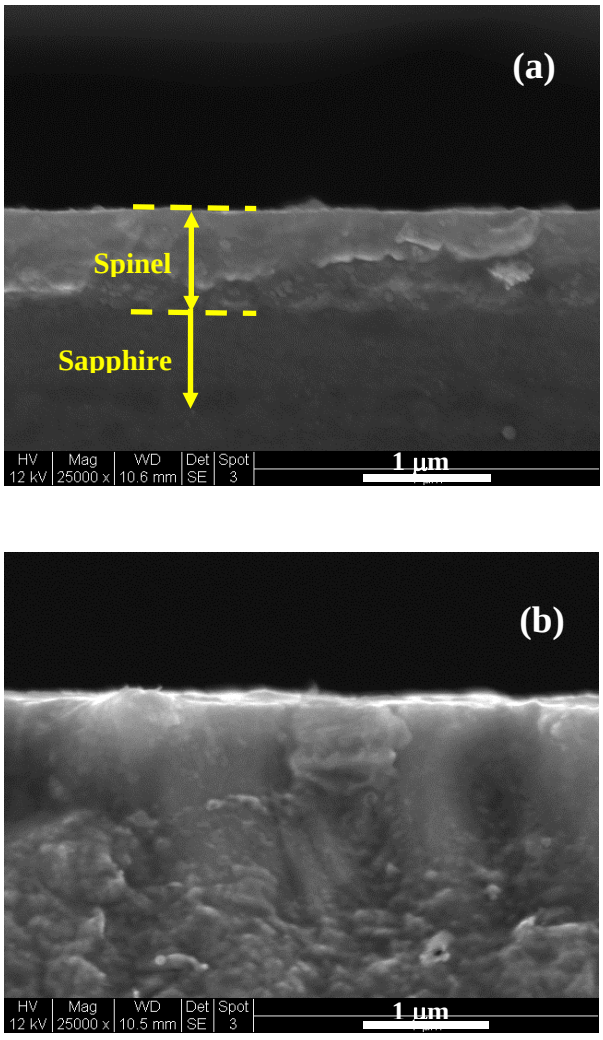

Figure 21-9. The cross-section SEM images of the spinel films on sapphire wafers after being annealed at 1300°C for (a) 24h and (b) 48h, respectively.

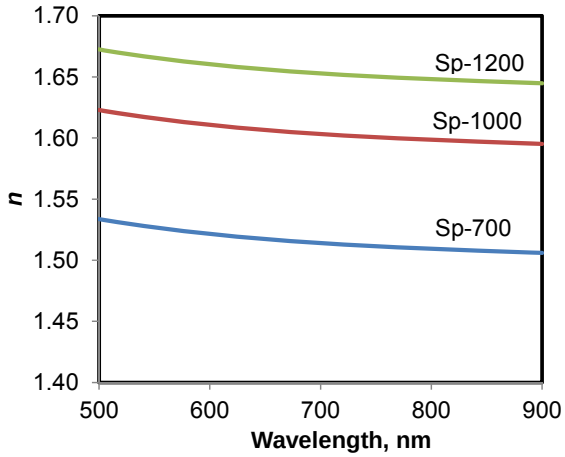

Figure 21-10. Refractive index (n) for the spinel films on sapphire after annealing at different temperatures.

To study the cladding effect, the 800-nm-thick $MgAl_2O_4$ film coated sapphire fiber (Figure 21-4 (c)) was tested by NA measurement after being annealed at 1000°C for 168 h. The sapphire fiber used in NA measurements was 8-cm-long after cutting and polishing the two ends. The NA measurements were performed for three different distances (d = 2, 4, and 10 mm) between the end of the light source SMF and the input end of the sapphire fiber. An uncoated blank sapphire fiber of same length was also tested under identical conditions for comparison. The results of the measurements are presented in Figure 21-11 and Table 21-1. The NA value reflects the reception angle (2θ) of the cone of light that can be admitted into the sapphire fiber. For an optical fiber, small values of NA (=sinθ) indicate high waveguide effectiveness in terms of preserving the transmitting optical signal intensity and integrity that is critical to fiber optic sensor development. Compared to the uncoated fiber, the 2θ and NA values of the spinel-coated sapphire fiber were significantly reduced. The detected power distribution curves of the spinel-coated fiber are smoother and the peak intensities are stronger than those of the uncoated fiber. In addition, the 2θ value of the coated fiber was essentially independent of its distance from the light source

SMF while the 2θ value of the uncoated fiber increased significantly as this distance increased from 2 to 10 mm. These results demonstrate that the $MgAl_2O_4$ thin film after annealing at high temperature (e.g. >1000°C) can be used as effective cladding for the sapphire fiber.

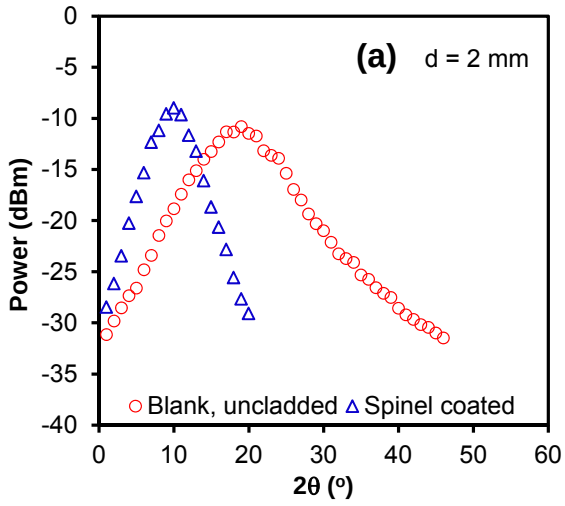

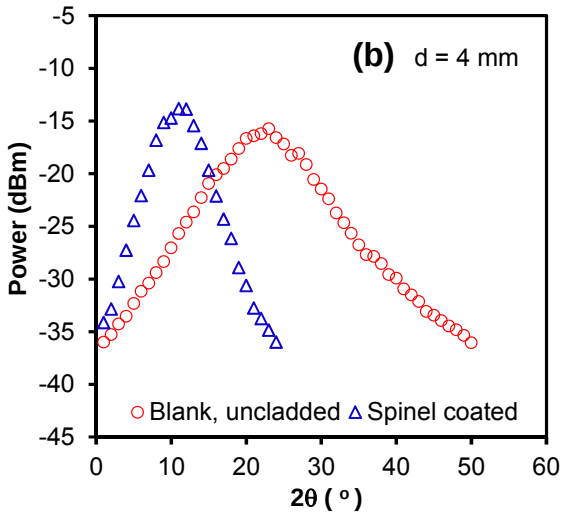

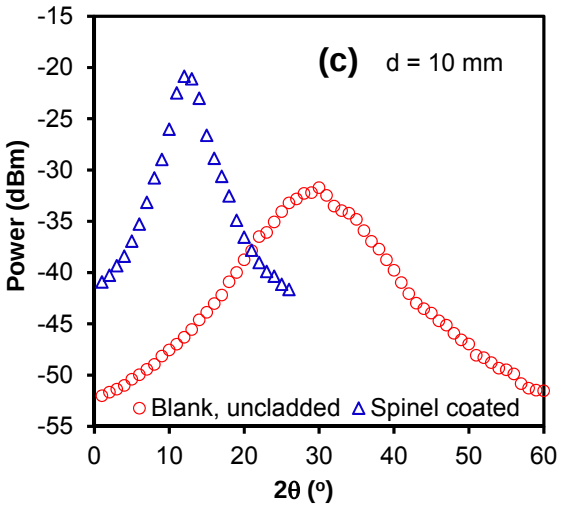

Figure 21-11. Results of NA measurements for the uncoated and $MgAl_2O_4$-coated sapphire fibers (source light λ: 1520 ~ 1560nm): (a) d = 2 mm; (b) d = 4 mm; and (c) d = 10 mm.

Table 21-1 Results of NA measurements for the uncoated and spinel-coated sapphire fibers (determined at output power of 1% of the maximum power)

	2θ (NA=Sinθ)		
Distance, mm	2	4	10
Uncoated	41º (0.350)	48º (0.407)	58º (0.485)
Spinel-coated	22º (0.191)	23.5º (0.204)	23.5º (0.204)

21.4 Summary

The spinel $MgAl_2O_3$ thin films were coated on the ϕ75-μm single crystal sapphire fiber and sapphire wafer using the facile polymeric precursor method. The polymeric precursor method avoids the extremely high temperature treatments that are needed for the conventional synthesis techniques to achieve dense $MgAl_2O_4$ films. The spinel films were demonstrated to possess long-term thermochemical stability on the sapphire substrate at up to 1200^{o}C. The extraordinary stability of the $MgAl_2O_4$/sapphire layered structure is based on a unique thermodynamic property that the spinel $MgAl_2O_4$-sapphire (α-alumina) equilibrium compositions remain virtually independent of temperature up to ~1250^{o}C. The $MgAl_2O_4$ films, after being annealed at 1000^{o}C and 1200^{o}C, obtained refractive indices which were close to its single crystal value and meanwhile slightly smaller than the index of the sapphire single crystal. The 800-nm-thick $MgAl_2O_4$ film coated sapphire fiber was able to dramatically reduce the NA values and improve the transmitting light intensity as compared to the uncoated fiber. Results of this research demonstrate that the spinel $MgAl_2O_4$ films are suitable as sapphire fiber cladding for long-term applications at high temperatures of up to 1200^{o}C. Although we are currently unable to anneal the $MgAl_2O_4$-coated fiber at above 1000^{o}C due to the small chamber size of our high temperature furnace, it is anticipated that annealing at 1200^{o}C will further improve the cladding effectiveness and long-term stability in applications at <1200^{o}C. Our future research will be directed to further understanding the effects of annealing temperature and duration and spinel film thickness on the cladding effect and structural stability at high temperatures. Improvement of the coating technique is also needed for reducing the required coating cycles and enhancing the fabrication efficiency.

21.5 References

1. B.T Chorpening, D. Tucker, S.M. Maley, IEEE Sensor 1-3 (2004) 1153.
2. J.T. Wu, K.L. Deng, Z. Wang, B. Lee, R. Guida, in: F.T.S. Yu, S. Yin (Ed.), Photorefractive Fiber and Crystal Devices: Materials, Optical Properties, and Applications XII, SPIE Proceedings, 6314 (2006) Z3140.
3. J.R. Pedrazzani, In: A. Mendez, T.F. Morse (Ed.), Specialty Optical Fibers handbook, Elsevier, Burlington, USA, 2007, p651.
4. D.H. Jundt, M.M. Fejer, R.L. Byer, Appl. Phys. Lett. 55 (1989) 2170.
5. X. Fang, R.G. May, A.Wang, R.O. Claus, Sensor Actuat A-Phys. 44 (1994) 19
6. M. Busch, W. Ecke, I. Latka, D. Fischer, R. Willsch, H. Bartelt, Measure. Sci. Technol. 20 (2009) 115301.
7. L.H. Ye, Z.P. Shen, L.M. Tong, Y.H. Shen, in: J. Yao, Y. Ishii (Ed.), Advanced Materials and Devices for Sensing and Imaging, Proceedings of SPIE 4919 (2002) 161.
8. A.R. Raheemkizchery, S.B. Desu, R.O. Claus, in: E. Udd (Ed.), Fiber Optic Smart Structures and Skins II, Proceedings of IEEE, 1170 (1990) 513.
9. J.B. Davis, L.P.A. Lofvander, A.G. Evans, E. Bischoff, M.L. Emiliani, J. Am. Ceram. Soc. 76 (1993) 1249.
10. L.R. Ping, A.M. Azad AM, T.W. Dung, Mater. Res. Bull. 36 (2001) 1417.
11. H.L. Tang, J. Xu, H.J. Li, Y.J. Dong, F. Wu, M.Q. Chen, J. Alloy Compd. 479 (2009) L26.
12. G. Han, J. Ryu, W.H. Yoon, J.J. Choi, B.D. Hahn, J.W. Kim, D.S. Park, C.W. Ahn, S. Priya, D.Y. Jeong, J. Appl. Phys. 110 (2011) 124101.
13. M.A. Janney, R.G. May, S.D. Nunn, Cladding for High Temperature Component and Method of Making Same, U.S. Patent # 6968114 B2 (2005).
14. J. Shen, Y. Shen, Sensors and Actuators A 147 (2008) 99.
15. H.A. Prescott, Z.J. Li, E. Kemnitz, A. Trunschke, J. Deutsch, H. Lieske, A. Auroux, J. Catal. 234 (2005) 119.
16. H.U. Anderson, M.M. Nasrallah, C.C. Chen, (1996) US Patent No. 5,494,700.
17. K. Remmel, H. Jiang, X. Tang, J. Dong, X. Lan, H. Xiao, Sensor Actuat B-Chem. 160 (2011) 533.

18. A. Kulkarni, A. Bourandas, J. Dong, P.A. Fuierer, H. Xiao, J. Mater. Res. 21 (2006) 500
19. X. Tang, K. Remmel, X.W. Lan, J. Deng, H. Xiao, J. Dong, Anal. Chem. 81 (2009) 7844.
20. Z.M. Ni, A.M. Chen, C.P. Fang, L.G. Wang, W.H. Yu, J. Phys. Chem. Solid. 70 (2009) 632
21. B. Hallstedt, J. Am. Ceram. Soc. 75 (1992) 1497.

22. Sapphire Fiber Sensor Packaging

22.1 Introduction

To be able survive and operate in any high temperature, high pressure harsh environment, the sensor has to be properly packaged. Although an assembly-free sensor fabricated by fs laser micromachining has greatly improved the survivability of the sensor device, the sensor still needs to be properly packaged no matter how simple it becomes. To package the developed sapphire fiber sensors, there are two critical technical challenges that must be resolved. The first challenge is to permanently connect the sapphire fibers with fused silica optical fibers. This is not only to save the cost because sapphire fibers are expensive, but also to improve the optical performance because sapphire fibers have a much larger optical loss than a fused silica fiber. It is common to use sapphire fibers in a high temperature environment while the rest of the system is placed in a low temperature environment. However, due to the crystal nature of sapphire fibers, it is very difficult to fusion splice them together just like fusion splicing two glass fibers together. In this project, we have developed a special fusion splicing program to permanently join a sapphire fiber and a fused silica fiber together.

Another challenge is to design and implement a sensor package to protect the sensor from the adverse environment. The protections include reducing the chance of breakage caused by excess heat, avoiding optical contaminations to the sapphire sensor, relieving thermal stresses caused by high temperature, and assisting sensor mounting to the equipment under monitoring. In the project, we have designed, implemented and tested a package to host the developed sapphire fiber sensors for temperature measurements inside a hot zone. The package for sapphire fiber based pressure and strain sensors can follow the similar design guidelines.

22.2 Fusion Splice a Sapphire Fiber with a Silica Fiber

It has barriers to splicer silica fiber and sapphire fiber together using traditional fusion method because there are differences in their physical properties, including differences in thermal expansion coefficients and the 400ºC difference in their melting points. Fortunately, we found a method to permanently spice the sapphire fiber with a regular silica fiber. The method was based on a large-core fusion splicer (3SAE)—LDS, which is designed for splicing optical fibers and other optical devices that are beyond the capability of conventional optical fiber splicers. The LDS is a semi-automated fiber processing station that provides far more range of positioning adjustment than conventional optical fiber splicers. Depending on different selected options, up to ten separate angular and positional axes can be controlled, allowing unprecedented adjustment of the geometry of the splice. Therefore, by adjusting different options, we could change the preheating/heating/annealing arc power, fusion position, fusion pushing force, annealing pulling force, to perform our experiments. Moreover, the Ring of Fire technology provides a highly controllable plasma field that completely surrounds the fibers for even heat distribution. Basically, the adjustable positioning features and the Ring of Fire plasma technology allow us access the operation of splicing sapphire fiber and silica fibers together, manually or semi-automatically.

First, the fusion position needs to be determined. We placed the arc probes surrounding the sapphire fiber side (typically with 300~400 μm offset) because sapphire fiber has much higher melting point, larger thermal expansion coefficient (CTE) and better heat transfer capability. As the splicing process started, the large CTE will induce the sapphire fiber to expand itself, which is equivalent to a ‘push’ movement towards the silica fiber; then a slightly push was applied to contact the sapphire fiber with silica fiber and these two fibers began to be fused together. The

third procedure, which is called as annealing treatment, is critical in the whole splicing process. The arc power needs to be gradually lowered until the fibers stopped glowing, so that the fibers would not separate due to the rapid change in temperature. The heating area before and after fusion, sapphire and silica fibers are shown in Figure 22-1. The diameters of the sapphire fiber and silica fiber are both 125 micron. In this figure, a piece of single crystal sapphire fiber (125 μm in diameter and 1.8 m in length) was successfully fused with a multimode fiber. A series of sapphire fiber with different lengths were also successfully fused with multimode silica glass fibers.

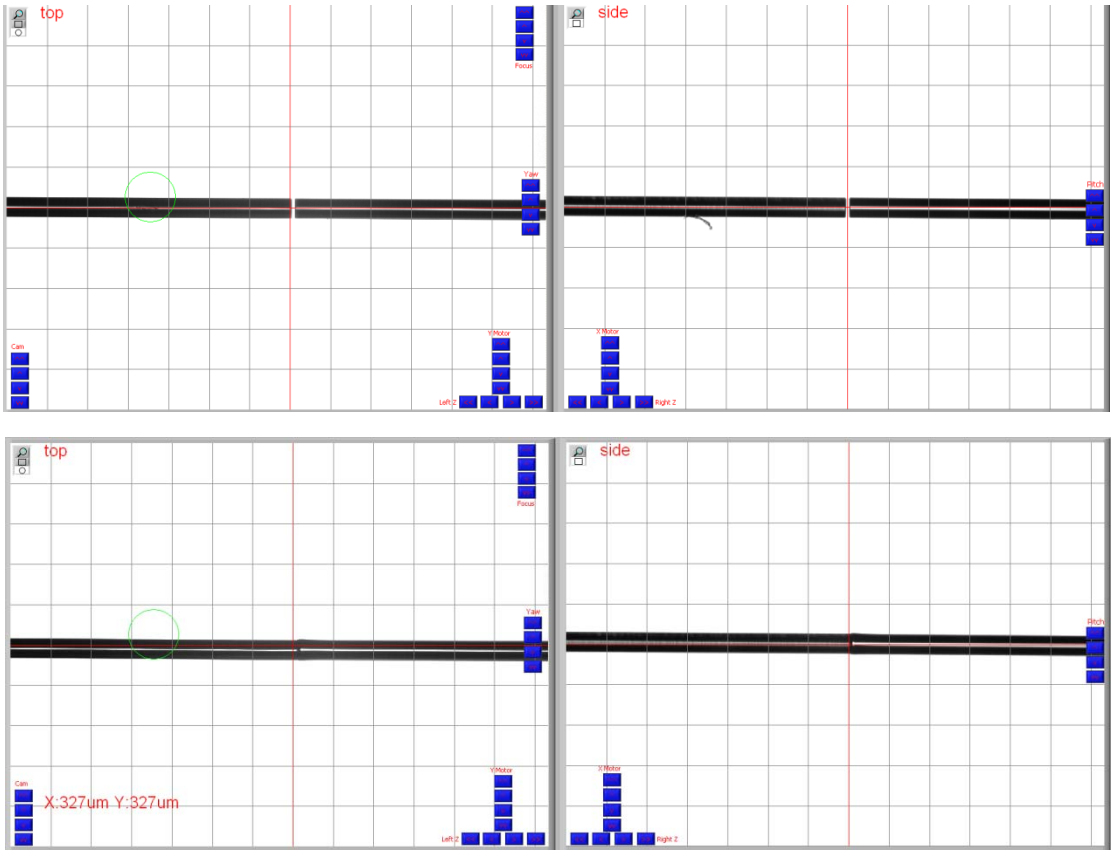

Figure 22-1. Images of two fusion points of the sapphire fibers and the silica with top views (left) and side views (right).

As shown in Figure 22-1, two pieces of single crystal sapphire fibers (125 μm in size) were successfully fused with the multimode fibers. The splice points were examined through the OCMI system, which was delivered to the fusion filed to in situ monitor the quality of the fusion point, as shown in Figure 22-1. We modified the fusion system by adding a measurement system and an improved recipe to ensure that we can obtain two balanced reflection beams. The measurement system consists of an optical source, a high speed photo detector and a vector network analyzer that synchronizes the light modulation and signal detection.

As shown in Figure 22-2 (a), a laser diode (LD) with the bandwidth of around 1 nm is directly modulated by the microwave signal from the Port 1 of the VNA. The center wavelength and the modulation bandwidth of the light source are 1307 nm and 300 KHz to 6 GHz, respectively. The microwave-modulated light is sent into one arm of the 2x2 coupler. The fiber coupler is used to route the input microwave-modulated light into and the output signal out of the Michelson interferometer. After reflected from the sapphire fiber endfaces, the beams are detected by a high speed photodetector (PD) via another arm of the coupler. The photodetector has a detection bandwidth of 6 GHz and a multimode detection area of 62.5 μm in diameter and is connected to Port 2 of the VNA, where the amplitude and phase of the signal are extracted. By sweeping the VNA frequency, the microwave spectrum of the Michelson interferometer is obtained (i.e., the S21). By extracting the time domain signal, two reflection beams can be identified with distinguished amplitudes, as shown in Figure 22-2 (b).

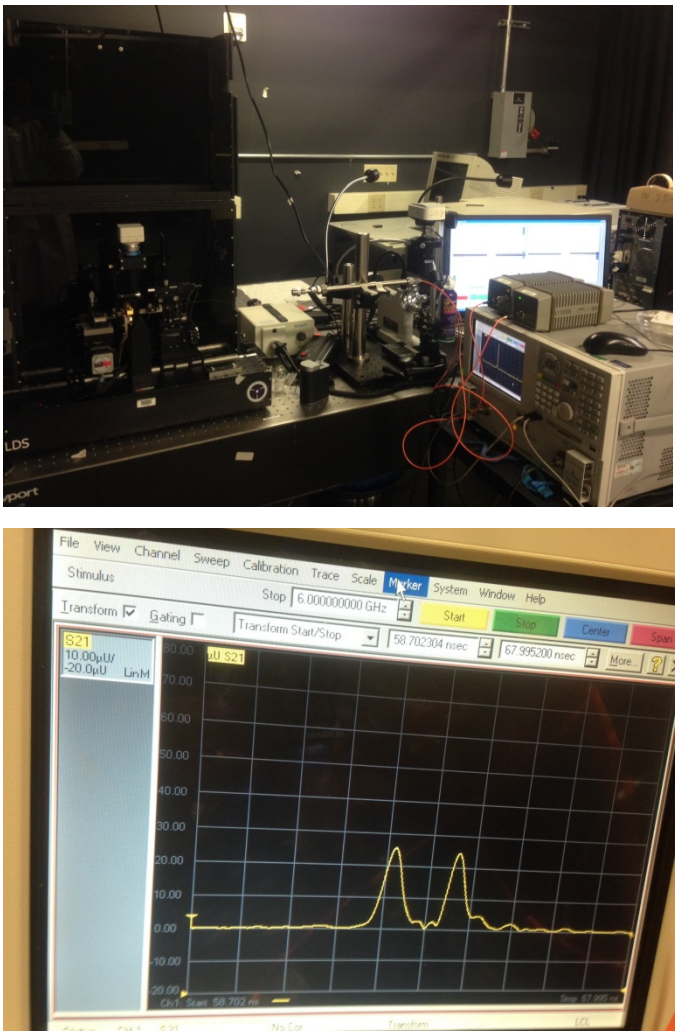

Figure 22-2. (a) Photograph of the improved fusion system with the in situ monitoring capability, including large fusion splicer, a VNA, a light source, a photo detector, the packaging tube and lead-in fibers; (b) two balanced reflections in the time domain.

Our target is to make the two reflections have the same amplitudes using the improved fusion recipe, which is achieved by fine tuning different fusion parameters and adding another fusion circle after the first annealing treatment. The second fusion circle re-heats the joint with minor pushing force and gentle plasma flame. The critical part is combining the monitoring system and fusion splicing process together. The monitoring results provide a feedback to the re-fusion

process and ensure the final balanced amplitudes. So far, we have improved the reflection power by using this method and better interference spectrum has been obtained.

22.3 Packaging Sapphire Fiber High Temperature Sensors

To provide good mechanical stability without compromising the optical response of the senor, as well as to protect the fiber sensor from other damaging effects induced by harsh industrial environments, we have designed the sensor packaging as detailed in Figure 23-3.

The package design has considered many factors to enhance the sensor survivability and long term stability by minimizing the adverse impacts from the harsh environment. The sensor package has two general sections: 1) the hot zone which is mainly made of a ceramic tube with two bored inner holes to host the sapphire fiber sensor and 2) the lead zone which is mainly made of stainless steel tubes and fittings to protect the lead-in fibers, the fiber coupler, and to reduce the stresses on the fiber.

To minimize the contact loss of the uncladded sapphire fibers, a number of ceramic ferrules were evenly spaced to support the fiber inside the ceramic tube. The ferrules have an inner diameter of 130 μm, which fits the sapphire fibers with a diameter of 125 μm. The outer diameter of the ceramic tube is a little smaller than the inner diameter of the stainless steel tube so that the ceramic tube can be inserted into the stainless steel tube and fixed using high temperature ceramic adhesives.

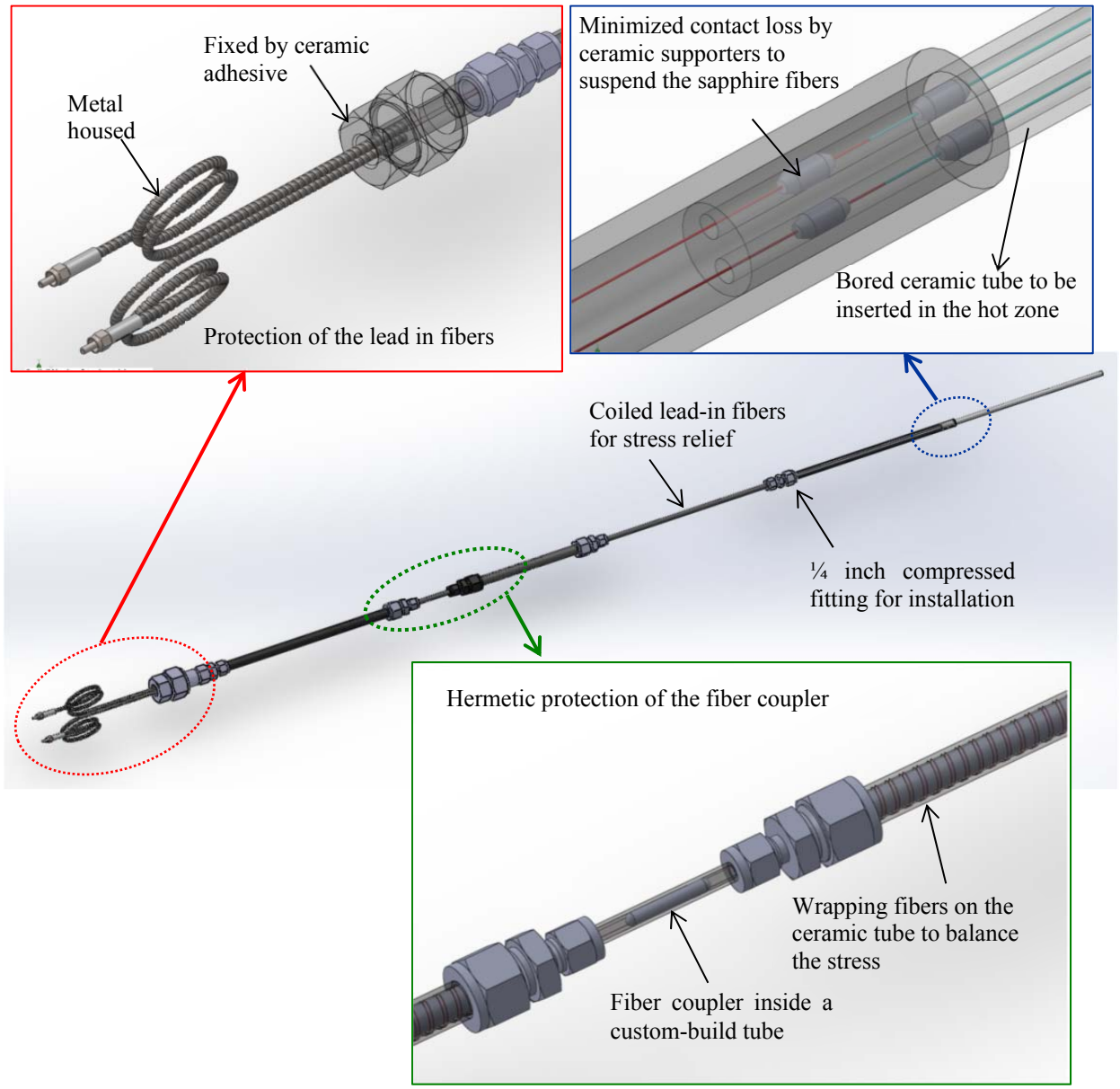

Figure 22-3. 3D CAD drawing of the packaged sapphire fiber sensor.

Stainless steel tubes and fittings were used to construct the lead-in fiber protection section of the packaged sensor. The insertion portion is designed to interface a ¼ inch port using a compressed fitting for easy sensor installation. After the insertion port, a ¼ inch stainless steel tube is used to host another section of ceramic tube. The lead-in fibers were co-wrapped around

the ceramic tube to minimize the thermal expansion induced stress. As the temperature changes, the two lead-in fibers varied at the same rate. As a result, the mismatches between the two leads are minimized. This section of 1/4" tube is also useful to provide a better adjustability for different length of extending fibers. At the end of the stress relief section, another section of 1/4" tube is added for protection of the fiber coupler. At the very end of the sensor packaging, a custom-machined fitting is used to host two metal housed flexible fiber cables with FC connectors for optical connections.

22.4 Preliminary Tests of the Packaged Sapphire High Temperature Sensors

Figure 22-4 shows the photograph of a fully assembled/ packaged sapphire fiber sensor, with its ceramic tip inserted into the high temperature furnace at a temperature of 1450℃.

Figure 22-4. Fully packaged sapphire fiber sensor inserted into a hot furnace. The sapphire sensor showing is the longest sensor for the purpose of in situ monitoring of the gasification process (to be inserted from the top). Other sensors with shorter lengths are being constructed for monitoring other power systems such as a gas turbine.

A packaged sensor has been placed inside the furnace for 10 hours. The sensor have successfully survived the high temperature of 1400°C. Figure 22-5 shows the time domain signal of the sensor, where the two reflections have good contrast and signal-to-noise ratio when the sensor is placed in the high temperature zone. The results indicated that the packaged sensors successfully survived the high temperature environment.

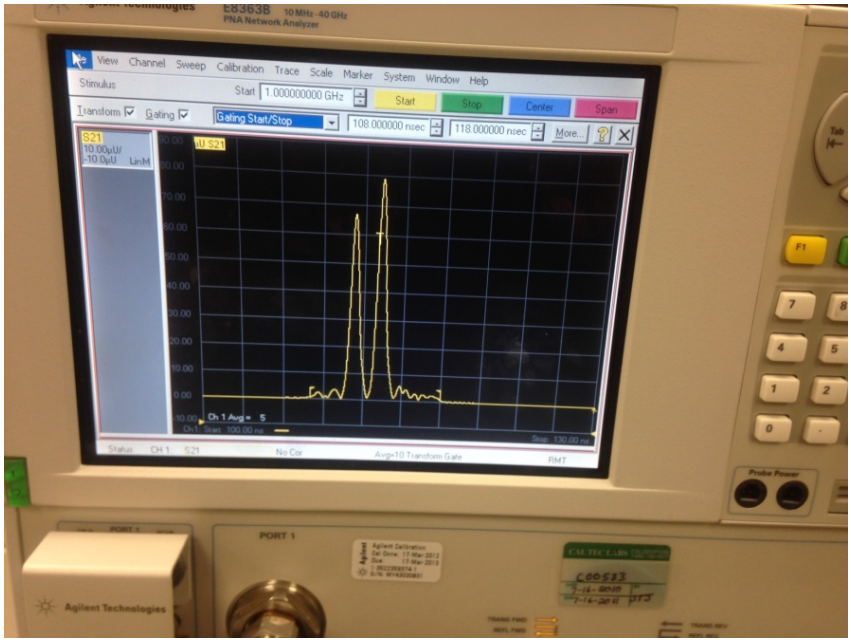

Figure 22-5. Time domain reflections of the packaged sapphire fiber sensor at a high temeprature of 1000°C. The sensor successfully survived the high temperature.

23. Sapphire Fiber OCMI Sensor for High Temperature Sensing

23.1 Introduction

Silica glass optical fibers have been extensively used for sensing applications in the past few decades, showing advantages such as low loss, light weight, immunity to electromagnetic interference, and resistance to corrosion [1]. However, when used in harsh environments, especially in high temperatures above 1000 °C, the softening of the silica glass material and the diffusion of the dopants (e.g., Germanium) inside the fiber core raised a concern on the long-term stability of the sensors. For better survivability and stability in high temperatures, single-crystal sapphire optical fibers have been used for sensor development due to their high melting point (2040 °C) and hardness [2].

Sapphire material has low transmission loss in a wide spectrum range and a large numerical aperture [2]. The early sapphire optical fiber sensors utilized these features for temperature measurement by coating the fiber tip with a thin layer of metal and monitoring the blackbody (thermo) radiation [3, 4]. The blackbody radiation based temperature measurement worked well at high temperatures but had low resolution at the low temperature region. Later, various sensor devices, e.g., fiber Bragg gratings [5-7] and Fabry-Perot interferometers [8-10], have been developed using sapphire fibers aiming to enhance the measurement resolution as well as for measurements of other parameters such as strain and pressure.

However, sapphire fibers are highly multimode owning to their large core diameters, uncladded structure and large numerical apertures. As a result, it is generally very difficult to make sapphire sensors with satisfactory performance. Despite high temperature coatings [11-13] have been developed to improve the waveguiding properties by decreasing the numerical

aperture to a certain degree, the optical mode number was still larger than the conventional multimode fiber. Because of the multimodal influence, it is difficult to fabricate a Bragg grating or an interferometer using a sapphire fiber with good signal quality. For example, to construct a Fabry-Perot interferometer on a sapphire fiber, the two reflectors must be precisely fabricated with good smoothness and aligned exactly in parallel. An angle of 10^{-2} misalignment could reduce the fringe visibility significantly [14]. In addition, the input light source must be well collimated to reduce the number of excited optical modes. While most of the sapphire fiber sensors are based on optical DC detection, the background blackbody radiation in the sapphire material at high temperatures may severely interfere with the sensors' signals. In summary, the combination of multimodal influence, requirement of high fabrication precision and interference of background blackbody radiation have placed a bottleneck on the development of high quality sapphire fiber sensors.

A research area known as the microwave-photonics has been explored over the past 30 years aiming to bring together the strengths from both microwave and optics. It intrigued us to explore the possibility of combining microwave and optics for sensing applications, which has led to our recently proposed concept of the optical carrier based microwave interferometry (OCMI) [15, 16]. By interrogating an optical interferometer in microwave domain, the OCMI concept integrates the strengths of optics and microwave, providing several unique features that are particularly advantageous for sensing application, including low dependence on the types of optical waveguides, insensitive to variations in optical polarizations, high signal quality, relieved fabrication requirements, and spatially continuous distributed sensing. In addition, OCMI uses coherent detection in which the modulation, detection and demodulation are all synchronized and

phase-locked to the same microwave frequency. The influence of background blackbody radiation can be drastically reduced when the sensor is used in high temperatures.

In this project, we developed a microwave interrogated sapphire fiber Michelson interferometer for high temperature sensing using the OCMI technology. The OCMI concept can also be implemented for other types of sapphire fiber interferometers such as a Fabry-Perot or Mach-Zehnder configuration. The interferometric sensor can also be used for measurement of other parameters such as strain and pressure in high temperatures.

23.2 Experiments

While there are many ways to implement the OCMI concept, Figure 23-1 illustrates an example system configuration where a microwave vector network analyzer (VNA) is used as the microwave source and signal detector. A broadband light source (BBS) with the bandwidth of 50 nm is intensity modulated using an electro-optic modulator (EOM) driven by the microwave signal from the Port 1 of a VNA (HP 8753es). The VNA output is amplified to achieve a high modulation index. A fiber inline polarizer and a polarization controller are used for better modulation. The modulated light is then sent into an optical interferometer (the sapphire fiber sensor) whose output is detected by a high speed photodetector. The photodetector has a detection bandwidth of 6 GHz and a detection area of 62.5 μm in diameter. A 3 dB fiber coupler is used to route the input microwave-modulated light into and the output signal out of the fiber sensor. After DC-filtering, the photodetector output is connected to Port 2 of the VNA, where the amplitude and phase of the signal are extracted. By sweeping the VNA frequency, the microwave spectrum of the sensor is obtained (i.e., the S_{21} of the VNA).

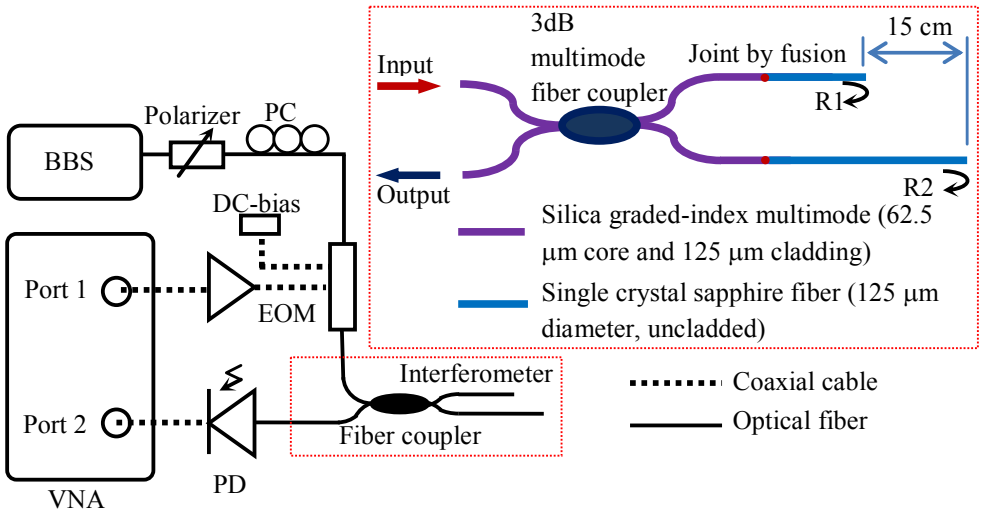

Figure 23-1. Schematic of an OCMI interrogation system. VNA: Vector network analyzer. BBS: Broadband source. PC: Polarization controller. EOM: electro-optic modulator. MA: Microwave amplifier. PD: Photodetector. Color inset: Schematic of the sapphire fiber based Michelson OCMI.

A single crystal sapphire fiber based OCMI Michelson interferometer was demonstrated for measurement of high temperatures. As shown in the inset of Figure 23-1, the Michelson interferometer was made by fusion splicing two sapphire fibers onto the two leads of a 3 dB, 2×2 multimode fiber coupler. The fiber coupler was made of graded-index fibers with core and cladding diameters of 62.5 and 125 μm, respectively. The single crystal sapphire fibers (MicroMaterials, Inc.) were uncladded with a diameter of 125 μm. The two leads of the multimode fiber couplers were cleaved to have the same length. The far ends of the sapphire fibers were fine polished.

The incident microwave-modulated light is first split into two paths through the fiber coupler. One beam is reflected from the endface of the sapphire fiber #1; the other beam is reflected from the endface of sapphire fiber #2. The two reflected beams are then recombined at the fiber

coupler. The superposition of the two beams results in an interference signal that is a function of the optical path difference (OPD) between the two different paths. The OPD of the proposed interferometer is longer than the coherence length of the optical source but shorter than the coherence length of the microwave source. As such, the optical carrier waves build up incoherently while the microwave signals (envelopes) build up coherently to form an interferogram in the microwave domain [15].

To reduce the reflection and the transmission attenuation of the joint of silica and sapphire fibers, the sapphire fibers were permanently fusion spliced to the two lead silica fibers of the coupler. A large-core fusion splicer (3SAE) was used to precisely push the sapphire fiber step by step while heated. Then the joint was gradually annealed to release the stress caused by the fusion.

In the experiment, the intermediate frequency bandwidth (IFBW) and the sampling point of the VNA were set to be 700 Hz and 16001, respectively. The driving power from port 1 was 4 dBm. The microwave frequency was swept from 2 to 5 GHz. Without taking averages in data acquisitions and processing, it took about 7 seconds to acquire a microwave spectrum (S_{21}).

23.3 Results and Discussions

Figure 23-2 shows the time domain signal after applying a complex and inverse Fourier transform to the recorded microwave spectrum. The first peak represents the reflections from the fusion points between silica and sapphire fibers. Because the two splice points have almost the same length measured from the coupler, the two reflections generated at the splice points were inseparable in the time domain.

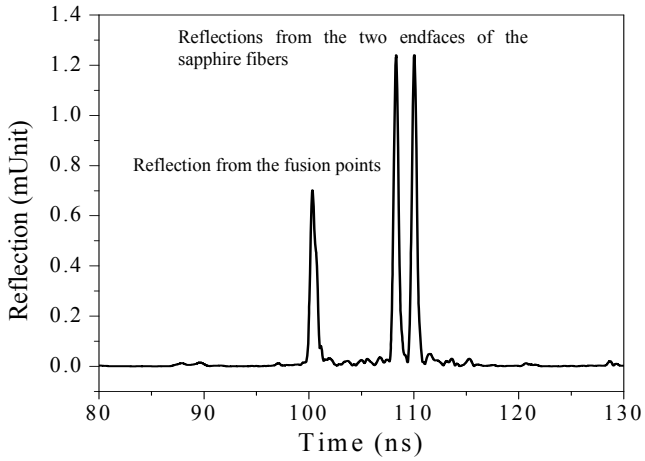

Figure 23-2. Time domain signal after applying a complex and inverse Fourier transform to the recorded microwave spectrum (S_{21}).

The two other two peaks, representing the reflections from the two sapphire endfaces at the far end, can be clearly identified. As illustrated in Figure 23-2, a gate function was applied in the time signal to cut out the two reflections from the sapphire fibers and eliminate the reflections from the silica-sapphire joints. Then the cut-out data was complex Fourier transformed to reconstruct the interferogram as shown in Figure 23-3. This interferogram is the result of the coherent superposition of the two far-end sapphire fiber reflections in the microwave domain, i.e., the OCMI interferogram of the sapphire fiber Michelson interferometer. The fringes are clean with a visibility exceeding 40 dB at the microwave frequency of about 3500 MHz. It is obvious that the multimodal interference in a sapphire fiber does not influence the interferogram in microwave domain, indicating that the OCMI technology is basically insensitive to the multimodal influence. The free spectral range (FSR) was measured to be 571.5 MHz. Based on the equation in [15], the OPD of the interferometer was calculated to be 52.50 cm. Assuming 1.74 to be the effective refractive index of sapphire fiber, the length difference of the two

interferometer arms was estimated to be 15.08 cm, which agreed well with the 15 cm measured by a caliper.

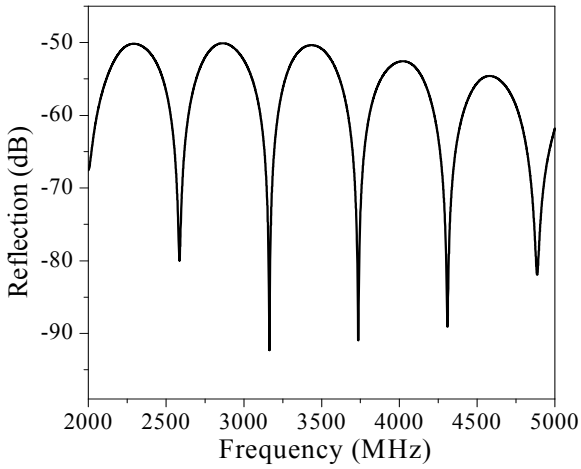

Figure 23-3. Microwave interferogram of the sapphire fiber Michelson OCMI showing a visibility exceeding 40 dB at the microwave frequency of about 3500 MHz.

To avoid breakage and keep them in parallel during test, the two sapphire fiber arms of the interferometer were inserted into a ceramic tube with an inner diameter of 0.5 mm. The ceramic tube hosted sensor was then placed in a programmable tubular electric furnace for characterization of its capability for high temperature sensing. The temperature was increased from 100 to 1400 °C and then decreased back to 100 °C at an incrementing/decrementing step of 100 °C. As the surrounding temperature increased, the OPD of the two beams increased due to the combination of the thermo-optic effect and the thermal expansion of the sapphire material. The increase of OPD induced an interference spectrum shift towards the lower frequency region.

Figure 23-4 (a) and (b) show the interference fringes at different temperatures during increasing and decreasing steps, respectively. The fringe moved towards the low/high frequency regime as the temperature increased/decreased, indicating the optical length of the interferometer increased/decreased correspondingly. It is interesting that the fringe visibility and intensity did

not change too much at temperatures lower than 1000 °C, while it dropped dramatically when the temperature is above 1000 °C. There exist two possible reasons. The first reason could be the large black body radiation of the sapphire fiber at high temperatures functioning as an undesired DC-component, would probably offset the signal and cause saturation to the high-speed photodetector. A possible solution is to add an optical band-pass filter before the photodetector to suppress the radiation in visible and IR regimes. Another possible reason is the thermally induced attenuation in sapphire fibers at high temperature [17]. The attenuation increases almost exponentially at high temperature (up to 1000 °C) and causes huge drop to the fringe intensity shown in Figure 23-4. The deceasing of the fringe visibility is due to the unbalanced reflection from the two arms with different lengths in the heated region. During the temperature deceasing cycle shown in Figure 23-4 (b), the fringes went back their original waveforms indicating a good repeatability.

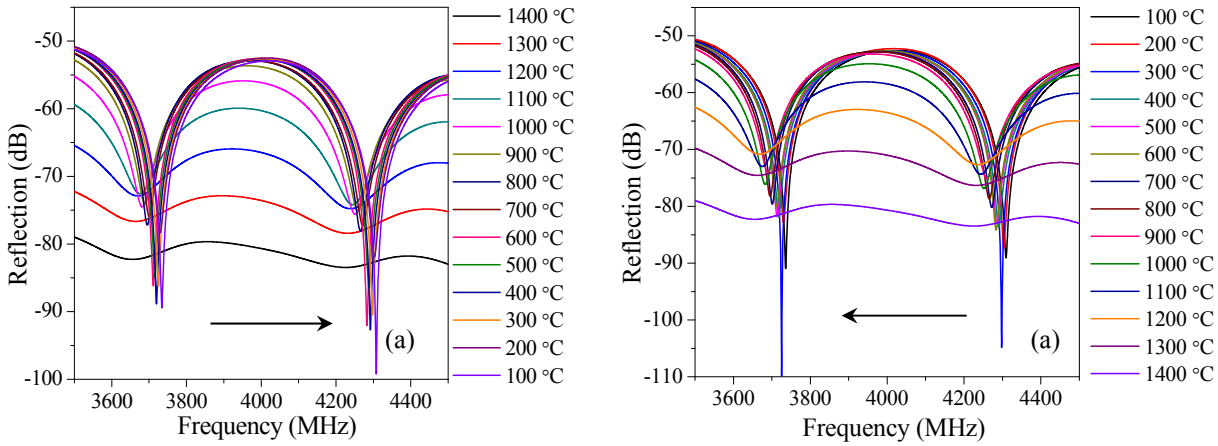

Figure 23-4. Interference fringes of the sapphire fiber based OCMI at different temperatures during (a) increasing and (b) decreasing steps, respectively.

Figure 23-5 plots the center frequency of the interferogram valley at about 4300 MHz at different ambient temperatures. A non-linear relation was observed. The higher the ambient temperature, the slightly larger the temperature sensitivity became. The average temperature sensitivity of the sapphire fiber sensor was estimated to be –64 kHz/°C, demonstrating that the developed sapphire fiber Michelson OCMI could be used as a high temperature sensor with good sensitivity. The temperature responses at the increasing and decreasing cycles also agreed well and showed no obvious hysteresis, indicating a good reversibility of the temperature sensor.

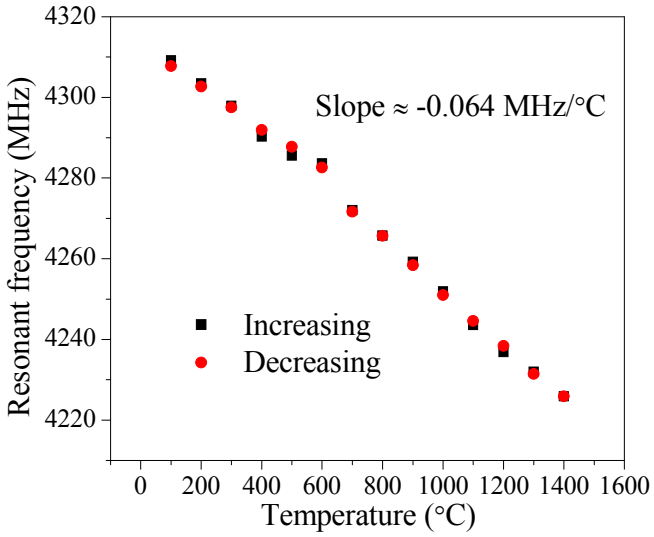

Figure 23-5. The center frequency of the interferogram valley at about 4390 MHz at different ambient temperatures during the temperature increasing and decreasing cycles.

The stability of the sapphire fiber sensor was also characterized. The sensor was placed inside the furnace with temperature rising rate of 100 °C per 30 minutes. The dwelling time at each temperature step was set to be 4 hours during the temperature increasing process. Figure 23-6 (a) and (b) show the recorded sensing data in the duration of more than one hour at 1000 and 1400 °C, respectively. Based on the experimental data, the standard deviation of frequency at 1000 °C were calculated to be ± 0.3 MHz, corresponding to a temperature variation of ± 4.7 °C,

or a relative variation of 4.7×10^{-3}. The standard deviation of frequency at 1400 °C was calculated to be ± 0.45 MHz, corresponding to a temperature variation of ± 7.0 °C, or a relative variation of 5.0×10^{-3}. The results demonstrate good stability of the proposed sensor for high temperature sensing.

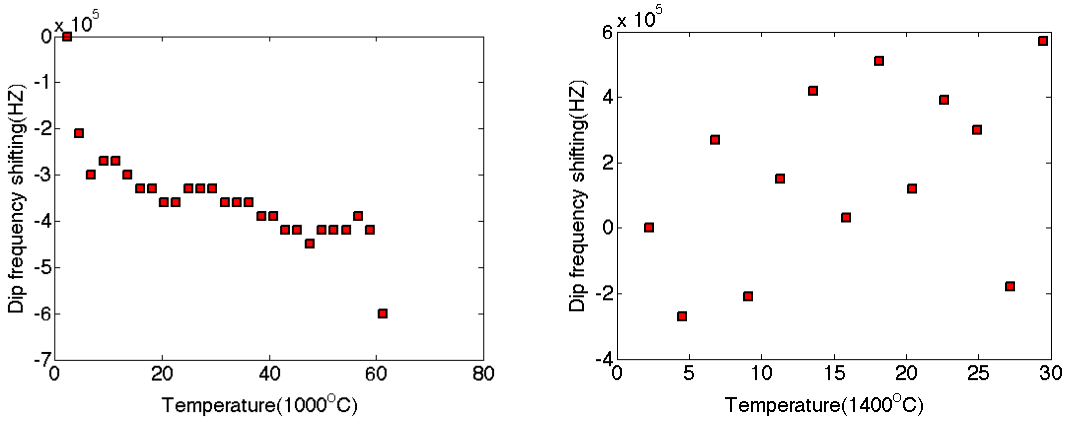

(a) (b)

Figure 23-6. (a) Stability test of the sapphire fiber based Michelson OCMI at (a) 1000°C and (b) 1400°C.

23.4 Summary

In summary, a microwave interrogated sapphire fiber Michelson interferometer was demonstrated for high temperature sensing. Using the optical carrier based microwave interferometry, a high quality interference spectrum of the sapphire fiber interferometer was obtained with a fringe visibility exceeding 40 dB in microwave domain. The sensor was tested from 25 to 1400 °C, showing good sensitivity, reversibility and stability for high temperature sensing. By interrogating the optical interferometer in microwave domain, the OCMI technique offers many unique features including low dependence to the multimodal influences, high signal quality, relieved fabrication precision, and insensitivity to background blackbody radiation when

the sensor is used in high temperature. It is envisioned that the proposed technique can be implemented in other types of sapphire fiber interferometers for measurement of various parameters in high temperature harsh environments.

23.5 References

1. T. G. Giallorenzi, J. A. Bucaro, A. Dandridge, G. Sigel, J. H. Cole, S. C. Rashleigh, and R. G. Priest, "Optical fiber sensor technology," *Microwave Theory and Techniques, IEEE Transactions on* 30, 472-511 (1982).
2. R. K. Nubling, and J. A. Harrington, "Optical properties of single-crystal sapphire fibers," *Applied Optics* 36, 5934-5940 (1997).
3. Y. Shen, L. Tong, Y. Wang, and L. Ye, "Sapphire-fiber thermometer ranging from 20 to 1800 C," *Applied Optics* 38, 1139-1143 (1999).
4. R. Dils, "High-temperature optical fiber thermometer," *Journal of Applied Physics* 54, 1198-1201 (1983).
5. D. Grobnic, S. J. Mihailov, C. W. Smelser, and H. Ding, "Sapphire fiber Bragg grating sensor made using femtosecond laser radiation for ultrahigh temperature applications," *Photonics Technology Letters, IEEE* 16, 2505-2507 (2004).
6. S. J. Mihailov, D. Grobnic, and C. W. Smelser, "High-temperature multiparameter sensor based on sapphire fiber Bragg gratings," *Optics Letters* 35, 2810-2812 (2010).
7. T. Elsmann, T. Habisreuther, A. Graf, M. Rothhardt, and H. Bartelt, "Inscription of first-order sapphire Bragg gratings using 400 nm femtosecond laser radiation," *Optics Express* 21, 4591-4597 (2013).
8. A. Wang, S. Gollapudi, K. A. Murphy, R. G. May, and R. O. Claus, "Sapphire-fiber-based intrinsic Fabry–Perot interferometer," *Optics Letters* 17, 1021-1023 (1992).
9. Y. Zhu, Z. Huang, F. Shen, and A. Wang, "Sapphire-fiber-based white-light interferometric sensor for high-temperature measurements," *Optics Letters* 30, 711-713 (2005).

10. H. Xiao, J. Deng, G. Pickrell, R. G. May, and A. Wang, "Single-crystal sapphire fiber-based strain sensor for high-temperature applications," *Journal of Lightwave Technology* 21, 2276 (2003).

11. H. Jiang, Z. Cao, R. Yang, L. Yuan, H. Xiao, and J. Dong, "Synthesis and characterization of spinel MgAl< sub> 2</sub> O< sub> 4</sub> thin film as sapphire optical fiber cladding for high temperature applications," *Thin Solid Films* 539, 81-87 (2013).

12. Y. Shen, L. Tong, and S. Chen, "Performance stability of the sapphire fiber and cladding under high temperature," in Photonics East'99 (International Society for Optics and Photonics1999), pp. 134-142.

13. R. K. Nubling, R. L. Kozodoy, and J. A. Harrington, "Optical properties of clad and unclad sapphire fiber," in OE/LASE'94 (International Society for Optics and Photonics1994), pp. 56-61.

14. F. Pérennès, P. C. Beard, and T. N. Mills, "Analysis of a low-finesse Fabry-Perot sensing interferometer illuminated by a multimode optical fiber," *Applied Optics* 38, 7026-7034 (1999).

15. J. Huang, X. Lan, H. Wang, L. Yuan and H. Xiao, "Optical carrier based microwave interferometers for sensing application," *Proc. SPIE* 9098, Fiber Optic Sensors and Applications XI, 90980H (2014)

16. J. Huang, X. Lan, M. Luo and H. Xiao, "Spatially continuous distributed fiber optic sensing using optical carrier based microwave interferometry," *Optics Express* 22, 18757-18769 (2014)

17. C.M. Petrie, T.E. Blue, "In Situ thermally induced attenuation in sapphire optical fibers heated to 1400 °C." *Journal of the American Ceramic Society* 13289 (2014)

24. Summary of Major Technical Accomplishments

Under the support of this research program, the team has successfully achieved the preset objectives to develop and demonstrate robust, multiplexed, micro-structured silica and single-crystal sapphire fiber sensors to be deployed into the hot zones of advanced power and fuel systems for measurements of high temperature and gas pressure. Specifically, the team has worked on four major technical areas, including

1) Development and demonstration of novel assembly-free microstructured fiber optic sensors by femtosecond laser micromachining.
2) Design, development and implementation of novel signal processing methods to multiplex and demultiplex cascaded optical fiber sensors for distributed measurements of various parameters.
3) Development and demonstration of a novel method to clad single crystal sapphire fibers for improved optical waveguiding properties and chemical stabilities at high temperatures.
4) Development of robust packages for the developed sensors and characterizations of the developed sensors in simulated high temperature and high pressure environments.

During the project period, we have made many technical breakthroughs that could provide potential solutions to the many challenging problems involved in sensing and monitoring under high temperature and high pressure harsh conditions. These accomplishments are summarized below:

1) Established the fs laser micromachining system with the full capability of automated 3D micromachining as well as material property modifications. The established micromachining system has been used for fabrication of various sensors and devices in different substrates as

well as for educational purposes. Our results have proven the superior properties of micromachined fiber optic sensors for applications in harsh environments.

2) For the first time to our knowledge, an open cavity optical fiber inline extrinsic Fary-Perot interferometer was successfully fabricated using fs laser micromachining technology. The sensor survived high temperatures and showed excellent capabilities towards various sensing applications including temperature-insensitive measurement of refractive indices, which is important for characterization of high temperature materials.
3) For the first time to our knowledge, a sealed cavity optical fiber extrinsic Fabry-Perot interferometer has been fabricated using fs laser micromachining. The sensor, with very short cavity and insensitivity to the outside refractive index changes, has been demonstrated for temperature-insensitive pressure measurement.
4) An intrinsic optical fiber inline Fabry-Perot interferometer has been successfully fabricated using fs laser micromachining. The sensor can be used for distributed measurements of temperature and strain in harsh environments.
5) An optical fiber hybrid extrinsic/intrinsic Fabry-Perot interferometer (HEIFPI) has been fabricated and demonstrated for simultaneous measurements of high temperature and pressure.
6) An optical fiber inline Michelson interferometer has been fabricated using fs laser micromachining and successfully demonstrated for high temperature measurements. The sensor has the unique advantage of insensitivity to fiber bending. In addition, it operates in a reflective mode that makes the sensor deployment convenient.
7) An optical fiber inline Mach-Zehnder interferometer has been fabricated using fs laser micromachining. The sensor device has the potential for measurement of gas variations in the

hot zone of an energy system.

8) Fiber Bragg gratings and long period fiber gratings have been successfully fabricated using the established fs laser micromachining system. The gratings have the unique advantage of surviving and operating in high temperature environments.
9) For the first time to our knowledge, a reflective mode surface enhanced Raman scattering fiber probe was fabricated using fs laser in various optical fibers (e.g., SMF, MMF, and sapphire). The probes have shown good performance for chemical detection and identification.
10) For the first time to our knowledge, optical fiber inline waveplates and optical fiber inline polarizers were fabricated using fs laser micromachining. These polarization dependent devices can be used not only for sensing but also in optical fiber communication systems.
11) For the first time to our knowledge, optical fiber inline microfluidic channels have been successfully fabricated using fs laser micromachining assisted by chemical etching. The microfluidc channels can be used for liquid/gas sensing/analysis, which has a great potential in biomedical applications.
12) We have successfully designed and demonstrated the proposed novel wavelength division multiplexing based signal processing method to simultaneous interrogation of a number of cascaded microstructured optical fiber sensors. The signal processing technique has been successfully used for simultaneous measurements of temperature and pressure using the fiber optic HEIFPI sensors.
13) We invented a brand new sensing concept – the optical carrier based microwave interferometry (OCMI) sensing technology. For the first time to our knowledge, gigh performance interferograms can now be obtained routinely using OCMI on highly multimode

optical fibers (including the uncladded sapphire fibers). By combining the advantages from optics and microwave, the OCMI has the unique advantages of high signal quality, relieved requirement on fabrication, low dependence on the types of optical waveguide, and insensitivity to the variations of polarization.

14) For the first time to our knowledge, spatially continuous, fully distributed sensing has been successfully demonstrated using the new OCMI technology together with the modern communication technology and fs laser micromachining technique.

15) We have successfully cladded the sapphire fibers and validated their performance up to 1200℃. This is the first demonstration of such optically-functional high-temperature cladding for sapphire fibers. We successfully synthesized spinel thin film as cladding coating of the sapphire fiber using polymeric precursor method. The coating process has been fully optimized to obtain defect-free and optically functional cladding layers. The coated sapphire fibers were fully characterized experimentally to show their superior optical properties and high temperature stabilities.

16) We have established a high temperature sensor testing facility with the full capability of testing the developed sensors under high temperature and high pressure conditions.

17) We have successfully designed and implemented a new method to package the developed sapphire fiber sensor for high temperature measurement and successfully validated the packaged sensor at high temperatures up to 1600°C.

Under the close collaborations among the three research groups, we have completed all the tasks and fulfilled the proposed research objectives. All the technical milestones have been achieved and the project has been completed successfully. The technical breakthroughs obtained under this project produced many novel harsh environment sensing technologies that could be

directly used in existing and next generation power and fuel systems for *in situ* monitoring and advanced control of key operational parameters to achieve the challenging goals of enhanced efficiency, reduced emission, and improved reliability/availability/maintainability. The research may also have profound impacts on the general field of harsh environment sensing as it fosters a number of new inventions that may benefit the sensors and instrumentation community as well as the entire energy sector.

25. List of Publications Resulted from the Funded Research

25.1 Journal Papers

1. L. Hua, Y. Song, J. Huang, X. Lan, H. Xiao1, "Microwave interrogated large core fused silica fiber interferometer for temperature insensitive strain sensing," Manuscript in preparation.
2. L. Yuan, J. Huang, J. Liu, H. Wang, X. Lan, H. Xiao, "Stress-induced birefringence and in-fiber polarization devices fabricated by femtosecond laser," Manuscript in preparation.
3. J. Huang, X. Lan, Y. Song, Y. Li, L. Hua and H. Xiao, "Microwave interrogated sapphire fiber Michelson interferometer for high temperature sensing," Manuscript under review.
4. Y. Zhang , J. Huang , X. Lan , L. Yuan, and H. Xiao, "Simultaneous measurement of temperature and pressure with cascaded EFPI and IFPI Sensors," *Optical Engineering*, Optical Engineering, vol. 53, pp. 067101, 2014.
5. L. Yuan, X. Lan, J. Huang, H. Wang, L. Jiang, and H. Xiao, "Comparison of silica and sapphire fiber SERS probes fabricated by a femtosecond laser," *IEEE Photonics Technology Letters*, vol. 26, pp.1299 - 1302, 2014.
6. J. Huang, X. Lan, A. Karl, H. Wang, L. Yuan, H. Xiao, "Temperature Compensated Refractometer based on a Cascaded SMS/LPFG Fiber Structure," *Sensors and Actuators: B-Chemical*, vol. 198, pp. 384–387, 2014.
7. L. Yuan, J. Huang, X. Lan, H. Wang, L. Jiang, Hai Xiao, "All-in-fiber optofluidic sensor fabricated by femtosecond laser assisted chemical etching," *Optics Letters*, vol. 39, pp. 2358-2361, 2014.
8. Y. Zhang, L. Yuan, X. Lan, A. Kaur, J. Huang, and H. Xiao, "High temperature fiber optic Fabry-Perot interferometric pressure sensor fabricated by femtosecond

laser," *Optics Letters*, vol. 38, pp. 4609-4612, 2013.

9. H. Jiang, Z. Cao, R. Yang, L. Yuan, H. Xiao, J. Dong, "Synthesis and characterization of spinel MgAl2O4 thin film as sapphire optical fiber cladding for high temperature applications," *Thin Solid Films*, vol. 539, pp. 81-87, 2013.
10. J. Huang, X. Lan, A. Kaur, H. Wang, L. Yuan, H. Xiao, "Reflection based Phase Shifted Long Period Fiber Grating for Simultaneous Measurement of Temperature and Refractive Index," *Optical Engineering*, vol. 52, id. 014404, 2013.
11. L. Yuan, T. Wei, Q. Han, H. Wang, J. Huang, L. Jiang, H. Xiao, "Fiber Inline Michelson Interferometer Fabricated by a Femtosecond Laser,"*Optics Letters*, vol. 37, pp. 4489-4491, 2012.
12. Q. Han, X. Lan, J. Huang, A. Kaur, T. Wei, Z. Gao, and H. Xiao, "Long-period grating inscribed on concatenated double-clad and single-clad fiber for simultaneous measurement of temperature and refractive index," *IEEE Photonics Technology Letters*, vol. 24, pp.1130 – 1132, 2012.
13. T. Wei, J. Huang, X. Lan, Q. Han, and H. Xiao, "Optical Fiber Sensor based on Radio Frequency Mach-Zehnder Interferometer," *Optics Letters*, vol. 37, pp. 647-649, 2012.
14. J. Huang, X. Lan, T. Wei, Q. Han, Z. Gao, Z. Zhou, and H. Xiao, "Radio Frequency Interrogated Actively Mode-locked Fiber Ring Laser for Sensing Application," *Optics Letters*, vol. 37, pp. 494-496, 2012.
15. I. Hamdorf, M. Olson, C.-H. Lin, L. Jiang, J. Zhou, H.L. Tsai, H. Xiao, "Femtosecond and nanosecond laser fabricated substrate for surface–enhanced Raman scattering," *Optics Letters*, vol. 36, pp. 3353–3355, 2011.
16. C.-H. Lin, L. Jiang, H. Xiao, S.-J. Chen, H.-L. Tsai, "Surface-enhanced Raman scattering

microchip fabricated by femtosecond laser," *Optics Letters*, vol. 35, pp.2937-2939, 2010.

17. Y. Han, T. Wei, H.L. Tsai, H. Xiao, "Measurement of refractive index change of optical fiber core induced by femtosecond laser scanning,"*Optical Engineering*, vol. 49, pp.064301, 2010.
18. C.H. Lin, L. Jiang, Y.H. Chai, H. Xiao, S.J. Chen, H.L. Tsai, "A Method to Fabricate 2D Nanoparticle Arrays," *Applied Physics A*., vol. 98, pp. 855-860, 2010.
19. C.H. Lin, L. Jiang, J. Zhou, H. Xiao, S.J. Chen, H.L. Tsai, "Laser-Treated Substrate with Nanoparticles for Surface-Enhanced Raman Scattering," Optics Letters, vol. 35, pp. 941-943, 2010.
20. C.-H. Lin, L. Jiang, Y.-H. Chai, H. Xiao, S.-J. Chen, and H.-L. Tsai, "One-step fabrication of nanostructures by femtosecond laser for surface-enhanced Raman scattering," Optics Express, vol. 17, pp. 21581-21589, 2009.

25.2 Conference Papers

1. H. Xiao, T. Wei, X. Lan, Y. Zhang, H. Duan, Y. Han, H.L. Tsai, "Optical Fiber Sensors for Harsh Environment Monitoring," ASCE Earth & Space 2010 Conference, Honolulu, Hawaii, 2010. (invited)
2. H. Xiao, T. Wei, X. Lan, Y. Zhang, H. Duan, Y. Han, H. L. Tsai, "Optical fiber sensors for high temperature harsh environment applications," Proc. of SPIE, vol. 7647, 76470U, 2010.
3. Y. Zhang, X. Lan, T. Wei, H. Duan, H. Xiao, "Side-coupled optical fiber devices for sensing applications," Proc. of SPIE, vol. 7682, 76820K, 2010.
4. H. Duan, X. Lan, T. Wei, Y. Zhang, H. Xiao, "Characteristics and application of phase

shifted long period fiber grating fabricated by CO2 laser," Proc. of SPIE, vol. 7682, 768207, 2010.

5. T. Wei, X. Lan, H. Xiao, Y.K. Han, H.L. Tsai, “Optical Fiber Sensors for High Temperature Harsh Environment Sensing,” 2011 IEEE International Instrumentation and Measurement Technology Conference, Hangzhou, China, 2011.
6. L. Yuan, H. Wu, C. Wang, Y. Yu, S. Wang, H. Xiao, "Fiber inline Michelson interferometer fabricated by one-step femtosecond laser micromaching for sensing applications," Proc. of SPIE, vol. 9044, 90441M, 2013.
7. L. Yuan, X. Lan, J. Huang, H. Wang, B. Cheng, H. Xiao, "Miniaturized optical fiber Fabry-Perot interferometer fabricated by femtosecond laser irradiation and selective chemical etching," Proc. of SPIE, vol. 8974, 89741A, 2014.